NATIONAL INSTITUTE FOR FUSION SCIENCE

Proceedings of JSPS-CAS Core University Program Seminar
on Production and Steady State Confinement
of High Performance Plasmas in Magnetic Confinement Systems
27-29 July, 2005, Hefei, China

B. Wan and K. Toi (Eds.)

**RESEARCH REPORT
NIFS-PROC Series**

TOKI, JAPAN

Proceedings of JSPS-CAS Core University Program Seminar
on Production and Steady State Confinement
of High Performance Plasmas in Magnetic Confinement Systems
27 - 29 July, 2005, Hefei, China

Edited by

Baonian Wan   and   Kazuo TOI

Abstract

The JSPS-CAS Core University Program (CUP) seminar on "*Production and steady-state confinement of high performance plasmas in magnetic confinement systems*" was held from 27 July to 29 July 2005 in Institute of Plasma Physics, the Chinese Academy of Sciences, Hefei, China. This seminar was organized in the framework of CUP in the field of plasma and nuclear fusion. About 50 persons including 20 Japanese attendees attended this seminar.

Long time sustainment of high confinement and high beta plasmas is crucial for realization of an advanced nuclear fusion reactor. This seminar was motivated to summarize the results of CUP obtained in four years activities of CUP, and to extract crucial issues to be resolved near future, which must drive near and mid- term collaborations in the framework of CUP.

Key words: advanced fusion reactor, magnetic confinement systems, improved confinement regimes, long time sustainment of plasma, MHD stability, high beta plasma and plasma collapse, edge plasma control and divertor, advanced heating methods, advanced plasma diagnostics for burning plasma.

Organizing Committee

Baonian WAN (Chairperson, Institute of Plasma Physics, Chinese Academy of Sciences, China)
Kazuo TOI(Chairperson, National Institute for Fusion Science, Japan)

Program Committee

T. Watari (National Institute for Fusion Science, Japan)

C. Namba (National Institute for Fusion Science, Japan)

T. Maekawa (Kyoto University, Japan)

K. Toi (National Institute for Fusion Science, Japan)

K. J. Wang (Institute of Plasma Physics, Chinese Academy of Sciences, China)

B. N. Wan (Institute of Plasma Physics, Chinese Academy of Sciences, China)

J. K. Xie (Institute of Plasma Physics, Chinese Academy of Sciences, China)

X. Gao (Institute of Plasma Physics, Chinese Academy of Sciences, China)

Conference Secretariat

Shaohua Dong (Secretary, Institute of Plasma Physics, Chinese Academy of Sciences, China)

Liqun Hu (Scientific secretary, Institute of Plasma Physics, Chinese Academy of Sciences, China)

Preface

The JSPS-CAS Core University Program (CUP) seminar on *"Production and steady-state confinement of high performance plasmas in magnetic confinement systems"* was held from 27 July to 29 July 2005 in Institute of Plasma Physics, the Chinese Academy of Sciences, Hefei, China. This seminar was organized in the framework of CUP in the field of plasma and nuclear fusion. About 50 persons including 20 Japanese attendees attended this seminar.

Long time sustainment of high confinement and high beta plasmas is crucial for realization of an advanced nuclear fusion reactor. Toward this target, a lot of collaboration programs between Japan and China have been carried out for past four years in the category of "improvement of core plasma properties" of CUP. This seminar was motivated to summarize the results of CUP and to extract crucial issues to be resolved near future. In this seminar, 32 oral presentations were made and focused on the following topics:

1. improved confinement regimes,
2. long time sustainment of plasma,
3. MHD stability, high beta plasma and plasma collapse,
4. edge plasma control and diverter,
5. advanced heating methods,

and

6. advanced plasma diagnostics for burning plasma.

These topics are important, regardless of the difference in magnetic configurations such as tokamaks and helical devices, and were intensively discussed from experimental and theoretical sides. In addition, engineering aspects were stressed on several topics.

This seminar was closed with great success, clarifying remarkable progress in researches related to these important topics through CUP. The organizing and program committees are grateful to all participants for their support and coorporation to this seminar.

Baonian WAN and Kazuo TOI

Chairpersons of the Organizing Committee

Contents

Preface

Contents

Photo of Participants

Talks

22. Measurement of zonal flows in a Tokamak using Langmuir probe array by G.S. Xu (ASIPP)

23. Suppression of neoclassical tearing modes towards stationary high-beta plasmas in JT-60U

      by A. Isayama (JAERI)

24. Overall feature of EAST operation space by using simple Core-SOL-Divertor model

      by R. Hiwatari (CRIEPI)

25. Assessments of flow drive by use of ion Bernstein wave on Heliotron-J and HT-7 devices

      by Y. Torii (Kyoto Univ.)

26. Advanced tokamak equilibrium theory by Shaojie Wang (ASIPP)

27. Magnetic sensorless control of plasma position and shape in a tokamak

      by K. Nakamura (Kyushu Univ.)

28. Low frequency instability in magnetized plasma column by Jinlin Xie (USTC)

29. Spectroscopic studies on impurity transport of core and edge plasmas in LHD

      by S. Morita (NIFS)

30. Impurity measurement and study on HL-2A divertor tokamak by Z. Y. Cui (SWIP)

31. The progress of ECEI diagnostic project on HT-7 by Jun Wang (USTC)

32. Dust particle behaviors in boundary plasma of fusion devices by Y. Tomita (NIFS)

Agenda

List of Participants

JSPS-CAS CUP Seminar on Production and Steady State Confinement of High Performance Plasmas in Magnetic Confinement Systems

27-29 July, 2005, Hefei, China

Long pulse operation of high performance plasmas in JT-60U

S. Ide and the JT-60 team

Naka Fusion Research Establishment, Japan Atomic Energy Research Institute
Naka, Ibaraki, 311-0193 Japan

Abstract : Recent experimental progress in JT-60U advanced tokamak research is presented; sustainment of the normalized beta (β_{N}) $\sim$ 3 in a normal magnetic shear plasma, the bootstrap current fraction (f_{BS}) $\sim$ 45% in a weak shear plasma and $\sim$ 75% in a reversed magnetic shear plasma in a nearly full non-inductive current drive condition for longer than the current relaxation time. Achievement of high-density high-radiation fraction together with high-confinement in advanced plasmas was demonstrated. Achievement and foundings in long pulse operations after system modification are presented as well. A 65 s discharge of $I_{\mathrm{p}} = 0.7$ MA was successfully obtained. As a result, high-β_{N} of 2.3 was successfully sustained for a very long period of 22.3 s. In addition, a 30 s standard ELMy H-mode plasma of I_{p} up to 1.4 MA has also been obtained. Effectiveness of divertor pumping to control particle recycling and the electron density under the wall retention was saturated was demonstrated. These achievement and issues in the development will be discussed.

1 Introduction

For development towards ITER advanced operations and steady-state (SS) tokamak fusion reactor, sustainment of high confinement with high normalized beta (β_{N}), high bootstrap current fraction (f_{BS}) to the total plasma current (I_{p}) and heat/particle handling to be compatible with the divertor is one of the most important issues. ITER hybrid operation is defined as high output long pulse discharge for high fluence, and ITER steady-state operation is defined as Q (fusion gain) $\geq$ 5 in a full non-inductive current drive (CD) steady-state. In a steady-state tokamak fusion reactor, a value $f_{\mathrm{BS}} \gtrsim 70\%$ is typically required [1], and $\beta_{\mathrm{N}} \sim$ 3.5 or even more (4–5) would be required. This is the so-called advanced tokamak (AT) concept. Towards these targets, JT-60U AT-relevant plasmas, one with weak magnetic shear ("high-β_{p} plasma", β_{p} denotes the poloidal beta) and one with reversed magnetic shear ("RS plasma"), have been pursued by utilizing various heating/current drive systems (neutral bema (NB); positive-ion base NB: P-NB, negative-ion based NB: N-NB, radio frequency (RF); elecgtron cyclotron range of frequency: ECRF, lower hybrid range of frequency: LHRF). Both plasmas have good confinement characteristics owing to a formation of the internal transport barrier (ITB). An ITB is also beneficial to raise f_{BS}. An edge transport barrier, in other word the H-mode pedestal, also contributes to improve confinement and to raise f_{BS}. A high-β_{p} plasma has monotonic or weak magnetic shear and attained very high β_{N} up to 4.8, high f_{BS} of about 70% and full non-

inductive CD. On the other hand a RS plasma has reversed magnetic shear with high q_0 (the safety factor at the plasma center) or sometimes a current hole in the core region and attained high β_N of 2.5–2.8 and high f_{BS} up to about 80% and full non-inductive CD. Both plasmas have good confinement characteristics owing to a formation of the internal transport barrie. Recent JT-60U experiments have achieved sustainment of good candidate plasmas for ITER advanced operations and an SS reactor based upon these JT-60U AT relevant plasmas long enough in view of current profile relaxation. For assessment of long pulse operation in ITER and future reactors, modification on the JT-60U operation system was carried out to extend the maximum pulse length from 15 to 65 s. In this paper, the achievements and issues in the development will be discussed [2].

2 Development AT relevant plasmas towards ITER advanced operations and a steady-state reactor

As described above, high-β_N and high-f_{BS} are key issues. Towards establishment of these goals, a profile of the current density $j(\rho)$ (ρ is the flux normalized radius) or the safety factor $q(\rho)$ is an important factor. In this section, achievement in AT development towards ITER advanced operation and an SS reactor is described in view of $q(\rho)$ and its sustainment relative to the current relaxation time (τ_R). In this paper, τ_R is defined as $\mu_0 \langle \sigma \rangle a^2 / 12$, where $\langle \sigma \rangle$ is the volume average of the plasma conductivity and a is the plasma minor radius [3].

2.1 High β_N sustainment in a monotonic shear plasma

As described above, the purpose of ITER hybrid operation is to obtain high fusion power for long duration for high-fluence. For this, higher β_N is preferable. And q_0 close to but above unity would be preferred for higher output and sawtooth avoidance. That is a monotonic magnetic

shear with $q_0 \sim 1$ would be expected in this regime. One of the most important instabilities that prevent sustainment of high-β_N is the neo-classical tearing mode (NTM) in this domain. In JT-60U, it has been shown optimization of the current and pressure profiles is a key to avoid occurrence of an NTM [4]. And we had succeeded in sustaining $\beta_N = 2.7$ for 7.4 s [5]. By further optimization of a high-β_p ELMy H-mode plasma in a very low-q_{95} regime of 2.2–2.8 (here q_{95} is the safety factor at the 95% toroidal flux) with $I_p = 1$ MA and $B_t = 1.66$ T (the toroidal magnetic field at the plasma major radius) and high-β_N of 3 was successfully sustained for 6.2 s as shown in Fig. 1 [4, 6]. In JT-60U,
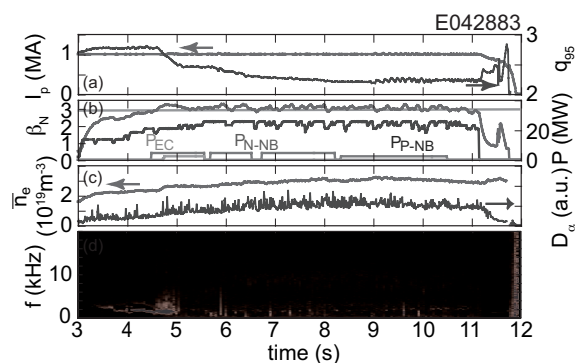
Fig. 1: Typical waveforms of the $\beta_N = 3$ discharge. (a) I_p and q_{95}, (b) β_N and the heating powers (P-NB, N-NB and ECRF), (c) $\bar{n}_e$ and D_α intensity, (d) the magnetic fluctuation. No clear activity is observed in (d) during $\beta_N = 3$.

discharges with this high β_N but at higher q_{95} above 3 usually suffer from NTM, however in the discharge, no distinct NTM had been observed. This could be attributed partly to the very low-q operation. Since q_0 was found to be kept around unity in the discharge, lowering q_{95} shifted the NTM resonant surfaces, $q = 1.5$ or 2 rational surfaces, outwards where the pressure gradient is generally less steep and favorable to avoid the NTM. Moreover, the downward shift of the plasma made the NB deposition profile broader, thus the pressure gradient became smaller as well. This is also preferable for NTM avoidance. The duration of the high-β_N sustainment, 6.2 s, corresponds to 4.1 times τ_R, although q_{95} kept decreasing until about 8 s

it could be expected that the current profile had almost reached the equilibrated state. Since the pressure profile could reached the steady-state in much shorter time scale, that is the energy confinement time (τ_E), the discharge could be a demonstration of an NTM-free high-β_N operation. The result is contributing to development of ITER hybrid operation domain.

2.2 Sustainment of weak shear plasma in nearly full-CD with high f_{BS}

As mentioned before, f_{BS} around 50% or higher is expected in the ITER steady-state scenario. Various q profiles can be consistent with this level of f_{BS}, from one with (weak) positive shear to one with (weak) negative shear profile. Among them, a flat q profile with $q_0 \sim 1.5$–2.5 could be preferable, in view of MHD stability, α-particle confinement, f_{BS}, and easier external $j(\rho)$ control. In JT-60U, this domain has been investigated with the high-β_p ELMy H-mode [7]. Sustainment of an ITER steady-state relevant plasma with a weak shear profile under full-CD condition for long enough in terms of current profile relaxation was investigated with negative-ion based NB (N-NB) [8]. A rate of I_p ramp-up and timing and waveform of the NB heating were optimized so as to prevent q_0 from falling to unity and to develop ITB to increase off-axis bootstrap current to raise q_0 and to form a weak shear. As a result, a discharge with $I_p = 1$ MA at $B_t = 2.40$ T and $\bar{n}_e \sim 2.7 \times 10^{19}$ m^{-3} was successfully maintained under almost full non-inductive state, the fraction of the non-inductively driven current (BS and NBCD) to the plasma current (f_{CD}) > 90%, with $f_{BS} \sim 45\%$ is maintained for 5.8 s (Fig. 2). Due to the off-axis BS current, the q profile is almost flat, with slight reversal in the core region. The minimum in the q profile (q_{min}) is around 1.5, as shown in Fig. 3. Since this was not full-CD, q_{min} decreased slightly. However, no clear NTM was observed during the 5.8 s period, probably because q_{min} stays just around 1.5. The duration, 5.8 s, was determined by the N-NB injection, and corresponded to 2.8 τ_R.

As well as the previous plasma, this duration can be long enough in view of current relaxation to confirm the applicability of this operation to the ITER steady-state operation. It should be stressed here that not only the current drive capability (f_{BS} and f_{CD}), but the value of β_N obtained in this plasma ($\beta_N = 2.4$) is also close to that expected in ITER steady-state operation. The confinement improvement factor to the ITER L-mode scaling H_{89P} was 1.9–2.2 and that to the ITER ELMy H-mode scaling ($HH_{98(y,2)}$) corresponding to H_{89P} of 2.2 was about unity.
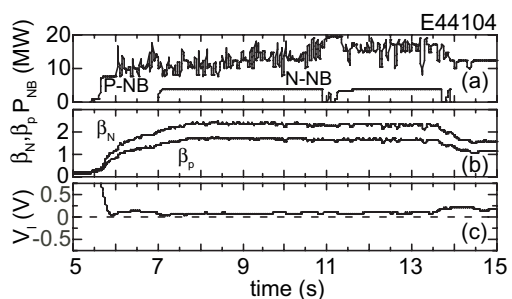
Fig. 2: Typical waveforms of the weak shear ELMy H-mode discharge with $f_{BS} \sim 45\%$ under nearly full non-inductive current drive: (a) injected P-NB and N-NB powers, (b) β_N and β_p, (c) the surface loop voltage (V_l). Nearly full-CD was maintained with constant β_p.
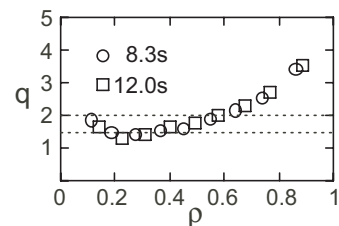
Fig. 3: The safety factor profiles of the E44104 at 8.3 (open circles) and 12 s (open squares).

2.3 Sustainment of RS plasma with very high f_{BS}

In a reactor design, f_{BS} of 70% or higher is expected. An RS plasma is expected to be well consistent with such a high-f_{BS} operation. Since in an RS plasma a strong ITB is often found to

be formed and the ITB improves the confinement characteristics. The ITB formation contributes to increasing the bootstrap current at the ITB that is off-axis location, and this off-axis bootstrap current maintains or even elevates the central q. A very high f_{BS} (80%) RS plasma ($I_p = 0.8$ MA, $B_t = 3.4$ T) was obtained and that high f_{BS} was sustained for 2.7 s with $f_{CD} \sim$ 100% in JT-60U [9]. Further optimization of a similar plasma ($I_p = 0.8$ MA, $B_t = 3.4$ T) had been performed in order to extend long enough compared to τ_R the duration in order to confirm capability of a high-f_{BS} RS discharge for a steady-state operation. Off-axis NB heating was constantly injected to maintain the ITB. Discharges have often suffered a collapse or a disruption when q_{min} crosses four. Avoidance of a collapse was a key to extend the pulse duration. Change in the toroidal velocity profile had been found to modify the ITB strength [10], and this technique was adopted by switching off the on-axis counter (to the I_p direction) parallel P-NB just before q_{min} crossed four. As a result, the disruption was avoided, and a high f_{BS} of $\sim$ 75% is successfully sustained for 7.4 s with very high confinement of $HH_{98(y,2)} = 1.7$ ($H_{89P} \sim$ 3.0) (Fig. 4) [8]. The duration corresponds to $\sim$ 2.7 τ_R. As shown in Fig. 5, the q profile almost had reached the steady-state.

Fig. 5: Evolution of the q profile in E43046.

3 Extension of JT-60U pulse towards long pulse discharge

As described above, extension of AT relevant plasmas over several times τ_R had been successfully demonstrated. For further assessment in a condition where the current and pressure profiles are both fully frozen and to investigate issues in long pulse operation that had not unveiled in conventional pulse length, the maximum pulse length of a JT-60U discharge was extended up to 65 s from 15 s. This was done by modification of the controls in the operation, heating and diagnostics systems of the JT-60U facility without major hardware upgrade. The maximum heating duration of the P-NBs was extended from 10 s to 30 s, as well. As a result, a 65 s discharge with $I_p = 0.7$ MA (flat top of $\sim$ 60 s) was obtained. And a 30 s NB heated plasma has been obtained with I_p up to 1.4 MA.

3.1 Long pulse high-β_N discharge

As described before, we have succeeded in increasing sustainable β_N up to 3. We also have aimed at extending duration of high β_N sustainment much longer. That is one of the most important purposes of the JT-60U pulse length extension modification. By optimizing high-β_p ELMy H-mode plasmas at $I_p = 0.9$ MA at $B_t = 1.56$ T and $q_{95} \sim 3.2$, $\beta_N = 2.3$ was successfully maintained for 22.3 s (Fig. 6) [6]. This corresponds to 13.1τ_R. Sustainment of higher β_N of 2.5 was also achieved but with little shorter sustained duration of 16.5 s. The evolution of β_N was carefully optimized in order to maximize β_N while avoiding the neo-classical tearing mode, since the sustainable power is not enough

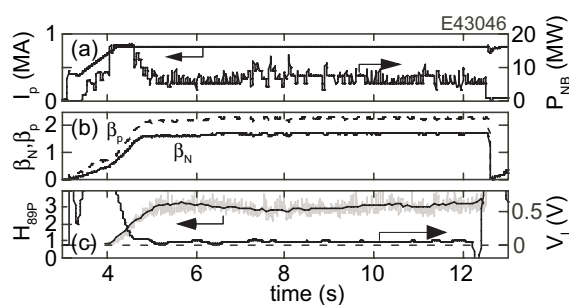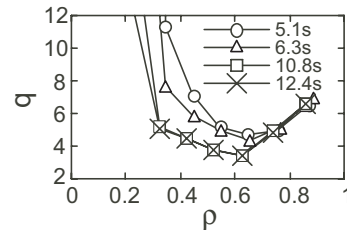

Fig. 4: Typical waveforms of the high-f_{BS} ($\sim$ 75%) reversed shear ELMy H-mode discharge under nearly full non-inductive current drive: (a) I_p and P_{NB}, (b) β_N (solid curve) and β_p (dotted curve), (c) H_{89P} and V_l.

4

to raise β_N with an NTM. As a result, no distinct NTM was observed for these discharges. A factor $H_{89P}\beta_N/q_{95}^2$, which is a figure of merit of the fusion performance, was kept $\gtrsim 0.4$ for 22.3 s. In ITER standard ELMy H-mode scenario with $Q = 10$, $H_{89P}\beta_N/q_{95}^2 \sim 0.4$ is expected, while in ITER steady state scenario with $Q = 5$, $H_{89P}\beta_N/q_{95}^2 \sim 0.3$ is expected. Achievement in these parameters indicates that these JT-60U charges in this domain can be candidates for ITER hybrid operation. No significant phenomena that prevents high-β_N sustainment has occurred in such a very long duration relative to τ_R. This would be encouraging for ITER hybrid operation. Progress of sustainable β_N is shown in Fig. 7.
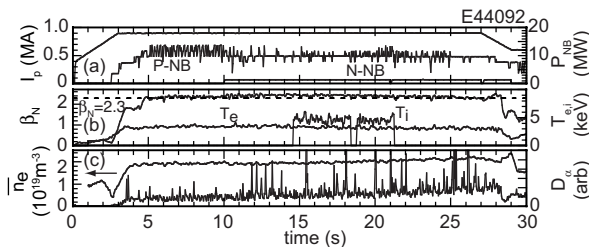

Fig. 6: Typical waveforms of the high-β_N (= 2.3) long sustainment discharge: (a) I_p and the NB powers (P-NB and N-NB), (b) β_N and T_e and T_i near the plasma center. (c) $\bar{n}_e$ and the D_α intensity.
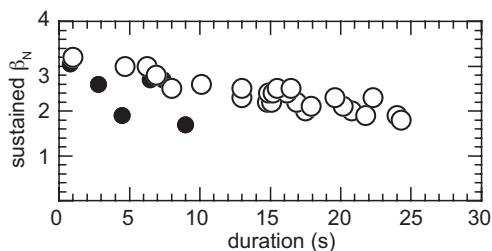

Fig. 7: Progress of sustainable β_N, sustained β_N is plotted against sustaining duration. Closed circles indicate the results obtained before the long pulse modification, while open circle represents the result after the conference.

3.2 Effect of divertor pumping in a high-recycling ELMy H-mode

Another important issue in long pulse operation is a change in wall recycling that has a longer time scale than the current diffusion. As shown in Fig. 6, β_N gradually decreased in the later phase. This indicates that confinement was decreased. At the same time an increase in the wall recycling that appeared as an increase in the D_α line brightness (Fig. 6 (c)) was observed. Decrease in the confinement accompanied by increasing D_α intensity has been often observed in JT-60U long pulse discharges. Therefore, the degradation of confinement is attributed to the increase in recycling whether directly or indirectly. Therefore it is important to control wall recycling in a long pulse operation. In order to investigate control of wall recycling, a high-recycling ELMy H-mode plasma had been studied [11]. It was shown that with gas-puffing and/or series of high-recycling discharges, the wall retention could be saturated in a later half of a long pulse high-recycling ELMy H-mode discharge. When the wall retention saturated, both n_e and D_α increased uncontrollably. The divertor of JT-60U is the so-called 'W-shaped' divertor [12]. The pumping slots are located at both ends of the dome, and divertor pumping works when one or both divertor leg(s) is located near the slot. Effect of divertor pumping when the wall retention was almost saturated was investigated in high-recycling ELMy H-mode plasmas mainly by changing the distance between the inner divertor leg and the pumping slot. It is shown that the rate of increases of the total ion population (dN_i/dt, where N_i is the number of the total deuterons in the plasma) monotonically decreases as the divertor pumping rate increases. It should be noted here that the saturation in wall retention became observable in JT-60U only with the extension of the pulse length. That is, modification for long pulse discharge has opened new domain not only for high-β_N sustainment but also for particle recycling studies.
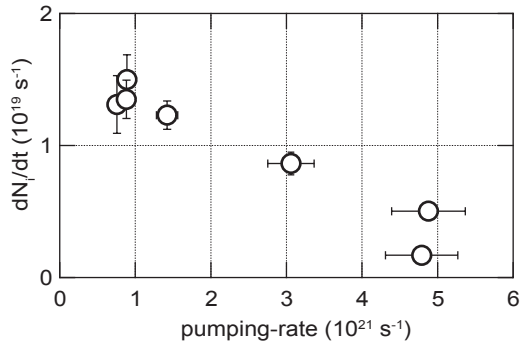
Fig. 8: Increase rate of number of deuterons in the core plasma as a function of divertor-pumping-rate under the condition of wall-pumping rate of ~ 0.

4 Summary

Recent experimental progresses in JT-60U advanced tokamak research are presented; sustainment of $\beta_N \sim 3$ in a normal magnetic shear plasma, the bootstrap current fraction (f_{BS}) $\sim$ 45% in a weak shear plasma and $\sim$ 75% in a reversed magnetic shear plasma in a nearly full non-inductive current drive condition for longer than the current relaxation time (τ_R). These results contribute to ITER advanced operations and a steady-state tokamak reactor development. Also achievement and foundings in long pulse operations after system modification are presented. A 65 s discharge of $I_p = 0.7$ MA was successfully obtained. As a result, high-β_N of 2.3 was successfully sustained for a very long period of 22.3 s. In addition, a 30 s standard ELMy H-mode plasma of I_p up to 1.4 MA has also been obtained. Effectiveness of divertor pumping to control particle recycling even under the wall retention saturated was demonstrated.

Acknowledgment

References

[1] M. Kikuchi, Nucl. Fusion **30**, 265 (1990).

[2] S. Ide and the JT-60 Team, *Overview of JT-60U Progress towards Steady-state Advanced Tokamak*, submitted to Nuclear Fusion .

[3] D. R. Mikkelsen, Phys. Fluids **B1**, 333 (1989).

[4] A. Isayama and the JT-60 Team, Phys. Plasmas **12**, 056117 (2005).

[5] A. Isayama, *et al.*, Nucl. Fusion **43**, 1272 (2003).

[6] T. Suzuki *et al.*, *Steady State High β_N Discharges and Real-Time Control of Current Profile in JT-60U*, submitted to Nuclear Fusion .

[7] Y. Kamada and JT-60 team, Nucl. Fusion **41**, 1311 (2001).

[8] Y. Sakamoto, *et al.*, Nucl. Fusion **45**, 574 (2005).

[9] T. Fujita, *et al.*, Phys. Rev. Lett. **87**, 085001 (2001).

[10] Y. Sakamoto, *et al.*, Nucl. Fusion **41**, 865 (2001).

[11] T. Nakano *et al.*, *Impact of nearly-saturated divertor plates on particle control in long and high-power heated discharges in JT-60U*, submitted to Nuclear Fusion .

[12] N. Hosogane, *et al.*, J. Nucl. Mat. **266-269**, 296 (1999).

Long Pulse Discharges on the HT-7 Tokamak

HT-7 team, presented by Junyu Zhao

Institute of Plasma Physics, Chinese Academy of Science, Hefei, Anhui 230031, P. R. China

Abstract

To obtain long sustained plasma operation with high integrated performance on the HT-7 superconducting tokamak, several important technical modifications have been realized in the last few years. The special doped graphite coated by SiC film was used as limiter material. Two full poloidal limiters and one inner toroidal belt limiter, two additional toroidal doubler-ring graphite limiters located at the top and bottom of the inner wall were adopted for steady-state plasma operation, all of which are actively water-cooled. Twenty-four pieces of a ferromagnetic material—ferritic steel have been installed inside the vacuum chamber, to be used as plasma facing components and for the reduction of the magnetic ripple. The new CW LHCD system with 1.2MW 2.45GHz has been installed into the machine. The grill of the LHCD has been changed to 3×16 multi-junction and coated with TiN film. The 1.5MW ion-cyclotron-resonance-frequency (ICRF) system and a 0.35MW ion Bernstein wave (IBW) system in frequency range of 18-30MHz with CW operation capacities have been applied to drive and heat the HT-7 plasma so as to realize active control for the current density and pressure profile. Two crypumps with $10m^3/L$ pumping speed were installed to enhance the particle exhaust. The rf wall conditioning technique has been well developed and routinely used in HT-7 tokamak, which contribute to the significant reduction of the impurity radiation and edge recycling. By combining ion Bernstein wave and lower hybrid current drive edge-localized-mode-free limiter H-mode discharges with $H_{89}\sim2$, $\beta_N*H_{89}>3$ have been obtained that lasted for 53 τ_E. The central electron temperature is about 2.6 keV and density above 2×10^{19} m^{-3}. With reduced plasma parameters of central $T_e\sim1.5$ keV and $n_{e0}\sim2 \times 10^{19}$ m^{-3}, $H_{89}\sim1.45$, $\beta_N\sim1.1$, the improved confinement phase lasts for more than 100 τ_E with the non-inductive driven current fraction$\sim70\%$. Nearly full non-inductive current driven plasma (I_p=120-180kA, B_t=1.5-2.0T, Te(0)=2-4keV, and $<n_e>$=1.0-2.5$\times10^{19}m^{-3}$) had been achieved with a duration of more than 10s. For lower performance operation (I_p=55kA, T_e(0)=0.5-1.0keV, and a central density n_{e0}=0.5-1.0$\times10^{19}m^{-3}$), a reproducible long pulse discharge with the operational pulse length up to 240 seconds was sustained by the LHCD (<200kW) on the HT-7.

1. **Introduction**

In steady state operation of tokamak plasma, the plasma current is entirely sustained by non-inductive current drive means and the self-generated bootstrap current. The problems involved can be solved by using superconducting techniques, development of non-inductive current drive, plasma control, effective heating, advanced fuelling, removal of particles and heat flux to the first wall, etc. The HT-7 is a circular limiter tokamak with a major radius of 1.22m, a minor radius of 0.27m, and a stainless steel liner in a radius of 0.32m. The limiter was made of molybdenum before 2000 and doped graphite tile with a SiC gradient coating after 2000. Its ohmic heating transform has an iron core and can offer a magnetic flux of up to 1.8VS. 24 superconducting coils located between two layers of thick copper shells produce and maintain the toroidal magnetic field $B_T \leq 2.5T$ [1–3].

Main objective of the HT-7 tokamak is the exploration of high-performance plasma operation under steady-state conditions and relevant physics. To realize the mission, system with a multi-junction coupler in the spectrum range of $n_{//}=1.8-3.5$ [4], a 1.5MW ion-cyclotron-resonance-frequency (ICRF) system in frequency range of 30-110MHz and a 0.35MW ion Bernstein wave (IBW) system in frequency range of 15-30MHz [5], all with CW operation capacities, were developed to heat and drive the HT-7 plasma for active control of the current density and pressure profiles. Other systems including one inner toroidal belt limiter in high field side (HFS) and two poloidal graphite limiters with active coolant and stainless steel heat sink, ferretic steel liner, real-time feed-back control, et al., were employed as well. The doped graphite tile with about 100μm SiC gradient coating by chemical vapor reaction (CVR) has high thermal conductivity up to 180W/m·K and good thermal shock resistance to withstand 6MW/m^2 for 30s. The SiC coating is very effective to reduce the chemical sputtering and suppress the radiation-enhanced sublimation [6-8]. From the autumn campaign in 2003, new additional toroidal double-ring graphite limiters located symmetrically at the top and bottom of the inner wall were adopted to accommodate requirements for steady-state plasma operation, which are actively water-cooled and made of same doped graphite coated by SiC film. It has larger plasma facing surface and higher heat exhausting capability. The poloidal field power supply and its feedback control system were upgraded with the real-time operation system to eliminate the limitation of discharge duration from the old operation system. After these modifications, plasma discharge duration enables to extend up to several minutes. A variety of discharges with a normalized performance $\beta_N H_{89} > 1\sim3$ for a duration of several hundred energy confinement time τ_E was produced in HT-7. At the reduced

performance of $H_{89}>1.2$ with $\beta_N\sim1$, a plasma with a duration of near 8 s, longer than 400 τ_E, had been achieved with more than 90% non-inductive current fraction, which was sustained by LHCD and bootstrap current. For lower performance operation ($I_p=55kA$, $T_e(0)=0.5-1.0keV$, and a central density $n_{e0}=0.5-1.0\times10^{19}m^{-3}$), a reproducible long pulse discharge with the operational pulse length up to 240 seconds was sustained by the LHCD (<200kW) on the HT-7.

2. Key issues of long duration plasma discharges

For long pulse discharge, heat exhaust is unavoidable due to the interaction between plasma and plasma facing material, the impurity produced during the process will go into plasma and affect the drive efficiency. The key issues for the steady-state condition are plasma facing components (PFCs), wall recycle, and plasma control. The problems involved are non-inductive current drive, wall conditioning, reduction of high impurity radiation, heat exhaust and particle removal, etc.

2.1 Wall conditioning techniques [9, 10]

Radiofrequency ICRF conditioning technique, including removal of hydrogen, isotope control, impurity cleaning, boronization and siliconization are the routine first wall conditioning way on HT-7 during experiments because of the presence of a permanent toroidal magnetic field. A non-toxic and non-explosive solid, carborane ($C_2B_{10}H_{12}$) powder, was used for the wall boronization material by means of RF producing plasmas. The high energy ions and the mechanism of the ICRF plasma made the film highly adhesive, hard, amorphous, deeply penetrating and uniform in both the radial and toroidal directions. Analysis of the B/C coating on the graphite specimen showed that it consisted of a fine amorphous C/B, hydrogen film with very strong adhesion to the first wall. Even after 250 shots of ICRF and LHCD launch with about 400 kW RF power, as shown in Fig.1, the structure of the coating is nearly the same as that of fresh films and the ratio of B to C varied not too much, from 2.8 to 3 over a depth of 250 nm, except thickness reduction of 50 nm.

By choosing the proper RF conditioning parameters after RF boronization, the hydrogen recycling and H/(H+D) ratio could be easily handled. After boronization, the ratio of H/(H+D) was as high as 60% since a large amount of hydrogen gas was absorbed in the fresh boron film, could be reduced to 15% after two periods of 30 min. RF discharge with deuterium gas. A good impurity cleaning effect and very high hydrogen desorption rate were obtained in helium working gas. The cleaning efficiency is much better than that obtained by glow discharge cleaning (GDC) and Taylor discharge cleaning (TDC).

After RF boronization and conditioning, the plasma performance was significantly improved with an influx reduction of carbon and oxygen by a factor of 3, a reduction of Z_{eff} from 4 to 2 at a density of $2 \times 10^{19} cm^{-3}$ close to unity at a density of higher than $3 \times 10^{19} cm^{-3}$. The hugill stability operation region was extended. Compared with the common boronization method, it shows much better film properties, such as a high ratio of boron to carbon, a longer lifetime of the coating about 1500 shots, and a higher LHCD efficiency for longer full wave current drive period. The particle removal rate and cleaning efficiency are higher by a factor of 3. This special technique has been demonstrated to be highly efficient, fast and easily controllable means of the wall conditioning with reduction of the impurity and wall recycling for future large superconducting tokamak devices in the presence of high magnetic fields.

2.2 **Ripple reduction experiments with ferritic steel**

Using the ferritic steel is one of good methods to reduce toroidal field ripple [11]. The toroidal field ripple in HT-7 is relatively strong (around 4% at the plasma edge) and resulted high input power losses during ion cyclotron resonance frequency (ICRF) heating. Fast ion ripple loss causes overheating load in the first wall [12], and produces large impurity due to energetic particles striking the wall. The recycle of particles between the plasma and the wall will be changed. So the plasmas character will be degraded deeply. The impurity radiation causes the auxiliary heating efficiency decrease, even the plasma disruption. Ferritic steel installation for reducing the toroidal field ripple in HT-7 is useful in suppressing the fast ion ripple loss especially during the auxiliary heating discharge and for the extension of advanced tokamak scenarios to long pulse operation

The surrounding 24 superconducting coils generate a toroidal magnetic field (B_T) up to $2.5T$. A $1.7Vs$ iron core transformer provides ohmic heating. The feedback control system for the HT-7 tokamak is a multi-variable feedback controller due to the strong coupling between the ohmic heating coil and vertical field coil. Twenty-four pieces of a low activated materials; the ferritic steel (GYJ060: 6.5%Cr+1.5%Si+0.2%Mn+Fe remainder) has been installed just under each toroidal field coil inside the vacuum vessel in HT-7. This ferritic steel is in-vessel material and outgassing rate is less than $18.63 \times 10^{-6} Pa \cdot L/s$ after sixteen hours baking at $200^{o}C$. The residual magnetism is about 200 Gauss, coercive force is several ten Oersted, the saturated magnetism is near 20000 Gauss and Curie temperature is high. Each ferritic steel size is $600 \times 150 \times 18$ (mm), its radius is 323mm and center is set on middle-plane and center is set on middle-plane and covered the toroidal coil connection. They are isolated from the vacuum vessel at one end and protected by the stainless steel liner with baking wires. The

toroidal magnetic field ripple δ= [(Max.field-Min.field)/2]/Averagefield can be reduced from 4% to 1.6% according the calculation (Fig.2). Up to 1MW power F=2.45GHz, phase variable LHW system; and f = 24~30MHz, P_{RF} = 300KW with Step-tuner matching T-type antenna Ion Bernstein wave heating system are the main external current driving and plasma heating means. During the experiment campaign, some manmade serious conditions, such as quench, hard disruption were produced, there are no any bad effects caused by the ferromagnetic steel installation such as plasma production, plasma control, etc. The fuel hydrogen retention or recycling was similar to that of the normal stainless steel and also in the case of wall conditioning (such as boronization and lithium coating).

After the FS installation, the impurity activity was improved during the auxiliary heating and the hard X-ray radiation was reduced during the high power LCHD experiments. The temperature decay time became from 20ms to 55ms after ICRH turn off measured by ECE. It has been demonstrated that high fast ion loss during RF heating was significant reduced (Fig.3).

2.3 **Plasma control [14, 15]**

Plasma control is one of key issues to achieve steady state plasma discharges. During HT-7 plasma discharges, the central line averaged electron density was controlled by feedback gas injection using a pulsed electric piezo-valve, and the plasma current and position were preset and then feedback controlled by the ohmic poloidal system. In the present HT-7 experiments, preset of the plasma position depends on the experience, unreasonable position would cause strong interaction between plasma and the first wall and result in continuous rise of the limiter temperature, which was responsible for the strong outgassing and uncontrollable density rise and ultimately led to the termination of the discharge.

For HT-7 long pulse discharges, adjustment of the injection power of LHW to control the loop voltage is the most important and effective way for steady-state operation. It is known that discharges inside the waveguide tube of the LHW system cause a decrease of the LHW injected power, induced variation of plasma current will increase the interaction between plasma and plasma facing material, and produce impurity. Impurity spurting leads to termination of full current drive discharge. Therefore, except common control of plasma density, plasma current and plasma position, additional control loop based on the variation of Volt-Second was adopted on HT-7 for steady-state operation. The magnetic flux of the transformer was feedback controlled by the LHW power in two ways: rough adjustment by turning-on/off one or two klystrons and fine adjustment by changing applied voltage on all klystrons.

3. Long pulse high-performance discharges approaching steady-state operation

The key points to obtain long duration high-confinement plasmas are controlling edge transport and recycling, avoidance or suppressing of MHD instability, suppressing edge turbulence and maintenance of low impurity. They are challenges for approaching steady-state high-performance plasma.

It is very important to utilize the IBW local heating to increase the high-confinement volume for the synergetic discharge of LHCD and IBW for the steady state high-performance. Two operation scenarios are routinely employed: off-axis IBW with on-axis LHCD or off-axis LHCD. In synergetic discharge of on-axis LHCD and off-axis IBW, LHCD is usually launched into plasma during the initial plasma current rise phase to extend the plasma duration as long as possible as to obtain maximum gain. In synergetic discharge of off-axis LHCD and off-axis IBW, more than 80% of the plasma current was sustained by the LHCD and the bootstrap current. While the IBW resonant layer is near the rational surface, the improved edge and core confinement results in a large pressure gradient and large edge bootstrap current density, in which often drives MHD instabilities and degrades the plasma performance or terminates the discharge. Therefore, avoidance or suppression of $m/n=2/1$ resistive tearing mode instability is most crucial issue for the extension of advanced performance scenario, two approaches by redistributing plasma current density profile through active external control of LHCD or IBW waves have been successfully carried out in HT-7. One is dynamic stabilization of MHD perturbation by modulation of toroidal current, power or frequency of LH or IBW waves. The other is modifying electron pressure profile and impacting MHD activities by optimizing IBW off-axis heating through changing the toroidal magnetic filed strength, moving IBW resonant layer position and so injecting IBW power near the rational surface.

By proper optimization of LHCD launched wave spectra, plasma parameters and toroidal magnetic field to decrease pressure steep to avoid these MHD activity, a normalized performance $H_{89}>1.2$ with β_N close to unity for nearly 8s and with an ITB-like profile of electron temperature and density, as illustrated in Fig.4, more than $400\tau_E$ was achieved. An typical long pulse high-confinement discharge by synergy of LHCD and IBW heating shown in Fig.5 with a optimized performance indicated by product of $\beta_N H_{89}\sim2.3$ was sustained for 4.6s, about $235\tau_E$ and longer than $20\tau_{CR}$ (τ_{CR}, current diffusion time), and with a stationary ITB at the footprint of the minimum q, all plasma parameters and their profiles reached stationary. The analysis of these discharges by EFIT and ONETWO shows that current profile

had a negative shear in a stationary state and more than 80% of the non-inductive plasma current was sustained by LHCD and bootstrap current. A transport barrier at the edge of plasma was also observed from the reciprocating Langmuir probe measurements, which means an H-mode edge in such reversed shear operational mode.

The reproducible long pulse discharges with a duration more than 200s, Te(0)~1keV and central electron density ne(0)~0.8×10^{19}m^{-3} were obtained under the genuine steady-state operation. The longest discharge of 4 minute, shown in Fig.6 was achieved in 2004, During such a 4 minute discharge, among all 32 thermocouples on the toroidal limiters for temperature measurement, only one temperature on the location of lower toroidal limiter raised quickly over 350℃ at about 220s, corresponding to about -0.3cm of vertical plasma position, others were kept below 200℃. It indicates necessity of the fine alignment for all PFCs.

Wall saturation and refresh process was observed only in discharges with a duration longer than 200s. When the global recycling coefficient R became more than unity, the gas feed was automatically stopped to keep central line averaged electron density constant by the feedback control system. At about 180s, R decreased below unity and gas supply started. It is noted from Fig.6 that the electron density was decreased dramatically and could not be compensated in following period of 180-220s by valid gas supply through feedback control. It means that the wall repeated a process of being saturated and refreshed. This indicates importance of investigation on the wall equilibrium at ultra-long duration discharge, which will be one of the key issues for the steady state tokamak operation.

3. Summary

Heat exhaust and particles control, wall recycle, PFCs, MHD instability, and plasma control are challenges for approaching steady-state high-performance plasma. To explore longer sustained plasma operation with high integrated performance and relevant physics on HT-7 tokamak, several important technical modifications have been made in recent years, including new actively water-cooled toroidal double-ring graphite limiters made of the doped graphite coated by SiC film with special design. Based on the understanding on interaction of plasma and wall, benefit from those important technical improvements, and combing with good wall boronization and conditioning by means of RF producing plasmas, significant progress in achieving high performance discharges under steady-state condition in HT-7 has been realized. High-performance plasma is produced by the synergy of LHCD and IBW with a broadened current profile and broadened ITB on electron density and temperature profiles.

MHD behaviors and thermal instabilities which limited the high performance operation were studied in detail as well.

Nearly full non-inductive current driven plasma at high performance (Ip=120-180kA, Bt=1.5-2.0T, Te(0)=2-4keV, and <ne>=1.0-2.5×10^{19}m^{-3}) was achieved by LHCD with a duration of up to 10s. A long pulse high-performance discharge with the product of β^*_NH$_{89}$~2.3 was sustained for 4.6s, about 235τ_E and longer than 20τ_{CR}. The transport analysis showed that about 80% non-inductive current was generated by the synergy of LHW and IBW. For lower performance operation, a reproducible long pulse discharge (#71377, Ip~55kA, Te(0)~1.0keV, and a central neo=0.7-1.0×10^{19}m^{-3}) with the operational pulse length up to 240s was sustained by the LHCD (<200kW) in the HT-7, almost in steady-state condition. The progresses for long pulse discharge approaching steady-state operation on HT-7 device in past decade are strongly correlated with technical modifications. The actively cooled toroidal double-ring graphite limiter and new manual control for plasma position are expected to take the important rule on heat exhaust and particles control for advanced steady state operation on HT-7 in the near future.

Acknowledgement

References

[1] Jikang Xie, et al., Proc. Of 16th IAEA Conf. Fusion Energy, IAEA-CN-64/AP1-13, Montreal, 1996.

[2] Yuanxi Wan, et al., Nucl. Fusion 40 (2000) 1057.

[3] J. Xie, et al., Nucl. Fusion 41 (2001) 1495.

[4] G. Kuang, et al., Fusion Technology, 36 (1999) 212.

[5] Y.P. Zhao, et al., Pl. Phy. Contr. Fus. 43 (2001) 343.

[6] J. Li, et al., J. Nuc. Materials 313–316 (2003) 1188.

[7] Q. Guo, et al., J. Nuc. Materials 313–316 (2003) 144.

[8] Baonian Wan, et al., J. Nucl.Mat.313–316 (2003)127.

[9] Jiangang Li, et al., Nucl. Fusion 39 (1999) 973

[10] Y.P. Zhao, Chin. Phy. Lett.14 (1997) 916

[11] H. Kawashima, et. al., Nuclear Fusion, 41 (2001) 257.

[12] V. Basiuk, V. Bergeaud, et. al., 27th EPS Conference on Contr. Fusion and Plasma Phys. Budapest, 12-16 June 2000 ECA Vol. **24B** (2000) 784.

[13] Jiansheng Hu, et al., Fus. Eng. Design, 72(2005)377

[14] Baonian Wan, et al., Proc. Of 20th IAEA Conf. Fusion Energy, OV/5-1Rb, Portugal, Nov. 2004.

[15] X.D. Zhang, et al., Proc. Of 20th IAEA Conf. Fusion Energy, EX/P4-36, Vilamoura, Portugal, Nov. 2004.
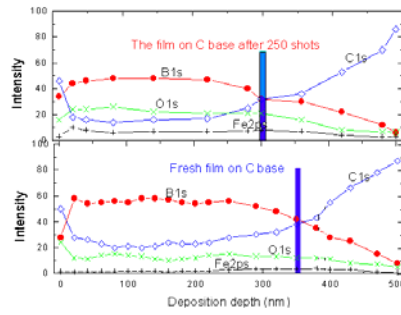
Fig.1 Analysis results on the graphite specimen by X ray photoelectron analysis (XPA) (Boron film properties for the fresh film and the film after 250 shots at the RF plasma conditioning parameters of B_T=1.8T, P_{RF}=10kW, f=30MHz and P=0.3Pa)
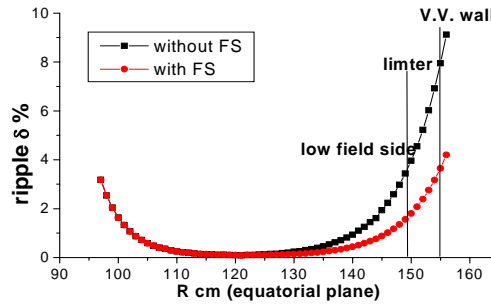
Figure 2. The toroidal magnetic field ripple was reduced from 4% to 1.6% at B_t=2 T according the calculation.

$$\delta = \frac{Max.field - Min.field}{2*Average field}$$
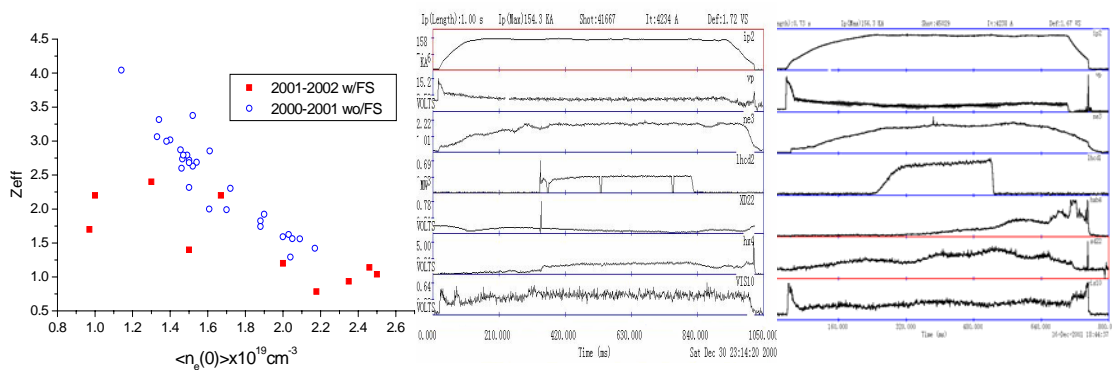
Figure 3. After the ferritic steel installation, the impurity content was reduced during the auxiliary heating viewing from the bremsstrahlung emission and carbon C-III spectrometer, and the hard X-ray emission from the limiter was depressed during the high power LCHD experiments.

10
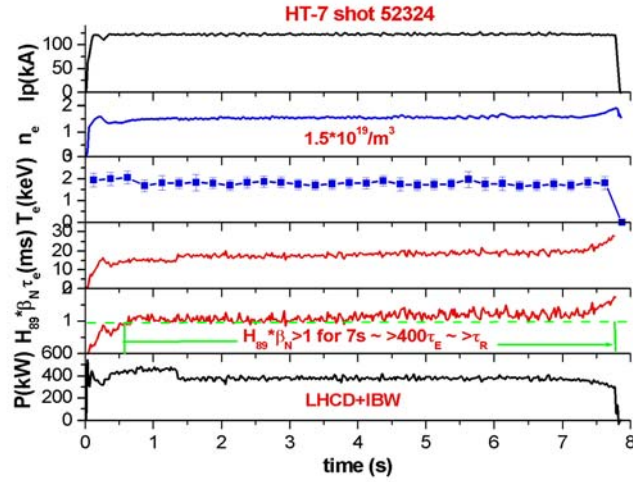
Fig.4 A normalized performance $H_{89}\beta_N > 1.2$ for nearly 8s
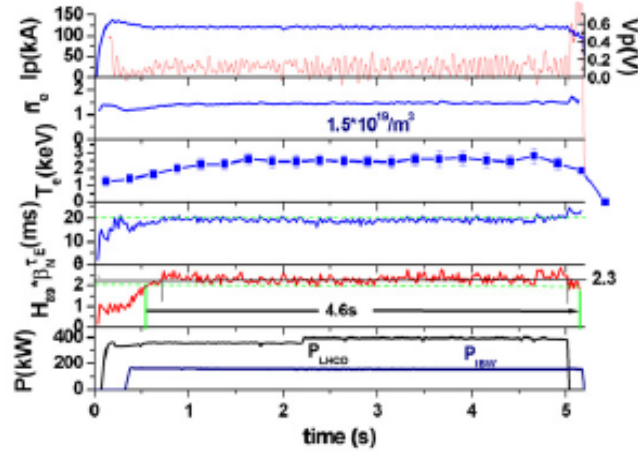
Fig.5 A long high-performance discharge by synergy of LHCD and IBW heating (Ip=120kA, B_T=1.7T, $\overline{n_e}(0)$ =1.6×10^{19}m^{-3}, Te(0)>2.0keV, Ti(0)>1.2keV, P_{LHW}=0.4MW, P_{IBW}=0.18MW (27MHz), q_a~4.6, $\beta^*_N H_{89}$~2.3 for 4.6s, about 235τ_E, >20τ_{CR}, , Vp~0.25V)

Fig. 6 4 minutes long pulse plasma discharge

ICRF Heated Long-Pulse Plasma Discharges in LHD

R.Kumazawa, T.Seki, T.Mutoh, K.Saito, T.Watari, Y.Nakamura, M.Sakamoto[1],
T.Watanabe, S.Kubo, T.Shimozuma, Y.Yoshimura, H.Igami, Y.Takeiri, Y.Oka,
K.Tsumori, M.Osakabe, K.Ikeda, K.Nagaoka, O.Kaneko, J.Miyazawa, S.Morita,
K.Narihara, M.Shoji, S.Masuzaki, M.Goto, T.Morisaki, B.J.Peterson, K.Sato,
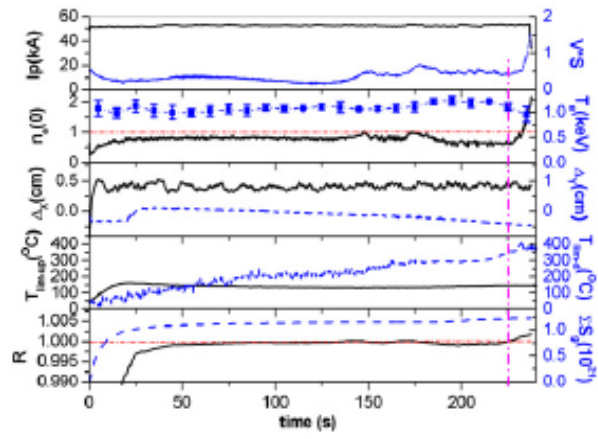T.Tokuzawa, N.Ashikawa, K.Nishimura, H.Funaba, H.Chikaraishi, T.Notake[2],
Y.Torii[3], H.Okada[3], M.Ichimura[4], H.Higaki[4], Y.Takase[5], H.Kasahara[5], F.Shimpo,
G.Nomura, C.Takahashi, M.Yokota, A.Kato, Y.Zhao[6], J.S.Yoon[7], J.G.Kwak[7],
H.Yamada, K.Kawahata, N.Ohyabu, K.Ida, Y.Nagayama, N.Noda, A.Komori, S.Sudo,
O.Motojima and LHD experiment group

National Institute for Fusion Science, Toki, Japan
1) Kyusyu University, Kasuga, Japan
2) Nagoya University, Faculty of Engineering, Nagoya, Japan
3) Kyoto University, Institute of Advanced Energy, Uji, Japan
4) Tsukuba University, Plasma Research Center, Tsukuba, Japan
5) Tokyo University, Graduate School of Frontier Sciences, Tokyo, Japan
6) Institute of Plasma Physics, Academia Sinica, Hefei, 230031, P.R.China
7) KAERI, 150 Deogjin-dong, Yuseong-gu, Daejeon, Korea Rep.

Abstract

A long-pulse plasma discharge for more than 30 min. was achieved on the Large Helical Device (LHD). A plasma of $n_e=0.8 \times 10^{19} m^{-3}$ and $T_{i0}=2.0 keV$ was sustained with $P_{ICH}=0.55MW$, $P_{ECH}=0.1MW$ and averaged $P_{NBI}=0.06MW$. Total injected heating energy was 1.3GJ, which was a quarter of the prepared RF heating energy. One of the keys to the success of the experiment was a dispersion of the local plasma heat load to divertors, accomplished by shifting the magnetic axis inward and outward.

1. Introduction

An improvement of core plasma performance has been achieved in various magnetic configurations over the past decades. Almost all the data were achieved in short-pulse plasma discharges. Now a goal of fusion research is to demonstrate a long-pulse/steady-state plasma discharge with high performance, integrating the experimental and technological knowledge so far obtained. In tokamaks such a discharge has been carried out in several superconducting devices; 1.1GJ of heating energy was successfully injected for 6min. in Tore Supra[1]. In JT-60U 350MJ was injected for 65s[2]. More than 5hours of the plasma discharges was achieved in TRIAM-1M[3].

In the helical configuration the long pulse plasma discharge is being carried out on the Large Helical Device (LHD)[4], which is a superconducting device. The achievement of a steady-state plasma discharge is one of the main objectives in the LHD project. For that purpose technological development had been carried out on plasma heating devices for several years before the LHD experiment was started; an electron cyclotron heating (ECH), a negative ion-based neutral beam injection (NNBI) and an ion cyclotron frequency range (ICRF) heating. Among them a steady-state operation on the ICRF power generator was successfully carried out on the MW level for more than 1 hour[5]. A liquid stub tuner was invented to make feedback control in the impedance matching possible[6,7]. In addition a transmission system including an antenna was tested to verify its capability to transfer the

RF power on the MW level in the steady-state[8,9]. An encouraging experiment was made where the plasma was sustained on the CHS (Compact Helical System) by the ICRF heating power only[10].

The ICRF heating was successfully carried out on the LHD [11-14]. Following the long-pulse operation of the NNBI heated plasma discharge, a trial using an ICRF heated plasma was started in the 3rd LHD experimental campaign (1999), and a 68sec plasma discharge was achieved [15]. The pulse length was limited by an RF generator problem. Then it was gradually prolonged to 127sec in the 4th LHD experimental campaign [16,17]. In the 6th LHD experimental campaign, the plasma duration time was found to be limited by the electron density increase due to the hydrogen out-gassing. In the 8th LHD experimental campaign (2004), the steady-state discharge was selected as the main object of the experiment and many trials were done.

In this paper the achievement of a long-pulse plasma discharge is described. In Sec.2 the experimental setup is reported including the ICRF heating system and a heat removal system. In Sec.3 the typical long-pulse plasma discharge is described. Then the causes limiting the plasma duration are discussed. In Sec.4 the experimental data are compared with results obtained from the orbit calculation of high-energy ions and a fusion triple product vs. duration time is summarized. We conclude in Sec. 5.

2. Experimental Setup

The LHD is the largest superconducting heliotron-type device, with R_{ax}=3.4~3.9m, a=0.6m and B=2.5~2.9T. Three plasma heating devices are installed on the LHD; NNBI, ECH and ICRF heating. The maximum heating power so far achieved is 14MW for NNBI, 2MW for ECH and 2.5MW for ICRF heating, respectively.

2.1 ICRF heating system

The ICRF heating was carried out using two pairs of loop antennas 0.6m in length, 0.46m in width and 0.17m in thickness. The antennas are installed from the upper and lower ports of LHD and located on the higher magnetic field side on the outboard side of the torus. The surface of the antennas is twisted to fit the shape of the plasma boundary. Faraday shields in a single layer are placed parallel to the lines of magnetic force. Graphite protectors are attached to both sides of the antennas. The RF components of an antenna strap, Faraday shields and a back plate are cooled by water for a steady-state operation. The antenna's position is movable in the radial direction by 15 cm. The RF power is fed to each antenna by its own RF generator, which is adjusted for steady-state operation.

Four RF generators were prepared for the experiment. The long pulse operation was carried out as shown in Fig.1. Here the output of RF power of 0.25, 0.5 and 1.0 MW is also plotted as reference parameter in time and input RF energy space. Typical operations are 0.5MW/0.5hour or 1.0hour and 0.25MW/1hour. The total prepared heating energy is about 6GJ in the four RF generators.

Fig.1 Available RF heating energy with duration time of four RF generators.

2.2 Heat removal system

A main part of the plasma energy is carried off to the divertor plates. The plasma is diverted along the magnetic field line connected to the last closed magnetic surface at the elongated axis of
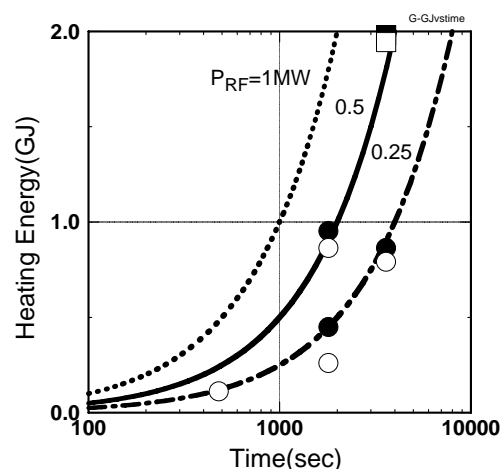
the plasma cross section. 1700 divertor plates made of isotropic graphite are installed along the helical divertor traces. They are connected to water cooling pipes sandwiching copper heat sinks. A maximum heat flux of $0.75MW/m^2$ is the design value of the divertor plate. The thermo-couple is installed to 90 plates among them. The measuring point is 10mm beneath the surface of the divertor plate[18].

3. Experimental results

3-1. Long pulse plasma discharge

Time evolutions of the plasma parameters of a typical long-pulse plasma discharge are plotted in Fig.2; this is the case of the longest plasma discharge. A plasma with an electron density $n_e=8\times10^{18}m^{-3}$ and the electron temperature at $\rho=0.14$ of $T_{eECE}=1.4keV$ and the ion temperature on the magnetic axis of $T_{i0}=2.0keV$ was produced with $P_{ICH}=0.55MW$, $P_{ECH}=0.1MW$ and a ten-time intermittent NNBI heating, i.e., $P_{NBI}=0.45MW$ for 20s. The key which led to the success of the experiment was a swing of the magnetic axis, i.e., $R_{ax}=3.67m\sim3.70m$ in the period of 100sec as shown in Fig.2. The dispersion of the plasma heat load to the divertors decreased the temperature to less than 250^oC. The line average electron density was controlled with a He gas puffing feedback system using a measured micro-wave interferometer signal, but could not be kept constant because of a lack of the feedback control gain. The plasma duration was more than 30min. and the total injected heating energy was $W_h=1.29GJ$, which consisted of $W_{ICH}=0.98GJ$, $W_{ECH}=0.19GJ$ and $W_{NBI}=0.12GJ$.
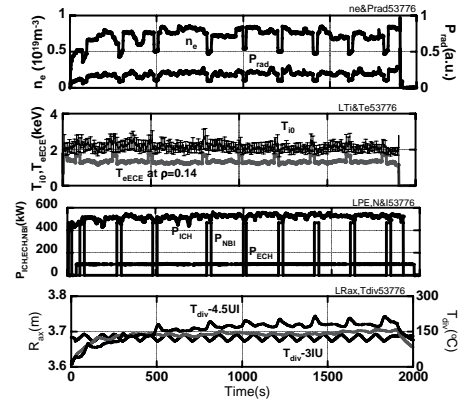
Fig.2 Time evolutions of n_e, P_{rad}, T_e, T_{i0}, heating power of P_{ICH}, P_{ECH}, P_{NBI}, T_{div} and R_{ax}.

3-2. Key to successful long-pulse plasma discharge

The average magnetic axis R_{axav} and the swing width δR_{ax} were the important factors in prolonging the pulse duration (in solid circles) and increased the heating energy as shown in Fig.3. R_{axav} was changed from $R_{axav}=3.55m$ to $R_{axav}=3.685m$. A local plasma heat load position could be moved by the swing of R_{ax} in accordance with the diverted plasma analysis[19]. However the swing width was determined by the hot spot near the ICRF antenna observed in the outer magnetic axis, i.e., $R_{ax}=3.7m$. In addition a plasma heat load to one of divertor plates (referred to as P_{div} and in open squares) is plotted in this figure, which is calculated using measured values.

3-3. Causes limiting the plasma discharge duration

The duration of the plasma discharge is limited by several factors including; 1) the work of the interlock systems, 2) the gradual increase in the uncontrollable density, 3) the abrupt increase in the density and the radiated power due to penetrated heavy impurity.

Fig.3 The relation between duration time, P_{div} and R_{avax} with δR_{avax}.

1. Work of interlock systems

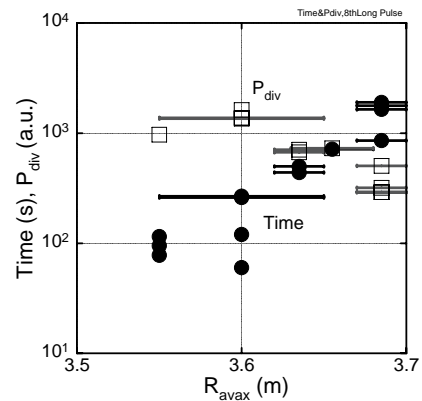Many interlock systems are employed in the ICRF heating system to protect RF components, which are a tetrode tube, a transmission line and the ICRF heating antenna, etc. Two of these interlock systems, i.e., a reflected power and a maximum RF voltage monitor, sometimes come into action during a long-pulse discharge experiment. The reflected power monitor works in the case of the RF breakdown at the antenna or the transmission line. The maximum RF voltage is set at $V_{RF}=35kV$, although the transmission system and the antenna have a capability of more than $V_{RF}=40kV$ for steady-state operation. During a long-pulse plasma discharge the reflected power is gradually increased almost to the interlock level of $P_{ref}/P_{fw}=20\%$. The cause of the increase in the reflected power is a thermal extension of the transmission line. The frequency control method was employed to reduce the reflected power, but an available range of $\Delta f/f$ was restricted to 0.1% due to the requirement of the RF generator to acquire the stable and high RF power. Instead of this method a liquid stub tuner was mainly used by shifting the liquid surface level using a cylinder linked with a computer system as shown in Fig.4. At the beginning of the discharge, i.e., 100sec a shifted direction of the liquid surface was selected wrong, therefore the reflected RF power fraction was increased. After that it was gradually decreased and was kept in less than 4%.
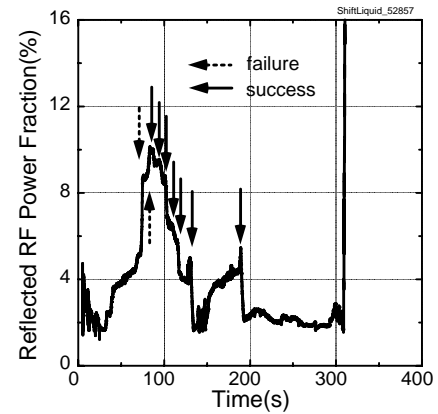

Fig.4 Reflected RF power fraction using feedback control of liquid stub tuner.

2. Gradual increase in the electron density

This phenomenon was sometimes observed in the beginning of the experimental campaign before sufficient aging of the divertor plates. A typical example is shown in Fig.5. After 90 sec the electron density increases with time. The electron density increases up to $n_e=1\times10^{19}m^{-3}$ and the radiated power increases P_{rad} to 250kW at 150 seconds. Time evolutions of the visible emission of Hα and HeI, and the temperatures increases in the divertor plates are plotted in Fig.5: The vacuum pressure is increased by $3\times10^{-5}Pa$ from $P_V=2\times10^{-4}Pa$ after 90s. The intensity of the Hα signal near the ICRF heating antenna is increased by a factor 3, whereas HeI intensity is almost constant.

3. Abrupt increase in the density and the radiated power due to penetrated heavy impurity

Two abovementioned causes could be eliminated by employing the feedback control in the liquid impedance matching systems and by increasing the
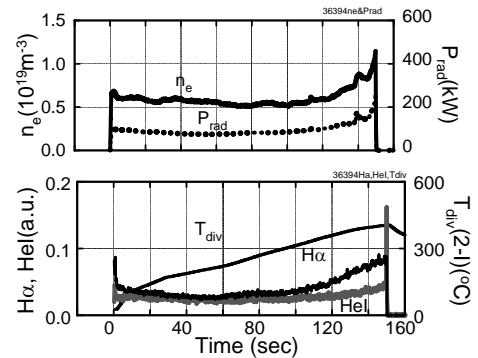
Fig.5 Time evolutions of plasma parameters In the collapse due to the increase in the Electron density.

out-gassing from the divertor plates. At the present time the steady-state discharge operation is confronted with the penetrated heavy impurity, though a long-pulse discharge of more than 30min. was achieved. A typical example is shown in Fig. 6, which was obtained toward the end of the plasma discharge, i.e., at the time between 1640 and 1644sec. After observed arcing near 7-I port at 1641.34s intensities of FeX (174.52nm), n_e and P_{rad} suddenly increase followed by an increase in CIII (977.02nm) at the time of the lower electron temperature. Although the reflected power fraction (P_r/P_f) did not exceed the interlock level, the RF power generator was turned off manually after the plasma, shown on

a TV screen, was judged abnormal. We examined the LHD vacuum wall and the divertor plates near the 7-I port. However we could not find any serious damage on the surface of the plasma facing components. Nevertheless, many thin stainless flakes were found at the 4.5 U&L ICRF heating antennas, which were not used in the 8th experimental campaign. It was thought that the thin stainless flake had penetrated into the plasma and become a cause of the increase in the intensity of FeX. However it was not understood why the thin stainless flakes had been produced in the unused ICRF heating antennas.

Fig.6 Time evolution of plasma parameters, P_r/P_f and R_p during the plasma collapse due to penetrated Fe ions.

4. Discussion
4-1. Local plasma heat load to divertor plate

An asymmetry of the temperature increase in the divertor plates was observed in the toroidal direction; it was obtained in the plasma discharge of P_{ICH}=0.5MW for 150 sec at R_{ax}=3.6m, already shown in Fig.5. The temperature increase was remarkable in the 2-I and 3-I divertor plates among 10 divertor plates; here it should be noted that the ICRF heating antenna is located at the vacuum ports of 3.5U&L. The cyclotron resonance layers are separately located on the saddle points in the mod B surface. In this magnetic configuration the behavior of high-energy ions was examined using the full orbit calculation [20]. Two thousand high-energy ions with a low energy are started from the upper and the lower ion cyclotron resonance layers, respectively. Ions accelerated by RF electric field of 20kV/m and trapped in the helical ripple move in the poloidal direction influenced by a grad B drift. Some of them hit the divertor plates within one circulation along the toroidal direction [21]. The numbers of high-energy ions hitting at each of ten divertor plates on the inboard side have a very close correlation with the measured temperature increase.

4-2. Fusion triple product vs. duration time

A scaling of a fusion triple product is experimentally derived using the confinement scaling of ISS95 in the following equation [12],

$$n\tau_E T_{i0}(\times 10^{20} m^{-3} keVsec) =$$

$$0.0133A^2 \cdot n^{1.02}(10^{19} m^{-3})P_{ICH}^{-0.18}(MW)$$

A is the improvement factor of the energy confinement time; A=1.5 at R_{ax}=3.6m and A=1.0 at R_{ax}=3.75m. Fusion triple products of the long-pulse discharge so far achieved are plotted using open (before) and solid circles (in 8th experimental campaign) as shown in Fig.7, where these obtained in Tore Supra, JET and JT-60U are also plotted. The fusion triple product of half an hour plasma discharge is $n\tau_E T_{i0}$=2.0x10^{18}m^{-3}seckeV as shown in Fig.7. A higher fusion triple product, i.e., $n\tau_E T_{i0}$=8.0x10^{18}m^{-3}seckeV was obtained in a short pulse discharge of 7sec with P_{ICH}=1.6MW and n_e=2.6x10^{19}m^{-3}. In the next 9th experimental

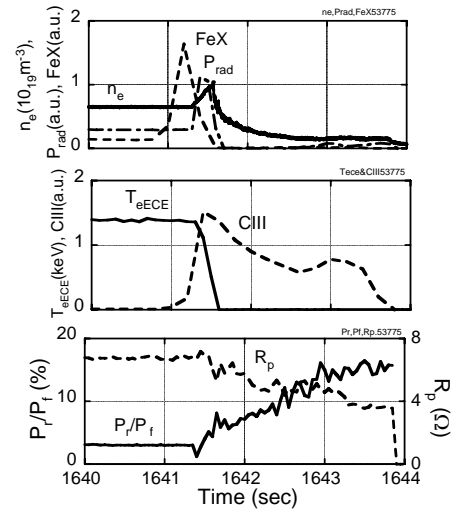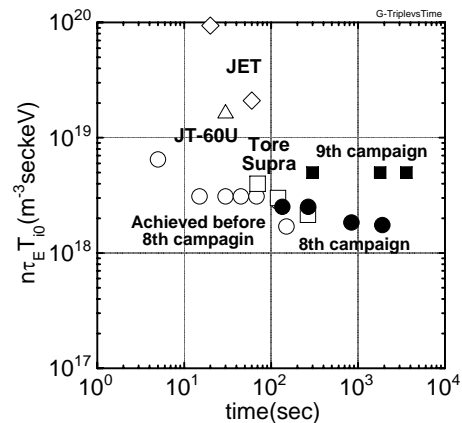Fig.7 Fusion triple product vs. operation time.

campaign the target of the long-pulse plasma discharge is a one hour discharge with $n\tau_E T_{i0}=5.0\text{x}10^{18}\text{m}^{-3}\text{seckeV}$.

5. Conclusion

In the 8th experimental campaign on the LHD a long-pulse plasma with more than 30min. operation was achieved. A plasma of $n_e=0.8\text{x}10^{19}\text{m}^{-3}$ and $T_{i0}=2.0\text{keV}$ was produced with $P_{ICH}=0.55\text{MW}$, $P_{ECH}=0.1\text{MW}$ and average $P_{NBI}=0.06\text{MW}$. The total input heating energy reached 1.3GJ. Two of the three main problems hampering the long-pulse plasma discharge were conquered, by 1) reducing the reflected RF power by employing the frequency control or the surface level control in the liquid stub tuner, and 2) reducing the temperature increase in the divertor plates and graphite protectors of the antenna. However, a penetrating heavy impurity limited the plasma discharge duration time. A total heating energy of 6GJ was prepared for the steady-state operation. An improvement of the heat conduction on the divertor plates and prevention of heavy impurities from penetrating into the plasma will lead to greater success in the next experimental campaign.

Acknowledgement

References
[1] J.Jacquinot et al., 20th IAEA Fusion Energy Conf. (2004), OV/2-2.
[2] H.Ide et al., 20th IAEA Fusion Energy Conf. (2004), OV/1-1.
[3] H.Zushi et al., 20th IAEA Fusion Energy Conf. (2004), OV/5-2.
[4] O.Motojima et al., 20th IAEA Fusion Energy Conf. (2004), OV/1-4.
[5] T.Seki et al., Fusion Technology, **40**(2001), 253.
[6] R.Kumazawa et al., Review of Scientific Instruments **70**(1999), 555.
[7] K.Saito et al., Review of Scientific Instruments **72**(2001), 2105.
[8] R.Kumazawa et al., Journal of Plasmas and Fusion Research, **75** (1999), 842.
[9] T.Mutoh et al., Fusion Engineering and Design, **26**(1999), 387.
[10] S.Masuda et al., Nucl. Fusion **37**(1997), 53.
[11] T.Mutoh et al., Physical Review Letter **85**(2000), 4530.
[12] R.Kumazawa et al., Physics of Plasmas **8**(2001), 2139.
[13] T.Watari et al., Nucl. Fusion **41**(2001), 325.
[14] K.Saito et al., Nucl. Fusion **41**(2001), 1021.
[15] R.Kumazawa et al., J. Plasma and Fusion Research, SERIES Vol.3(2000), 352.
[16] K.Saito et al., 15th Top. Conf.(2003), AIP Conf. Proc. **694**,58.
[17] T.Mutoh et al., Nuclear Fusion **43**(2003), 738.
[18] S.Masuzaki et. al., Nuclear Fusion, **42**(2002)740.
[19] T.Morisaki et al., Contrib. Plasma Physics, 42(2002), 321.
[20] T.Watanabe et al., 20th IAEA Fusion Energy Conf. (2004), EX/P4-47.
[21] K.Saito et al., J. Nucl. Mater, 337-339(2005), 995.

Ion Bernstein Wave Heating Experiments in HT-7 Superconducting Tokamak

ZHAO Yanping

Institute of Plasma Physics, Chinese Academy of Sciences, 230031, PRC.

Zhao_yp@ipp.ac.cn

Abstract: Ion Bernstein Wave (IBW) experiments have been carried out in recent years in the HT-7 superconducting Tokamak. The electron heating experiment has been concentrated on deuterium plasma with an injecting RF power up to 350kw. The globe heating and localized heating can be seen clearly by controlling the ICRF resonance layer's position. On-axis and off-axis electron heating have been realized by properly setting the target plasma parameters. Experimental results show that the maximum increment in electron temperature has been more than 1keV, the electron temperature profile has been modified by IBW under different plasma conditions, and both energy and particle confinement improvements have been obtained.

Introduction

Ion Bernstein Wave (IBW) heating is an ion-cyclotron-resonance-frequency heating concept using the directly launched IBW to carry RF power deep into the dense plasma core. The strong ion heating is realized when the wave passes the resonant layers, where strong ion cyclotron damping happens. Good ion heating results by IBW have been observed on JIPP-II-U, PLT, PBX and Alcator-C. IBW heating has also been investigated in the HT-7 superconducting tokamak deuterium plasma with an injecting RF power up to 350kW. The globe heating and localized heating can be seen clearly by controlling the ICRF resonance layer position. On-axis and off-axis electron heating have been realized by a proper arrangement of the target plasma parameters. Experimental results show that the maximum increment in electron temperature is more than 1keV, electron temperature profile is modified by IBW under different plasma conditions, and both energy and particle confinement improvements have been obtained.

Experimental setup

HT-7 is a medium-sized superconducting tokamak with a limiter configuration. Its major radius is 122 cm and minor radius is 27.5 cm. Plasma current is about 100~220kA, and toroidal magnetic field is about 1.0~2.0T. Plasma density is in the range of

$0.5 \sim 5 \times 10^{13}$ cm^{-3}. The electron and ion temperatures are about 700eV and 400eV respectively. One of the main subjects of HT-7 experiments is to inveterate the steady-state operation by full lower hybrid wave current drive (LHCD). Higher electron temperature can benefit the current driven efficiency. The electron-heating mode for IBW heating experiments is concentrated in HT-7 to get higher electron temperature.
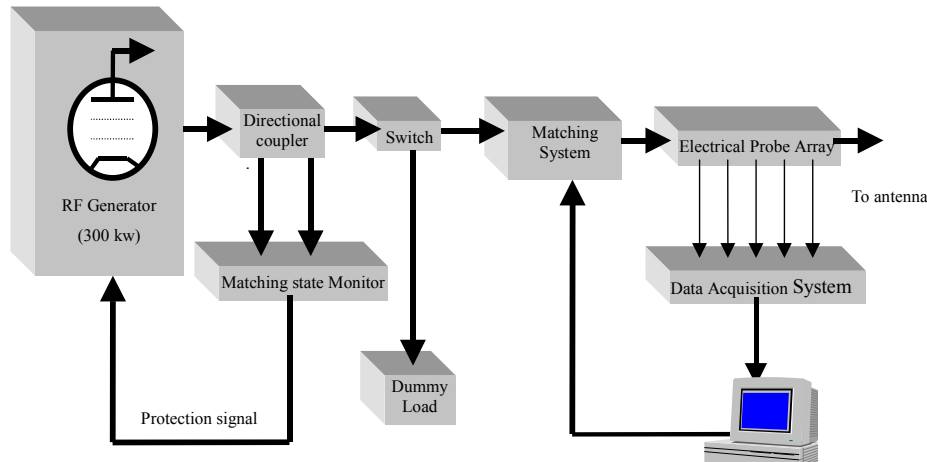
Fig.1   ICRF Heating System for HT-7 Superconducting TOKAMAK

The ICRF heating system for HT-7 has a capacity of 350kW continuous wave (CW) output power, and its frequency range is from 15 to 30MHz. The generator can operate in short pulse, multi-pulse and continue wave (CW) modes. It provides great flexibility for the experiments. Fig.1 shows ICRF system for HT-7. The system includes a RF generator, transmission lines, three liquid stub tuners and antennas. The IBW antenna is sited at an equator plane on the low field side of the tokamak. The central conductor and Faraday shielding are made of stainless steal and graphite, respectively. The radii of the central conductor and Faraday shielding are 32cm and 28.5cm respectively. Maximum RF power of the generator is 350kw. Three liquid step-tuners are used for the matching the impedance of the antenna. Deuterium working gas is adopted with the hydrogen minority. The toroidal magnetic field is chosen to make the Ω_H layer located in the center region of the plasma or off-axis location.

IBW Experiments

IBW heating was investigated in the HT-7 super-conducting tokamak deuterium plasma. An asymmetric quadruple T-antenna was used with a central feeder and short ends. The antenna was oriented in the toroidal direction. The $n_\parallel$ spectrum was peaked at 8，9，and 10 for the frequency 24MHz,27MHz and 30MHz respectively.

For 30 MHz, when B_T was chosen 2.0Tesla, the $2\Omega_D$ resonance layer was sited at the center of plasma, and the $5/2\Omega_D$ layer was near the plasma edge on the low field side. Under this experimental condition, a significant particle confinement improvement,

energy confinement improvement and very peaked density profile were observed during IBW heating. The particle confinement and energy confinement were improved by a factor of 3 and 1.5, respectively. When IBW power was around 200kw, electron and ion temperature were increased about 1keV and 0.3keV. When IBW power was lower than 120kw, no heating and confinement improved phenomenon was observed.
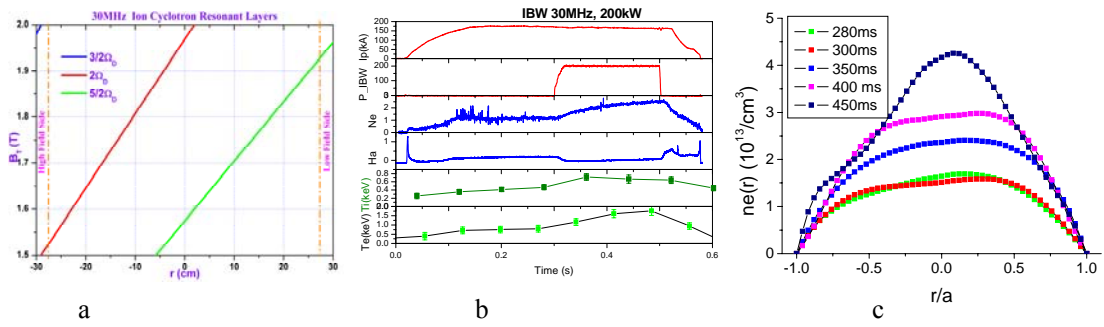
Fig.2 30MHz IBW heating experiment I. a: B_T against resonance layers position; b: Plasma discharge with IBW heating;   c: the density profiles during IBW heating.
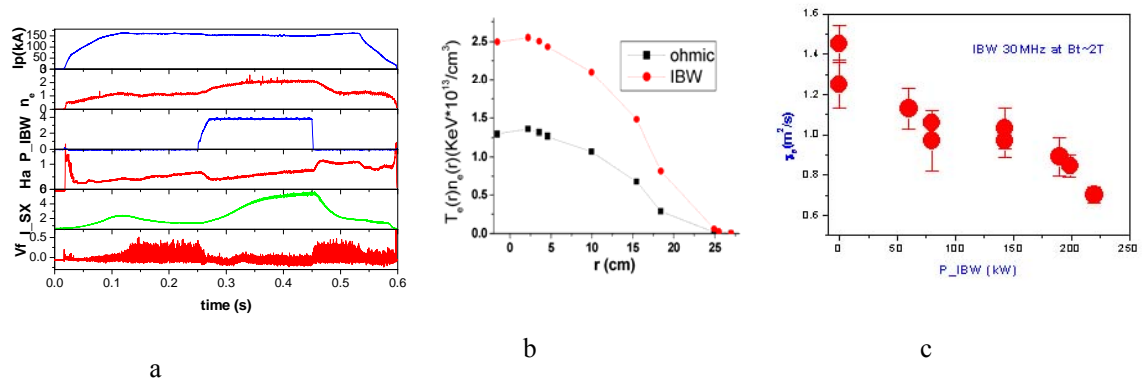
Fig.3 30MHz IBW heating experiment II. a: edge fluctuation was suppressed by IBW; b: Pressure profile was peaked during IBW;   c: χ_e against IBW heating power

For 27 MHz, $2\Omega_D$ resonant layer was located in the plasma. The global electron heating and localized heating were obtained for different $2\Omega_D$ resonant layer positions. No serious impurity problem was found with a boronized wall even if IBW power rose up to 350kw.

When the $2\Omega_D$ resonant layer position was changed from 5cm to 15 cm (B_T was changed from 2.0 tesla to 1.88 tesla), on-axis and off- axis heating effect was observed. For on-axis heating, the global electron heating was obtained. And for off-axis heating, the localized heating was obtained. τ_E and τ_p were increased in both the on- and off-axis heating modes. Confinement improved in the off-axis heating mode was better than in the on-axis heating mode. Meanwhile a very broad n_e profile was obtained. The experimental

data for 27MHz IBW heating are shown in fig.4.-Fig.7.

a   b   c
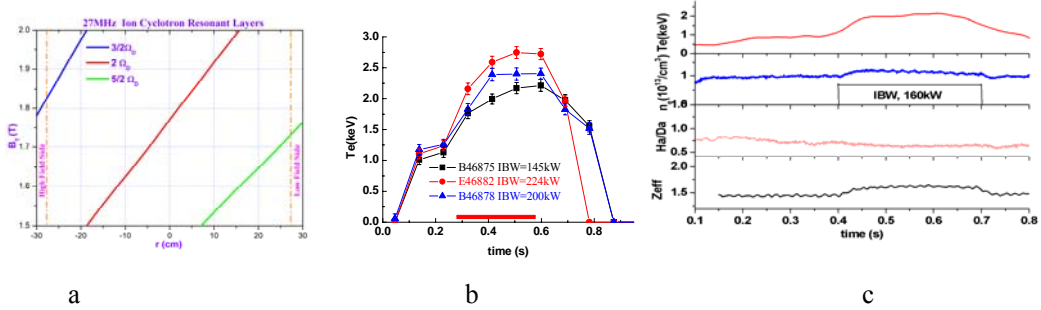
Fig.4 27MHz IBW heating experiment I. a: B_T against resonance layers position; b :Electron temperature profile;   c: Plasma discharge
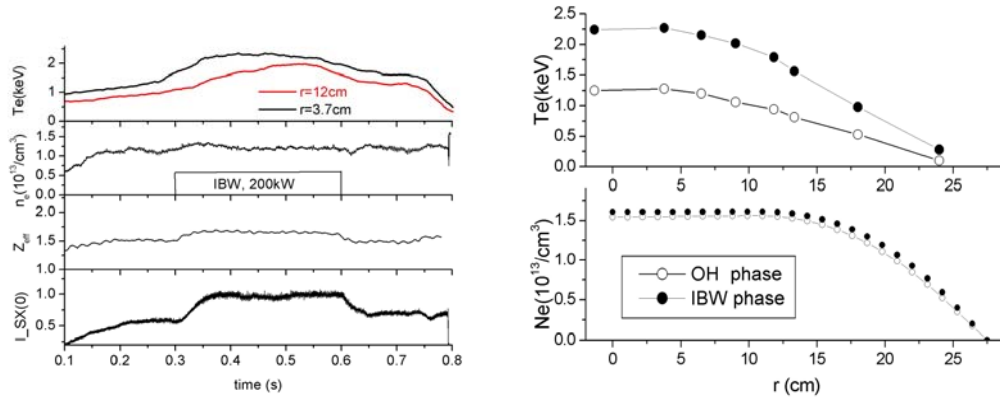
Fig.5   27MHz IBW heating experiment II On-axis heating, B_T=1.88T, $r_{\Omega H}$ ~ 5cm
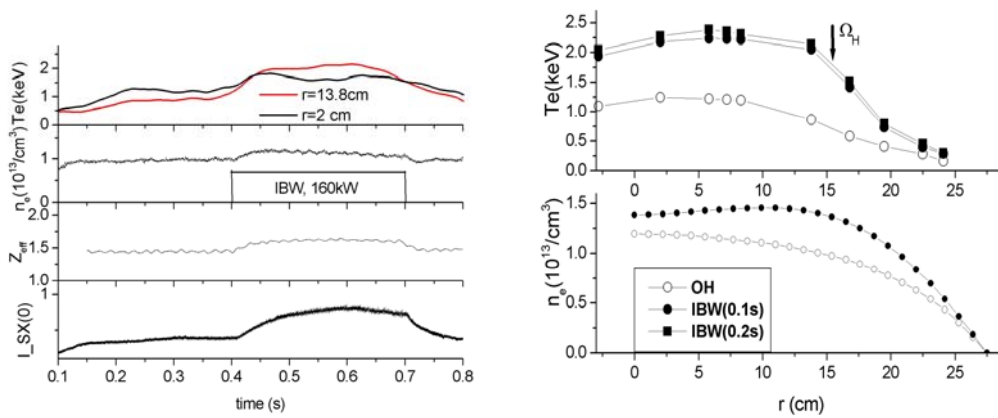
Fig.6   27MHz IBW heating experiment III Off-axis heating, B_T=2T, $r_{\Omega H}$ ~ 15cm
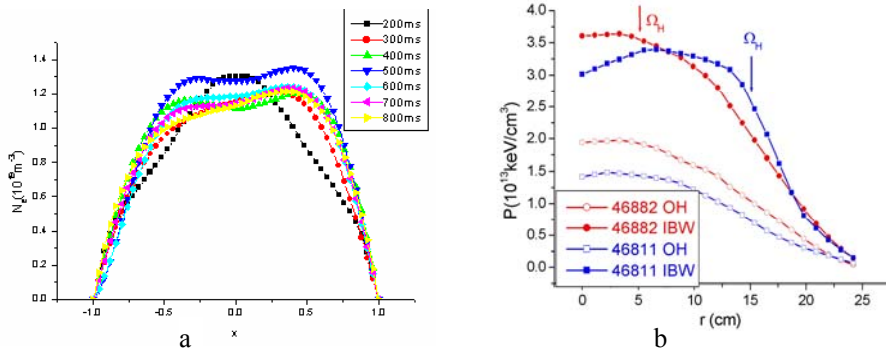
Fig.7   27MHz IBW heating experiment IV: a: Density profile;   b: Pressure profile

For 24 MHz, the $3/2\Omega_D$ resonant layer position was inside the plasma; the $2\Omega_D$ resonant layer position was near the edge on the low field side. The best heating was electron temperature rising about 400eV for 220kW IBW power. The density profile remained almost with no change. No particle confinement improvement was observed even if IBW power was up to 270kW. The experimental data are shown in Fig.8.
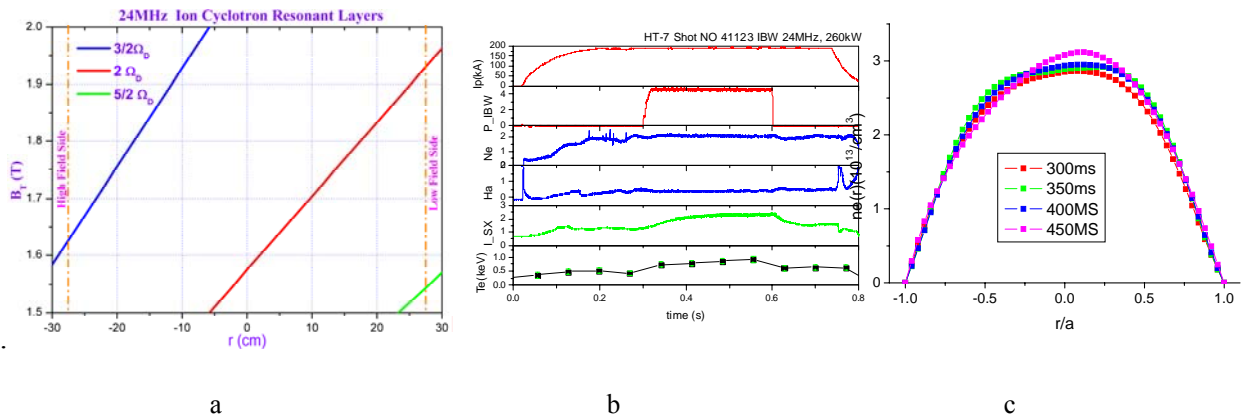
Fig.8 24MHz IBW heating experiment. a: B_T against resonance layers position; b: Plasma discharge;   c: Plasma density profile;

Summary

IBW heating was successfully carried out for the electron-heating mode after intensive RF boronization and helium cleaning. Both on-axis and off-axis electron heating were realized by proper arrangement of the target plasma parameters. Maximum increment in electron temperature

was about 1 keV. The maximum input RF power was 350kW. The fast increase in electron temperature and the low increment in ion temperature gave the evidence that the electron heating was formed by electron Laundau damping.

Both electron and ion heating were observed, and τ_E and τ_p were improved at 30 MHz and 27MHz IBW heating. Electron temperature and pressure profiles can be controlled by varying the ion cyclotron resonant layer for 27MHz IBW heating.

No significant density drop was observed during 24 MHz IBW heating. Only electron heating was observed in the 24MHz heating experiments.

References
[1] M.Ono, Phys. Fluids **B5**, 241 (1993).
[2] A.Cardinali, C.Castaldo, R.Cesario, F.De Marco and F.Paoletti, Nucl. Fusion **42** 427 (2002).
[3] A.Cardinali and F.Romanelli, Phys. Fluids **B4** 504 (1992)
[4] L.A.Berry, E.F.Jaeger and D.B.Batchelor, Phy. Rev. Lett. **82** 1871 (1999).
[5] E.F.Jaeger, L.A.Berry and D.B.Batchelor, Phys. Plasma **7** 3319, (2000)
[6] B.LeBlanc et al, Phy. Rev. Lett. **82** 331 (1999).
[7] K.H.Burrel, Phys. Plasma **6** 4418, (1999).
[8] Y.P.Zhao et al, Plasma Phys. Control. Fusion **43** 343 (2001)
[9] J.Li, Y.Bao, Y.P.Zhao, et al Plasma Phys. Control. Fusion **43** 1227 (2001)
[10] B.N.Wan et al,, "PSI Issues toward to Steady State Plasmas in the HT-7 Tokamak" 15th PSI, I-11, May27-31 2002, Gifu, Japan
[11] F.Paoletti et al Phys. Plasma **6** 863, (1999).
[12]Y.Bao, Doctoral thesis, Institute of plasma physics, Chinese Academy of Sciences, 2001, Hefei, China.

High Power Neutral Beam Injection in LHD

K. Tsumori, Y. Takeiri, K. Nagaoka, K. Ikeda, M. Osakabe, Y. Oka, O. Kaneko,
M. Shibuya, T. Kondo, M. Sato and E. Asano.
National Institute for Fusion Science, 322-6 Oroshi Toki, Gifu, 509-5292 Japan.
e-mail: tsumori@nifs.ac.jp

Abstract

The results of high power injection with a neutral beam injection (NBI) system for the large helical device (LHD) are reported. The system consists of three beam-lines, and two hydrogen negative ion (H$^-$ ion) sources are installed in each beam-line. In order to improve the injection power, the new beam accelerator with multi-slot grounded grid (MSGG) has been developed and applied to one of the beam-lines. Using the accelerator, the maximum powers of 5.7 MW were achieved in 2003 and 2004, and the energy of 189 keV reached at maximum. The power and energy exceeded the design values of the individual beam-line for LHD. The other beam-lines also increased their injection power up to about 4 MW, and the total injection power of 13.1 MW was achieved with three beam-lines in 2003. Although the accelerator had an advantage in high power beam injection, it involved a demerit in the beam focal condition. The disadvantage was resolved by modifying the aperture shapes of the steering grid.

keywords : *NBI, negative ion source.*

1. Introduction

Neutral beam injection is a powerful and reliable method for plasma heating. As the sizes of plasma confinement devices become larger, the beam energy of the NBI should be higher to deposit the beam power at the core part of the plasmas confined in the device. Hydrogen negative ions have much higher neutralization efficiency than hydrogenous positive ions in the energy range of more than 100 keV [1].

The LHD consists of super-conducting coils to investigate steady state confinement plasmas [2]. The thermal insulating structure for the super-conductor is thick to make the NBI ports narrow and long. This requires the beam divergent angle should be less than 10 mrad. The typical major radius of the LHD plasma is 3.7 m and the aspect ratio is six. Considering the shine-through ratio and beam deposition profile, the maximum energy of the LHD-NBI is designed to be 180 keV. The beam power is chosen 5 MW per beam line, and the equivalent hydrogen atom (H^o) current corresponds to ~28 A at the energy of 180 keV. The cesium seeded H$^-$ ion source is adopted to enhance the H$^-$ current and to reduce the beam divergence, simultaneously. The pulse duration for beam injection is normally set at 10 sec.

The LHD experiments with NBI have started with two beam-lines since 1998 [2], and the third beam line has been built in 2001 [3]. The layout of these beam-lines is shown in Fig. 1. All the beam axes are set in the direction tangential to the magnetic axis of the target plasma confined in LHD. One of the beam-lines, beam-line 2, is oriented to the injecting direction opposite to the other beam-lines. In the high power injection, the voltage breakdown at the accelerator has limited the injection power and beam energy. In order to remove the breakdown problem, a new beam accelerator has been developed and applied to the ion sources for the beam-line 1 since 2002 [4]. The accelerator includes the combination of multi-hole electrode grids and multi-slot grid to reduce the heat load onto it. The accelerator contributes to the increase in the injection power and pulse duration.

In this article, we describe the structure of the ion source for high power injection, the

beam characteristics of the source and progress of the injection records of the high power short pulse injections, the disadvantage of the accelerator with MSGG and its solution.

2. Negative Ion Sources for LHD-NBI

The detailed explanations about the negative ion sources for LHD are described elsewhere [5-7]. Figure 2 shows a short side cross-sectional view of the hydrogen negative ion sources for LHD-NBI beam-line 1. The structures of the ion sources for the beam-lines 2 and 3 are similar to that for the beam-line 1 except for some small differences. The ion source can be divided into two parts at the plasma grid, which separates the arc chamber and the beam accelerator. The chamber wall made of oxygen free copper (OFC) and its inner size is 1400 mm in height, 350 mm in width and about 230 mm in depth. The arc plasmas are confined by the magnetic field induced by the multi-cusp and a pair of filter magnets, which cause the dipole magnetic field inside the chamber to be parallel to the chamber short side. The electrons emitted from the filaments are trapped in the filter field, and they decrease their energy by the collisions with neutral hydrogen gas inside the chamber. The energies are low enough to avoid the distraction process of H^- ions with electrons. The production rate of H^- ions is able to rise by seeding Cs vapor into the arc plasmas, and the vapor is injected by three Cs lines set at the backside plate of the arc chamber.

Figure 3a shows the layout of the accelerators, which consists of three electrode grids called plasma grid (PG), extraction grid (EG) and grounded grid (GG), and all the grids have a multi-hole structure. The apertures of the EG exit and GG are displaced to converge the all H^- beamlets at the pivot point of about 13m apart from the GG. The PG of the other grids are made of molybdenum (Mo) and OFC with water-cooling channels, respectively. Figure 3b indicates the accelerator with the multi-slot grounded grid (MSGG), whose single slot corresponds to a row of the multi-hole grounded grid (MHGG) shown in Fig. 3a. The transparency of the MSGG is about twice as large as that of the MHGG. Differing from the acceleration of positive hydrogenous ions, H^- ions separate into hydrogen atoms and electrons (stripped electron) via the collisions with neutral hydrogen gas leaking from the arc chamber. The stripped electrons and H^o carries the heat load onto the grids, and the heat load to the GG is much larger than the other grids. The heat load is considered to become lower with the increasing grid transparency. The heat load onto the MSGG was decreased 50 % of that onto the MSGG [5]. The reduction of beam heat load is expected to decrease the frequency of the voltage breakdowns between SG and GG. In the accelerator with the MSGG, the beamlets cannot be converged in the direction parallel to the long axis of the slots, and then a new grid with displaced circular apertures is added. The grid is called the steering grid (SG), which is made of Mo for the purpose of decreasing the sputtering and thermal distortion caused by the back-streaming positive ions onto the grid.

3. High Power Beam Injections

The injection power as a function of the beam energy is shown in Fig. 4. The dotted line indicates the 5/2 power of the beam energy; it originates from the Child-Langmuir's low. The beam energy achieved the value of 189 keV at the maximum in 2003. Most of the plot points follow the Child-Langmuir's low, while the data obtained in 2004 exceed the line around the energy of 170 keV. Although it is not clear why the saturated H^- current increases beyond the Child-Langmuir's low, such current jumps are sometimes observed after a large amount of Cs is seeded in the arc chamber. In the same year, the injection power of 5.7 MW is achieved with the energy of 186 keV. Last year the power of 5.7 MW was obtained with a lower beam energy of 175 keV. The difference between both cases is considered the amount of seeded Cs into the arc chamber.

The progress in the maximum injection powers since 1998 is shown in Fig. 5. The

beam injection using the accelerator with the MSGG has started since 2002. The data is compared within the record of the beam line 1. After applying the MSGG, it was possible to increase the injection power to more than 3.5 MW, the design energy value of 180 keV. As the next step, the H- current was planned to increase the injection power in 2003. The H- current value is sensitive to the amount of Cs in the arc chamber and the PG temperature, which is risen by the radiation of arc plasmas and heat flow carried by charged particles in the plasmas. Therefore, arc balance in the long axis direction of the arc chamber was tuned carefully. The injection power went up to 5.7 MW with the energy of 186 keV by this tuning [7]. In 2004, the same maximum power was obtained, although the beam energy was lower than 180 keV. Additional to the merit of the new accelerator is its conditioning time. It takes a considerably shorter time to reach the maximum energy of 180 keV, because of the decrease of the voltage breakdowns between the SG and MSGG.

Progress of the total injection power with three beam-lines is indicated in Table 1. It is shown in the table that there is a large improvement of the injection power, which is brought about by the addition of the beam-line 3. The same multi-hole grounded grids are installed in the beam-line 2 and 3, the flow rates cooling-water for the MHGGs are about 20 m^3 / hour. The flow rates are much higher comparing to that in the MSGG for beam-line 1. With the aid of the higher heat removal rate, which is proportional to the water flow rate, both of the beam-lines 2 and 3 achieved the maximum injection powers of around 4 MW. Improvement for every beam-line has been successively made. The injection power has increased year by year, consequently. In 2004, the injection power decreased comparing to the previous year, and that was caused by the mechanical fatigue of the parts of the ion sources.

Year	1998	1999	2000	2001	2002	2003	2004
Total injection power	3.7 MW	4.5 MW	5.2 MW	9.0 MW	10.3 MW	13.1 MW	11.3 MW

Table 1. Progress of the total injection power with three beam-lines for LHD

4. Disadvantage of the Accelerator with MSGG and the Solution

Although the accelerator with MSGG has the advantage to obtain high injection power, the system involves a large disadvantage caused by the different symmetry of electric field near the SG and MSGG. The influence is observed as the separation of focal condition in the direction of the slot long and short axes; the separation is not observed in accelerators consisting of multi-circular aperture grids. Figure 6 shows the typical focal characteristics in the accelerator with the combination of the SG with circular apertures and the MSGG. The e-folding half widths in the directions parallel and perpendicular to the slot long axis is plotted with respect to the change in the voltage ratio (*Rv*) of the acceleration voltage (*Vacc*) to extraction voltage (*Vext*). As shown in this figure, it is clear the minimum beam widths are obtained at different *Rv*. In the practical operation, the Rv is set within the range indicated by the gray part in Fig. 6. The beam profile elongates in the direction perpendicular to the slot long axis.

The elongation of the beam profile induces the irregular concentration of the beams on the surfaces of the components inside the beam-line. The beam injection port and beam dump have melted [8]. The investigation has been done to decrease the separating focal condition using a small-scaled ion source consisting of the SG with multi-racetrack apertures. The dimension of the racetrack aperture is 13 mm x 10 mm, and the long axis of the racetrack is oriented to the direction of the MSGG slot long axis. There are some differences between the small-scaled source and LHD ion source, for instance the grid gaps, applied voltages and so on. The SG with racetrack apertures is investigated to confirm the validity for the reduction to focal

separating characteristics in LHD-NBI. The focal characteristic with a combination of the SG racetrack apertures and MSGG is indicated in Fig. 7. The long and short axes of the racetrack are 13 and 10 mm, and the long axis corresponds to the slot long axis of the MSGG. The voltage ratios obtaining the minimum widths in the long and short direction of MSGG slot become closer in the system with racetrack-SG apertures comparing to that with circular apertures. By modifying the shape of SG aperture, the damage inside the beam line is believed to decrease, and the beam port-through efficiency is expected to increase. The new SG with the racetrack apertures is scheduled to be installed in the ion source of beam-line 1 in 2006.

Acknowledgements

REFERENCES

[1] K. H. Berkner et al., Nucl. Fusion, **15** (1975) 249.

[2] O. Motojima et al., Phys. of Plasma, **6** (1999) 1843.

[3] O. Kaneko et al., Nuclear Fusion, 43 (2003) 692.

[4] K. Tsumori et al., Rev. Sci. Instrum, **75** No. 5 (2004) 1847-1850-.

[5] Y. Takeiri, et al., Rev. Sci. Instrum, **69** No.2 (1998) pp.977-979.

[6] Y. Takeiri, et al., Rev. Sci. Instrum, **71** No.2 (2000) pp. 1225-1230.

[7] K. Tsumori et al, proceedings of the 20th IAEA conference FT/1-2b, Vilamoura (2004).

[8] K. Tsumori et al, "Production and Neutralization of Negative Ions and Beams",

   AIP Conference Proceedings Vol. 763, AIP. Melville, New York (2005) pp. 35-46.

FIGURE CAPTIONS

Fig. 1. Bird's-eye view of the Large Helical Device (LHD) and three beam-lines; every beam-line is equipped with two ion sources. The beam directions of all the beam-lines are tangential to the LHD magnetic axis.

Fig. 2. A cross-sectional view of a hydrogen negative ion source for LHD. The view indicates the short side cross-section.

Fig. 3. Schematic views of the accelerators with the multi-hole grounded grid (a) and the multi-slot grounded grid (b). The former is installed in the ion sources for the beam-lines 2 and 3, and the latter is installed in the sources for beam-line 1.

Fig. 4. Progress of the maximum injection power. Open squares and solid circles indicate the injection power obtained using the accelerators with the MHGG and MSGG, respectively.

Fig. 5. Injection power as a function of beam energy. The data is obtained in the beam line 1 whose ion source is applied to the multi-slot grounded grid. Dotted line indicates the 5/2 power of beam energy.

Fig. 6. e-folding half width of beam profile as a function of voltage ratio (*Rv*) of acceleration voltage (*Vacc*) to extraction voltage (*Vext*). The solid circles and solid diamonds indicate the widths parallel and perpendicular to the slot long axis of the MSGG, respectively. The shape of the SG aperture is circular with a diameter of 13 mm.

Fig. 7. e-folding half width of beam profile as a function of voltage ratio (*Rv*). The data was obtained with use of the accelerator with MSGG and racetrack SG apertures (10x13 mm).

FIGURES
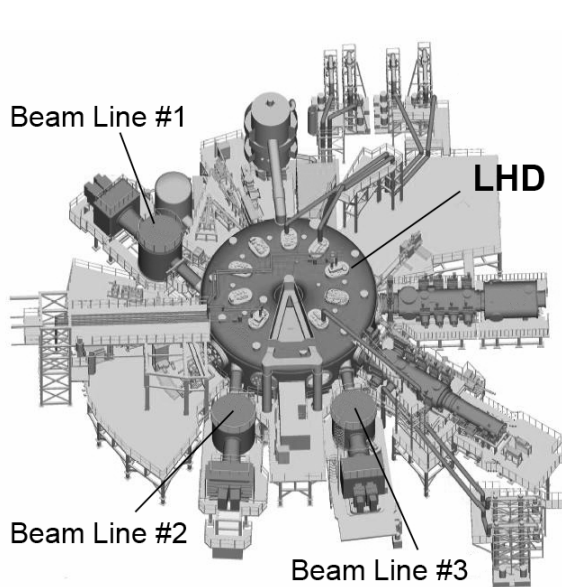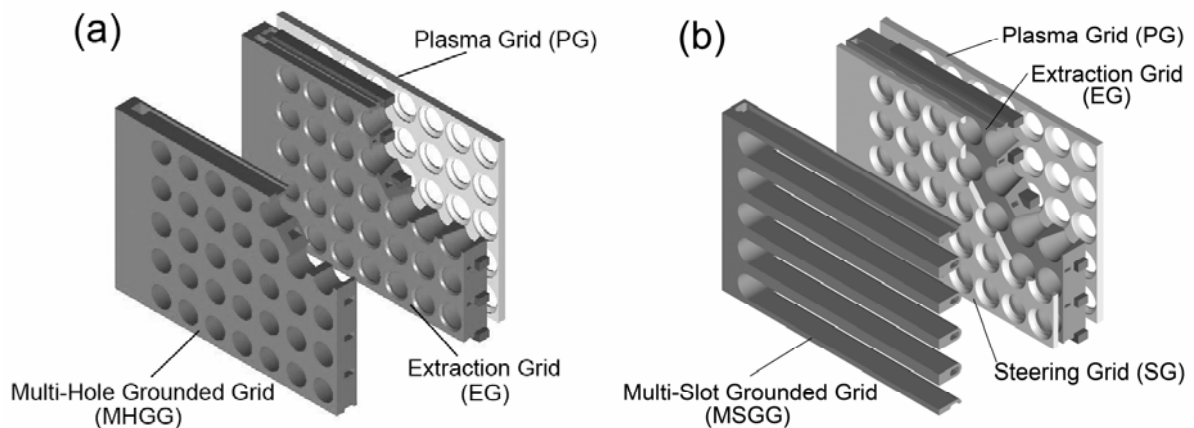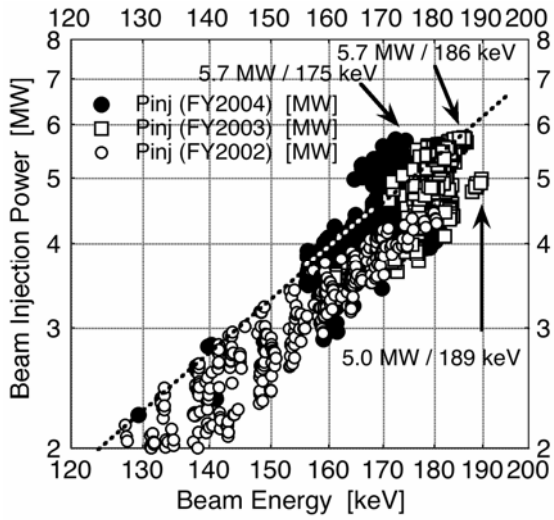

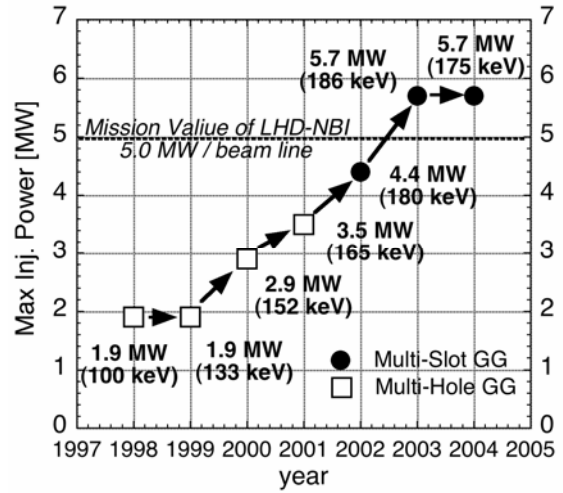*Figure 1*
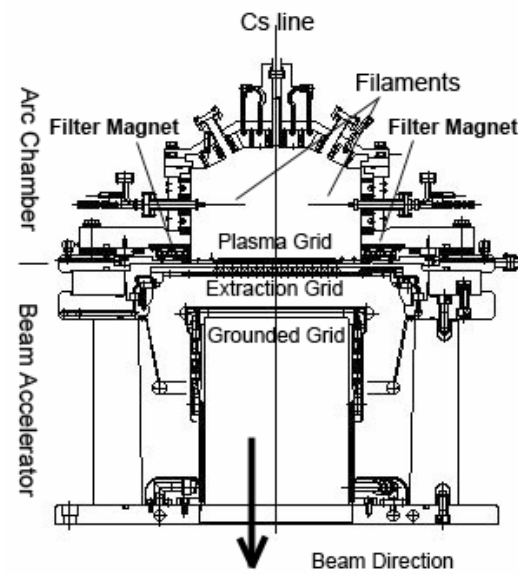
Figure 2

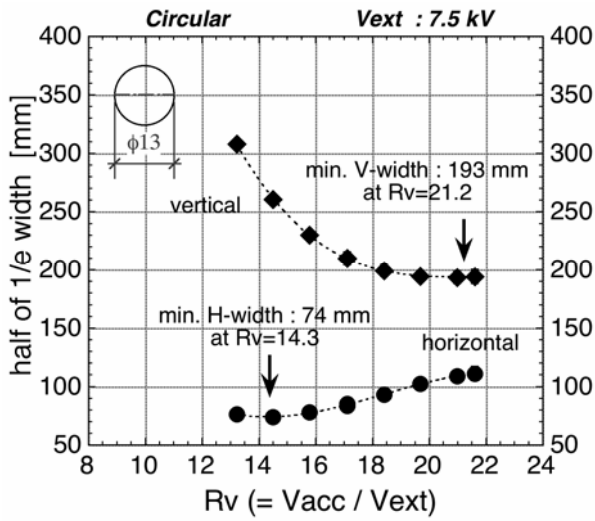*Figure 3a and 3b*

Figure 4

Figure 5

Figure 6
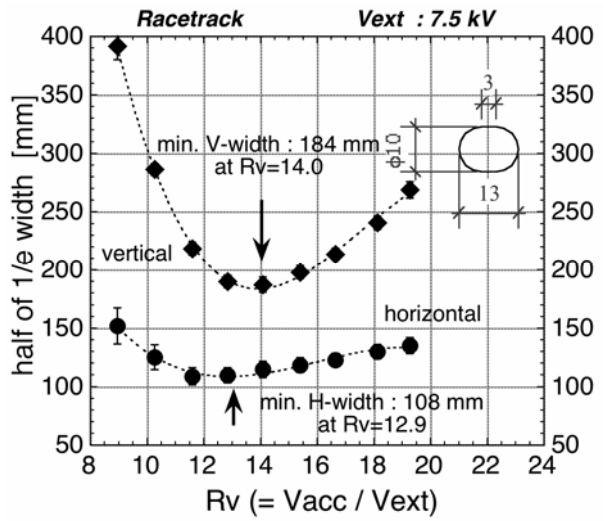
Figure 7

Experimental observation of the pulse high pressure gas puffing on HL-2A

Shi Zhongbing, Ding Xuantong, Yao Lianghua, Liu Zetian, Chen Chengyuan,

Yang Qingwei, Feng Beibin, Zhou Yan, Yan Longwen, Liu Yi, Liu Yong.

Southwestern Institute of Physics, PO BOX 432, Chengdu 610041, China.

Abstract

Asymmetric cold pulse propagation has been observed by means of ECE and soft-X-ray array during pulse-modulated molecular beam injection experiments on HL-2A. The propagation depth is about 30cm on the low field side and only about 10cm on the high field side. The cold pulses cannot propagate to the plasma center from either the low field side or the high field side. The electron temperature in the plasma center does not change during MBI, but electron density pulse perturbations can be observed in the plasma center from the ECE 3rd harmonic measurements, which correspond to the results from the far-infra-red (FIR) laser interferometer.

As an advanced fuelling method on the tokamak, supersonic molecular beam injection (MBI) has successfully been developed in HL-1M[1] first and applied to HT-7[2], Tore Supra[3] and HL-2A later. Many advantages[1~4] such as peaked density profile and improved energy confinement time have been found in the previous MBI experiments. The mechanism of the interaction of the hydrogen molecular beam with plasma has been discussed[4~7] and two basic shielding models have been suggested[5~6]. But up to now the detailed mechanism of the MBI is not clear.

In the present experiment the pulse-modulated MBI is applied to HL-2A. With this method, asymmetric electron temperature (cold) pulse propagation has been observed during MBI. The propagation depth is about 30cm on the low field side (LFS) and only about 10cm on the high field side (HFS). The cold pulse cannot propagate to the plasma center from either LFS or HFS, but the interesting thing is that the large-scale electron density perturbation can be observed in the plasma center. By the way, the experimental results may provide some circumstantial evidence for the shielding models.

HL-2A is a divertor tokamak[8] with the following parameters in this experiment: R=1.65m, a<0.45m,

Fig. 1. Arrangement for MBI in the HL-2A tokamak

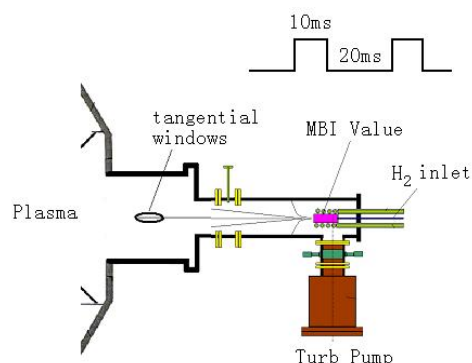$I_p = 0.32\,\text{MA},\ \overline{n_e} = 4.2 \times 10^{19}\,\text{m}^{-3}$, T$_e$=800eV, B$_t$=2.2T. The gas source pressure of MBI is about 0.4MPa.

Fig. 1 shows the experimental set-up of the MBI in the HL-2A tokamak. The molecular beam is injected from LFS. The pulse-modulated molecular beam is driven by an electric-magnetic valve. The width and the period of the pulse are 10ms and 30ms, respectively. Ten pulses of the molecular beam can be injected during one discharge.

More than 30 diagnostics have been developed on HL-2A in recent years. In this observation the FIR laser interferometer, soft-X-ray and ECE have been used. The FIR laser interferometer has one channel through the central plane. Four soft-X-ray arrays in the HL-2A have been arranged and every array has 20 channels. The soft-X-ray intensity is sensitive to the electron temperature, electron density and effective charge. As shown in the formula $I_{sxr} \propto n_e^2 T_e^{\alpha} f(Z_{eff})$, here the exponent α is an increasing function of the absorber foil thickness; its value is usually between 2 and 3. It should be noted that the data of the FIR laser interferometer and soft-X-ray are the central chord line-average signals and chord integrated signal

respectively. Only the ECE gives local parameters. The main results are obtained by means of ECE diagnostic, so the ECE diagnostic on HL-2A will be given in the next paragraph in detail.

The ECE diagnostic system on HL-2A is a 2mm sweeping heterodyne radiometer. The temporal, spatial and frequency resolutions are 4ms, 3cm and 3GHz, respectively. The sweeping frequency range   covers from 104 to 181GHz in 4ms and 20 channels can be

Fig. 2. ECE spectra at 244ms in shot 2988
(stars: 2nd harmonic, squares: 3rd harmonic, crosses: harmonic overlap, solid lines: fitting curves of 2nd and 3rd harmonics)

obtained in one sweeping. In the case of B$_t$=2.5T, we obtain the total second harmonic that provides the full temperature profile. But in the present MBI experiment, B$_t$=2.1T, the frequency ranges of 2nd and 3rd harmonics are from 94 to 156GHz and from 142 to 232GHz, respectively. So only partial 2nd and 3rd harmonics can be obtained. Fig.2 shows the ECE spectrum, which has been obtained in one sweeping at 244ms in shot 2988 with B$_t$=2.1T, $I_p = 0.26\,\text{MA}$, $\overline{n_e} = 1.3 \times 10^{19}\,\text{m}^{-3}$. We can find that the second harmonic frequency in the plasma center is about 117GHz, and the harmonic overlap range is about 142 to

156GHz. They are just in consistency with the values mentioned above. Both the horizontal and vertical displacements of the plasma are less than 3cm in the experiments which would not affect the measurement results. In consideration of the effects of the harmonic overlap and optical thickness profile, the relationships between the intensities of the 2nd or 3rd harmonics and the plasma parameters on HL-2A are given as follows [9]:

$$
\begin{cases}
I_{2\omega_{ce}} \propto kT_e & |r| < 24cm \\
I_{2\omega_{ce}edge} \propto (kT_e)^2 n_e & |r| > 28cm \\
I_{3\omega_{ce}} \propto (kT_e)^3 n_e & |r| < 22cm
\end{cases}
\tag{1}
$$

Fig.3 shows the evolution of the ECE 2nd harmonic at the different radius during pulse-modulated MBI. The minus sign before r in Fig.3 denotes HFS and the plus sign denotes LFS. The propagation of the cold pulses from plasma edge to its inside has been observed obviously. In HFS the cold pulses propagate from r = 41cm to r = 30cm. The amplitude of the cold pulse decreases with the decreasing of the minor radius. The phase difference of the cold pulses at the different radius is difficult to be distinguished because the time resolution of the ECE diagnostic is not high enough, so the phases of the cold pulses look very similar.

Fig. 3. Time evolution of the Te during MBI

On LFS the cold pulses can propagate to r = 12cm. The propagation depth of the cold pulse on LFS is much longer than that on HFS. The propagation depth of the cold pulse during the MBI is asymmetric. The intensity of the ECE 2nd harmonic at the edge of the plasma is not always propertional to the electron temperature because of the low optical thickness, but the propagation of the cold pulse is only related with the variation of the electron temperature obviously, because its phase is in consistency with the edge electron temperature measured by the electrostatic probe, which is shown at the bottom of Fig.3.

The asymmetric propagation of the cold pulse also can be observed by soft-X-ray array. The sight lines of the half detectors of the array pass through the plasma on HFS and half of them pass through the plasma on LFS. Fig. 4 shows the time evolution of the soft-X-ray intensity obtained from the array installed at the top-right of the tokamak. The r in Fig.4 expresses the radius of the middle point of the sight chord of the detector. It can be found that the phase of the SXR intensity pulses in the plasma center is reverse to the phase of the pulses at the plasma edge, which is in-phase with the ECE 2nd harmonic measurement. The SXR intensity pulses in the plasma center are related with variation of the electron density, which will be analyzed in the next paragraph. Because the diagnostic of the soft-X-ray is not local measurement, the features of the cold pulse propagation, for example the amplitude and the phase of the cold pulse, are not obvious, but it is obvious that the propagations depth of the temperature perturbation on LFS and HFS are different. The cold pulses of the soft-X-ray at the plasma edge have small phase shift. The propagation depths of the cold pulse on LFS and HFS are about 29cm and 14cm, respectively, which is in good

Fig. 4. Variations of SXR intensities during MBI

agreement with the results of the ECE 2nd harmonic measurement.

Five channels of the ECE 3rd harmonic which almost lie on LFS can be measured in the case of B_t=2.1T. Fig.5 shows the time evolution of the ECE 3rd harmonic during pulse-modulated MBI. The perturbations of the ECE 3rd harmonic have been observed during the gas injection, and the phase of the perturbation in the plasma center (r= 2cm and r= –4cm) is reverse to the phase of the pulse at r = 14cm and r= 8cm, which is in-phase with the ECE 2nd harmonic measurement. To check the physics meaning of the pulse perturbations measured by the ECE 3rd harmonic, comparison has been made between the signal of the ECE 3rd harmonic in plasma center and the signal of the line average density measured by the FIR laser interferometer. The bottom of Fig.5 shows the time evolution of the line average density. It can be found obviously that the line average density increases during MBI with pulse perturbations and the phase of the perturbation is

corresponding to that of the ECE 3rd harmonic in the plasma center, indicating that the perturbation of the ECE 3rd harmonic in the plasma center is really produced by variation of the electron density. According to Eq. (1), the intensity of the ECE 3rd harmonic is proportional to the electron density and the cube of the electron temperature. The perturbations of the ECE 3rd harmonic at r = 14cm and r= 8cm are mainly related with the perturbations of electron temperature, because the intensity of the 3rd harmonic decreases during the gas injection and the temperature perturbation has been observed at r= 12cm by the ECE 2nd harmonic also. But the electron temperature in the plasma center (from 6cm to –6cm) is not changed as mentioned above, therefore the perturbations of the ECE 3rd harmonic at r = 2cm and r= -4cm are only related with the electron density. The soft-X-ray perturbations in

Fig. 5. Time evolution of 3rd harmonic and n_e

the plasma center have the same phase features, which means that the soft-X-ray perturbations are also related with the electron density, instead of electron temperature. All of these diagnostics show that the electron density pulses can be observed in the plasma center during the MBI.

The experimental results can be summarized as follows:

1) The heat pulses propagation is asymmetric during MBI. The propagation depth is about 30cm on LFS and only about 10cm on HFS.

2) The electron temperature pulses cannot propagate to the plasma center from both LFS and HFS and the electron temperature in the plasma center is not changed during MBI, but large-scale electron density pulse perturbations are observed in the plasma center.

Studies of the MBI physics deal with the shielding mechanisms, including the gas dynamic shielding caused by collisions between the hot plasma and the cold supersonic molecular beam (SMB) particles, the magnetic shielding caused by the partial expulsion of the magnetic field from the SMB interior by the expanding plasma and the associated

Fig. 6. Diagram of the shielding model

reduction of the flux of energy carriers and the electrostatic shielding due to the negative charge accumulation of the cold SMB aspect to the hot plasma. Figure 6 shows the diagram of the shielding model. According to these shielding mechanisms, it is possible to form a "cold channel", through which the particles of the cold SMB can penetrate into plasma more deeply. Because the shielding layers exist on both sides of the SMB, which is cross over the magnetic surface, so it will affect the transport along the magnetic line. The heat pulse propagation along the magnetic line may be much slower than that without the SMB. The asymmetric heat pulse propagation between the LFS and HFS indicate that the heat pulses produced on LFS have not propagated to the same depth at HFS along the magnetic line, therefore the observation results give evidence of the shielding mechanisms of the SMB physics indirectly.

According to the available numerical model of the SMB ablation and penetration[7], the particles of the MBI can penetrate into the plasma more deeply than the normal gas puffing in the middle size tokamaks, but it is difficult to penetrate into the plasma core. Indeed, the heat perturbation cannot be observed in the plasma center. So the density perturbation observed in the plasma core is not related with the particle penetration depth, otherwise it must be related with the transport features of the particles during the MBI, which is very important in understanding the improved confinement with this fuelling method. It will be the next step to investigate the particle transport features during the MBI with high spatial and time resolution diagnostics, for example the microwave reflectometry.

Reference:

[1] Yao Lianghua et al 1998 *Nucl. Fusion* **38** 631

[2] Gao Xiang et al 2000 *Nucl. Fusion* **40** 1875

[3] J Bucalossi et al 2002 *19th IAEA Fusion Energy Conf.* (Oct. 14-19, 2002, Lyon, France)

[4] Yao Lianghua et al 2001 *Nucl. Fusion* **41** 817

[5] Binren S. Nucl 2001 *Fusion Plasma Phys. (in Chinese)* **21** 200

[6] Song Xianming et al 2003 *J. Plasma Fusion Res.* **76** 282

[7] Jiao Yiming et al 2003 *Plasma Phys. Control. Fusion* **45** 2001

[8] Liu Yong et al 2004 *Nucl. Fusion* **44** 372

[9] Equipe TFR 1978 *Nuclear Fusion* **18** 647

Formation of Edge Transport Barrier
by LH Transition and Large Reversed Plasma Current on LHD

K. Toi, S. Ohdachi, F. Watanabe[1], K. Narihara, T. Morisaki,
X. Gao[2], M. Goto, K. Ida, S. Masuzaki, K. Miyazawa, S. Morita, S. Sakakibara,
K. Tanaka, T. Tokuzawa, K.W. Watanabe, L. Yan[3], M. Yoshinuma
and LHD Experimental Group

National Institute for Fusion Science, Toki, Japan
[1] Department of Energy Science and Engineering, Nagoya University, Nagoya, Japan
[2] Institute of Plasma Physics, Chinese Academy of Sciences, Hefei, China
[3] Southwestern Institute of Physics, Chengdu, China

e-mail: toi@lhd.nifs.ac.jp
key words: edge transport barrier, ergodic field layer, L-H transition, ELMs,
edge MHD modes

Abstract

On the Large Helical Device (LHD) where the nested magnetic surfaces are surrounded by an ergodic field layer, an edge transport barrier (ETB) was produced in neutral-beam-injection(NBI) heated plasmas through transition and non-transition processes. The former case is the ETB formation by L-H transition in relatively high beta plasmas, where characteristic features of L-H transition observed in a tokamak plasma are clearly recognized. The confinement improvement is modest, compared with the ISS95 international stellarator scaling. The threshold power for the transition is comparable or slightly smaller than the ITER scaling law established by tokamaks and compact tori. The former ETB extends into the ergodic field layer in the vacuum field, which suggests the healing of the ergodic layer. The ETB formation destabilizes the edge coherent modes such as m/n=1/1, 2/3, 1/2 and so on, because of the magnetic hill in the plasma edge. The formed ETB is partially and transiently destroyed by these coherent edge MHD modes and ELM activities having small amplitude. The latter ETB is observed in NBI heated plasmas with a large reversed NBI-driven current in the range of more than 100 kA at B_t=1T. In these plasmas, the edge magnetic shear is enhanced by the current and the rotational transform in the core region is expected to be appreciably reduced. Thus reduced rotational transform in the plasma central region enhances heat and particle fluxes toward the ergodic edge layer. The ETB with a steep electron temperature gradient up to ~5 keV/m is formed by blocking enhanced outward heat flux.

1. Introduction

Since the discovery of rapid transition from the low (L-mode) to high confinement regime (H-mode) in ASDEX[1], the L-H transition has been observed during the past two decades in various tokamak configurations [2]. The transition has also been observed in stellarators or helical devices[3-6]. A universally observed signature of the transition was the formation of the edge transport barrier (ETB). Although many theoretical models of the transition in tokamaks and helical devices have been proposed [7-9], the understanding of the L-H transition mechanism and the formation of ETB is still insufficient. In particular, the magneto-hydro-dynamic (MHD) stability of a plasma with ETB has attracted much attention due to its impact on the possibility of sustaining an H-mode plasma with favorable divertor action at steady state. In a tokamak, the plasma is situated at a magnetic well which enhances the MHD stability of the plasma, especially in the edge region. The edge localized modes (ELMs) [10] have variably been correlated with the stability of the ideal/resistive ballooning mode or kink/peeling mode. However, there is yet no complete understanding of the characteristics of the ELMs to allow their control during the operation of a reactor grade plasma. Recently, the experiment in DIII-D has demonstrated that type-I ELM can be effectively suppressed by introducing edge ergodization, without loosing the plasma performance [11]. In a tokamak with an axisymmetric poloidal divertor, regions of closed magnetic surface and open field line are clearly separated by the separatrix. However, externally applied resonant helical field, small misalignment of poloidal coils and/or edge MHD instabilities could generate magnetic islands near the separatrix and lead to ergodic separatrix [12].

Edge transport barrier (ETB) related to LH transition was observed in high beta regime on LHD [13,14]. The LHD has a magnetic configuration with a helical divertor, where nested magnetic surfaces are surrounded by an ergodic field layer. It is interesting and important to study how edge magnetic islands and field ergodization affect the formation of ETB and the characteristics of ELMs. The study of ETB plasmas in LHD may give us important information about field ergodization's effect on the ETB formation and ELM characteristics in toroidal plasmas.

This paper is organized as follows. In section 2, we show typical waveforms of an H-mode shot. The changes in electron temperature and density profiles across the transition are shown. In section 3, the threshold power for the transition is compared with the ITER scaling law established among various tokamaks and spherical tori. The global stability is experimentally studied and the results are shown in section 4. In section 5, ETB formed by a non-transition process in NBI heated plasmas with large reversed plasma current is briefly discussed. Finally, we summarize the experimental results on the ETB formation by transition and non-transition processes in LHD.

2. Characteristics of LH Transition and Structure of ETB

In LHD, ETB was obtained through L-H transition only by NBI heating more than ~1.4 MW and at a relatively low toroidal field of $B_t \leq 1.2$ T. So far, ETB was formed in the range of line averaged electron density from ~1×10^{19} m^{-3} to ~ 3×10^{19} m^{-3}. For this parameter range, the ETB plasmas are usually achieved in relatively high beta (more than ~1.5 % averaged diamagnetic beta). A typical waveform of H-mode hydrogen plasma

achieved at the highest toroidal field of B_t=1.2T is shown in Fig.1. The absorbed NBI power is ~4.3 MW. As seen from this figure, edge electron density starts to increase preferentially at the moment of the depression of Hα-light. This behavior of edge electron density and Hα-light is similar to that in a tokamak H-mode, but the drop of Hα light across the transition is fairly small. In this shot, the global energy confinement time is enhanced by ~10% in the stationary phase, and ~40% in the rising phase of the stored energy when the time derivative of the stored energy is taken into account. In this relatively high beta H-mode, ELMs and edge MHD modes are immediately excited with fairly short ELM free phase of ~20 ms, and stop the further increase in beta value. This detail is discussed in Section.**4**. In the last annual campaign, L-H transition was achieved at a fairly low density and low beta regime of $<n_e>$~1.3x10^{19} m^{-3} and $<\beta_{dia}>$~0.9 %, as shown in Fig.2. In this shot, ELM free phase of about 200 ms duration was realized and the beta value was continuously increased in the phase.

In H-mode shots of LHD, electron temperature profile remains unchanged having almost constant gradient, although edge electron density is obviously increased keeping a hollow profile. Figure 3 shows the change in electron and density profiles across the transition for the shot shown in Fig.1. It is obvious from this figure that ETB zone extends into the ergodic layer defined in the vacuum field. This result can be interpreted in two possible ways. One is that the ETB zone extends inside the ergodic field layer which is formed in the vacuum field and still exists in finite beta plasma. The other is that the ergodic field layer is partially healed by plasma effects and then ETB extends to the healed zone. The achieved gradient of Te is ~1.1 keV/m is modest in the ETB zone. This suggests that the ETB region may be in a region with almost nested magnetic surfaces which may be partially broken.

The poloidal rotation velocity was measured by charge exchange spectroscopy of Ne X spectral line from doped neon gas. The data indicates that the radial electric field *Er* in the H-phase obviously changed to an appreciably negative value over a relatively wide zone of the plasma edge (0.8 < ρ). However, the information of *Er* in the more edge region of ρ>0.9 reaching ETB "foot" is still missing. The space potential measurements in the edge region by the fast reciprocating Langmuir probe or heavy ion beam probe may be employed to get the information about Er over the ETB zone in the next experimental campaign.

3. Threshold Power for the Transition

The L-H transition observed in LHD has a lot of similarity to that in a tokamak H-mode. The ETB structure is somewhat different from that in tokamaks. It is interesting to compare the threshold power in LHD with the ITER scaling law for the threshold power which was established by the data of many tokamaks and two spherical tori. For hydrogen plasma, the threshold power is expressed as P_{th}=0.042$<n_e>^{0.64}B_t^{0.78}S^{0.94}$x2 (MW) by taking into account an isotope effect, where the units of $<n_e>$, B_t and S are 10^{20} m^{-3}, T and m^2, and S=4π2aR((1+κ^2)/2)$^{0.5}$ (a, R: minor and major radii in m, κ: elongation of the magnetic surface)[15]. Figure 4 shows the comparison. In last year's experimental campaign, the threshold power in LHD was

reduced down to ~90% of that predicted by the ITER scaling, although a detailed power scan has not been done yet.

4. Edge Stability and Edge Localized Modes

When ETB is formed near the edge, the edge coherent modes of which rational surfaces reside in the edge region are strongly excited (Fig.5).   Typically, edge modes such as m/n=1/1, 2/3 and so on are enhanced, where m and n are poloidal and toroidal mode numbers.   In the shot shown in Fig.5, the edge mode m/n=1/2 of which rational surface resides in the further outer region compared with that of m/n=2/3 is strongly enhanced, while the m/n=2/3 mode decays after the ETB formation.   The enhanced m/n=1/2 mode leads to saturation of $<\beta_{dia}>$.   In this shot, the m/n=2/5 mode is progressively excited.   These results suggest that the steep gradient region is expanded by ETB formation toward the further outer region where the ergodic layer is formed in the vacuum field.   Several sets of soft X-ray (SX) detector array revealed that the relative SX-fluctuation amplitude increases rapidly toward the relevant rational surface in the plasma edge.   This clearly indicates a characteristic of the edge MHD modes.   In ETB plasmas of LHD, Hα light exhibits frequent and small amplitude ELM like activities.   In addition to enhancement of the edge coherent modes, magnetic fluctuations up to 100 kHz are enhanced during the ELMing phase.   As an example, we show the change in the power spectrum of magnetic fluctuations in Fig.6.   This figure clearly indicates enhancement of the coherent modes having several satellites and incoherent components during H-phase with ELM activities.   These edge modes and their higher harmonic satellites excited in the edge region may suppress a strong density rise without large type-I ELM like spikes.   They have a similarity to edge harmonic oscillations observed in DIII-D [16].   If these edge MHD modes and ELM activities are favorably controlled, the plasma beta could be increased further without large amplitude singular ELMs.

5. Formation of ETB like Structure in Plasma with Large Reversed Plasma Current

In LHD, ETB is also formed non-transitionally in a particular discharge condition. In this discharge the reversed plasma current is driven by counter NBI up to a very large value corresponding to ~130 kA at B_t=1T, so that the magnetic shear near the edge is enhanced and the rotational transform in the plasma central region should be expected to be very small (Fig.6(a)).   This experiment was designed to investigate the role of edge magnetic shear on the edge MHD modes. It also aimed at simulating a current hole observed in a tokamak and studying the role of rational surface of $\iota/2\pi$=0 on MHD equilibrium and stability, and transport.   This experiment was conducted by injection of counter beams into mixture gas of hydrogen and neon in order to enhance the absorption rate of NBI and minimize the electron return current during NBI current drive. With the increase in the reversed current, Te-profile became flat having an asymmetric shape against the magnetic axis (Fig.6(b)).   A large reversed current driven by counter NBI was expected to decrease $\iota/2\pi$ near the plasma central region and to enhanced heat and particle fluxes toward the edge.   High magnetic shear region further increased by the reversed current blocked these fluxes appreciably and generated ETB.   The edge gradient in Te

reached up to ~5 keV/m.   It is interesting to clarify how large gradient in the edge can be sustained in high beta plasma with a large reversed plasma current.

6. Summary

In LHD of which magnetic surfaces are surrounded by an ergodic field layer in the vacuum field, ETBs are transitionally generated by L-H transition and non-transitionally by the large reversed plasma current.   ETB formed by L-H transition destabilizes the edge MHD modes and ELMs, which stop the further rise in plasma beta.   In the non-transition case, only the m=1/1 or 2/2 mode is destabilized but gradually decays with the increase in the reversed plasma current.   The power threshold to get H-mode is comparable to or slightly smaller than that from the ITER scaling.   So far, the confinement improvement is modest.   Suppression of the edge MHD modes enhanced in H-phase is crucial to achieve high confinement in the high beta regime.   Studies of ETB formation by transition and non-transition processes are very important to understand and improve the properties of MHD stability and transport in the edge region of LHD, where the edge magnetic field structure is very complicated because it is involved with various factors such as the magnetic hill, high magnetic shear and rotational transform, field ergodicity, helical diverter structure, and so on.

References

[1] F. Wagner, G. Becker, K. Behringer et al., Phys. Rev. Lett. 49, 1408 (1982).

[2] ITER Physics Expert Groups on Confinement and Transport, and Confinement Modeling and Database, Chap.2 of ITER Physics Basis, Nucl. Fusion 39, 2175 (1999), and references therein.

[3] K. Toi, S. Okamura, H. Iguchi et al., Proceedings of the 14th IAEA Conf. on Plasma Phys. and Control. Fusion Res., Würzburg, 1992, (IAEA, Vienna, 1993), Vol.2, p461.

[4] K. Toi, S. Ohdachi, T. Morisaki et al., Plasma Phys. Control. Fusion 38 (1996) 1289.

[5] V. Erckmann, F. Wagner, J. Baldzuhn et al.,Phys. Rev. Lett. 70, 2086 (1993).

[6] F. Wagner, J. Baldzuhn, R. Brakel et al., Plasma Phys. Control. Fusion 36, A61 (1994).

[7] J.W. Connor and H.R. Wilson, Plasma Phys. Control. Fusion 42, R1 (2000).

[8] K.C. Shaing, Phys. Rev. Lett. 76, 4364 (1996).

[9] L. Garcia, B.A. Carreras, V.E. Lynch, J.N. Leboeuf and D.E. Newman, Phys. Plasmas 4, 3282 (1997).

[10] J.W. Connor, Plasma Phys. Control. Fusion 40, 191 (1998).

[11] T.E. Evans et al., Phys. Rev. Lett.92, 235003-1(2004).

[12] J. Neuhauser et al., Plasma Phys. Contr. Fusion 31, 1551(1989).

[13] K. Toi et al., Nucl. Fusion **44**, 217(2004).

[14] K. Toi et al., Phys. Plasma **12**, 020701-1(2005).

[15] Snipes et al., Proc. of 19th IAEA fusion energy conference, Lyon, 2002, paper No. CT/P-04.

[16] C.M. Greenfield et al., Phys. Rev. Lett. **86**, 4544 (2001)
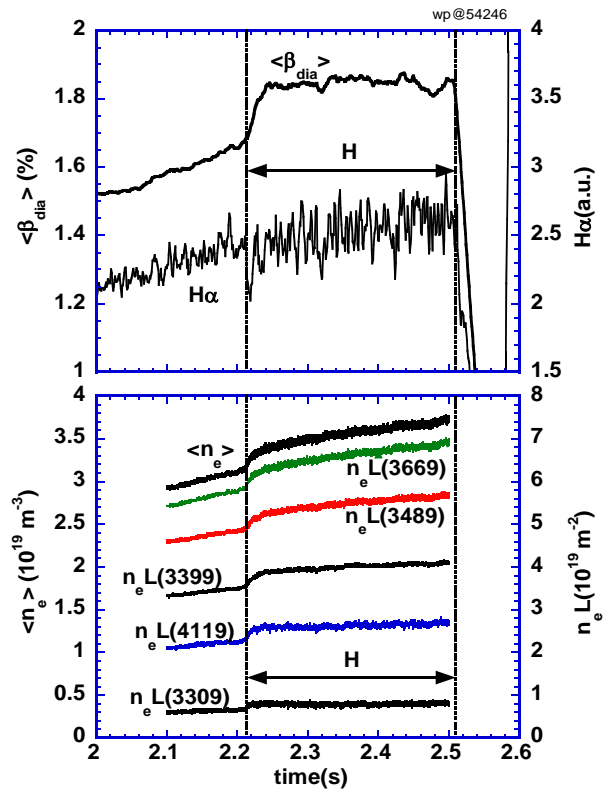
Fig.1. Typical waveform of a plasma with L-H transition achieved at Bt=-1.2 T with ~4.3 MW absorbed NBI power, where the magnetic axis position of the vacuum field is R_{ax}=3.6 m and the pitch parameter related to the plasma aspect ratio γ=1.22.
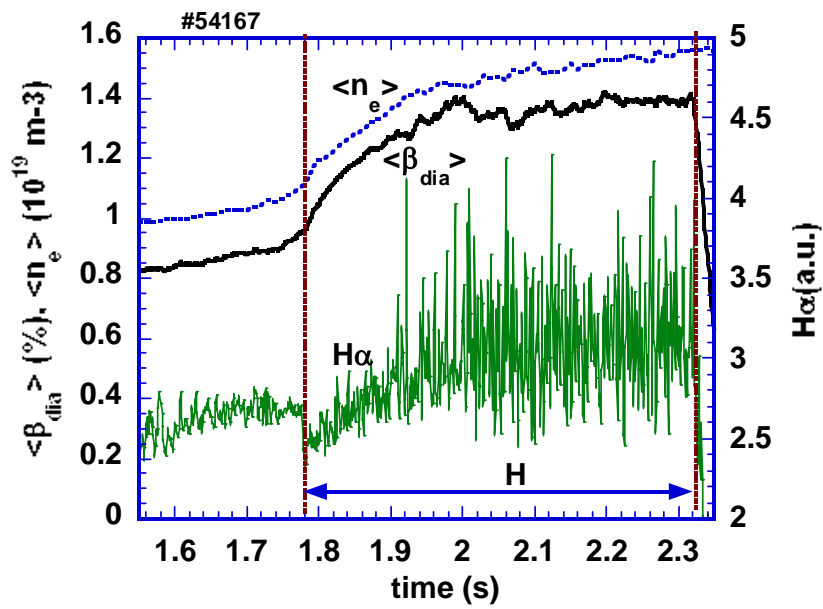
Fig.2 Waveform of an ETB plasma achieved in low beta regime.
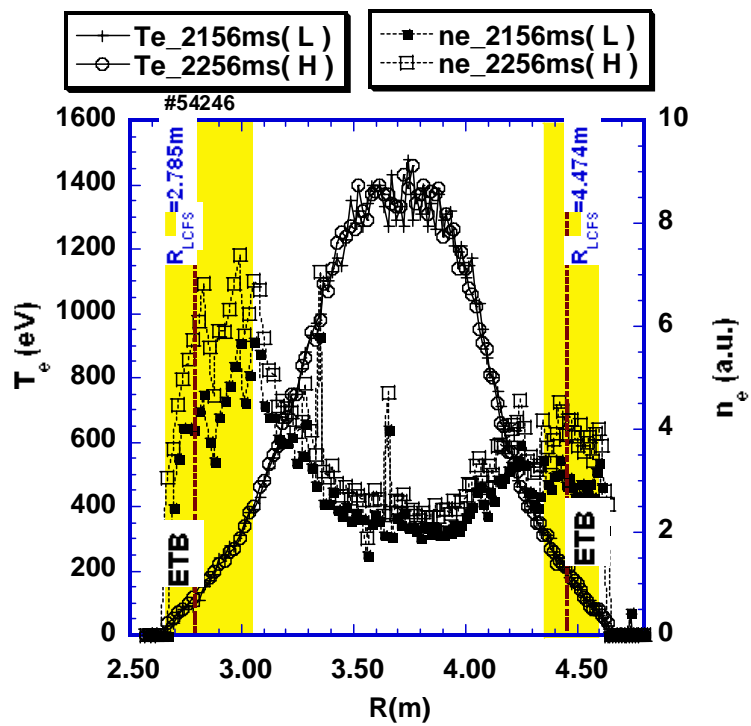
Fig.3 Radial profiles of electron temperature and density just before and after the transition in the shot shown in Fig.1. The word "R_{LCFS}" stands for the last closed flux surface defined in the vacuum field.
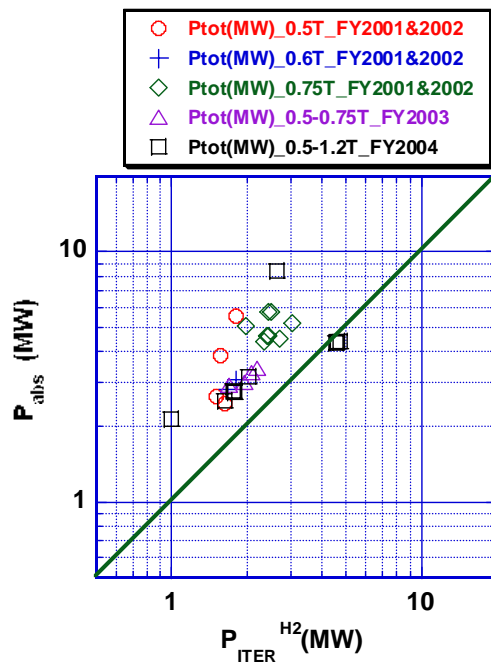
Fig.4 Comparison of absorbed NBI power to trigger the L-H transition with the ITER scaling of the threshold power.

(a)
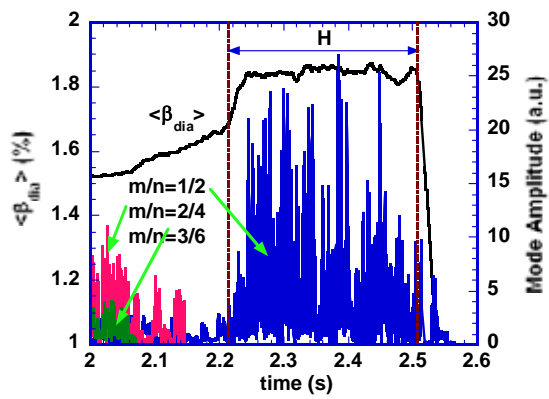
(b)
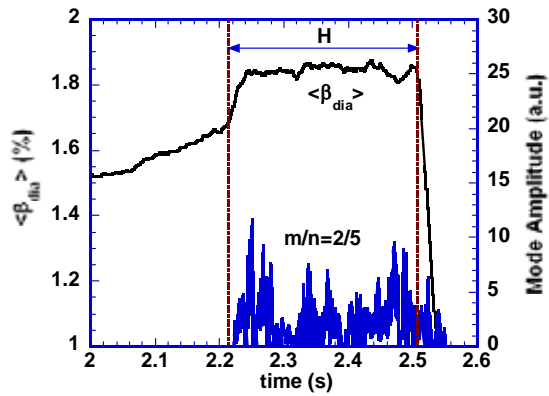
Fig.5 Time evolutions of magnetic fluctuations for m/n=1/2 and
the sattelittes(a), and m/n=2/5(b)
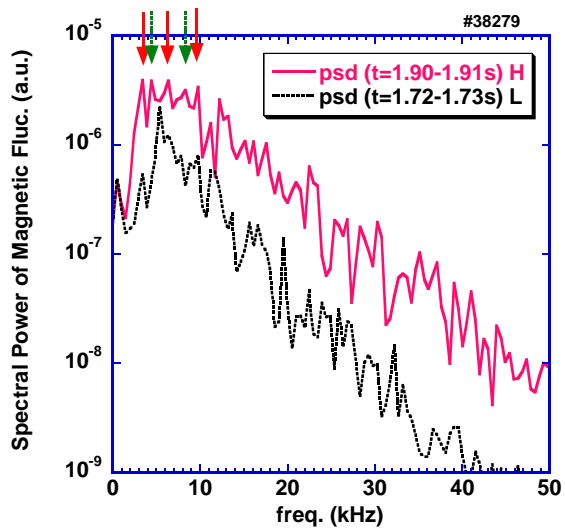
Fig.6 Power spectra of magnetic fluctuations just before and in the H-phase. Edge coherent mode of m/n=2/3 and the satellites, and m=1/2 (or m/n=2/5) and the satellites are strongly enhanced by the ETB formation. Arrows at the upper corner indicate dominant satellite peaks.

(a)

#47345
B_t=1T, R_{ax}=3.75 m, P_{NBI}(CTR)=4.9 MW

$<n_e>$

Hα

$<\beta_{dia}>$

Hα

Ip

$<\beta_{dia}>$(%), $<n_e>$(10^{19} m^{-3}), Hα(a.u.)

Ip(kA)

time(s)

(b)

○ T_e(1075ms)I_p=- 21kA   ◇ n_e(1075ms)I_p=- 21kA
○ T_e(1825ms)I_p=- 88kA   ◇ n_e(1825ms)I_p=- 88kA
● T_e(2725ms)I_p=-130kA   ◆ n_e(2725ms)I_p=-130kA

T_e (eV)

n_e (a.u.)

R_{LCFS}=2.937m

R_{LCFS}=4.569m

#47345

T_e

n_e

R(m)
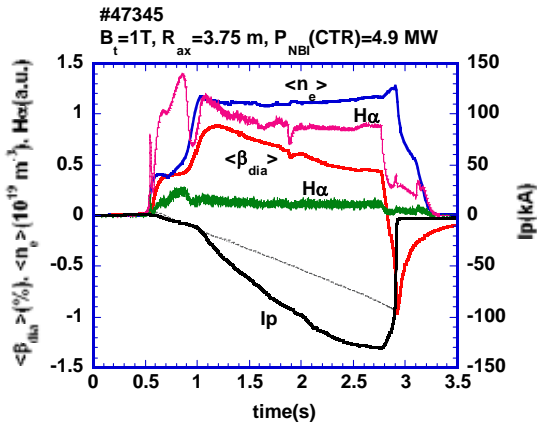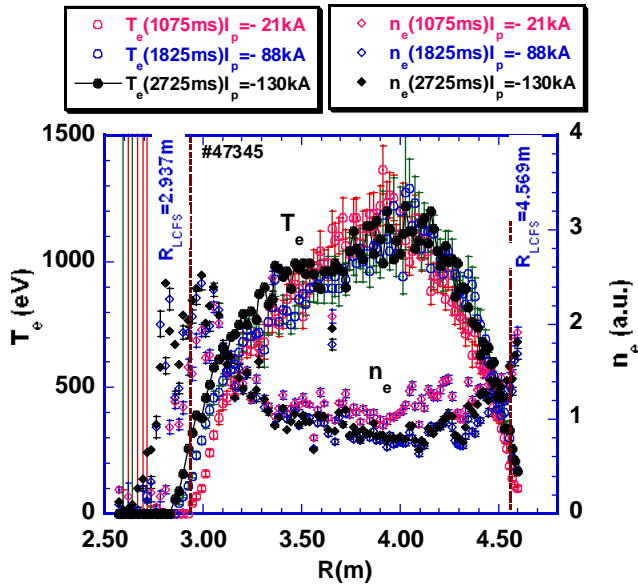
Fig.7(a) Waveforms of a discharge with large reversed current produced in the configuration of R_{ax}=3.75m at B_t=1T.   In order to enhance NBI driven current, neon gas is doped.   Note the decline of $<\beta_{dia}>$ is caused by failure of correction of the plasma current contribution in diamagnetic measurement.   (b) Radial profiles of T_e and n_e profiles with steep gradient near the edge for three time slices at various Ip. R_{LCFS} stands for the last closed flux surface of the vacuum field.

Dynamics of secondary large-scale structures in ETG turbulence simulations

Jiquan Li[1], Y. Kishimoto[2,3], J. Q. Dong[1], N. Miyato[3], T. Matsumoto[3]

1   *Southwestern Institute of Physics, P.O. Box 432, Chengdu, Sichuan 610041, China*

and   SWIP-DUT Joint Lab for Fusion Plasma Physics, Chengdu, China

2   *Department of Fundamental Energy, Kyoto University, 611-0011 Gokasho, Uji, Japan*

3   *Naka Fusion Research Establishment, JAERI, Naka, Ibaraki 311-0193, Japan*

e-mail contact of main author: lijq@swip.ac.cn

Abstract. The dynamics of secondary large-scale structures in electron-temperature-gradient (ETG) turbulence is investigated based on gyrofluid simulations in sheared slab geometry. It is found that structural bifurcation to zonal flow dominated or streamer-like states depends on the spectral anisotropy of turbulent ETG fluctuation, which is governed by the magnetic shear. The turbulent electron transport is suppressed by enhanced zonal flows. However, it is still low even if the streamer is formed in ETG turbulence with strong shears. It shows that the low transport may be related to the secondary excitation of poloidal long-wavelength mode due to the beat wave of the most unstable components or a modulation instability. This large-scale structure with low-frequency and long-wavelength may saturate, or at least contribute to saturating ETG fluctuations through a poloidal mode coupling. The result suggests a low fluctuation level in ETG turbulence.

1. Introduction

Much attention has been paid to the anomalous electron transport in magnetic confinement fusion plasmas. Recent renewed interest in this subject is the role of anisotropic large-scale structures, such as zonal flows, streamers and poloidal long-wavelength fluctuation, namely the Generalized Kelvin-Helmholtz (GKH) mode, in electron-temperature-gradient (ETG) driven turbulence and electron transport[1-6]. It is known that zonal flows can efficiently suppress turbulent heat transport through the shearing decorrelation of turbulence. Meanwhile, streamers may enhance the transport by increasing radial correlation length according to the mixing length estimate approximation. Both of such different patterns have been observed numerically in ETG

turbulence in the tokamak configuration, which are closely linked to the electron transport level [1-5]. However, recent gyrofluid and gyrokinetic ETG simulations show that the turbulent electron transport is still low even if the radially elongated streamers are formed in ETG turbulence[3-5]. The disparity of these results may be ascribed to the saturation mechanism of ETG turbulence since the transport level depends not only on the existence of streamers, but also on the ETG fluctuation amplitude. Generally speaking, anisotropic large-scale structures with low-frequency, such as zonal flows, streamers and GKH modes [6], may interact with the primary instability and play an essential role in turbulence saturation. Due to the different roles of such structures in plasma transport, it is worthwhile to systematically investigate some related issues, such as whether the zonal flows or streamers are preferentially generated in ETG fluctuations; what physical parameters may determine the formation of zonal flows or streamers in ETG turbulence; how the secondary streamers interact with the primary ETG turbulence; and what is the role of GKH mode in ETG turbulence and/or electron transport.

In this work, we perform 3D gyrofluid ETG simulations and develop simplified modeling analysis to understand the above-mentioned important questions. In Section II, structural bifurcation to zonal flows or streamers in ETG turbulence is considered. The role of magnetic shear in the generation of large-scale structures is discussed. In Section III, how secondary poloidal long-wavelength mode influences ETG saturation is studied. The conclusion and discussion are given in Section IV.

2. Structural bifurcation in ETG turbulence simulations

We employ a set of three-field nonlinear gyrofluid equations [3] (and/or a fluid model in [7]) to simulate the time evolution of slab ETG perturbations, electric potential ϕ, parallel flow $\upsilon_{//}$, and electron pressure p_e, i.e.,

$$d_t(1 - \nabla_\perp^2)\phi = (1 + K\nabla_\perp^2)\partial_y\phi + \nabla_{//}\upsilon_{//} + \mu_\perp\nabla_\perp^4\phi \quad , \tag{1}$$

$$d_t\upsilon_{//} = \nabla_{//}(\phi - p_e) - \eta_\perp\nabla_\perp^2\upsilon_{//} \quad , \tag{2}$$

$$d_t p_e = -K\partial_y\phi - \tfrac{5}{3}\nabla_{//}\upsilon_{//} + \sqrt{\tfrac{32}{9\pi}}|k_{//}|(p_e + \phi) + \chi_\perp\nabla_\perp^2 p_e \quad , \tag{3}$$

where $K = 1 + \eta_e$, $d_t = \partial_t + \vec{z} \times \nabla_\perp \phi \cdot \nabla_\perp$, $\nabla_\perp^2 = \partial_x^2 + \partial_y^2$, $\nabla_{//} = ik_{//} = \partial_z + \hat{s}x\partial_y$. The definition of other quantities and the normalizations are conventional as in [3,7].

Large-scale structures including zonal flows and streamers are nonlinearly generated through the three-wave coupling modulation in turbulent fluctuations. To understand the preferential generation of anisotropic structures, the three-wave modulation interaction is analyzed based on Hasegawa-Mima (HM) turbulence modeling among a 2D monochromic pump wave $\tilde{\phi}_p = \phi_0 e^{i\vec{k}_0 \cdot \vec{x} - i\omega_0 t} + c.c.$, a small secondary perturbation $\tilde{\phi}_q = \phi_q e^{i\vec{k}_q \cdot \vec{x} - i\omega_q t} + c.c.$, and the sidebands $\tilde{\phi}_\pm = \phi_\pm e^{i\vec{k}_\pm \cdot \vec{x} - i\omega_\pm t} + c.c.$ with frequency and wave-number matches $\omega_\pm = \omega_0 \pm \omega_q$ and $\vec{k}_\pm = \vec{k}_0 \pm \vec{k}_q$. Complicated algebraic derivation yields a dispersion relation of secondary instability, [8]

$$\omega_q(1 + k_q^2) + k_{yq} = -\frac{2k_q^2 \Lambda_-^2 (k_0^2 - k_q^2)[\omega_q(\Lambda_0 - 4\Lambda_+^2 / k_q^2) + k_{yq}]}{(2\omega_0\Lambda_+ + k_{yq} + \Lambda_0\omega_q)^2 - (\omega_0 k_q^2 + 2\Lambda_+\omega_q)^2}|\phi_0|^2 \quad , \qquad (4)$$

with $\Lambda_+ = k_{xq}k_{x0} + k_{yq}k_{y0}$, $\Lambda_- = k_{xq}k_{y0} - k_{yq}k_{x0}$, $\Lambda_0 = 1 + k_0^2 + k_q^2$. This formula shows that the zonal flow and streamer are two limits of anisotropic secondary structures with $k_{yq} = 0$ or $k_{xq} = 0$. Numerical calculations of the growth rates reveal a basic nature of secondary excitation: the pump waves with radially longer and poloidally shorter wavelengths tend to generate a zonal flow instability. Contrarily, poloidally longer and radially shorter wavelength pump modes tend to enhance streamer structures. This result may suggest a dependent relation of the excitation of secondary structures on certain parameters such as the magnetic shear. Note that the radial structure of the slab ETG mode becomes wider with the decreasing magnetic shear. It is expected that the magnetic shear may govern the preferential excitation of zonal flows or streamers in ETG turbulence.

The nonlinear evolution equations, (1)-(3), are numerically solved by using an initial value code with radially periodic boundary conditions[3]. 3D slab ETG simulations are performed for different magnetic shears from $\hat{s} = 0.05$ to $\hat{s} = 1.6$. It is found that ETG turbulence structures

bifurcate to the zonal flow dominated state for weak shears or to the streamer-like state in the case with strong shear, as shown in Fig.1. The electron transport is suppressed by enhanced zonal flows in the former case. However, it is still low at around the gyro-Bohm level even if the streamers are formed in ETG turbulence with stronger shears. In addition, the ETG fluctuation is characterized by a homogeneously turbulent structure for moderate magnetic shears. These results show that the magnetic shear plays a key role in controlling the structural bifurcation in ETG turbulence.

3. Role of poloidal long-wavelength structures in ETG saturation

According to the mixing length estimate of turbulent transport, turbulent thermal conductivity can be simply expressed as $\chi_e \propto \gamma_{NL} L_{DC}^2$ with γ_{NL} and L_{DC} being the nonlinear growth rate and decorrelation length of turbulence, respectively. It shows that the transport is also dependent on the fluctuation level (i.e. saturation level of turbulence) besides the structure of turbulence. Generally speaking, the magnetic shear plays a stabilizing role in drift waves. This may be one of the mechanisms for low electron transport in the above simulations with streamer formation. On the other hand, it is observed that during the linear ETG evolution, poloidal long-wavelength fluctuation with $k_y = 0.1$, which is the poloidally longest wavelength mode in simulations, grows quickly as the beat wave of most unstable components ($k_y = 0.5 \sim 0.6$), as shown in Fig.2. As the amplitudes of the most unstable modes and the large-scale beat wave increase exponentially, other components grow dramatically faster than an exponential in time. Afterwards, the most unstable components decrease and the ETG fluctuations saturate at a lower level. These observations show that the large-scale fluctuations with poloidal long-wavelength may play an essential role in ETG turbulence saturation.

We have performed many simulations for different η_e and magnetic shear $\hat{s}$, the saturation processes of ETG turbulence are shown to be similar to that as illustrated in Fig.2. In some cases, the component with long-wavelength $k_y = 0.1$ quickly grows even faster than an exponential in time, suggesting a modulation instability due to the interaction between the beat

wave and most unstable pump modes. A derivation on the generation of poloidal long-wavelength structure through a beat wave or a modulation instability also reveals the possibility of such secondary excitation in ETG turbulence. Furthermore, a modeling calculation for linear ETG modes with imposed time-dependent streamer-like structure, which is the most simplified approximation of poloidal long-wavelength structures, shows that such poloidal long-wavelength mode can stabilize, even saturate ETG mode at some fluctuation level through a poloidal mode coupling. The details of these analytical calculations will be presented in a separate publication. To more clearly display the effect of large-scale structures on ETG turbulence, especially on the ETG saturation process, the time evolution of spatial spectral distribution of ETG fluctuations is analyzed at around the saturation, as shown in Fig.3. It is observed that as the primary unstable slab ETG modes with a spectral peak at $k_y = 0.5 \sim 0.6$ rise, another spectral peak at $k_y = 0.1$ emerges and becomes wider. Finally it evolves to connect and blend with the primary ETG spectra. This evidence supports the assumption that poloidal long-wavelength structures including the streamers may interact with the most unstable components through a poloidal mode coupling to saturate ETG turbulence, at least contribute to the ETG saturation. This finding seems to be related with the ETG saturation mechanism through the nonlinear toroidal coupling in recent global gyrokinetic particle simulation [4], in which the poloidal and toroidal mode numbers are linked by the safety factor $q = m/n$, in which m and n are the poloidal and toroidal mode numbers, respectively.

4.   Conclusion and discussion

In conclusion, structural bifurcation to the zonal flow dominated or streamer-like states in ETG turbulence depends on the spectral anisotropy of the turbulent fluctuations. The turbulence with radially longer and poloidally shorter wavelengths tend to generate a zonal flow instability. Contrarily, poloidally longer and radially shorter wavelength modes tend to enhance streamer structures. The magnetic shear plays a key role in the structural bifurcation through controlling the spectral structure of turbulent fluctuations. It is found that poloidal long-wavelength structure, which is driven through the beat wave of the most unstable ETG components or a modulation

instability, can saturate ETG turbulence through a poloidal mode coupling, at least contribute to the ETG saturation. This result suggests that the amplitude of ETG fluctuations may be limited by the secondary excitation of poloidal long-wavelength or GKH modes including the streamers, the turbulent electron transport can be reasonably low. It may be helpful to understanding the low electron heat transport observed in some recent ETG simulations.

Acknowledgement

References

[1] F. Jenko, *et al*. Phys. Plasmas **7**, 1904(2000); W. Dorland, *et al*., Phys. Rev. Lett. **85**, 5579(2000)

[2] Y. Idomura, M. Wakatani and S. Tokuda, Phys. Plasmas **7**, 3551(2000)

[3] Jiquan Li and Y. Kishimoto, Phys. Plasmas **11**, 1493(2004)

[4] Z. Lin, L. Chen and F. Zonca, Phys. Plasmas **12**, 056125(2005)

[5] B. Labit and M. Ottaviani, Phys. Plasmas **10**,126(2003)

[6] E. Kim and P. Diamond, Phys. Plasmas **9**, 4530(2002)

[7] W. Horton, B. G. Hong and W. M. Tang, Phys. Fluids **31**, 2971(1988)

[8] Jiquan Li and Y. Kishimoto, Phys. Plasmas **12**, 054505(2005)
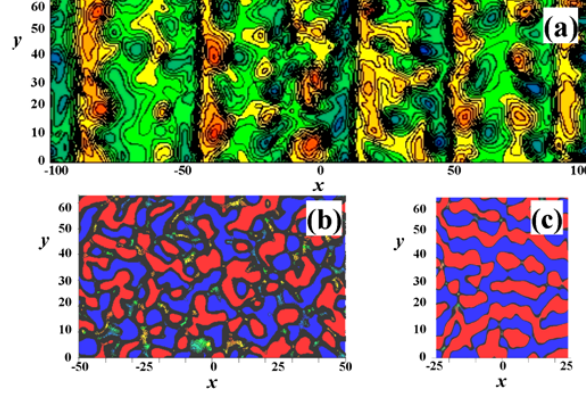
Fig.1 Structural bifurcation to zonal flow dominated (a), homogeneous turbulent (b) and streamer-like (c) states in well-developed ETG turbulence for different magnetic shear: $\hat{s} = 0.1$ (a); 0.4(b) and 1.6(c). Other parameters are $\eta_e = 6$, $\mu_\perp = \eta_\perp = \chi_\perp = 0.5$. The simulation domains are chosen as $L_x = 200\rho_e$ (a); $100\rho_e$ (b); $50\rho_e$ (c). $L_y = 20\pi\rho_e$, $L_z = 2\pi L_n$.
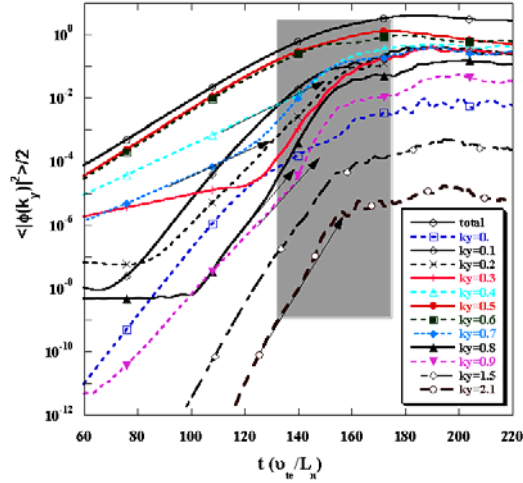
Figure 2: Time evolution of 3D slab ETG potential for different k_y components. The parameters are $\eta_e = 6$, $\hat{s} = 0.1$, $\mu_\perp = \eta_\perp = \chi_\perp = 0.5$. The simulation domains are chosen as $L_x = 50\rho_e$, $L_y = 20\pi\rho_e$, $L_z = 2\pi L_n$. The direction of the arrows marks an exponentially growing tendency.
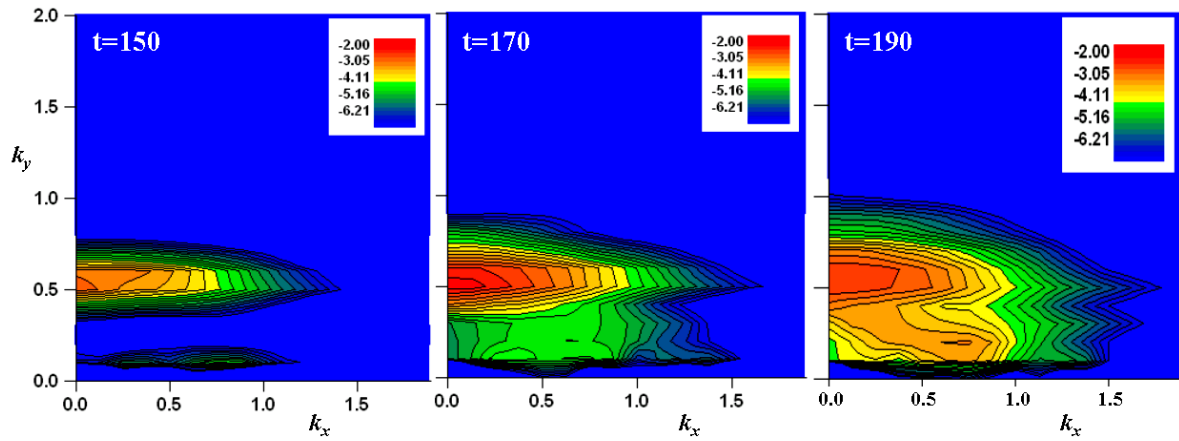
Fig.3   Time evolution of spectral distribution in $k_x - k_y$ plane during ETG saturation. The parameters are the same as in Fig.2. It shows the dynamics of how a poloidal long-wavelength structure is excited, interacts with the ETG modes, and saturates ETG turbulence.

Formation of Low Aspect Ratio Torus Equilibria by ECH

in the LATE Device

Takashi Maekawa, Hitoshi Tanaka, Masaki Uchida and Tomokazu Yoshinaga

Graduate School of Energy Science, Kyoto University, Kyoto 606-8502, Japan

E-mail:maekawa@energy.kyoto-u.ac.jp

Abstract. By ECH under a steady B_v field, a closed field equilibrium of low aspect ratio as low as R/a=1.4 is spontaneously formed in the LATE device. After the spontaneous formation, the plasma current has increased further up to I_p = 7.2 kA by 2.45 GHz 30 kW and I_p= 11 kA by 5 GHz 120 kW, by increasing the microwave power with a slow ramp of B_v for the equilibrium of the plasma loop at larger currents. Both amount to 12% of the total toroidal coil current. ECH/ECCD at 2nd harmonic resonance of EBW supports the plasma. Outline of the theoretical considerations for the formation process is given.

1. Introduction

The Spherical Tokamak (ST) concept is attractive since it maintains high beta plasmas in a compact shape of low aspect ratio [1]. Without a central Ohmic solenoid, the structure of the ST reactor is greatly simplified. We need a non-inductive method for plasma initiation and current start up. The electron cyclotron heating and current drive (ECH/ECCD) is potentially an attractive candidate for this purpose since plasma initiation and current start-up might be realized simultaneously by microwaves launched far from the plasma with a simple launcher. We have attempted ECH experiments in the Low Aspect ratio Toru Experiment (LATE) device and found that low aspect ratio equilibria with the toroidal currents up to11 kA are obtainable. In the present paper we describe briefly the main experimental results and the present understanding of the formation process from the multi-points of view of equilibrium, magnetic field topology, wave physics and current generation mechanism. Understanding of the physical process of ST equilibrium formation is important for future development of the ECH/ECCD method.

2. Experimental Apparatus

LATE is a tiny device with a vacuum chamber made of stainless steel in the shape of a cylinder with a diameter of 1.0 m and a height of 1.0 m [2]. The center post is a stainless steel cylinder with an outer diameter of 11.4 cm, enclosing 60 turns of conductors for the toroidal field. The return conductors are grouped into six limbs and go around far from the vacuum vessel, which allows good accessibility to the vacuum chamber and suppresses toroidal field ripple at a low level (1.5 % at R=50 cm and 0.07% at R=30 cm). There are four sets of poloidal field coils. One is for feedback control of the vertical position of the plasma loop, and the rest are for the vertical field for equilibrium and their currents are preprogrammed. There is no central solenoid for inductive current drive. Three 2.45 GHz magnetrons, including two 5kW CW tubes and a 20 kW 2 seconds tube, and a 5 GHz klystrons (200kW, 100msec) are used for ECH. In all cases, microwaves are injected from the radial ports with injection angles slightly deviating (about 15 degrees) from normal to the toroidal field.

3. Experimental Results

It is interesting that a closed flux surface can be spontaneously produced by ECH under a steady B_v field. This had been already reported to be possible in CDX-U and DIII-D at a large decay index of B_v [3]. A characteristic in the present LATE case is the appearance of a clear current jump or rapid current increase, where plasma current increases rapidly in the time scale of a few milliseconds even at a low decay index of $n < 0.1$. After the jump a closed flux surface is formed.

Figure 1 shows a case for injection of a 5 GHz microwave pulse of 130 kW under B_v=85 Gauss. Time evolution of the plasma images on the video camera shows that the breakdown takes place at the fundamental ECR layer at R=10 cm and the plasma expands quickly to the lower field side. In accordance with the plasma expansion, a plasma-current starts to flow and grows slowly up to 2 kA, and then suddenly it rises rapidly and reaches 6.8 kA, after which the current is maintained to the end of the microwave pulse as shown in figure 1 (a). Time evolution of the plasma current distribution is analyzed by using the magnetic data from thirteen flux loops and displayed in figures 1 (b)-(g). The distribution just before the first jump is stretched vertically near the second harmonic resonance layer as shown in figure 1 (c). After the first jump, it expands to the stronger field side and a small closed flux surface touching the center post appears (figure 1 (e)).　After the second jump, the current distribution as well as the closed flux surface expands to the lower field side (figure 1 (f)). At the final stage the current distribution is detached from the center post and a broad current profile expanded to the outboard wall of the vessel is formed as shown in figure 1 (g). The location of the plasma current center (+) in the final stage is between the second and third harmonic resonance layers. The line averaged electron density exceeds significantly the plasma cutoff density. These results suggest that the electron Bernstein waves (EBW) supports the plasma. It is remarkable that the open field configuration of external fields spontaneously changes into a closed field configuration by ECH alone as shown in figures 1 (h) and (i).

Once a closed flux surface is completely formed via the rapid current rise under a steady B_v field, the plasma current is further ramped up by increasing the microwave power with a slow ramp of B_v for the equilibrium of the plasma loop at larger currents. Figure 2 shows a case of the 2.45 GHz microwaves, where the final current reaches 7.2 kA at B_v=78 Gauss by 30 kW of total injection power from the three magnetrons. This current amounts to 12 % of the total toroidal coil currents of 60 kA flowing through the center post. In the case of　5GHz experiments, the plasma current has ramped-up and reached 11 kA at B_v=100 Gauss by 120 kW of injection power after slow formation of Ip=5 kA under a steady field of B_v=50 Gauss.

4. Equilibrium, Field Topology and Current Generation Mechanism

For analytical simplicity we consider equilibria of the plasma loops by using the Shafranov formula;

$$B_v = \frac{\mu_0 I_p}{4\pi R}\left(\ln \frac{8R}{a} + \frac{l_i}{2} - \frac{3}{2} + \beta_p \right) \quad \text{, where} \quad \beta_p = \frac{2\mu_0 \langle p \rangle}{B_a^2} \propto \frac{\langle p \rangle}{I_p^2} \quad \text{, and} \quad B_a = \frac{\mu_0 I_p}{2\pi a}$$

The formula can be cast into the dimensionless form;

$$\overline{B_v} = \left(\ln \frac{8R}{a} + \frac{l_i}{2} - \frac{3}{2} \right)\cdot \overline{I_p} \quad + \quad \frac{1}{\overline{I_p}}$$

, where

$$\overline{B_v} = \sqrt{\frac{2}{\mu_0}} \frac{(R/a) \cdot B_v}{\sqrt{\langle p \rangle}} \quad , \text{ and } \quad \overline{I_p} = \sqrt{\frac{\mu_0}{8}} \frac{I_p}{\pi a \sqrt{\langle p \rangle}}$$

Here, the first term is proportional to the plasma current and responsible for the current-hoop-force and the second term is inversely proportional to the plasma current and responsible for the pressure-hoop-force. The equilibrium characteristics of various aspect ratios of R/a are plotted in figure 3. Both terms become the same at the pressure-current turning point in this figure and the left part from this point is the pressure-hoop-force dominant regime and the right part is the current-hoop-force dominant regime.

At the initial stage of discharge, Ip is low and the pressure term is dominant;

$$\overline{B_v} = 1 \Big/ \overline{I_p} \quad , \text{ or } \quad I_p = 2 \pi a^2 \langle p \rangle \Big/ R B_v$$

, suggesting that the toroidal current for the equilibrium is driven by the plasma pressure [4]. The mechanism may be explained as follows. First, charge separation takes place vertically due to the ∇B drifts in the external fields. Electrons returns back along the helical field line to cancel the charge separation, which generates this toroidal currents. In the experiments with a low microwave injection power for the Langmuir probe measurement, plasma currents at the initial stage of discharges much before the rapid current rise have been confirmed to agree with this formula [5].

On the other hand, the experimental result that after the spontaneous formation the plasma current ramps up with the B_v ramp indicates that the equilibrium has already entered the current-hoop-force dominant regime after the spontaneous formation. It seems that the equilibrium goes through the point by the rapid current rise. The characteristics of equilibrium near the pressure-current turning point in figure 3 indicates that $\overline{I_p}$ increases with keeping $\overline{B_v}$ constant when the equilibrium goes through the point. This implies that an efficient current generation mechanism is required for equilibrium to go through the turning point in the sense that current is generated with no or a very small increment of plasma pressure (Note that B_v is constant in the experiments). The very rapid current rise within several milliseconds also suggests that there must be another efficient current generation mechanism responsible for the rapid current rise.

An important characteristic observed in the experiments is the change of the field topology during the rapid current rise; the purely open field structure just before the rapid current rise changes into the closed field structure. The current generation mechanism may have something to do with the topology change [6]. Before going into a detailed consideration, it is useful to consider the electron orbit in the external field with no plasma current. Vertical drift velocity of electron is given by

$$v_z = v_{//} \frac{B_v}{B_t} - \frac{m (v_{//}^2 + v_{\perp}^2/2)}{e R B_t}$$

When $v_z=0$, the electron makes a circular orbit along the toroidal field on the equatorial plane. This condition becomes an ellipse in the velocity space of electron; $(v_{//} - g/2)^2 + v_{\perp}^2 = (g/2)^2$, where $g = eRB_v/m$. This $v_z=0$ ellipse locates at the velocity side of the current carrying electrons, manifesting the asymmetric confinement of electrons along the parallel direction to the magnetic field line. In order to investigate the electron confinement in the presence of the self field from the plasma

current, the electron orbits, which start at the vessel center (R=25 cm and z=0 cm) with various velocities and pitch angles, are numerically calculated. The following conditions are assumed in the calculation. (1) The external B_v field is weakly mirror-shaped with the decay index of n=0.1. (2) B_v=30 Gauss and B_t=500 Gauss at R=25 cm. (3) The current profile is parabolic with the circular boundary of the minor radius of a.

Figure 4 shows the numerical results. Because of the mirror shaped B_v, some electrons around the v_z=0 ellipse are also confined in the external field only in the sense that their orbits do not hit the vessel wall. Confinement asymmetry is enhanced by the increase of self-field B_a from I_p. Especially, the lower energy electrons only in the forward $v_{//}$ direction becomes all confined as B_a approaches B_v. Since there are much more electrons in the lower energy range, the current increase is quickly accelerated. Furthermore, the increment of pressure is mostly small in increasing the current for these lower energy electrons. Interestingly, when the aspect ratio is low, the point where B_a=B_v is coincident with the pressure-current turning point on the characteristic curves as shown in figure 3. At low aspect ratio both transitions in the magnetic field topology (from open to closed fields) and the equilibrium (from pressure-hoop to current-hoop) coincide. Thus, spontaneous formation of ST equilibrium in the current-hoop dominant regime is realized via the rapid current rise due to the selective confinement for the forward electrons in the low energy range at the transition from open to closed field configuration. After B_a~B_v, ECCD may become effective and take over the above selective confinement mechanism since forward electrons are all confined.

Summary

By ECH under a steady B_v field, the initial current grows slowly due to pressure driven current under external open fields, then the current rises rapidly and a closed field equilibrium in the current-hoop-force regime is formed. Asymmetric confinement in electron velocity space may be responsible for the rapid current rise. This may be realized only when the aspect ratio is sufficiently low. Once a closed field equilibrium is formed, ECCD may become effective in keeping the current. After the spontaneous formation, the plasma current has increased with B_v ramp, up to Ip = 7.2 kA by 2.45 GHz 30 kW and I_p= 11 kA by 5 GHz 120 kW. Both amount to 12% of the total toroidal coil current. ECH/ECCD at the 2nd harmonic resonance of EBW supports the plasma. In conclusion, ECH/ECCD is effective for the formation of ST equilibria without an OH solenoid.

References

[1]   Y-K. M. Peng and D.J. Stricker, Nuclear Fusion **21**, (1986) 769.
[2]   T. Maekawa et al., Proc. 20th IAEA Fusion Energy Conf. 2004, IAEA-CN-116/EX/P4-27.
[3]   C.B. Forest et al., Phys. Plasmas **1** (1994) 1568.
[4]   L.E. Zakharov and G.V. Pereverzev, Sov. J. Plasma Phys. **14** (1988) 75.
[5]   T. Yoshinaga et al., J. Plasma Fusion Res. **81** (2005) 333. and EPS.
[6]   T. Shimotsuma et al., J. Phys. Soc. Jpn. **54** (1985) 1360.
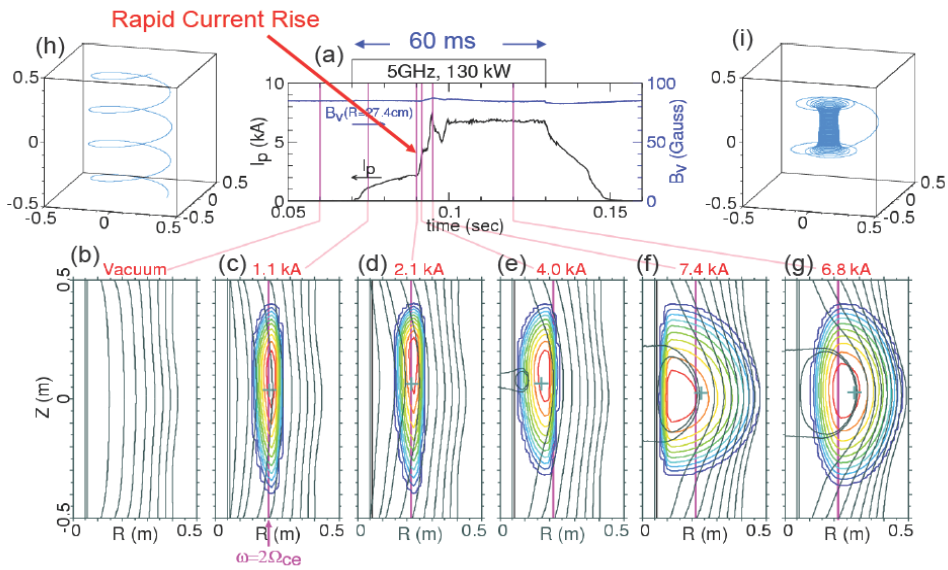
Figure 1. (a) Time traces of spontaneous formation of ST equilibrium. (b)-(f) Evolution of current distribution and poloidal flux surface. (h) and (i) Field topology changes spontaneously from open field before ECH to closed field.
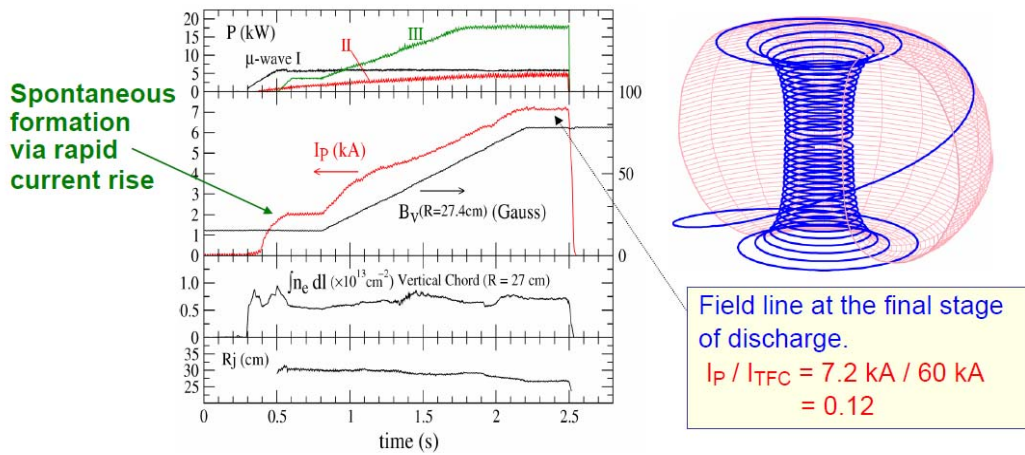
Figure 2. Time traces of 2.45 GHz discharge and the field line on the last closed flux surface at the final stage of discharge. After spontaneous formation of an initial ST equilibrium, the plasma current ramps up further by increasing microwave power with B_V ramp.

$$\overline{B_v} = \{\ln(8R/a) + l_i/2 - 3/2\} \cdot \overline{I_p} + 1/\overline{I_p}$$

$$\overline{B_v} = \sqrt{\frac{2}{\mu_0}} \frac{(R/a) \cdot B_v}{\sqrt{<p>}}$$

Bv=Ba   R/a = 8   3   2

Pressure - Current
Turning Point

$$\overline{B_v} = 1/\overline{I_p}$$

$$\overline{I_p} = \sqrt{\frac{\mu_0}{8}} \frac{I_p}{\pi a \sqrt{<p>}}$$
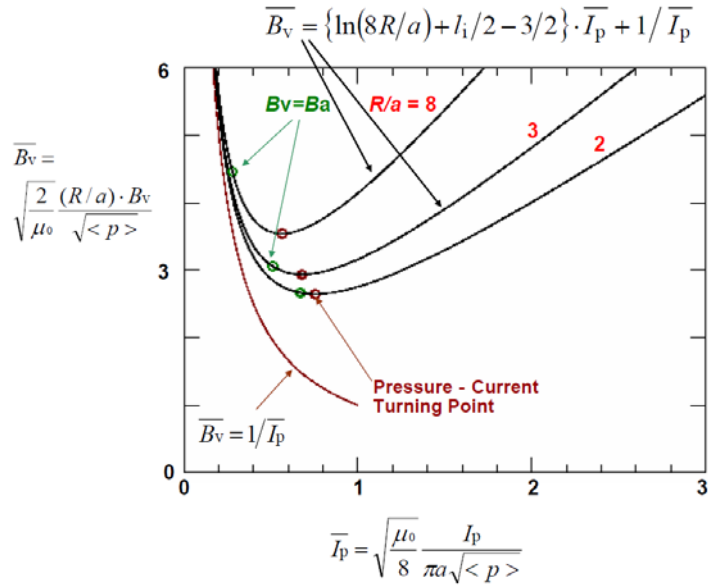
Figure 3.   The relationship between the plasma current and the external vertical field for the equilibrium in the radial force balance along the major radius direction for the case of l_i=0.96.

$B_a / B_v = 0$

$$B_a = \frac{\mu_0 I_p}{2\pi a}$$

Confined Area

$v_z = 0$ ellipse

$B_a / B_v = 0.4$

Plasma current Boundary

Trapped Area

$B_a / B_v = 0.8$

$B_a / B_v = 1.2$

Confinement Asymmetry is enhanced by the increase of self-field Ba from Ip.

Since there are much more electrons in lower energy range, Current increase is quickly accelerated as Ba approaches Bv.

After Ba~Bv, ECCD becomes effective since forward electrons are completely confined.

Figure 4.   Poloidal field structures and confined areas in the electron velocity space for various cases of self poloidal field from the plasma current. The confined area around the v_z=0 ellipse for the external B_v expands as the self field increases.

Preliminary Experiment of Non-Induced Plasma Current Startup on

SUNIST Spherical Tokamak

* HE Yexi, ZHANG Liang, XIE Lifeng, TANG Yi, ** YANG Xuanzong, FU Hongjun

Abstract：Non-inductive plasma current startup is an important motivation on the SUNIST spherical tokamak. In this experiment, a 100 kW, 2.45 GHz magnetron microwave system has been applied to the plasma current startup. Besides the toroidal filed, a vertical field was applied to generate a preliminary toroidal plasma current without action of the central solenoid. 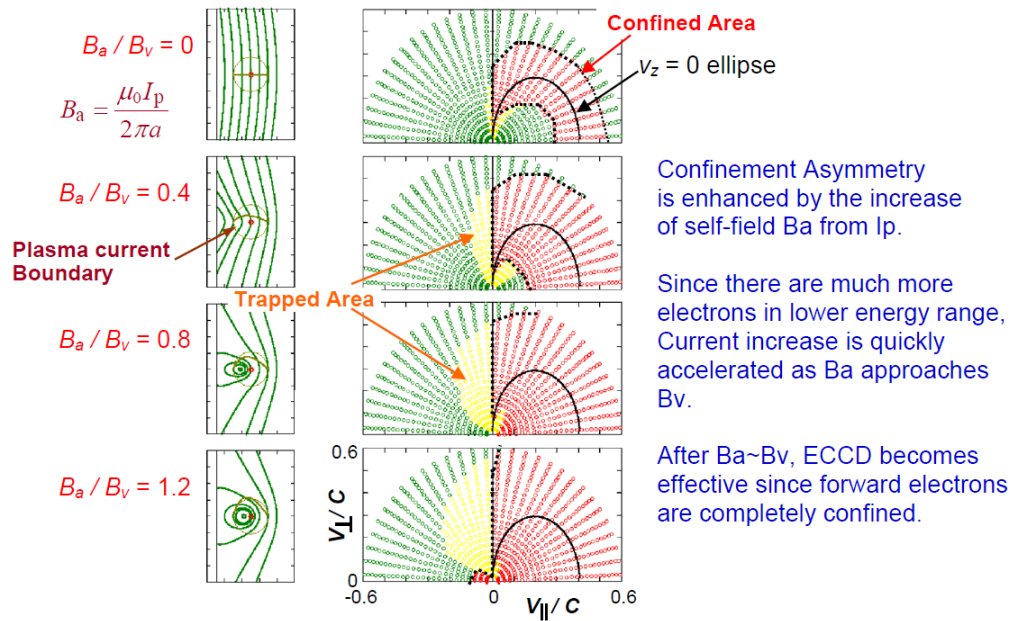As the evidence of the plasma current startup by the vertical field drift effect, the direction of the plasma current is changed with the changing direction of the vertical field during ECR startup discharge. We have also observed the plasma current maximum by scanning the vertical field in both directions. Additionally, we have used electrode discharge to assist the ECR current startup.

Keywords: ECR preionization, electrode discharge assistant

I. Introduction

ECR (Electron Cyclotron Resonance) is one of the non-inductive plasma current startup schemes. From 1980s, a number of ECR preionization experiments have been done on many tokamaks. These experiments have showed that the plasma current could be started up and sustained by electron cyclotron waves alone without ohmic heating. [1-7]

According to Ref. [8], the electrode discharge assisted ECR current start up has been experimentally demonstrated on the CT-6B tokamak. According to that experiment, we also used electrode discharge in our experiment to observe its characteristics.

SUNIST(Sino UNIted Spherical Tokamak) is a small device. Its parameters are as follows:

major radius	R	0.3	m
minor radius	a	~ 0.23	m
aspect ratio	A	~ 1.3	
elongation	κ	~ 1.6	
toroidal field at R_0	B_{T0}	~ 0.15	T
plasma current	I_P	0.05	MA
flux swing	$\Delta\Phi$	0.06	Vs

A magnetron microwave generator with a frequency of 2.45 GHz, output power of 100 kW and pulse length of 30 ms, is used for the experiment of the SUNIST ECR startup. The detectors for injected and reflected waves, absorbed loading of the reflected waves, vacuum and dc breakers are installed in the feeding line. In the preliminary experiment, a rectangular horn antenna injects waves to the plasma in the perpendicular direction with plasma torus.

II. Preliminary experimental results

* SUNIST Laboratory, Department of Engineering Physics, Tsinghua University, Beijing 100084, P.R.Cnina
** SUNIST Laboratory, Institute of Physics, Chinese Academy of Sciences, Beijing 100080, P.R.China

ECR wave current startup

The toroidal field, from to Gauss, has been selected to locate resonant layers in the appointed position inside the plasma. A small vertical field was applied during the microwave power pulse for the driving toroidal plasma current by the electron drift effect. A piezoelectricity valve supplied working gas pulse into the vacuum vessel with the $< 1\times10^{-5}$ Pascal of background pressure to keep above $\sim 5\times10^{-3}$ Pascal of hydrogen pressure during when the microwave power was applied. Microwave output power was kept around 20 kW because we could not improve the quality of the plasma current any higher above the power injected. One typical discharge is shown in figure 1 (A) on a large time scale and (B) on a short time scale for showing the discharge sequences and details. The plasma light signals extend as long as the microwave power is applies as usual, but the plasma current is just a peak with a hundred millisecond of bottom width. Sometimes, usually in a lower toroidal field, a group of plasma current peaks could be observed during the microwave, as shown in figure 2, accompanied by a group of plasma lighting signals.

（A）   （B）
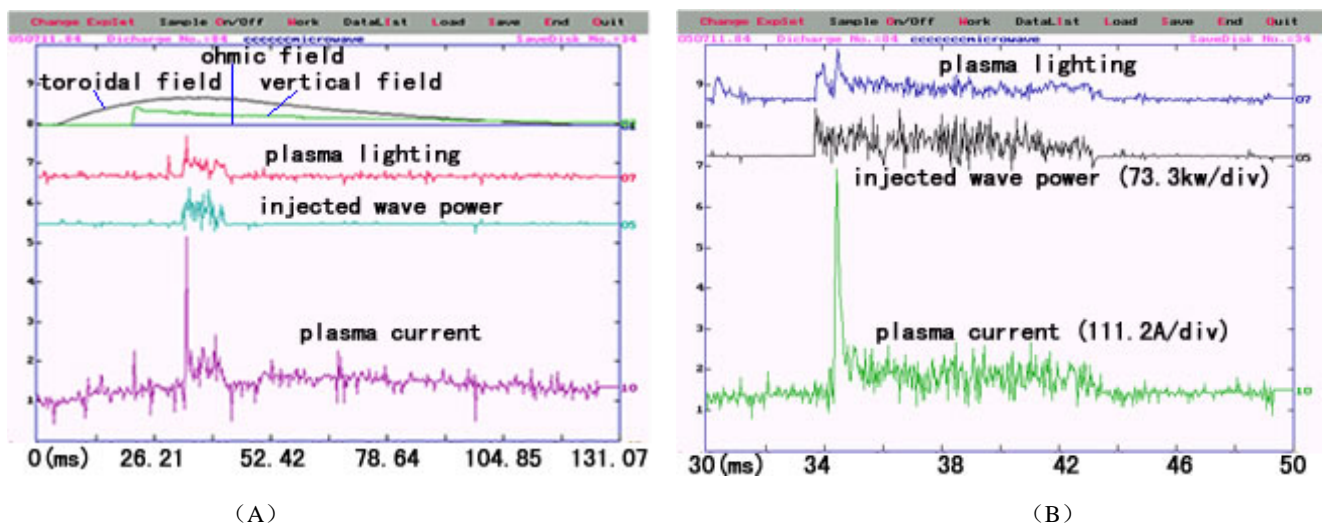
Fig. 1 Typical discharge of ECR current startup, A and B in large and small time scales respectively
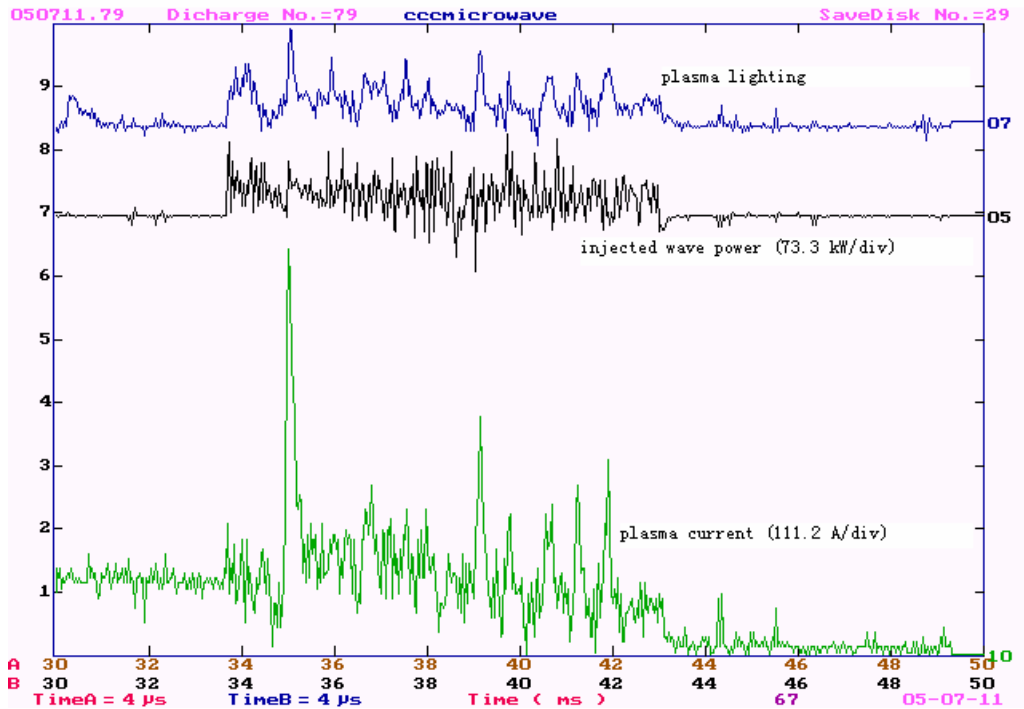
Fig. 2 A group of plasma current peaks

Figure 3 shows a driven plasma current changes along with the vertical field, which is evidence of driving the net toroidal plasma current by the vertical field drift effect in ECR plasma. The scattering higher I_P data relate to the wall condition.

Fig. 3 Plasma current vs vertical field

ECR wave startup with the **assistance of electrode discharge**

We have tried to apply a voltage between a pair of electrodes located at the top and the bottom respectively, scanned the electrode voltage and changed the voltage direction. Preliminary results have shown the plasma

current could increase above 10% (Fig. 4) in the common direction of the two kinds of driven mechanisms; contrarily, the plasma current would be counteracted more obviously (Fig.5). But just in the counter-direction electrode discharge we can observe the electrode current.

(A)   (B)
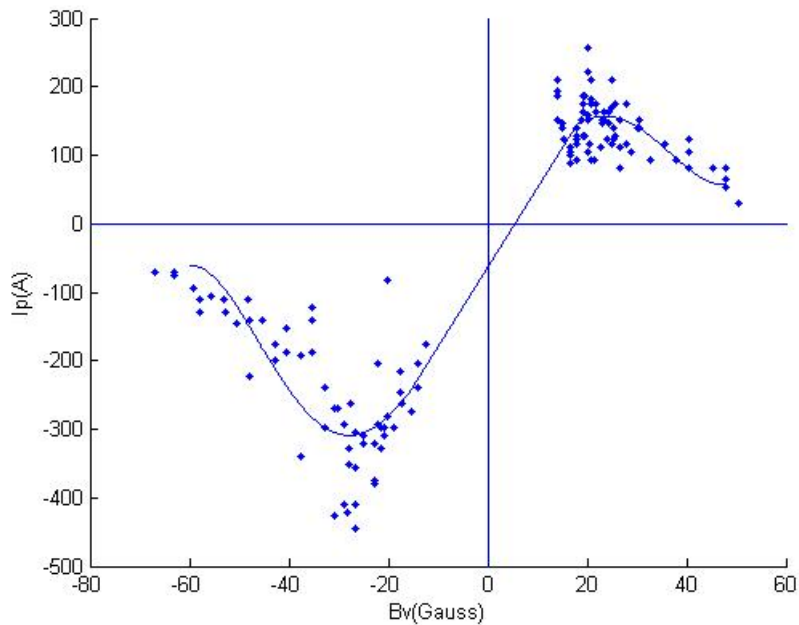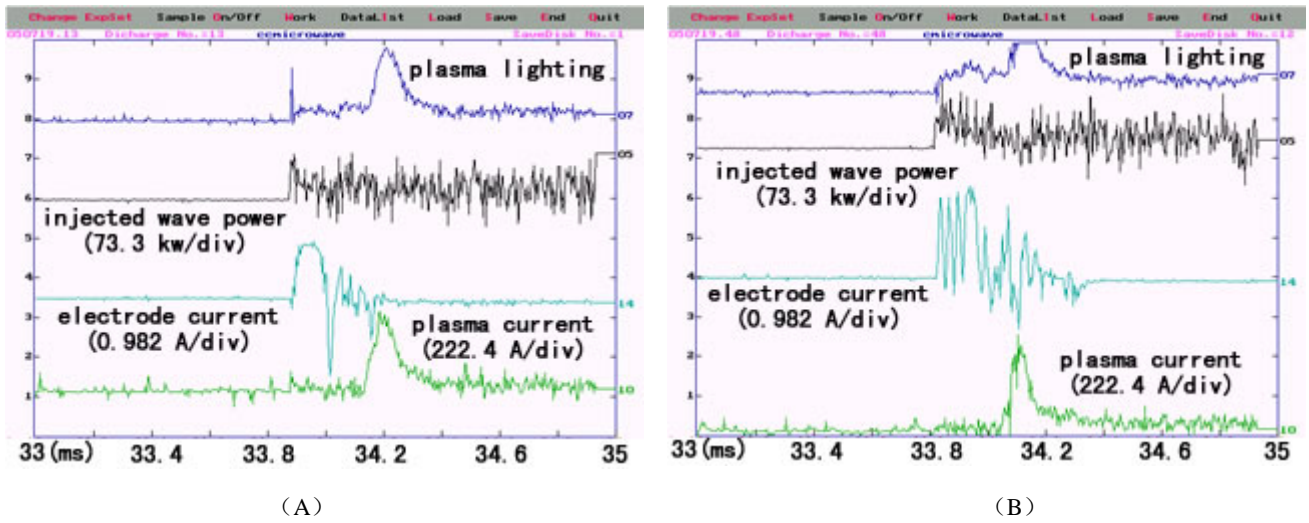
Fig. 4 ECR current startup with electrode discharge's assistance in common direction, A and B without/with electrode discharge

(A)   (B)

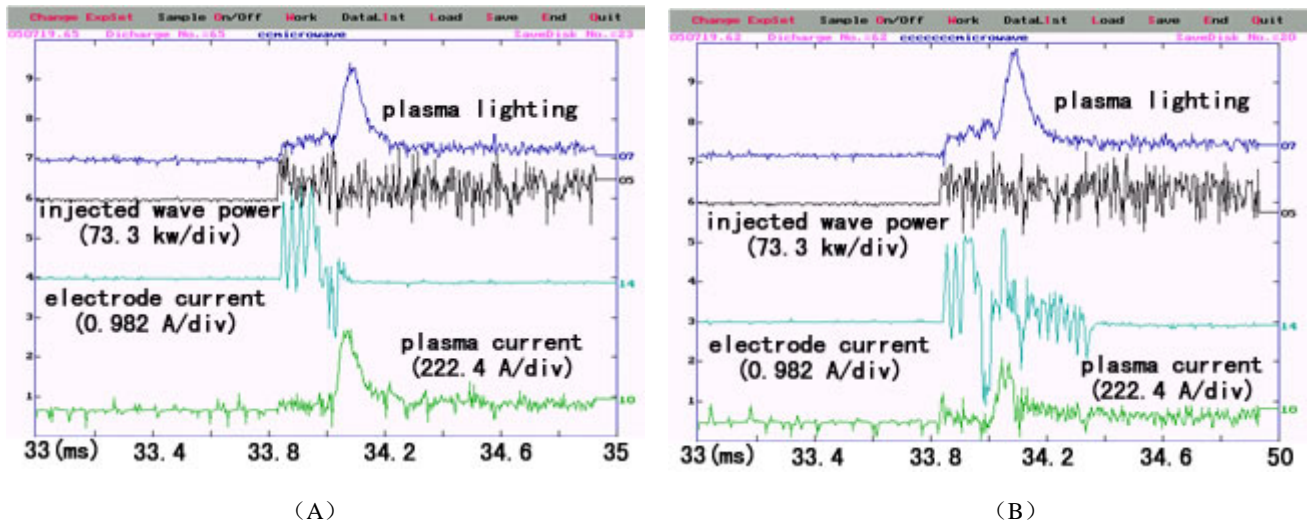Fig. 5 ECR current startup with electrode discharge's assistance in counter direction, A and B without/with electrode discharge

Usually, the electrode current is limited by an ion saturation current and exists in the same pulse duration with the ECR plasma current. We have obtained one special discharge that the current of plasma and electrode is cutoff with the same time scale of the injected wave (Fig. 6).
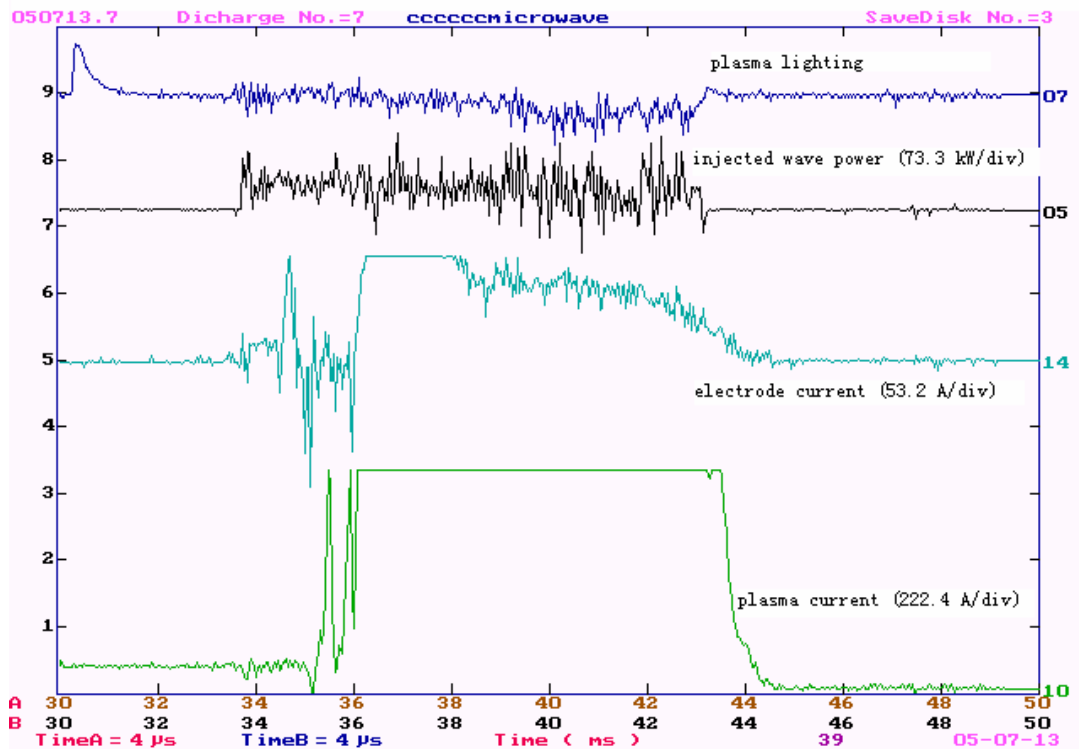
Fig. 6 Special discharge of ECR current startup with electrode assistance

III. Remaining questions

The preliminary results of the ECR plasma current startup with/without the electrode's assistance have indicated that a suitably applied vertical field could drive the toroidal plasma current, but it is more important to address a series of issues for the upcoming experiments.

Firstly, this kind of plasma current peak is impossible to develop to a typical ST plasma current. We have not considered the mode conversion to EBW in a microwave launch system, and then we face the density cut off problem of the ECR wave propagation in plasma. Modifying the feeding line and antenna is the only way to convert the mode to electron Bernstein wave.

The discharge shown in Fig. 9 suggests that there is a discharge regime with no density cut off problem in the ECR current startup with the assistance of the electrode discharge. The question is how to find it and to develop it from an occasional event to being reproducible. There were a few special discharges in the ECR current startup with the electrode assisting on the CT-6B tokamak. The currents of the electrode and plasma extended over the injected wave. There have been comments that that would be the arc phenomena, which should be avoided. But from the ratio between the plasma and electrode current, it is consistent with the plasma current driven mechanism by electrode discharge.

In preliminary experiments, the background pressure of the vacuum vessel increased from less than 1×10^{-5} Pascal up to a balanced value, $\sim 3 \times 10^{-5}$ Pascal. The driven plasma current decreased with the increase in the background pressure just like scanning the fuelling gas to a higher pressure. It is necessary to control the wall condition for further experiments.

Acknowledgements

10375089).

References

[1]GILGENBACH, R.M., et al., Nucl. Fusion 21 (1981) 319.
[2]NAKAO, S., OGURA, K., et al., Phys. Lett. 94A (1983) 405.
[3]CHO, T., et al., J. Phys. Soc. Jpn. 53(1984) 187.
[4]KUBO, S., et al., Phys. Rev. Lett. 50 (1983) 1994.
[5]SHIMOZUMA, T., et at., J. Phys. Soc. Jpn. 54(1985) 1360.
[6]TANAKA, H., et al., Nucl. Fusion 31(1991) 1673.
[7]HAN G., YAO X., et al., Nucl. Fusion, Vol. 38, No. 2 (1998) 287.
[8]ZHENG S., YANG X., et al., Nucl. Fusion, Vol. 40, No. 2 (2000) 155.

Analysis Scheme of Density Modulation Experiments for Particle Confinements Study

K. Tanaka, C. Michael, K. Kawanata, T. Tokuzawa, M. Shoji, K. Toi, X.Gao[1)],Y.X.Jie[1)] HT7
experimental group and LHD experimental group

National Institute for Fusion Science, Toki 509-5292, Japan

[1)] *Institute of Plasma Physics, Chinese Academy of Science, China*

e-mail: ktanaka@nifs.ac.jp

Abstract

Density modulation experiments are one of the powerful experimental schemas to study particle confinements. The diffusion coefficients (D) and convection velocity (V), which is impossible to evaluated from particle balance in equilibrium state, can be separately obtained. And the estimated value of D and V are determined independent of absolute value of particle source rate, which is difficult to be obtained experimentally. However sensitivities and interpretation of D and V from modulation experiments should be taken care. In this paper, numerical techniques to solve particle balance equation of modulation components are described. Examples of analysis are shown from the data of LHD. And interpretations of results of modulation experiments are studied.

keywords: *density modulation, particle confinements, diffusion coefficient, convection velocity*

1. Introduction

Particle transport of bulk ions and electrons is one of the most important issues of magnetically confined plasma research. However, compared with energy transport study, fewer works have been done. This is because of the difficulties of the experimental estimation of the particle source and the existence of the convection term in the particle balance equation. These make estimation of particle transport coefficients, i.e., diffusion coefficients (D) and convection velocity (V) impossible from simple particle balance analysis in the equilibrium state. The diffusion coefficients and convection velocities are separately estimated from the propagation of periodically modulated density by controlling the gas puff.

This technique was done at T10 [1] for the first time and then developed at TEXT and ASDEX [2,3]. The theoretical consideration of the interpretation was done by Gentle [4]. On JT60U, these experiments were done by Nagashima[5] and Takenaga[6]. Takenaga did modulation He puffing and studied He transport of reversed shear discharge. Recently the experiments were done at W-7AS[7], LHD [8,9] and HT7[10].

2. Density modulation analysis

2.1 Qualitative character of particle transport in equilibrium state in LHD

The equation of the particle balance in the equilibrium state was described as follows,

$$\frac{dn_{eq}}{dt} = -\nabla \cdot \Gamma_{eq} + S_{eq}$$

n; electron density, Γ particle flux, S; particle source rate   (1)

Subscript eq indicates equilibrium value.

The equilibrium particle flux can be defined as follows.

$$\Gamma_{eq} = -D_{eq}\nabla n_{eq} + n_{eq}V_{eq} \tag{2}$$

In eqation2 , D_{eq} and V_{eq} are diffusion coefficients and convection velocity in equilibrium state. In the steady $dn_{eq}/dt = 0$ and in the plasma inertia, $S_{eq} \approx 0$, then $\Gamma_{eq} \approx 0$ and

eq.(2) becomes $D_{eq}\nabla n_{eq} \approx n_{eq}V_{eq}$. This indicates, if density gradient exists, where particle source is negligible, particle convection exists.

Figure 1 shows electron temperature, density and particle source rate profiles of LHD under different NBI heating power in the equilibrium state. As shown in Fig.1 (c), the peak of particle source rate is located at $\rho = 1.05$, which is outside of last closed flux surface, and reduces exponentially to plasma interior. The particle source rate becomes two order magnitudes lower at $\rho = 0.8$ compared with peak value.   Therefore, at $\rho < 0.8$, $S_{eq} \approx 0$ and

$\Gamma_{eq} \approx 0$ is well satisfied. However, as shown in Fig.1 (b), negative density gradient are observed at $\rho < 0.8$ of 1MW and $0.6 < \rho < 0.8$ of 2.7 MW heating case and positive density gradient are observed at $\rho < 0.6$ of 2.7 MW and at $\rho < 0.8$ of 2.7 MW of 8MW heating case. For particle balance, positive and negative gradient require outward and inward particle convection. The measurements of equilibrium density profiles in LHD tell existence of particle convection.

2.2 Analysis of density modulation

For quantitative study of the particle transport, density modulation experiments are powerful. Here, we assume the equilibrium and modulated component are independent.

$$n = n_{eq} + \tilde{n}, \Gamma = \Gamma_{eq} + \tilde{\Gamma}, S = S_{eq} + \tilde{S} \quad (3)$$

$$\tilde{S} = \tilde{S}e^{i\omega t}, \tilde{n} = \tilde{n}e^{i\omega t}, \partial\tilde{n}/\partial t = i\omega\tilde{n} \quad (4)$$

Then the following particle balance equations for modulated components, of which modulation frequency is ω, are obtained.

$$\frac{\partial^2 \tilde{n}}{\partial r^2} + \left(\frac{1}{r} + \frac{1}{D}\frac{\partial D}{\partial r} - \frac{V}{D} \right)\frac{\partial \tilde{n}}{\partial r} - \left(\frac{V}{rD} + \frac{1}{D}\frac{\partial V}{\partial r} \right)\tilde{n} - i\frac{\omega}{D}\tilde{n} + \frac{\tilde{S}}{D} = 0 \quad (5)$$

In eq.(5), $\tilde{n}$ is a complex function, and its real part $\tilde{n}_R$ and imaginary part $\tilde{n}_I$ satisfy the following equations.

$$\frac{\partial^2 \tilde{n}_R}{\partial r^2} + \left(\frac{1}{r} + \frac{1}{D}\frac{\partial D}{\partial r} - \frac{V}{D} \right)\frac{\partial \tilde{n}_R}{\partial r} - \left(\frac{V}{rD} + \frac{1}{D}\frac{\partial V}{\partial r} \right)\tilde{n}_R + \frac{\omega}{D}\tilde{n}_I + \frac{\tilde{S}}{D} = 0 \quad (6)$$

$$\frac{\partial^2 \tilde{n}_I}{\partial r^2} + \left(\frac{1}{r} + \frac{1}{D}\frac{\partial D}{\partial r} - \frac{V}{D} \right)\frac{\partial \tilde{n}_I}{\partial r} - \left(\frac{V}{rD} + \frac{1}{D}\frac{\partial V}{\partial r} \right)\tilde{n}_I - \frac{\omega}{D}\tilde{n}_R = 0 \quad (7)$$

Then, equation (6) and (7) can be solved numerically with finite difference method under the following boundary condition.

$$\partial \tilde{n}_R / \partial r = \partial \tilde{n}_I / \partial r = 0 \text{ at } r = 0 , \quad \tilde{n}_R = \tilde{n}_I = 0 \text{ at } r = a \qquad (8)$$

$$a \text{ is average radius of the plasma boundary}$$

We applied Nagashima's matrix technique[11] to solve eq. (6) and (7).

The first and second order derivatives are defined in the finite difference expression as follows for real and imaginary part.

$$\frac{\partial \tilde{n}_k}{\partial r_k} = \frac{\tilde{n}_{k+1} - \tilde{n}_{k-1}}{2h}, \frac{\partial^2 \tilde{n}_k}{\partial r_k^2} = \frac{\tilde{n}_{k+1} - 2\tilde{n}_k + \tilde{n}_{k-1}}{h^2} \qquad (9)$$

The index k is index number of numerical solution of $\tilde{n}$ and h is the space of the neighbor solution. Then the following terns are defined

$$F_k = \frac{1}{r_k} + \frac{1}{D(r_k)}\frac{\partial D(r_k)}{\partial r_k} - \frac{V(r_k)}{D(r_k)}$$

$$A_k = \frac{V(r_k)}{r_k D(r_k)} + \frac{1}{D(r_k)}\frac{\partial V(r_k)}{\partial r_k}$$

$$B_k = \frac{\omega}{D(r_k)} \qquad (10)$$

$$C_k = \frac{S(r_k)}{D(r_k)}$$

Then, equation (7) and (8) become

$$\frac{\partial^2 \tilde{n}_{Rk}}{\partial r_k^2} + F_k \frac{\partial \tilde{n}_{Rk}}{\partial r_k} - A_k \tilde{n}_{Rk} + B_k \tilde{n}_{Ik} + C(r_k) = 0 \qquad (11)$$

$$\frac{\partial^2 \tilde{n}_{Ik}}{\partial r_k^2} + F_k \frac{\partial \tilde{n}_{Ik}}{\partial r_k} - A_k \tilde{n}_{Ik} - B_k \tilde{n}_{Rk} = 0 \qquad (12)$$

Then equation (11) and (12) can be expressed in the finite differential equation as follows.

$$\frac{\tilde{n}_{Rk+1} - 2\tilde{n}_{Rk} + \tilde{n}_{Rk-1}}{h^2} + F_k \frac{\tilde{n}_{Rk+1} - \tilde{n}_{Rk-1}}{2h} - A_k \tilde{n}_{Rk} + B_k \tilde{n}_{Ik} + C_k = 0$$

$$\left(1 - \frac{h}{2}F_k\right)\tilde{n}_{Rk-1} + (-2 - h^2 A_k)\tilde{n}_{Rk} + \left(1 + \frac{h}{2}F_k\right)\tilde{n}_{Rk+1} + B_k h^2 \tilde{n}_{Ik} = -h^2 C_k \qquad (13)$$

$$\frac{\tilde{n}_{Ik+1} - 2\tilde{n}_{Ik} + \tilde{n}_{Ik-1}}{h^2} + F_k \frac{\tilde{n}_{Ik+1} - \tilde{n}_{Ik-1}}{2h} - A_k \tilde{n}_{Ik} - B_k \tilde{n}_{Rk} = 0$$

$$\left(1 - \frac{h}{2}F_k\right)\tilde{n}_{Ik-1} + (-2 - h^2 A_k)\tilde{n}_{Ik} + \left(1 + \frac{h}{2}F_k\right)\tilde{n}_{Ik+1} - B_k h^2 \tilde{n}_{Rk} = 0 \qquad (14)$$

At the plasma center k=0, at plasma boundary, k=n.   At the plasma center, since derivative of $\tilde{n}_R$ and $\tilde{n}_I$ is zero then $\tilde{n}_{R0} = \tilde{n}_{R1}$ and $\tilde{n}_{I0} = \tilde{n}_{I1}$. Then eq (13) and (14) at k=1 become as follows

$$\left(-1 - \frac{h}{2}F_1 - h^2 A_1\right)\tilde{n}_{R1} + \left(1 + \frac{h}{2}F_1\right)\tilde{n}_{R2} + B_1 h^2 \tilde{n}_{I1} = h^2 C_1 \qquad (15)$$

$$\left(-1 - \frac{h}{2}F_1 - h^2 A_1\right)\tilde{n}_{I1} + \left(1 + \frac{h}{2}F_1\right)\tilde{n}_{I2} - B_1 h^2 \tilde{n}_{R1} = 0 \qquad (16)$$

At plasma boundary, $\tilde{n}_R = \tilde{n}_I = 0$, then $\tilde{n}_{Rn} = \tilde{n}_{In} = 0$ Then eq. (13) and (14) at k=n-1 become as follows

$$\left(-1 - \frac{h}{2}F_{n-1}\right)\tilde{n}_{Rn-2} + \left(-2 - h^2 A_{n-1}\right)\tilde{n}_{Rn-1} + B_{n-1} h^2 \tilde{n}_{In-1} = h^2 C_{n-1} \qquad (17)$$

$$\left(-1 - \frac{h}{2}F_{n-1}\right)\tilde{n}_{In-2} + \left(-2 - h^2 A_{n-1}\right)\tilde{n}_{In-1} - B_{n-1} h^2 \tilde{n}_{In-1} = 0 \qquad (18)$$

Equation (11) and (12) becomes as following matrix equation including boundary condition.

$$M \cdot \tilde{N}_R + B_V h^2 \tilde{N}_I = -h^2 C_V \tag{19}$$

$$M \cdot \tilde{N}_I - B_V h^2 \tilde{N}_R = 0 \tag{20}$$

Here, the vector B_V and C_V are $B_V = (B_1, B_2, \cdots\cdots, B_{n-1})$, $C_V = (C_1, C_2, \cdots\cdots, C_{n-1}) = (S_1/D_1, S_2/D_2, \cdots\cdots, S_{n-1}/D_{n-1})$ and matrix M is n-1 x n-1 matrix, whose elements are coefficients of the first and second term of eq. (13) and (14). The first and last line of matrix M are boundary condition, which is described in eq.(15)~(18). The vector $\tilde{N}_R$ and $\tilde{N}_I$ are series of radial profile of modulation components, which contains $\tilde{n}_{Rk}$ and $\tilde{n}_{Ik}$ for k=1~n-1. Finally vector $\tilde{N}_R$ and $\tilde{N}_I$, which are the solution of eq (11) and (12) are obtained from following simple matrix calculation.

$$\tilde{N}_R = -h^2 \left(M + B_V{}^2 h^4 M^{-1} \right)^{-1} C_V \tag{21}$$

$$\tilde{N}_I = B_V h^2 M^{-1} \tilde{N}_R \tag{22}$$

The final purpose of the analysis is an estimation of D and V profile. The profile of D and V are expressed by using several fitting parameters. The modulation radial profile, which are vector $\tilde{N}_R$ and $\tilde{N}_I$, are calculated from eq.(21) and (22) for modeled D and V. Then, fitting parameters are determined to fit calculated $\tilde{N}_R$ and $\tilde{N}_I$ to experimentally measured $\tilde{N}_R$ and $\tilde{N}_I$. In principle, to solve eq. (21), (22), absolute value of particle source rate, which is include vector C_V, is required However, as shown in eq. (21) and eq.(22), change of the absolute value of particle source rate, change same factor of $\tilde{N}_R$ and $\tilde{N}_I$. Therefore, normalized shape of modulation amplitude profile ($\propto \sqrt{\tilde{N}_R{}^2 + \tilde{N}_I{}^2}$) and phase profile ($= \tan^{-1}(\tilde{N}_R/\tilde{N}_I)$) are not affected. The fitting is done to fit normalized amplitude profile and phase profile or normalized profile of real and imaginary part of modulation amplitude. No need of absolute value of particle source rate is major advantage of this technique. However, because of the limitation of the measured data, number of the fitting parameter is limited, so, fine spatial profile of D and V are difficult from fitting procedure

Takenaga performed different analysis technique [6]. From the modulated particle flux profile, D and V profile are directly calculated. In this scheme, any model of D and V are not required. However the analysis is limited in the plasma interior region, where particle

source is negligible and the estimated D and V profile is sensitive to the smoothness of the modulation profile.

2.3 Experimental data of modulation experiments in LHD

In this section, examples of experimental data of density modulation and analysis results from LHD are described. Figure 2 shows measured cross section and chords of FIR interferometer[12]. A ten channels of 13 channel are used for the analysis. Interferometer can measure temporal evolution of line integrated density with good enough time response (~1μsec) to measure density perturbation.

Figure 3 (a) shows typical wave from of modulated density. In order to modulate under constant background density, density feedback control was done. Given reference signals, the applied voltage to gas control valve was automatically adjusted to modulate under constant background density. Without feedback, the background density gradually increases. As shown in Fig.3 (d), gas puff fuelling rate varies in time. Total particle fuelling, which include both fuelling from gas puffing and recycling, should be controlled. Therefore, the gas puff fuelling rate was reduced in order to compensate the increase of the background density due to the recycled fuelling as shown in Fig.2 (d). The resultant particle fuelling and density was sinosoidally modulated under a constant background between t = 1.4 and 2.9 sec as shown in Figs.3 (a) and (c) respectively. The central averaged density was controlled within ±3%. And diamagnetic stored energy was controlled within ±5% indicating averaged temperature was controlled within ±2%.

In HT7, instead of feed back control if gas puffing, a 10 Hz preprogrammed signal was used [10]. Because of the low recycling, density modulation under constant background density was possible without feedback control

The integrated modulation amplitude and phase are calculated by the correlation analysis after subtracting background averaged density. Figure 4 shows the amplitude spectrum of modulated density components of Fig.3 (a). As shown in Fig.4, the harmonic components are less than 10% of fundamental 5 Hz components so that it should not cause significant non-linear effect. The error was determined as a standard deviation within frequency resolution (δf), which is determined by the data length of modulation analysis.

The profile of D and V are each described by two parameters. One is the core value (D_{core}, V_{core}) and the other is edge value (D_{edge}, V_{edge}) as shown in Fig.5. The profiles of D are assumed to be flat in the core and edge and change at $\rho = 0.7$. The value of V is zero at $\rho = 0$ and V profiles are assumed to vary linearly with ρ, changing slope at $\rho = 0.7$. The values of V at $\rho = 0.7$ and $\rho = 1.0$ are taken to represent V_{core} and V_{edge} respectively. The transition points of D and V are fixed at $\rho = 0.7$ because density gradients change at around $\rho = 0.7$ as shown in Fig.1 suggesting that transport changes at this location.

Followings are examples of determinations of the transport coefficient for the different heating power of two discharges, one 5.2MW NBI heating with 5Hz modulation and

the other 1 MW heating with 2Hz modulation. The temperature and density profiles are shown in Figs.6. Figure 7 shows integrated amplitude and phase profile of both two cases. A clear difference was observed in two heating cases. Modulation frequency was 5Hz for 5.2MW heating case and 2Hz for 1MW heating case. Because of the lower transport at lower heating power, lower modulation frequency allows a deeper penetration of the perturbation.

As shown in Fig.8, the modulation amplitude is localized in the edge region. This makes accurate reconstruction in the central region. In this paper, fitting to determine D and V was done not to radial profile (Fig.8) but to integrated profile (Fig.7) of modulation. This is because the fitting procedure is to be free from error of radial reconstruction of modulated part. With use of more accurate reconstruction with use of more number of channels by using a CO_2 laser imaging interferometer or with use of direct measurements of radial profile of modulated part by using a microwave reflectmeter, the fitting to radial profile will be possible. For present analysis, the following χ^2 was minimized to determine fitting parameter of D and V profiles.

$$\chi_{\mathrm{mod\_int}}^2 = \sum_{ch}\left(\left(\int \tilde{n}_{R\_\exp}dl - \int \tilde{n}_{R\_calc}dl\right)^2 + \left(\int \tilde{n}_{I\_\exp}dl - \int \tilde{n}_{I\_calc}dl\right)^2\right) \qquad (23)$$

In equation (23), $\tilde{n}$ is radial profile of modulated components. The subscript 'R' and 'I' indicate real and imaginary part of the modulated components and the subscripts .'exp' and 'calc' indicate experimental measured and numerically calculated values. The integration was done along viewing chords of the interferometer. The real and imaginary part of integration from experiments are calculated form measured integrated amplitude and phase in Fig.7. Here integrated values are normalized by the values of the central chord. As described in the previous sections, without use of absolute value, the fitting to normalized value was done. The summation is sum of 10 channels data of interferometer.

Figure 9 shows estimated D and V profiles form modulation experiments. Around factor four larger diffusion was obtained at 5.2MW heating case compared with 1MW heating case. The convection profiles do not show dramatically difference between two cases. Figure 10 shows comparison of integrated amplitude and phase profile between experimental value and calculated value with fitted D and V profile. Calculated values fit to the experimental values almost within the measurements error as shown in Fig.10.

3 Discussion about the modulation results

There is an argument about the discrepancy between transport coefficient of equilibrium state and transport coefficient from modulation analysis [4]. For energy transport analysis, the difference between thermal diffusion coefficients from power balance analysis and the coefficients from transient analysis is not negligible on tokamak. For the particle transport analysis, as shown in eq. (2), the existence of the off diagonal term, which is the second term of eq.(2), is a priori included. However, the nonlinearity of the particle flux and

temperature perturbation can affects the particle transport coefficients from modulation analysis.

Equation (2) indicates Γ_{eq} is function of $. n$ and ∇n. And Fig.1 suggests temperature profile can influence on density profile, so, Γ_{eq} can be also function of electron temperature and its gradients. The modulated flux can be written by the following equation.

$$\delta\Gamma_{eq} = \frac{\delta\Gamma_{eq}}{\delta\nabla n}\delta\nabla n + \frac{\delta\Gamma_{eq}}{\delta n}\delta n + \frac{\delta\Gamma_{eq}}{\delta\nabla T}\delta\nabla T + \frac{\delta\Gamma_{eq}}{\delta T}\delta T$$

$$= \quad -D_{mod}\delta\nabla n \quad + \delta n V_{mod} \tag{24}$$

In the eq.(24), D_{mod} and V_{mod} can be written as follows.

$$D_{mod} = \frac{\partial\Gamma_{eq}}{\partial\nabla n} = \frac{\partial D_{eq}}{\partial\nabla n}\nabla n + D_{eq} - n\frac{\partial V_{eq}}{\partial\nabla n} \tag{25}$$

$$V_{mod} = \frac{\partial\Gamma_{eq}}{\partial n} + \frac{1}{\delta n}\frac{\partial\Gamma_{eq}}{\partial T}\delta T + \frac{1}{\delta n}\frac{\partial\Gamma_{eq}}{\partial\nabla T}\delta\nabla T$$

$$= -\frac{\partial D_{eq}}{\partial n}\nabla n + V_{eq} + n\frac{\partial V_{eq}}{\partial n} + \frac{1}{\delta n}\left(-\frac{\partial D_{eq}}{\partial T}\nabla n + n\frac{\partial V_{eq}}{\partial T}\right)\delta T + \frac{1}{\delta n}\left(-\frac{\partial D_{eq}}{\partial\nabla T}\nabla n + n\frac{\partial V_{eq}}{\partial\nabla T}\right)\delta\nabla T$$

$$\tag{26}$$

The modulation experiments estimates D_{mod} and V_{mod}, which are described by eq.(25 and (26). As shonwn in eq.(25), the ∇n dependence of D_{eq} and V_{eq} can affects D_{mod}. For example if $\Gamma_{eq} = \nabla n^2, D_{eq} = \nabla n, V_{eq} = 0$, then $D_{mod}=2D_{eq}$. The interpretation of V_{mod} is further complicated. Not only $n, T, \nabla T$ dependence of D_{eq} and V_{eq} but also temperature and temperature gradient perturbation ($\delta T, \delta\nabla T$) can affects the V_{mod} as well.

One of the possible study about the discrepancy between D_{mod}, V_{mod} and D_{eq}, V_{eq} are to compare calculated density profile with D_{mod} and V_{mod} under ω=0 in eq.(5), which corresponds to equilibrium profile and measured radial density profile. This comparison can judge the difference of V_{mod}/D_{mod} and V_{eq}/D_{eq} because shape of equilibrium profile (normalized profile) can be determined by V/D.

Figure 11 shows comparison between calculated and measured profiles. Figure11 does not show strong discrepancy between measured and calculated profile. The case of 1 MW heating, both agree within estimation error. The case of 5.2MW heating, there is a visible difference. The discrepancy of V_{mod}/D_{mod} and V_{eq}/D_{eq} are modest but not negligible in the 5.2MW case.

Here we examine the $D_{mod} = \frac{\partial\Gamma_{eq}}{\partial\nabla n}$ from the temporal evolution the density profile after pellet injection. Figure 12 shows change of density profile. Pellet deposited at around ρ = 0.8. Just after pellet injection, density profile became hollow then it changes to peaked one. The particle flux was calculated from following equation, which is integration from of eq.(1).

Here particle source was neglected.

$$\Gamma(r) = -\frac{1}{r}\int_0^r r\frac{dn}{dt}dr \qquad (27)$$

Figure 13 shows temporal change of the normalized particle flux Γ/n_e after pellet injection. In If $\dfrac{\partial \Gamma_{eq}}{\partial \nabla n}$ is constant according to ∇n, this plot becomes straight line and D_{mod} equals to D_{eq}.

Figure 13 shows the plot becomes almost straight line at ρ=0.225, but it becomes no linearly increases at ρ =0.525 and ρ =0.725. This indicates $\dfrac{\partial \Gamma_{eq}}{\partial \nabla n}$ is not constant according to ∇n at these location. The value of D_{mod} can be different from D_{eq}. This is qualitative examination. For precise examination about 5.2MW heating case, electron temperature and its gradients should be same as the ones in 5.2MWcase. However, Fig.13 suggest non linearity Γ_{eq} to ∇n is possible and can cause discrepancy between . D_{mod} and D_{eq}. The experiments to measure non linearity Γ_{eq} to ∇n like Fig.13 changing ∇n with use of pellet injection or gas puffing under different background T and ∇T are required to find a complete picture of non linearity Γ_{eq} to ∇n. If we have an idea qualitative difference of the D_{mod} and D_{eq}, then, V_{eq} can be obtained from the fitting to the equilibrium density profile with D_{eq}.

Assuming $D_{mod}=D_{eq}$, correction of the V was tried. In Fig.14 (a), V_{eq} was determine to fit equilibrium profile with $D_{mod}=D_{eq}$. As shown in Fig.13 (b), the calculated profile with $D_{mod}=D_{eq}$ and V_{eq} fits measured radial density profile. In the edge region, V_{eq} becomes more inward directed than V_{mod}. However, the assumption, which is $D_{mod}=D_{eq}$, should be experimentally studied.

4. Summary

A schema to solve particle balance equation by using a numerical finite difference method was described. The equation was solved by simple matrix calculation. The example of analysis of density modulation was described, and possible discrepancy of modulation and equilibrium transport coefficients are studied. Before study systematic parameter dependence of the transport coefficients, precise physics understanding of the modulation experiments are important.

References
[1] N.L. Vasin, V.A. Vershkov, and V.A. Zhuravlev, Sov. J. Plasma Phys. **10** (6) Nov-Dec. 645, (1984)

[2] K.W. Gentle, B. Richards and F. Waelbroeck, Plasma Phys. Contr. Fusion **29**,1077(1987)

[3] K.W. Gentle, O. Gehere and K. Krieger, Nucl. Fusion **32**, 217 (1992)

[4] K.W. Gentle Phys. Fluids **31**, 1105 (1988)

[5] K. Ngashima, A. Sakasai, and T. Fukuda, Nucl. Fusion **33**, 1677 (1993)

[6] H. Takenaga, K.Nagashima, A. Sakasai, T.Oikawa and T. Fujita, Plasma Phys. Contr. Fusion **40**,183(1998)

[7] J. P.T. Koponen, T. Geist, U. Stroth, H.-J. Hartfus et al., Nucl. Fusion **40**, 365 (2000)

[8] K. Tanaka et al., J. Plasma Fusion Res. Series, 4 (2001) 427.

[9] K. Tanaka et al., to be published Nucl. Fusion

[10]   K.Tanaka, , X.Gao,Y.X.Jie, R.Sakamoto, K.Toi and HT7 group, Chin. Phys. Lett. 21,2458 (2004)

[11]   **K. Nagashima and A.Sakasai Rep. JAERI-M 92-057.JAERI ,Ibaraki(1992).**

[12]   K. Kawahata et al., Rev. Sci. Instrum. **70**, (1999) 707.

[13]   K. Tanaka et al., Rev. Sci. Instrum. 75, (2004) 3429.

[14]   T.Kaneba, et al., Rev. Sci. Instrum., 75 (2004) 3846

Figure Caption

Fig.1 (a)Electron temperature (b) density profiles under different NBI heating power. At R_{ax}=3.6m, B_t=2.75T for 2.7 MW and 8.5MW heating, B_t=2.8T for 1MW heating. Symbols in Fig.1 (a) indicate corresponding chord position of interferometers and (c) the profile of partice lsource rate calculated from DEGAS code.

Fig.2 Measured cross section of FIR laser interferometer

Magnetic flux surfaces are shown every ρ = 0.1 step from ρ = 0.1 to 1.2. Magnetic configuration is standard configuration (R_{ax}=3.6m, β=0%). The red lines mark the path of FIR laser beam used for analysis. The ten of 13 channels, which was used for the analysis, are shown [9].

Fig.3 (a) The example of modulated density at 5Hz. Thin red lines indicate at R =3.309,3.399, 3.489, 3.579, 3.669m from bottom of the picture. Thick blue lines indicate at R =3.759, 3.849, 3.939, 4.029, 4.119, 4.209 from top of the picture.(b) Hα signal intensity and (c) gas puff fuelling rate[9]

Fig.4 Spectrum of modulated components of density[9].

Fig.5 Model of D and V

Fig.6 Temperature and density profile of 5.2 and 1MW NBI heating Rax=3.6m, Bt=2.8T[9]

Fig.7 Integrated modulation amplitude and phase profile.

Symbols indicate chord positions of the interferometer. A 5Hz modulation for 5.2MW and 2Hz modulation for 1MW injection were done[9].

Fig.8 Radial profile of modulation amplitude and phase

Symbols indicate corresponding chord position of the interferometer. Dotted lines are upper and lower error bar[9].

Fig.9 (a) D and (b) V profiles estimated from modulation experiments. The dashed lines indicates upper and lower fitting error.

Fig.10 Comparison of integrated amplitude (a),(b) and phase profile(c),(d).   (a),(c)are 5.2MW heating case and (b),(d)are 1MW heating case.

Fig,11 Comparison of reconstructed profile and calculated profile with D and V from modulation experiments (a) 5.2MW (b) 1MW. Dashed lines indicate upper and lower error.   Error is due to determination error of D and .V

Fig.12 Temporal change of (a) local density and (b) density profile after pellet injection. Pellet was injected at t = 0.96 sec and t = 1.86sec.

Fig.13 Plot of Γ/n_e vesus $-\mathrm{grad}\, n_e/n_e$ after pellet injection at (a) $\rho=0.225$, (b) $\rho=0.525$, and (c) $\rho=0.725$.

Fig.14 (a) Comparison of V_{mod} and V_{eq} (b) Comparison of calculated density profile and measured profile Dashed lines indicate upper and lower error.   Error of calculated profiel is due to determination error of D and .V
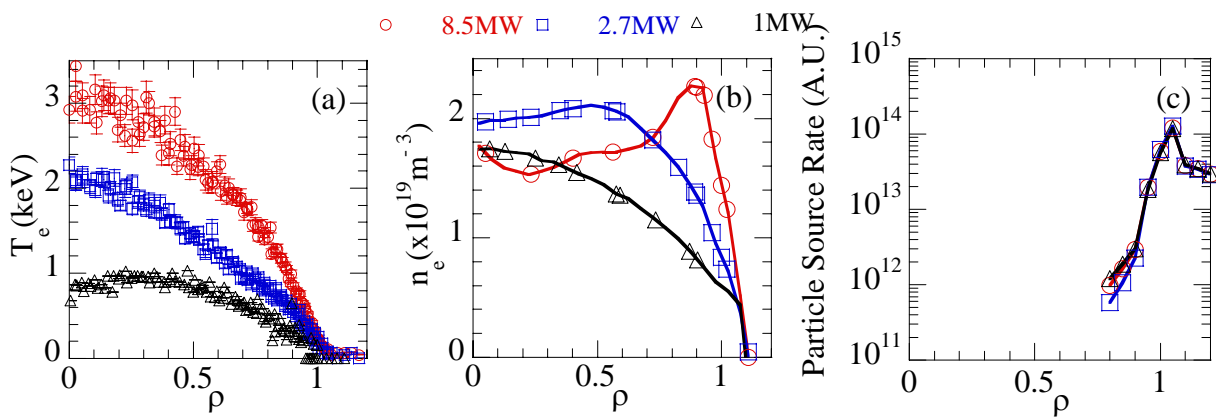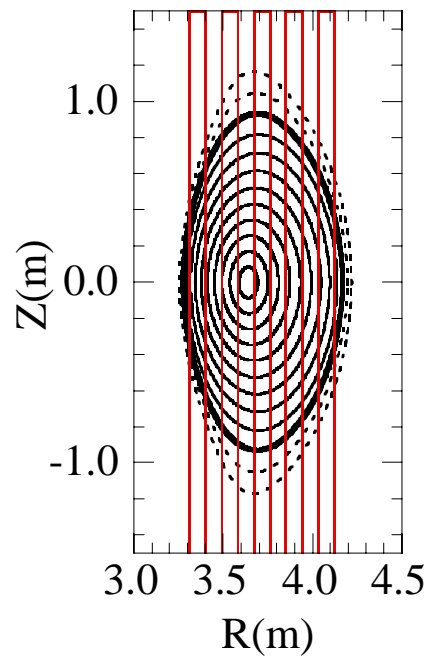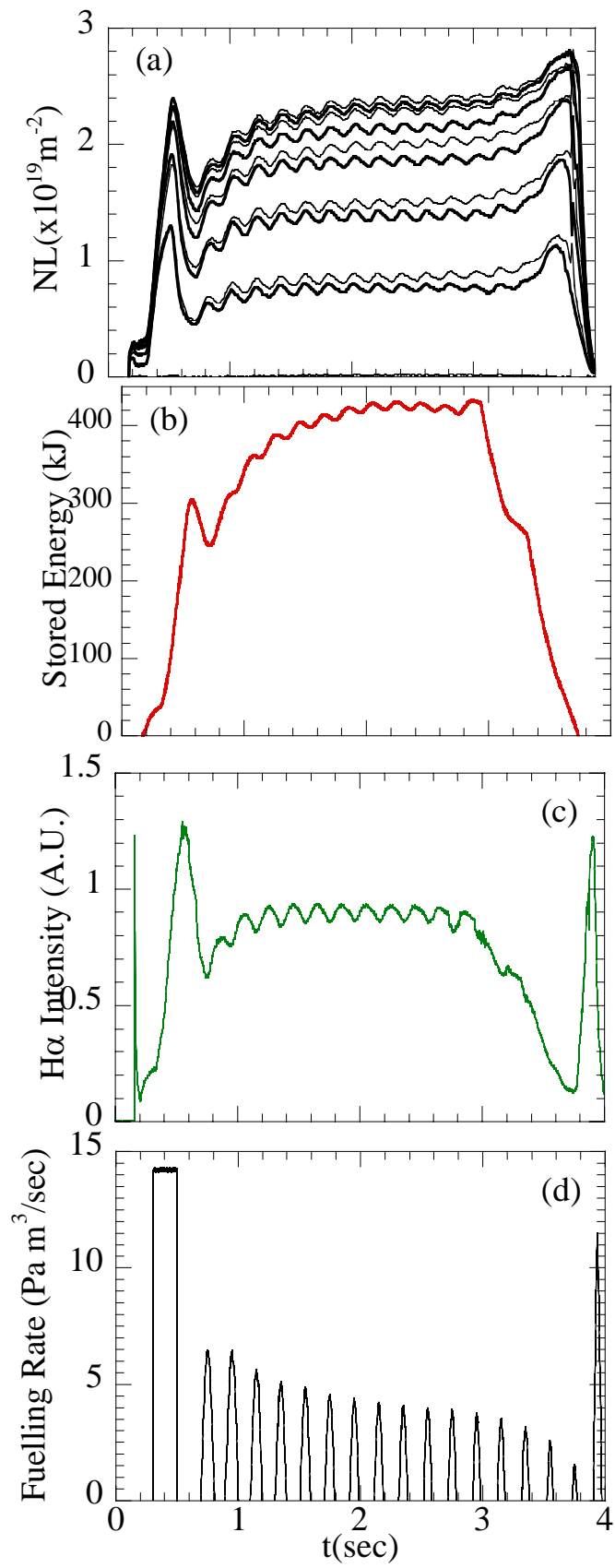
…..

Fig.1

Fig.2

Fig.3

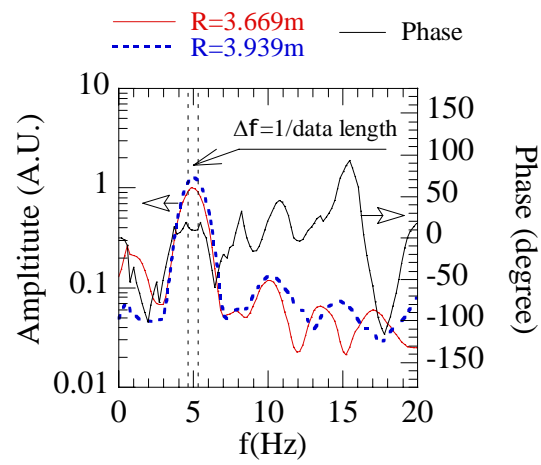Fig.4
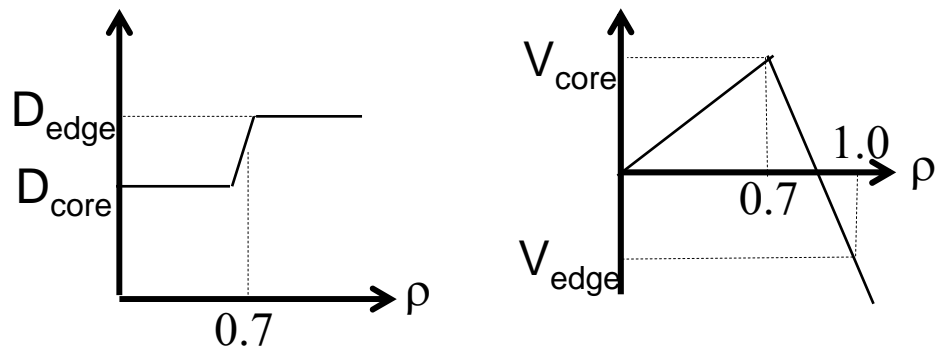
Fig.5
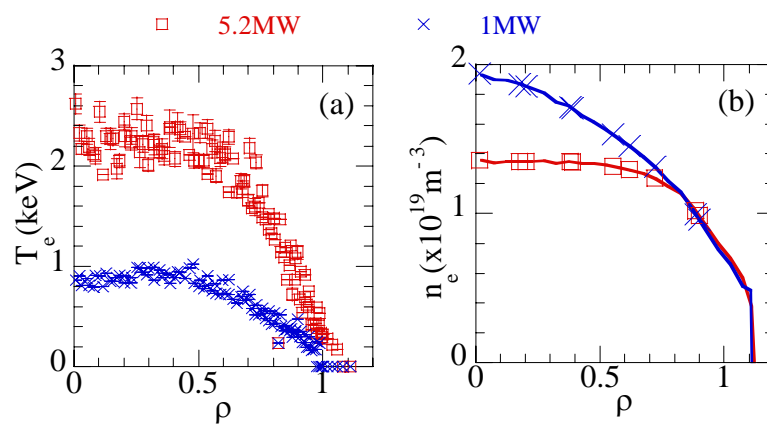
Fig.6
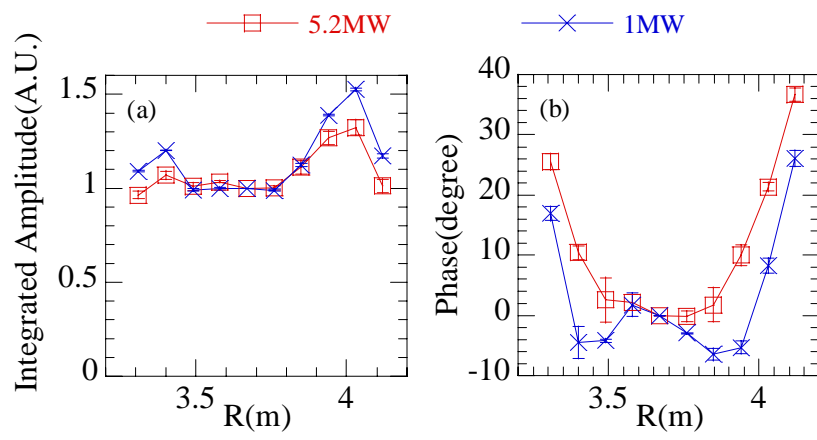
Fig.7

Fig.8

Fig.9

Fig.10

Fig.11

Fig.12

Fig.13

Fig.14

Dual-Electrode Biasing Experiments in *KT-5C Device*

YU Yi, LU Rong-Hua, WANG Chen, PAN Ge-Shen, WEN Yi-Zhi, YU Chang-Xuan,
MA Jin-Xiu, WAN Shu-De, LIU Wan-Dong

CAS Key Laboratory of Plasma Physics, School of Science,
University of Science and Technology of China, Hefei 230026, China

ABSTRACT

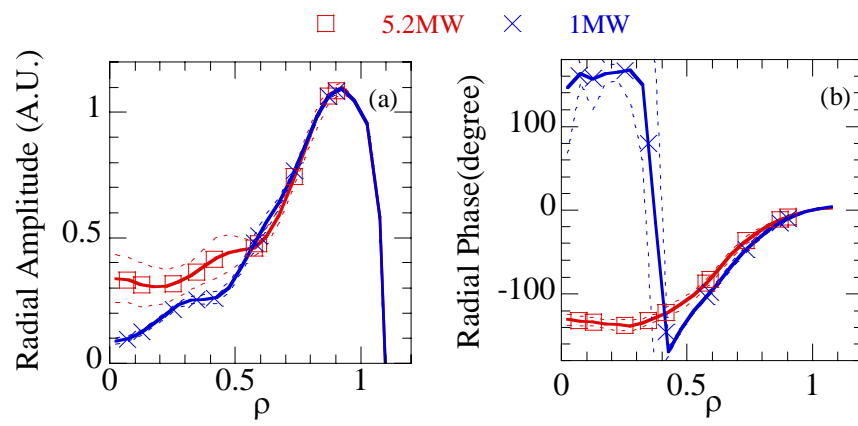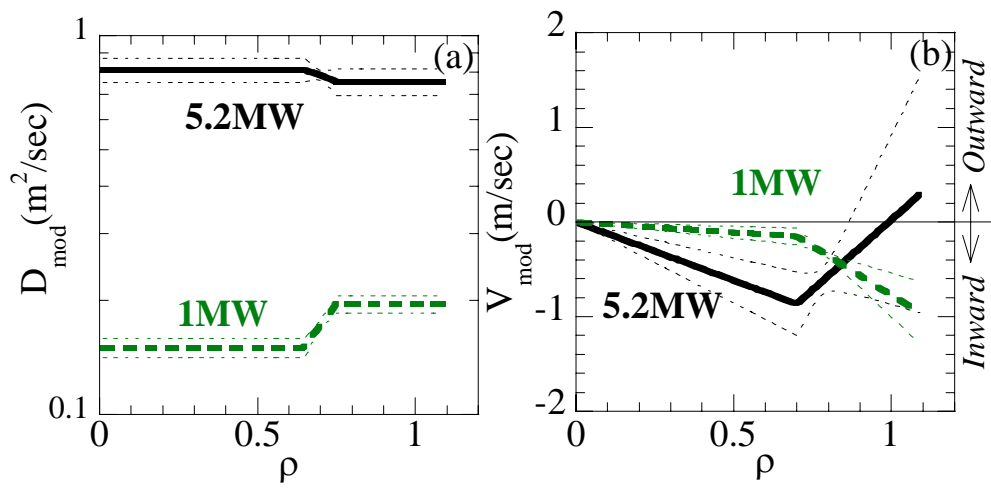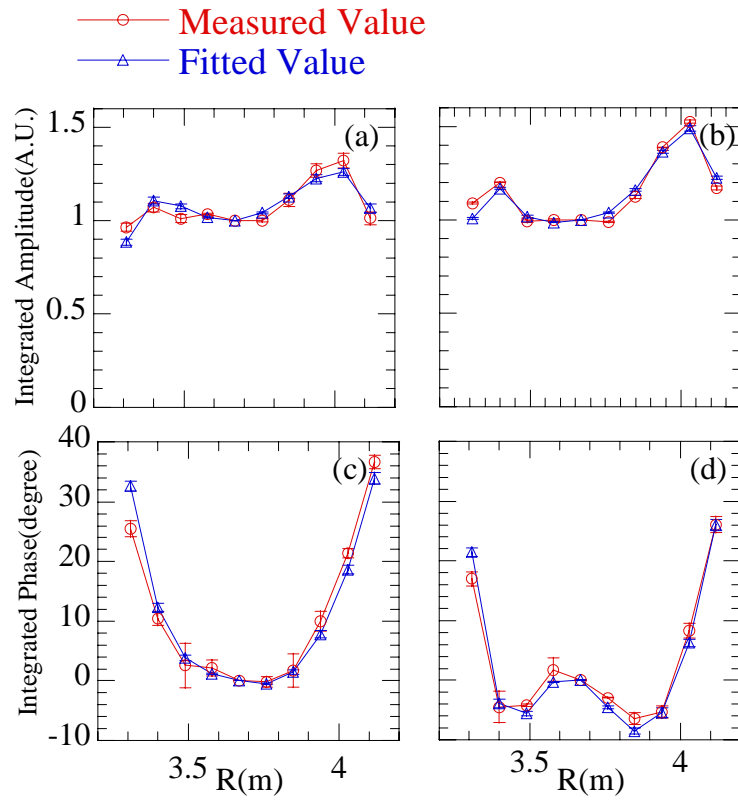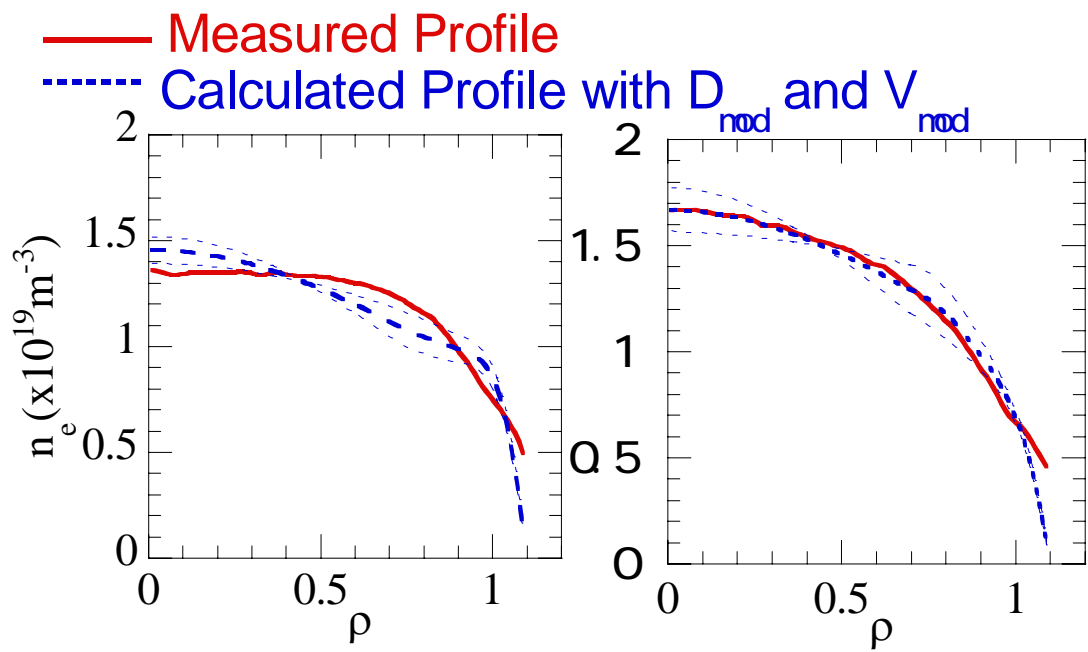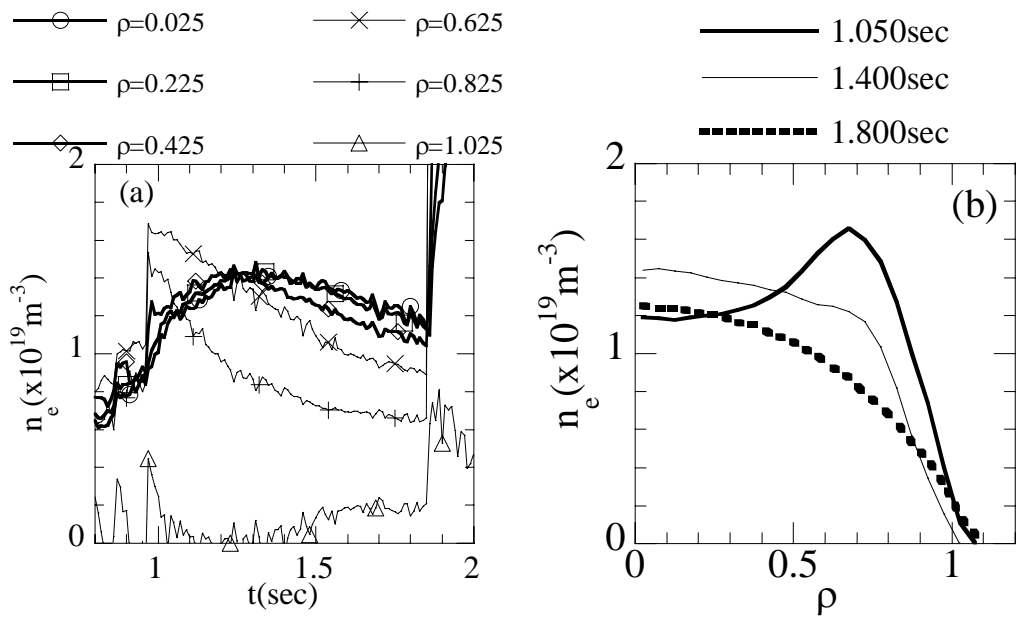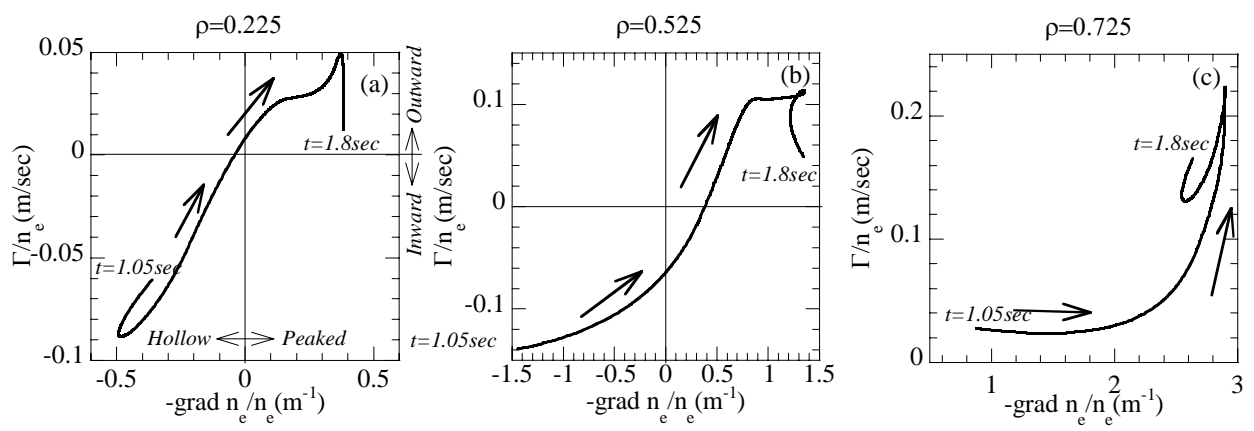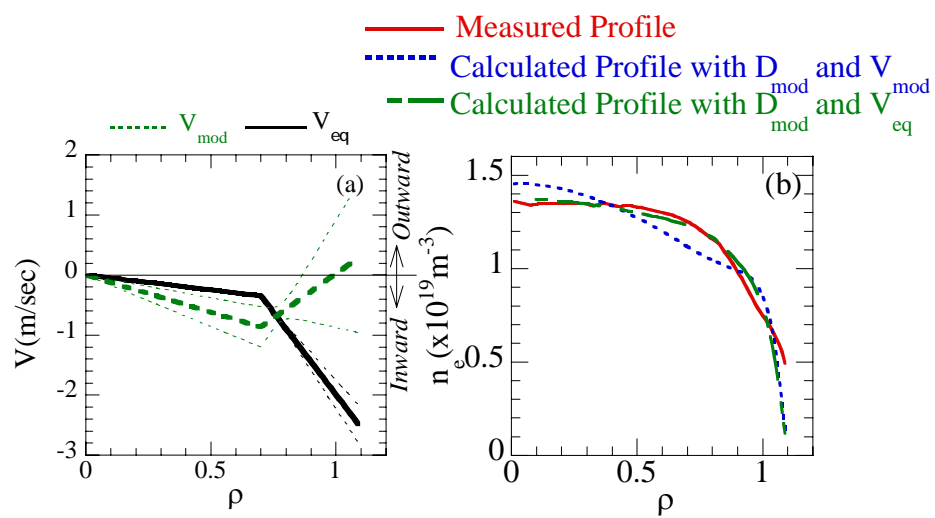Based on the single biasing electrode experiments to optimize the confinement of plasma in the device of KT-5C tokamak, dual-biasing electrodes were inserted into the KT5C plasma for the first time to explore the enhancement of the effects of biasing and the mechanisms of the biasing. By means of applying different combinations of biasing voltages to the dual electrodes, the changes in E_r , which is the key factor for boosting up the Er×B flow shear, were observed. The time evolution showed the inner electrode played a major role in dual-biasing, for it always drew a larger current than the outer one. The outer electrode made little influence. It turned out that the dual-biasing electrodes were as effective as a single one, in improving plasma confinement, for the mechanism of biasing was essentially an edge effect.

PACS: 52.55.Fa, 52.25.Gj, 52.35.Ra

Introduction

The Er×B shear flow stabilization model to explain the formation of edge transport barrier in the tokamak plasma has been developed and proved very successful since the last decade .[1] By shear decorrelation, the sheared poloidal **E$_r$** × **B** flow can effectively suppress the plasma turbulence and improve the confinement.[2] Many mechanisms in the generation of the poloidal sheared flow have been proposed, including Reynolds stress,[3-5] external biasing,[6-9] and others [12-16]. The relationship between the poloidal **E$_r$**×**B** sheared flow and all these mechanisms is given by

$$m_i n_i (\frac{\partial \vec{u}_i}{\partial t} + \vec{u}_i \cdot \nabla \vec{u}_i) - \frac{1}{n_i}(\vec{J} \times \vec{B}) = -\frac{\nabla \cdot \vec{p}_\alpha}{n_i} - m_e n_e (\frac{\partial \vec{u}_e}{\partial t} + \vec{u}_e \cdot \nabla \vec{u}_e)$$

For example, the external biasing can be put into the second term of the equation. The development of methods to control the sheared **E$_r$**×**B** flows is considered to be a key issue in the control of plasma turbulence and the optimization of plasma confinement. Therefore in such experiments, the radius electrical field **E$_r$** is an essential factor for the **E$_r$**×**B** flow shear effects to be observed.

The first biasing experiment was reported by Taylor in 1989.[7] We also have reported our single biasing work on our tokamak KT-5C.[9-11] Of all these experiments

only one electrode was used.[6,17,18] However, how would the Er have been changed if two electrodes were used? What differences might dual electrodes make? Could there be a stronger influence?

Let us first show some typical results of the single biasing on KT5C with the following parameters: R=32.5cm , a=8.5cm, I_p=10kA, B_ϕ=0.45T. Several sets of triple Langmuir probes are used to provide simultaneous and local measurements of the plasma conditions. A RFEA (Retarding field energy analyzer) is also used for getting the ion temperature. Figure 2 shows the radial profiles of the measured electron density n_e, electron temperature T_e and plasma potential f_p as well as of the radial electric field E_r derived from the f_p profile before and during the single positive biasing. In Fig.2 (a) and (b), one can see that the biasing causes a decrease in n_e and T_e over a broad edge region, and steepens their profiles in a narrow layer inside the limiter. The gradient of the radial ion temperature is also enlarged at the edge due to the biasing as shown in Fig 3. The biasing also induces a pronounced change in the plasma potential profile as shown in Fig.2(c) and (d), the plasma potential before the biasing peaks in the proximity of the limiter radius, which leads to a naturally spontaneous occurring E_r gradient layer where a small E_r well occurs which can been explained by ion-orbit loss. With the biasing, the plasma potential rises significantly over a wide edge region and its radial variation changes so that a modest E_r hill is developed. Fig.4 shows the radial profiles of the fluctuation levels given by the root-mean-square values. It exhibits the absolute fluctuation levels of n_e and T_e are reduced during the biasing, which indicates that the **E_r×B** flow shear is effective in fluctuation suppressing.

The floating potential fluctuations could increase at the edge region, which indicates that the absolute potential fluctuation level could have different behavior in responding to the biasing induced change in E_r, as compared with the response of $\tilde{n}_e$ $\,and\,$ $\tilde{T}_e$. So for simplicity, in the following experiments, we will emphasize the change of the key parameter E_r.

Dual-biasing experiments and the results

We began our work using dual-electrode biasing in the ohmically heated H_2 plasma in the KT-5C tokamak with parameters shown above. The two electrodes (stainless steel discs, 2cm in diameter and 0.4cm in thickness) were positioned at the place of r=3cm and r=7cm from the bottom of the device(Figure 1). The biasing voltages were supplied by two charged capacitor banks of 220uf×100 each through the thyristor switches. All the data were sampled at 1MHz by a multichannel 12-bit digitizer.

We performed several sets of dual-biasing experiments with different biasing voltage combinations to the two electrodes (Table 1).

Figure 5 shows the probe floating potential V_f profiles for set B, whose biasing configurations prove to be most effective in dual-biasing. It could be noted that there is only a little difference between inner electrode negative biasing (I_N), and inner electrode negative biasing together with outer electrode positive biasing (I_N_O_P).

Moreover, while the two electrodes are biased as I_N_O_P or I_P_O_N, the profiles of V_f between the two electrodes do not show much difference. The outer electrode seems to be shielded and has very little effect when the inner one is biased.

To explore this phenomenon more clearly, we observed firstly the time evolutions of the floating potential of different biasing. Figure 6 shows the floating potential changes due to single biasing almost instantaneously when positive biasing was applied; while it would change slower if negative biasing was imposed. That probably is due to the electrons responding to the positive biasing much faster than the ions to the negative biasing.

Fig.7 and Fig.8 show the time evolutions of the dual-biasing signals.

In Figure 7 in which I_N_O_P was imposed, when the outer electrode positive voltage V2 was applied, its current I2 changed almost immediately, while the inner electrode negative voltage V1 and current I1 changed much slower about 100μs later. The changes in floating voltage V_f and the resultant radial electrical field E_r actually obeyed the slower changes as the inner negative biasing, which demonstrated that the inner electrode played a dominant role.

While in Figure 8 with I_P_O_N, the inner positive V1 and I1 showed the same quick response. But with the outer negative, I2 was flat at the beginning, when the inner positive biasing was on, I2 fell to zero rapidly. This phenomenon again demonstrated that the inner positive electrode prevailed over the outer one. In brief, the dual electrode-biasing acts very similarly as single biasing in our dual biasing experiments

In the electrode biasing of most cases for set B, the edge E_r profiles changed significantly (Figure 9). The edge E_r trough was enlarged by negative bias, and reduced by positive biasing however a peak at a little inner radial position would occur. Both of them showed an enlarged Er gradient.

In fact, it was the inner electrode which always drew a larger current than the outer one as shown in table 1 and Figs.7 and 8. And the more current it drew, the more influence on the V_f and consequently the E_r it exerted.   It was the electrode current rather than the biasing voltage that produced the enhanced E_r gradient and boosted up the $\mathbf{E_r} \times \mathbf{B}$ flow shear effects on the plasma edge.

Conclusion

In conclusion, two separated biasing electrodes have been installed in the KT-5C tokamak to modify the radial electrical field E_r. When various combinations of biasing voltages are applied, the result is similar to the single electrode biasing. Neither single biasing nor dual-biasing electrode could hardly change the radial electrical field E_r in the interior of the plasma. The outer electrode seems almost to be shielded when the inner one is on. These results indicate that the mechanism of enhanced E_r gradient which implies the enhanced $E_r \times B$ flow shear by external biasing is intrinsically an edge effect due to the electrode induced current. A positive biasing seems to be more appreciated since it causes a larger electrode current.

After having finished the above experiments and during the period of

summarizing our dual-electrode biasing work and writing the reports, we noticed interestingly by chance a theoretical work published recently by Kasuya and Itoh et al [19]. The paper proposes dual-electrode biasing, and predicts that a double-peaked E_r structure (which means stronger shear) could be created if the applied dual biasing voltages ramp up within a certain rate.   In our experiments reported above we did not get the double-peak E_r, which might be due to the different experimental settings and conditions. But, it is really an intriguing issue that we would investigate in our future work.

Acknowledgements

References

[1] Burrel K H 1997 *Phys. Plasma* 4 1499

[2] Biglari H, Diamond P H and Terry P W 1990 *Phys. Fluids B* 2 1

[3] Craddock G G and Diamond P H 1991 *Phys. Rev. Lett.* 67 1535

[4] Diamond P H, Liang Y M, Carreras B A and Terry P W 1994 *Phys. Rev. Lett.* 72 2565

[5] Hidalgo C, Silva C, Pedrosa M A, Sanchez E, Fernandes H and Varandas CAF 1999 *PRL* 83 2203

[6] Sakai O, Yasaka Y and Itatani R 1993 *Phys. Rev. Lett.* 70 4071

[7] Taylor R J, Brown M L, Fried B D and Grote H 1989 *Phys. Rev. Lett.* 63 2365

[8] Tynan G R, Schmitz L, Conn R W, Doerner R and Lehmer R 1992 *Phys. Rev. Lett.* 68 3032

[9] Wang C, Pan G S, Wen Y Z, Yu C X, Wan S D, Liu W D, Wang Z J and Sun X 2001 *Chin. Phys. Lett.*18 257

[10] Wang C, Pan G S, Yu C X, Wen Y Z, Wan S D, Wang Z J, Liu W D, Sun X, Wang J and Gao H 2002 *IEEE Trans. Plasma Sci.* 30 625

[11] Gao H, Zhai K, Wen Y Z, Wan S D, Wang G D and Yu C X 1995 *Journal of Plasma Physics* 54 393

[12] Leblanc B*et al* 1995 *Phys. Plasma* 2 741

[13] LeBlanc B P, Bell R E, Bernabei S, Hosea J C, Majeski R, Ono M, Phillips C K, Rogers J H, Schilling C, Skinner C H and Wilson J R 1999 *Phys. Rev. Lett.* 82 331

[14] Shaing K C and Crume E C 1989 *Phys. Rev. Lett.* 63 2369

[15] String T E 1969 *Phys. Rev. Lett.* 22 770

[16] Hassam A B, Antonsen T M, Drake J F and Liu C S 1991 *Phys. Rev. Lett.* 66 309

[17] Isler R C *et al* 1992 *Phys. Fluids B* 4 2104

[18] Craig D, Almagri A F, Anderson J K, Chapman J T, Chiang C S, Crocker N A, Den Hartog D J, Fiksel G, Prager S C, Sar® J S and Stoneking M R 1997 *Phys. Rev. Lett.* 79 1865

[19] Kasuya N, Itoh K and Takase Y 2004 *Plasma Phys. Control. Fusion* 46 A235

[20] Terry P W 2000 *Rev. Mod. phys.* 72 109

[21] Cornelis J, Sporken R, Vanoost G and Weynants R R 1994 *Nucl.Fusion* 34 171

[22]LU Rong-Hua2005 *et al* 2005 *Chinese Physics Letters* 22 6
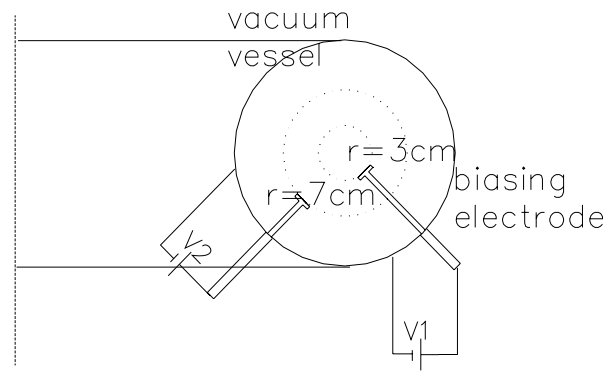
Fig.1. Setting of the dual-electrodes
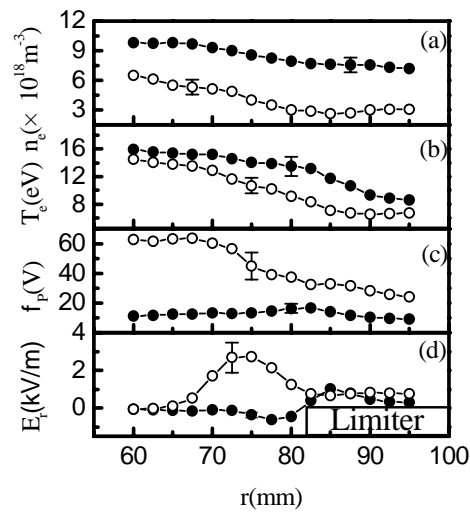
Fig.2. Radial profiles of the measured electron density,
Electron temperature, plasma potential and radial electrical field
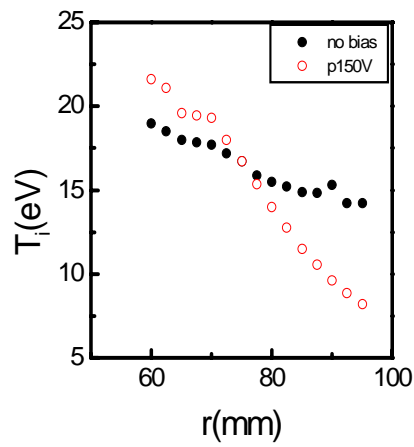
Fig.3. The radial profile of the ion temperature
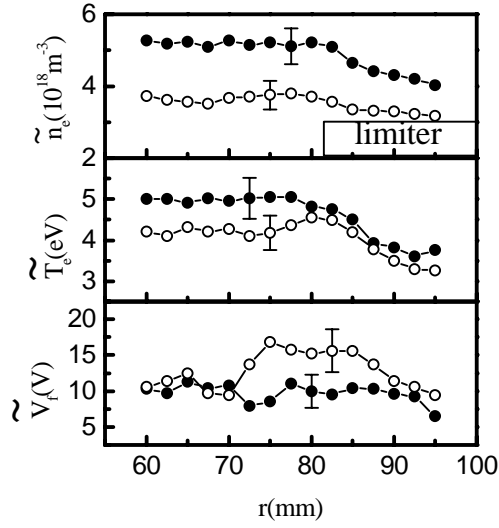
Fig.4. The radial profiles of the fluctuation levels

Set	$V_1(v)/I_1(A)$	$V_2(v)/I_2(A)$	mark
A	——	——	NB(No Biasing)
	+150/—	——	I_P(Inner Positive)
	——	+200/55	O_P(Outer Positive)
B	——	——	NB
	−200/120	——	I_N(Inner Negtive)
	−200/120	+200/90	I_N_O_P
	+200/150	−200/<10	I_P_O_N
C		——	NB
		+200/<10	I_P_O_N
		−200/45	I_N_O_P

Table 1. Different combinations of dual-biasing voltages
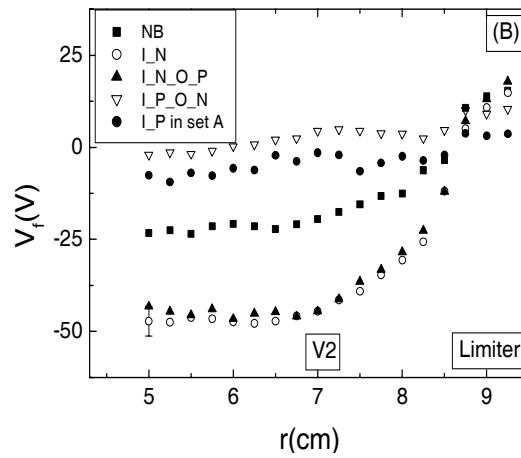
Fig.5. Profiles of V_f in Set B
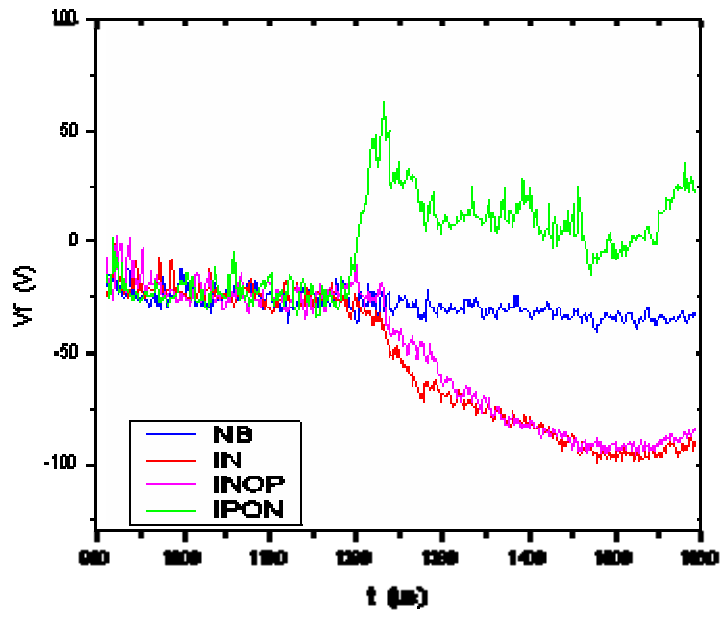
Fig.6. The time evolution of V_f
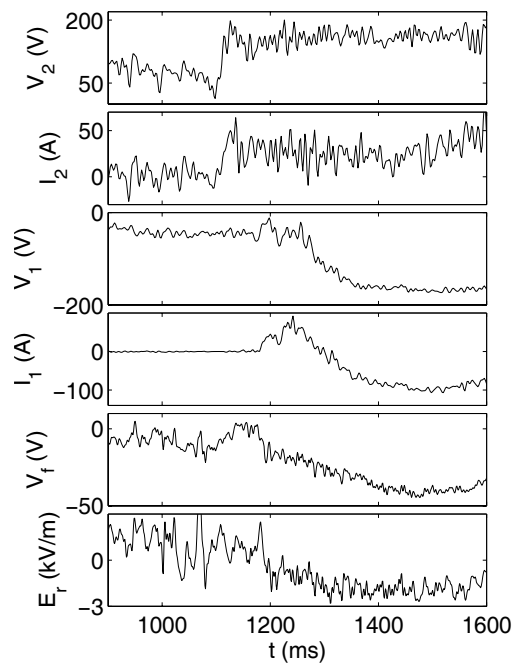
Fig.7. The time evolution of INOP in Set b
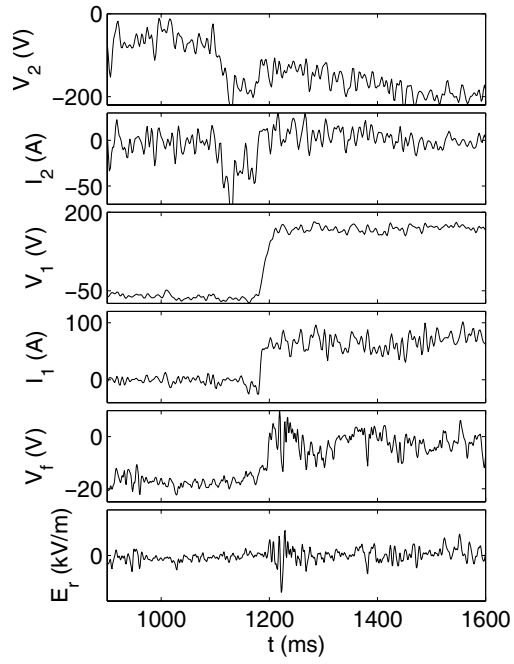
Fig.8. The time evolution of IPON in Set B
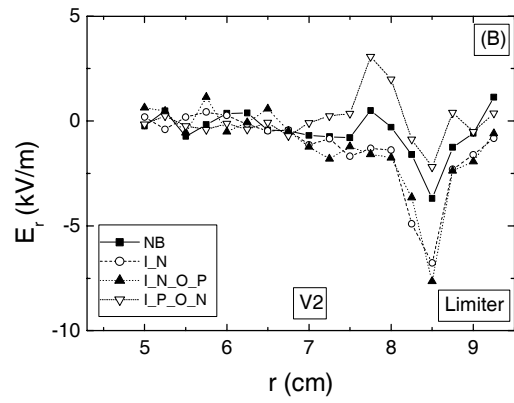
Fig.9. Profiles of Er at various biasing conditions in Set B

ICRF Experiments and Potential Formation on the GAMMA 10 Tandem Mirror

M.Ichimura, T.Cho, H.Higaki, M.Hirata, H.Hojo, T.Imai, K.Ishii, M.K.Islam,
A.Itakura, I.Katanuma, J.Kohagura, Y.Nakashima, T.Numakura, T.Saito,
Y.Tatematsu, M.Watanabe, M.Yoshikawa

Plasma Research Center, University of Tsukuba, Tsukuba, Ibaraki 305-8577, Japan
e-mail: ichimura@prc.tsukuba.ac.jp

Abstract

Target plasmas, on which the formation of the electrostatic potentials and the improvement of the confinement are studied, are produced with ICRF in the GAMMA 10 tandem mirror. The ion temperature of more than *10 keV* has been achieved in relatively low density plasmas. When the strong ICRF heating is applied, it is observed that the high frequency and the low frequency fluctuations are excited and suppress the increase in the plasma parameters. Recently, a new high power gyrotron system has been constructed and the plug ECRH power extends up to 370 kW. The improvement of the confinement due to the formation of the potential in the axial direction and the strong radial electric field shear has been observed.

keywords: *tandem mirror, ICRF plasma production, fluctuations, potential formation*

1. Introduction

The GAMMA 10 tandem mirror has MHD anchors with a minimum-B field and is arranged in an effectively axisymmetrized configuration [1]. The high-density plasma production and confinement with electrostatic potentials are the major important issues in the present experiments [2]. The ion cyclotron range of frequency (ICRF) waves are used for the initial plasma production and heating in the central cell. The electron cyclotron resonance heating (ECRH) is used for the potential formation in the plug/barrier region and for the electron heating in the central cell. The axisymmetrization of the heating system is important in relation to the radial particle transport. The improvement of the ICRF antenna system has been made because the antenna configuration in the central cell affects the plasma profile in the azimuthal direction [3]. In relatively low-density (order of $10^{18}m^{-3}$) plasmas, the hot ion mode operation has been realized and ion temperature of more than *10 keV* has been achieved [4]. In such a mode of operation, the plasmas with a strong temperature anisotropy are magnetically confined in the central cell. In the high-β, which is defined as the ratio between plasma pressure and magnetic field strength, plasmas with the strong temperature anisotropy, the Alfvén ion cyclotron (AIC) mode, which is one of the micro-instabilities are excited spontaneously [5]. The plasma confinement will be affected from the externally applied RF waves and also spontaneously excited waves in the plasma.

By using high power ERCH at the plug region, a positive potential is generated to improve the axial ion confinement [6,7]. And also at the barrier region, a thermal barrier potential (smaller than the potential in the central cell) is generated. When the plug ECRH is applied, the potential increases due to the induced electron loss in the axial direction and the positive potential with peaked profile in the center is formed in the central cell. The resultant electric field in the radial direction and its shear will suppress the fluctuations, for example, the drift-type low frequency instability [8]. Recently, the suppression of the large amplitude fluctuations has been clearly observed in the soft X-ray measurement [9].

In this manuscript, the recent results of the potential formation and ICRF experiments for the high-beta plasma production are described.

2. GAMMA 10 Device and ICRF Systems

Figure 1 shows the axial profiles of the magnetic field line, strength and plasma potentials on the typical discharge conditions in GAMMA 10. The axial location is represented on the basis of the midplane of the central cell, $z = 0$. The minimum-B anchor cells are located on both sides of the central cell and the axisymmetric plug/barrier cells are located at both ends. The magnetic field strength at the midplane of the central cell is 0.41T and the mirror ratio is 5 in a standard mode of operation. As indicated in the figure, the hill and well type potentials are formed in the plug/barrier region. ICRF powers (RF1,2 and 3) are only injected in the central cell. Two kinds of ICRF antennas are installed near both mirror throats of the central cell. One is the so-called Nagoya-type III antenna (Type III) [10] that is installed at $z = \pm2.2m$ where the mirror ratio R is 1.6. The other is the conventional double-half-turn antenna (DHT) that is installed at the location of $z = \pm1.7m$ where $R = 1.1$. Three ICRF systems (RF1, RF2 and RF3) are now in operation.

Principally, Type III is driven by the RF1 system and used for the plasma production in the central cell and the ion heating in the anchor cell [11]. The frequency is adjusted to the ion cyclotron frequency near the midplane of the anchor cell. The high-beta plasma production in the anchor cell is essential to sustaining the MHD stability of the whole GAMMA 10 plasma. DHT is driven by RF2 and used for the main ion heating in the central cell. The frequency is adjusted to the ion cyclotron frequency near the midplane of the central cell. In mirror plasmas, ions that are heated in the perpendicular direction are deeply trapped near the midplane. To avoid the energy loss due to the charge exchange reaction, the locations of the gas puffing are selected to be near the mirror throats where less hot ions exist. The radiated powers from each Type III and DHT are typically $100kW$ with a duration of $200ms$. RF3 is an additional system and used for high-density plasma production [12].

The high power gyrotron systems with a frequency of *28GHz* are used for the potential

formation. Fundamental ECRH is applied at the plug region (*B=1T*) between the midplane (*B=0.5T*) and the outer mirror throat (*B=3T*) of the plug/barrier cells. In addition to the plug ECRH, a second harmonic ECRH is applied to the midplane for creating the barrier potential. The radiated power is mostly coupled to the X-mode for the present geometry. The radiation pattern on the resonance layer is arranged to be nearly axisymmetric. Segmented end plates, which are electrically floated from the vacuum vessel by using large resistances, are installed at the end wall

3. Target Plasma Production and Low Frequency Fluctuations with ICRF

The plasma is started up by injecting short pulse (1*ms*) gun-produced plasmas (PG) from both ends and is sustained by applying RF1, of which frequencies of *9.9 MHz* (west) and *10.3 MHz* (east), in combination with a hydrogen gas puffing in the central cell. For the main ion heating, the RF2 pulse, of which frequency is *6.36 MHz*, is applied to the east DHT antenna. The additional RF3 pulse, of which frequency is *41.5 MHz*, is applied to the west DHT antenna. The temporal evolution of the plasma parameters is indicated in Fig.2. The line density increases with RF1 and diamagnetic signal increases with RF2. In the typical experiments, the saturation of the density is observed at the line density of near *4 times 10^{17} m^{-2}*. The mechanism of this saturation is interpreted as the eigenmode formation of the ICRF waves which satisfy the axial boundary conditions. In plasmas with a relatively low density (order of 10^{18} m^{-3}) and a small radius (a few tens cm), the wavelength is in the same order of the plasma size and eigenmodes are formed in both radial and axial directions. Because the wavelength depends strongly on the density, the density is likely to be clamped at the optimum value for the eigenmode formation [12]. When RF3 is applied, the density starts to increase again due to another eigenmode formation.

The plasma pressure increases almost linearly with the RF2 power. The highest ion temperature above *10 keV* has been achieved in the case of the magnetic field strength of 0.57*T*. As previously indicated in such high-β plasmas, the temperature anisotropy becomes more than 10. In GAMMA 10, electro-magnetic fluctuations due to the AIC modes have been observed experimentally in the parameter range of *$\beta A^2 > 0.3$* [13]. The behavior of the plasmas in the central cell is affected by the excitation of the modes [14, 15]. The effects of the AIC modes on the particle transport have been observed clearly in the behavior of the high-energy ions. The pitch angle scattering and the axial transport of the high-energy ions due to the AIC modes are clearly observed [3].

When the ICRF pulses are applied, the low frequency density fluctuations are detected in many diagnostics. Figure 3(a) shows the temporal evolution of the line density and diamagnetic signal on the typical discharge in which large amplitude fluctuations are observed. Figure 3(b) shows the density fluctuations in the peripheral region measured by an electrostatic probe. There are six

regions in which fluctuations are observed as indicated in Fig.3(b). The large amplitude drift-type fluctuations are clearly excited when the RF3 pulse is applied as shown in Fig.3. There are two types of fluctuations observed typically in GAMMA 10, that is, a drift-type (#1,2,3, and #5) and a flute-type (#4 and #6) fluctuation. The initial phase of the plasma build-up (#1), small fluctuations are excited due to the steep gradient of the density profile. When ICRFs for the plasma production are applied, the drift-type fluctuations are strongly excited (#2 and #3). These fluctuations are stabilized when ECRH is applied. The mechanism of the stabilization is considered to be strong shear of the radial electric field due to the potential formation. Instead of the drift-type fluctuation, the flute-type fluctuation is excited due to the E_r x B_z rotation [16]. When the ECRH pulse stops, the drift-type fluctuation is excited again as indicated by #5. When ICRF pulses stop, the strong flute-type fluctuations are excited due to lack of high-β plasmas in the anchor cell. In the RF3 period (#3), a frequency peak near *10 kHz* is observed that corresponds to the mode with the azimuthal mode number of m=+1, which rotates in the direction of the electron diamagnetic motion. In GAMMA10, these drift-type fluctuations are observed also at the plug/barrier cell with the same frequency as in the central cell. Both peaks in the frequency spectra have the strong coherence and with finite phase difference, that is, the drift-type fluctuations are propagating in the axial direction. On the other hand, the flute-type fluctuations have no phase differences. These fluctuations will be mainly driven by the density gradient. The density gradient is strongly affected from the gas puffing rate, and the RF1 and RF3 powers. A large amount of gas injection, that is, from the gas puffing and/or from the wall, intends to increase the edge density and decrease the density gradient. The drift-type fluctuations appear when the gas injection is reduced and/or the RF1 and RF3 power increases.

4. Potential Formation with ECRH

In previous sections, the behaviors of the target plasmas for studying the potential effect to the plasma confinement are investigated. On hot-ion mode plasmas with the ion temperature in the *keV* range, the plug and barrier ECRHs are turned on after the plasma reaches in a steady state. The plasma potentials from the vacuum vessel change in the step-like response. When the plug potential is formed, the reduction of the end-loss ion current and the increase of the line density in the central cell are clearly observed. Typical feature of the confinement improvement in the axial direction is shown in Fig.4. If one side of ECRH is only turned on, another side of the end-loss current increases and no increase of the line density are observed.

The plug potential Φ_p is determined from the energy spectrum of the end loss ions and is the highest value along the magnetic field line. The central cell potential Φ_c and barrier potential Φ_b are determined with beam probe measurements. The ion confining potential ϕ_c is defined by $\phi_c = \Phi_p$ -

Φ_c. In Fig.5, Φ_p and Φ_c are plotted as a function of the plug ECRH power. Recently, a new high power gyrotron system is constructed and the plug ECRH power extends to 370 kW [17]. The plug potential increases with the ECRH power, while the variation of the central cell potential is not so large. Then, the ion confining potential ϕ_c increases with Φ_p, that is, the plug ECRH power. The value of 2.1kV has been attained with the high power ECRH [18]. For efficient generation of the high potential with the high power ECRH, the induced diffusion of warm electrons in the velocity space is essential. The velocity space diffusion of electrons can be evaluated from the energy spectrum of the end-loss electrons. The mean energy of the end-loss electrons is strongly related to the ECRH power.

5. Summary

Target plasmas, on which the formation of the electrostatic potentials and the improvement of the confinement are studied, are produced with ICRF in the GAMMA 10 tandem mirror. A new high power gyrotron system is constructed and the plug ECRH power extends up to 370 kW. The improvement of the confinement due to the formation of the potential in the axial direction and the strong radial electric field shear has been observed.

Acknowledgements

References

[1] M.Inutake, et al., Phys. Rev. Lett. **53**, 783 (1984).

[2] K.Yatsu, et al., Nuclear Fusion **39**, 1707 (1999).

[3] M.Ichimura, et al., Nuclear Fusion **39**, 1995 (1999).

[4] T.Tamano, et al., in *Plasma Phys. and Controlled Nuclear Fusion Research 1994*, Vol.2, IAEA, Vienna (1995) p.399.

[5] R.C.Davidson and J.M.Ogden, Phys. Fluids 18, 1045 (1975).

[6] S.Miyoshi, et al., *in Plasma Physics and Controlled Nuclear Fusion Research 1990*, Vol.2, IAEA, Vienna (1991) p.539.

[7] T.Cho, et al., Phys. Rev. Lett. **86**, 4310 (2001).

[8] A.Mase, et al., Phys.Rev.lett., **64**. 2281 (1990).

[9] T.Cho, et al., Phys. Rev. Lett. **94**, 085002 (2005).

[10] T.Watari, et al., Nuclear Fusion **22**, 1359 (1982).

[11] M.Ichimura, et al., Nuclear Fusion **28**, 799 (1988).

[12] M.Ichimura, et al., Phys. Plasmas **5**, 2066 (2001).

[13] M.Ichimura, et al., Phys. Rev. Lett. **70**, 2734 (1993).

[14] T.Saito, et al., Phys. Rev. Lett., **82**, 1169 (1999).

[15] K.Ishii, et al., Phys. Rev. Lett., **83**, 3438, (1999).

[16] S.Tanaka, et al., J. Phys. Soc. Jpn., **67** 1963 (1998).

[17] T.Saito, et al., J. Plasma and Fusion Res. 81, 288 (2005).
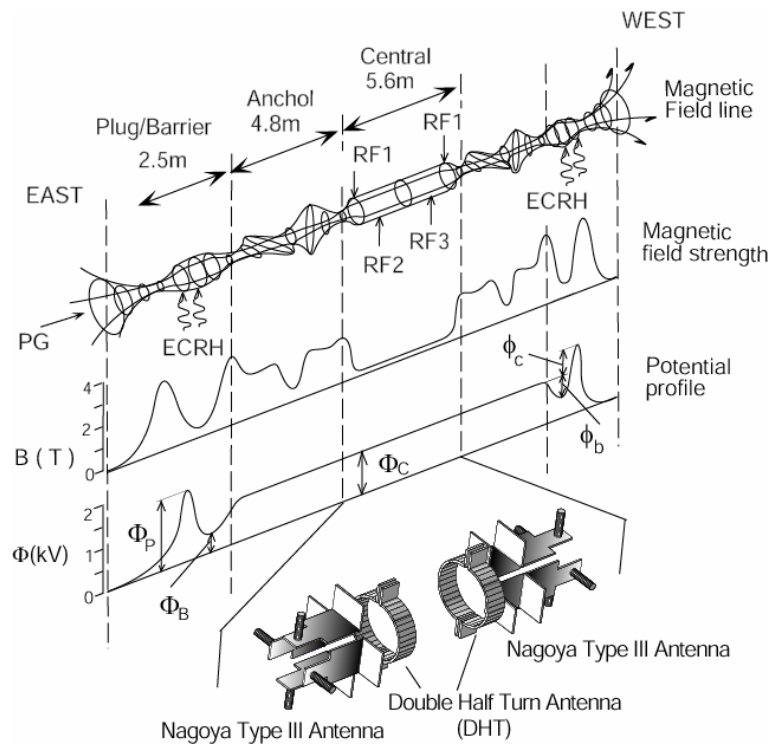
Fig.1 Schematic drawing of the GAMMA 10 tandem mirror

Fig.2 Temporal evolution of plasma parameters

(a)

RF1

RF2

RF3

ECRH

#181865

Line density [×10^{13}cm^{-2}]

Diamagnetism [×10^{-5}Wb]

10

10

5

5

0

0

(b)

Ion Saturation Current (a.u.)

1

0.5

0

#1   #2   #3   #4   #5 #6

0   100   200

Time   [msec]
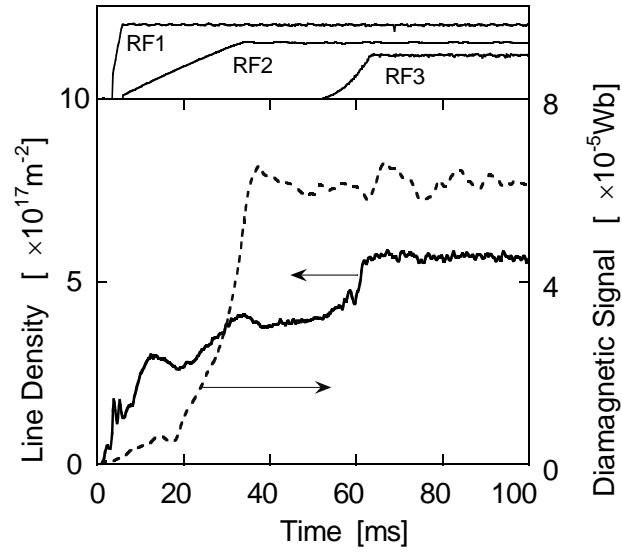
Fig.3 (a)Temporal evolution of plasma parameters
 (b)Ion saturation current of the electrostatic probe
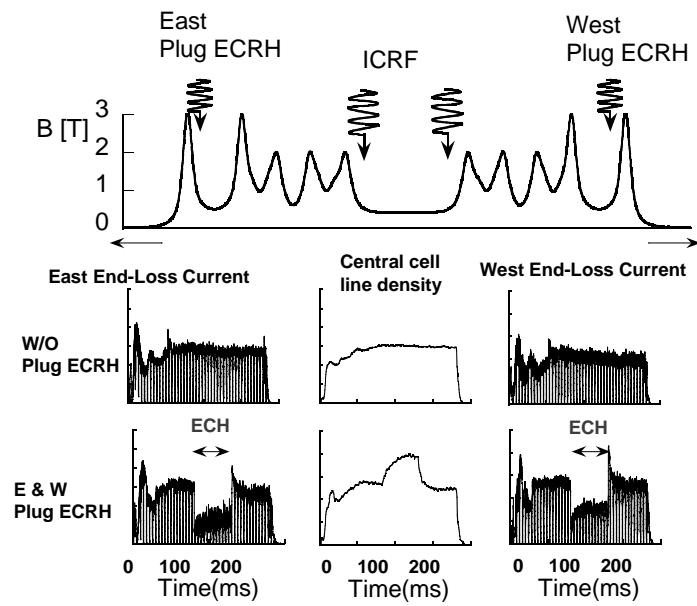
Fig.4 Typical feature of the confinement improvement
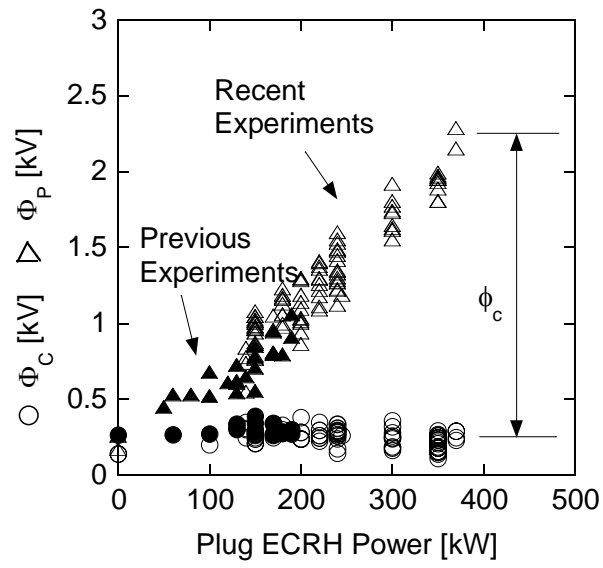
Fig.5 Central and plug potentials as a function of plug ECRH power

MHD flow layer formation at boundaries of magnetic islands in tokamak plasmas

Dong Jiaqi, Long Yongxing, Mou zongze, and Zhang Jinhua

Southwestern Institute of Physics

P.O. Box 432, Chengdu 610041, China

and SWIP-DUT Joint Lab for Fusion Plasma Physics, Chengdu, China

Abstract   Non-linear development of double tearing modes induced by electron viscosity is numerically simulated. MHD flow layers are demonstrated to merge in the development of the modes. The sheared flows are shown to lie just at the boundaries of the magnetic islands, and to have sufficient levels required for internal transport barrier (ITB) formation. Possible correlation between the laye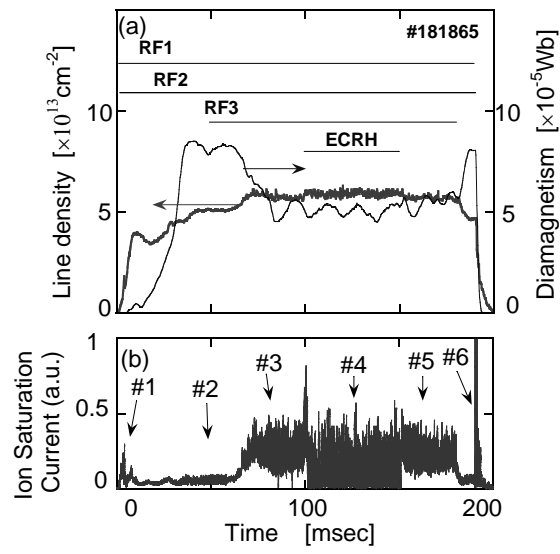r formation and triggering of experimentally observed ITBs, preferentially formed in proximities of rational flux surfaces of low safety factors, is discussed.

1.   Introduction

The important roles played by flows with shear in magnetically confined toroidal plasmas have been highly appreciated since the discovery that they suppress anomalous diffusion producing turbulence and lead to confinement improvement, such as low to high confinement mode transition and internal transport barrier (ITB) formation. Two kinds of flow have essentially been considered in the studies of turbulence-flow interaction.[1] The first is mean flow that is created by outside sources such as neutron beam injection, radio frequency wave launching and biased voltage application etc., or by variation of plasma equilibrium parameters. The second is zonal flow that emerges from nonlinear interaction of turbulence fluctuations themselves. In radial direction, both the mean and zonal flows vary with scale lengths comparable to turbulence correlation lengths. Theory and simulations indicate that plasma mass, velocity and energy diffusions across magnetic flux surfaces may be regulated by zonal flows in absence of mean flows. In addition, experimentally observed ITBs and external transport barriers (ETBs) in advanced tokamak discharges are believed to result from flow suppression of turbulent transport.

Comprehensive reviews on ITBs in tokamaks, including experiments and theories, were given by Wolf[2] and Connor *et al*[3]. Nevertheless, theory on creation mechanisms of the flows at the positions and times of, especially, ITB formation is still under development.

A third kind of flow–MHD flow may exist in tokamak plasmas and studied in this work.

It is well know that low order rational flux surfaces are prone to excitation of ideal and dissipative MHD instabilities and that magnetic energy released in the development of the modes may drive significant plasma flows. Therefore, besides fishbone oscillations, other MHD instabilities, forming magnetic islands are proposed as plausible triggering mechanisms for the formation of ITBs in the proximity of low order rational surfaces in ASDEX Upgrade reversed shear discharges.[4] However, the double ITB structure observed in JET reversed magnetic shear discharge has not been addressed in detail.[5] The linear and quasi-linear development of double tearing mode mediated by anomalous electron viscosity were studied in Ref. 6 and 7 where the possibility for such modes to create sheared flow layers triggering ITBs was also suggested. By simulating the non-linear development of the modes, we demonstrate in this work the creation of sizable sheared poloidal flow layers at the boundaries of the magnetic islands.

The remainder of this work is organized as follows. The physics model and equations are presented in Section II. The numerical results are described in Section III. Section IV is devoted to conclusions and discussion.

2.   Physical Model and Basic Equations

The physical model and basic equations employed in this work are the same as that in Ref. 7. Here, we repeat it briefly for the sake of completeness. A typical sheared slab of length a in the x-direction, with a current in the z- direction, and zero equilibrium flow velocity $\mathbf{V}_0 = 0$ embedded in the standard sheared magnetic field is employed,

$$\mathbf{B}_0(x) = B_{0y}(x)\widehat{\mathbf{y}} + B_{0z}(x)\widehat{\mathbf{z}}, \tag{1}$$

where $B_{0y}(x)$ equals zero at $x = \pm x_s$. The stability of this initial configuration will be examined with respect to two-dimentional, incompressible perturbations. The vector fields are expressible in terms of two scalar potentials : the flux function $\psi(x, y, t)$,

$$\mathbf{B}_\perp = \nabla\psi \times \widehat{\mathbf{z}}, \tag{2}$$

and the stream function $\phi(x, y, t)$,

$$\mathbf{V}_\perp = \nabla\phi \times \widehat{\mathbf{z}}. \tag{3}$$

With electron viscosity, the Ohm's law becomes

$$\mathbf{E} = \eta \mathbf{j} - \frac{1}{c} \mathbf{V} \times \mathbf{B} - \frac{m_e \mu_e}{n_e e^2} \nabla^2 \mathbf{j}. \tag{4}$$

Then, it is straightforward to write the two non-linear equations for ψ and ϕ as

$$\frac{\partial \psi}{\partial t} = \{\phi, \psi\} + \frac{1}{S} \nabla^2 \psi - \frac{1}{R} \nabla^4 \psi + E', \tag{5}$$

$$\frac{\partial}{\partial t}(\nabla^2 \phi) = \{\phi, \nabla^2 \phi\} - \{\psi, \nabla^2 \psi\}, \tag{6}$$

where $S = \tau_r/\tau_h$ is the magnetic Reynolds number with $\tau_r = 4\pi a^2/c^2 \eta$, $R = \tau_v/\tau_h$ is the viscosity diffusion Reynolds number, while $\tau_v = 4\pi a^4 n_e e^2/c^2 \mu_e m_e = \omega_{pe}^2 a^4/c^2 \mu_e$, η and μ_e are plasma resistivity and electron viscosity, respectively.

$$\{\phi, \psi\} = \frac{\partial \phi}{\partial x} \frac{\partial \psi}{\partial y} - \frac{\partial \psi}{\partial x} \frac{\partial \phi}{\partial y}$$

is the Poisson bracket. E' is the externally applied electric field to keep the total plasma current constant. Normalizing all lengths to a, time to $\tau_h = a/v_A$, the poloidal Alfvén time of a plasma column of scale width a, and the magnetic field to some standard measure B_0 has been performed. It is worthwhile to point out that the first term on the right hand side of Eq. (5) represents so called dynamo effect that may "reorganize" local current density and hence magnetic configuration including safety factor q profile through plasma motion.

In accordance with the parity of tearing mode structure, assuming the perturbation potentials

$$\phi = \sum_{m=1}^{\infty} \bar{\phi}_m(x,t) \sin(mky), \tag{7}$$

and

$$\psi = \delta\psi(x,t) + \sum_{n=1}^{\infty} \bar{\psi}_n(x,t) \cos(nky), \tag{8}$$

we obtain the following coupled nonlinear equations for the first harmonic perturbation,

$$\frac{\partial \delta\psi}{\partial t} = -\frac{k}{2}(\frac{\partial \bar{\phi}_1}{\partial x}\bar{\psi}_1 + \bar{\phi}_1 \frac{\partial \bar{\psi}_1}{\partial x}) + \frac{1}{S}(\frac{d^2 \psi_0}{dx^2} + \frac{\partial^2 \delta\psi}{\partial x^2}) - \frac{1}{R}(\frac{d^4 \psi_0}{dx^4} + \frac{\partial^4 \delta\psi}{\partial x^4}) + E' \tag{9}$$

$$\frac{\partial \bar{\psi}_1}{\partial t} = -k\bar{\phi}_1(\frac{d\psi_0}{dx} + \frac{\partial \delta\psi}{\partial x}) + \frac{1}{S}(\frac{\partial^2 \bar{\psi}_1}{\partial x^2} - k^2 \bar{\psi}_1) - \frac{1}{R}(\frac{\partial^4 \bar{\psi}_1}{\partial x^4} - 2k^2 \frac{\partial^2 \bar{\psi}_1}{\partial x^2} + k^4 \bar{\psi}_1) \tag{10}$$

$$\frac{\partial}{\partial t}(\frac{\partial^2 \bar{\phi}_1}{\partial x^2} - k^2 \bar{\phi}_1) = k(\frac{d\psi_0}{dx} + \frac{\partial \delta\psi}{\partial x})(\frac{\partial^2 \bar{\psi}_1}{\partial x^2} - k^2 \bar{\psi}_1) - k(\frac{d^3 \psi_0}{dx^3} + \frac{\partial^3 \delta\psi}{\partial x^3})\bar{\psi}_1. \tag{11}$$

3

3.   Numerical Results

Equations (10-13) are solved as an initial value problem - E' is chosen such that the equilibrium does not dissipate due to resistivity and viscosity.

For the magnetic field, we employ the configuration used in Ref. 6,

$$B_{0y}(x) = 1 - (1 + b_c)\text{sech}(\zeta x), \tag{12}$$

where

$$\zeta x_s = \text{sech}^{-1}[1/(1 + b_c)]. \tag{13}$$

The constant b_c is chosen such that $B'_{0y}(x_s) = \pi/2$. The resistivity and the viscosity are both assumed to be constant. The initial conditions for $\bar{\psi}_1$ and $\bar{\phi}_1$ are the linear eigenfunctions multiplied with a small number and $\delta\psi(t = 0) = 0$.[6] The boundary conditions are $\delta\psi(x) = \partial\delta\psi/\partial x = 0$, and the values provided by the initial conditions such as $\bar{\psi}_1(x) = 0$, $\bar{\phi}_1(x) = \partial\bar{\phi}_1/\partial x = 0$ for $x = \pm x_w$. The chosen parameters are $k = 0.25$, $R = 10^5$, $S = 9.4 \times 10^5$, $b_c = 0.233509$, $x_w = 4$, $\zeta = 2.68298$ corresponding to two rational surfaces at $x = x_s = \pm 0.25$. The results are checked to be independent of x_w, the grid size and the time-step. Total 1001 grid points are used in the simulation domain $[-x_w, +x_w]$ and time-step is 5×10^{-4} for the results given below.

The magnetic energy

$$E_m = \frac{1}{8\pi} \int (B_x^2 + B_y^2)dxdy = \frac{1}{8\pi} \int [(k\bar{\psi}_1 \sin ky)^2 + (\frac{\partial\psi}{\partial x})^2]dxdy, \tag{14}$$

and the kinetic energy

$$E_k = \frac{1}{2}\rho \int (v_x^2 + v_y^2)dxdy = \frac{1}{8\pi} \int [(k\bar{\phi}_1 \cos ky)^2 + (\frac{\partial\bar{\phi}_1}{\partial x} \sin ky)^2]dxdy, \tag{15}$$

as functions of time are given in Figs. $1(a)$ and (b). Here, the magnetic field is normalized to $B_{0y}(\pm\infty)$, while in the final expression of E_k the velocities are measured in units of the poloidal Alfvén velocity. It is clearly shown that the magnetic energy released in the reconnection process converts to kinetic energy and can drive large flows in the first stage of the mode development. Then the energy bounces back and forth between magnetic and kinetic for a couple of times with decaying amplitudes and finally goes into a stage when both the kinetic and magnetic energy keep approximately constant. The perturbed magnetic energy in harmonics $m = 0$ and 1 as functions of time is given in Fig. $1(c)$. It is clearly shown that the magnetic energy in harmonic $m = 1$, is higher than that in the harmonic

4

$m = 0$ for $t \leq 40$ that is the linear development stage. The latter grows rather fast after $t \sim 60$ and dramatically exceeds the former late.

In Fig.2, the profiles of (a) $\bar{v}_y = \partial \bar{\phi}_1 / \partial x$, and (b) $\bar{\psi}_1 = \bar{B}_x / k$ for $t = 100$, 200, 400 and 600 are presented. Two very important points emerge: 1) the amplitude of the poloidal velocity $\bar{v}_y$ reaches the level required by the condition for ITB formation,[8] and 2) the flow $\bar{v}_y$ remains at noticeable levels for $x \gtrsim 0.5$ where $\bar{B}_x$ is negligibly small. To make the latter clearer, shown in Fig. 3 are the profiles of $\bar{B}_x$ (the line with open circles) and $\partial \bar{v}_y / \partial x$ at t=100. It is clear that there is noticeable value of velocity shear at the boundaries of the magnetic islands, where the radial component of the magnetic field approaches zero.

Shown in Fig. 4 are the profiles of $B_{y0}(x)$ including both the equilibrium and $\delta \psi$ induced components at t=0, 100, 200, 400 and 600. There are two resonant surfaces, $B_{y0}(x) = 0$, at $x = \pm 0.25$ for t=0. Late, the profile evolves complicatedly as the tearing mode develops and reaches a shape where there are no resonant surfaces approaching full reconnection, finally. This is an idealized reconnection process and may not be true in a real system there are plasma heating and thermal transport that contribute to the evolution of the equilibrium configuration. However, this clearly show the reason for the evolution of energy partition presented in Figure 1.

4. Conclusions and Discussion

The electron viscosity mediated double tearing mode is shown to generate localized shear flows in plasma configurations with non-monotonic safety factor. Strong poloidal flow shear forms and leads to strong $\mathbf{E} \times \mathbf{B}$ sheared flows at island boundaries in the process of tearing mode development. The generated shear flows bear such striking qualitative and quantitative similarity to the flows that accompany ITB formation (located in the proximity of low order rational surfaces, and just outside the magnetic islands). This may provide a new physics understanding of how ITB trigger might be associated with low integer values of q and suggest that boundaries of an island represent transport barriers.

It has been pointed out that $\mathbf{E} \times \mathbf{B}$ shear flow may be generated by a variety of mechanisms.[1] The very stimulating observation that may provide supporting evidence for the new mechanism proposed in this work is that two radially separated ITBs simultaneously exist and follow the two $q = 2$ surfaces in a section of JET discharge pulse 51573.[5] Moreover, it is confirmed that the ITBs are terminated by an $m = 2$ MHD mode which extends from the inner to the outer foot point location of the two ITBs. This is precisely the defining theoretical characteristic of the proposed double tearing mode. One of the most striking points of

the experiments relevant to the model proposed in this work is that the onset of the double ITB structure exactly coincides with the onset of MHD activities that finally terminate the structure (See Fig. 8 of Ref. 5). These observations seem to support the thoughts proposed in this work.

ITBs occur under various conditions depending on interplay between mechanisms driving and suppressing plasma turbulence. The main driving mechanisms have been identified as gradients of plasma parameters such as density, velocity and temperature. Among them, ion and electron temperature gradients are the most plausible candidates. The major suppressing mechanisms are magnetic shear and $\mathbf{E} \times \mathbf{B}$ velocity shear. Therefore, ITB formation mechanism may be different under different discharge conditions due mainly to variation of generation mechanism of $\mathbf{E} \times \mathbf{B}$ sheared velocity layer. The mechanism proposed in this work is relevant only in plasmas with non-monotonic q profiles and appropriate parameters. At this stage there is no unique nor universal mechanism. Further theoretical and experimental studies in more detail are certainly needed for full understanding of the mechanisms.

Acknowledgements

References

1. Diamond P H, Itoh S-I, Itoh K, and Hahm T S, Plasma Phys. Control. Fusion, 2005, 47: R35.

2. Wolf R C, Plasma Phys. Control. Fusion, 2003, 45: R1.

3. Connor J W, Fukuda T, Garbet X, *et al.* Nucl. Fusion, 2004, 44: R1.

4. Jofrrin E, Challis C D, Conway G D, *et al.*, Nucl. Fusion, 2003, 43: 1167 and the references therein.

5. Jofrrin E, Gorini G, Challis C D, *et al.*, Plasma Phys. Control. Fusion, 2002, 44: 1739.

6. Dong J Q, Mahajan S M, Horton W, Phys. Plasmas, 2003, 10: 3151.

7. Dong J Q, Mou Z Z, Long Y X, Mahajan S M, Phys. Plasmas, 2004, 11: 5673.

8. Mahajan S M, Yoshida Z, Phys. Plasmas, 2000, 7: 635.

Figure Captions

1. The (a) magnetic energy, $(b)E_k$, kinetic energy E_m, and (c) energy in harmonics $m = 0$ and $m = 1$, E_{m0} and E_{m1}, versus time.

2. The profiles of (a) $\bar{v}_y$, (b) $\bar{\psi}_1$ at $t = 100$, 200, 400, and 600.

3. The profiles of (a) $\bar{B}_x$ and $\partial \bar{v}_y / \partial x$ at t=100.

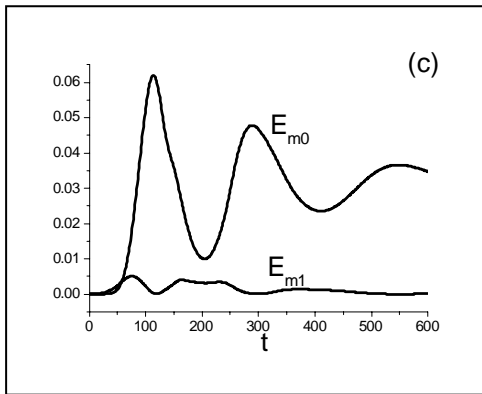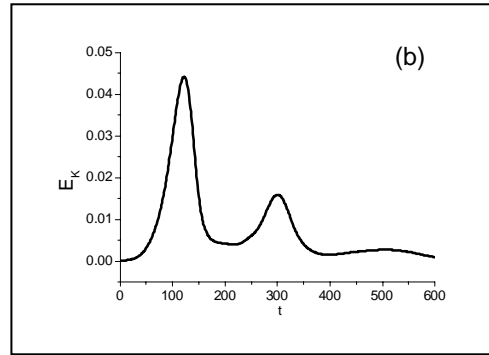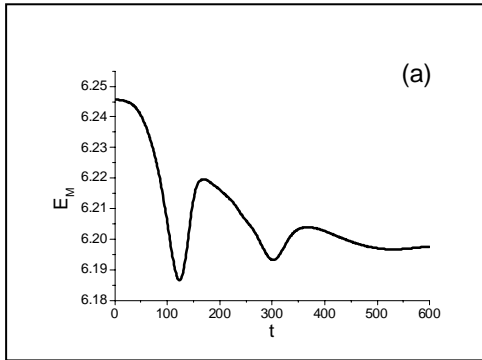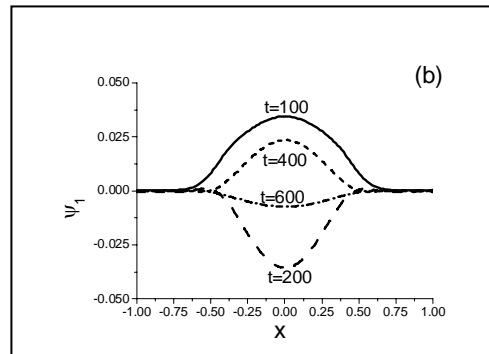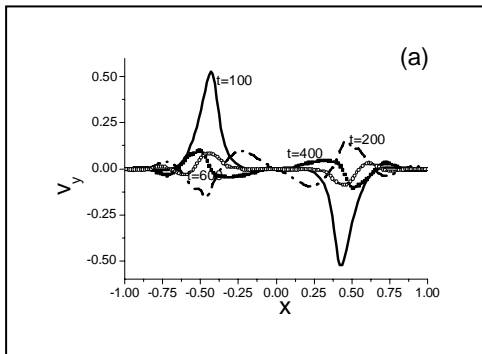4. The profiles of B_{y0} at $t = 0$, 50, 100, 200, 400, and 600.
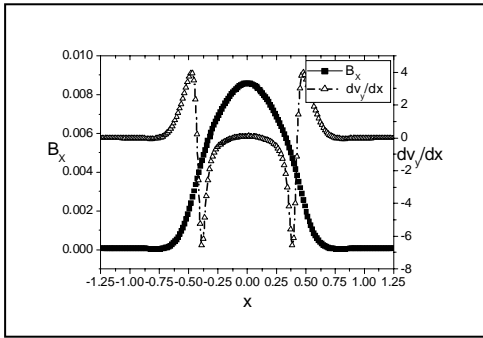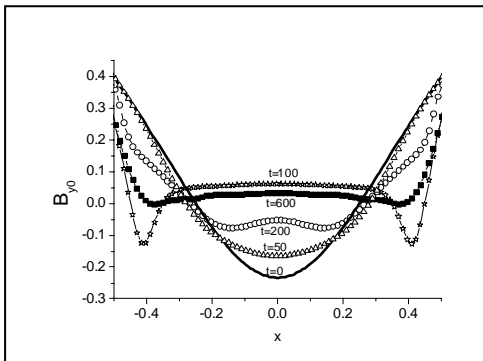
Fig1

Fig2

Fig3

Fig4

Magnetic islands observed by a fast-framing tangentially viewing soft X-ray camera on LHD and TEXTOR

S. Ohdachi, K. Toi, G. Fuchs[1], TEXTOR Team[1] and LHD Experimental Group

National Institute for Fusion Science, Toki 509-5292, Gifu, Japan

[1] Institut für Plasmaphysik, Forschungszentrum Jülich GmbH,
EURATOM Association, D–52425 Jülich, Germany

August 5, 2005

Abstract

The formation of magnetic islands within plasmas confined magnetically within tori does have significant influence upon their confinement and stability. To obtain experimental insight into the formation and dynamics of such island structures we employed a fast framing camera viewing the plasma tangentially in toroidal direction. The toroidal viewing direction does give the advantage that the islands are viewed almost tangentially and this does greatly ease the reconstruction of the local data from the line integrated ones. We discuss an effective method to do this inversion. To study the fluctuations seen in the video images we perform a singular value decomposition, afterwards we use a truncated least square method to infer their picture in space.

Keywords: magnetic island, fluctuation measurement, tomography

1 Introduction

The generation and evolution of magnetic islands within magnetically confined plasmas is of considerable interest. Magnetic islands play an important role in the confinement and stability of fusion plasmas. For example, the neo–classical tearing mode grows from seed islands being produced by small perturbations, and may finally limit the performance of tokamak plasmas. A tangentially viewing soft X-ray camera is suitable to study the dynamics of such magnetic islands. As the magnetic islands are formed around rational surfaces along undisturbed magnetic field lines, they can be visualized better when they are observed tangentially. Thereby, we can study the evolution of structures of islands with better spatial resolution. Nevertheless, the data analysis for this kind of systems is not straightforward. Within the paper we describe a method to resolve structures inside the plasma as magnetic island from the experimentally observed emission and the fluctuations on it.

First, a tangentially viewing soft X-ray camera system, which can measure fluctuation phenomena, is described. Then we briefly introduce the method of singular value decomposition (SVD) on 2–D data. We can thereby decompose, both in time and in space, the sequence of images into orthogonal components; this eases the interpretation of the measured data. To analyze two–dimensional line–integrated data, we might proceed as follows; first we perform a tomographic reconstruction of the images, then we analyze the result with the SVD method. However, this requires much CPU power and it amplifies noise during the inversion process. Therefore, we adopt another strategy; first we make a SVD analysis, then we do reconstruction to arrive at the result. As SVD and Radon transform are both linear operations, they do commute and one can reconstruct the local pictures from the SV decomposed spatial patterns

(TOPOS) only [1, 2]. Finally, we will discuss the inversion technique using the experimental data obtained in 3/1 mode DED experiments on TEXTOR tokamak [3] and sawtooth-like relaxation phenomena in the LHD.

2 Camera system

The fast–framing tangentially viewing soft X–ray camera system [4] has been developed by the National Institute for Fusion Science and the TEXTOR group. It has been installed, both on the Large Helical Device (R = 3.9m, $< a > = 0.6$m) and TEXTOR tokamak (R=1.75m, a = 0.46m). It is basically a pinhole camera (see, Fig. 1). The radiation from the plasma is converted to a visible one using a scintillator screen (CsI(LHD) / P47(TEXTOR)). Converted images are guided outside the strong magnetic field by use of a fiber array and then intensified by an electron–beam type image intensifier. They are then recorded by a fast-framing video camera system. The system can record soft X-ray (E > 1keV) images of the plasma with a framing rate up to 20kHz.

3 Data analysis using singular value decomposition

In order to study fluctuations, especially to investigate coherent MHD modes, one might e.g. use fast Fourier transforms FFT to decompose signals into trigonometric functions. In our case the SVD (singular value decomposition) method dose give the advantage that it decomposes the signal into space and time like functions, which are adapted to the processes under investigation [5]. Using SVD, a matrix A made up of n time series of m frames is decomposed into three matrices U, V and W, the latter being diagonal, such that $A = UWV^t$. The columns of U and V^t are spatial and temporal orthogonal vectors and are called Topos and Chronos, respectively. A time series a_i can be written by a combination of orthogonal components of the Topos and the Chronos type

$$a_i = w_1 \times v_{i1} \times u_1 + w_2 \times v_{i2} \times u_2 + \cdots + w_m \times v_{im} \times u_m. \tag{1}$$

Here, w_i is a diagonal components of W and w_i^2 is a measure of the contribution from a particular component to the total fluctuation power. In practice, a few of the larger components suffice to describe the nature of the fluctuations, meaning that we may interpret the data using a small number of orthogonal components only. Trigonometric functions, which is used in FFT based analysis as a base function, often do not describe well signals from real experiments, e.g. for internal relaxations like sawteeth on tokamaks.

The advantage given by the SVD method shows up in an example giving the sawtooth crash in TEXTOR (Fig. 2). The meaning of the each component is obvious; the component 0 shows the stationary plasma radiation, the component 1 shows sawtooth relaxations. From Topos (C1), the movement of the radiation profile from the core to the edge at the event can be seen. From component 2–4, oscillations having a poloidal mode number m = 1 together with the sawtooth crash can be seen.

4 Tomographic reconstruction

From one tangential view of the plasma only, it is not possible to reconstruct a three–dimensional radiation profile. We try to reconstruct the radiation profile at a poloidal plane from the line–integrated images, by assuming that there are symmetries in the plasma, sight lines can be projected onto that plane. In this way, we can make use of various sophisticated method developed for the reconstruction of usual 2–D tomography. From the nature of the magnetically confined plasma, two kinds of asymmetry are candidates. One is the toroidal asymmetry, which works if it comes to reconstruct images in tokamks with closed flux surfaces (e.g. Fig.2 (C0)). Another assumption could be that the radiation is constant

along the magnetic field lines. Since the wave number along the magnetic filed is small for most instabilities, this assumption could be used for the reconstruction of fluctuating components (e.g. Fig. 2 (C2)–(C4)).

A column vector $S(S_i = 1, 2, \ldots, M)$ representing measured signals or Topos can be expressed as a linear combination of the radiation profile E ($E_i = 1, 2, \ldots, K$) and the residual error vector e,

$$S = LE + e. \tag{2}$$

The matrix L gives a geometric weight along the lines of sight (M×K)) (Fig. 3). We assume that the magnetic disturbances are small and the field lines encountered along the lines of sight are (almost) tangent to undisturbed surfaces. These flux surfaces are circular and they are shifted by $\Delta = \Delta_0(1 - \rho^2)$, ($\rho = r/a$) for the TEXTOR case. Then all elements along a line of sight can be mapped to elements in a reference poloidal plane (P2 in Fig.3); note that this mapping modifies the weight L. We assume the q–profile to be, $q(\rho) = \rho^2/(1 - (1 - \rho^2)^{(q_a+1)}) q_a$. In this study, M ~2500 (effective channels looking at plasma within 64 ×64 pixels in the detector) and K ~ 550 (pixels where the line of sight penetrate within the poloidal cross section divided by 32× 32). The lines of sight at P2 are shown in Fig.4. In Fig. 4(A) toroidal asymmetry is assumed, constant radiation along the magnetic field is assumed in Fig. 4(B).

In a Heliotron-type device like LHD the flux surfaces do not have toroidal symmetry. We take the flux surfaces as calculated from the equilibrium code VMEC. The shape of k-th magnetic surface is then written as,

$$
\begin{aligned}
R &= \sum_{i=1}^{max-mode_k} R_{ki} \times \cos(\alpha_i), \\
Z &= \sum_{i=1}^{max-mode_k} Z_{ki} \times \sin(\alpha_i), \\
&(\alpha_i = \theta \times M_i - \phi \times N_i).
\end{aligned}
\tag{3}
$$

Here ϕ is the toroidal angle and θ is the poloidal–like angle in toroidal geometry. The average minor radius ρ_k is given as well. Since we give a series expansion, it is not easy to determine θ from R and Z, which is needed to estimate the magnetic field lines being tangent to the flux surfaces. We determine ρ and θ iteratively by the Newton method. Let the initial estimate of ρ and θ be ρ_0 and θ_0, respectively. R_0 and Z_0 are then calculated by Eq.(3).

$$
\begin{pmatrix} \frac{\partial R}{\partial \rho} & \frac{\partial R}{\partial \theta} \\ \frac{\partial Z}{\partial \rho} & \frac{\partial Z}{\partial \theta} \end{pmatrix} \begin{pmatrix} \Delta\rho \\ \Delta\theta \end{pmatrix} = \begin{pmatrix} R - R_0 \\ Z - Z_0 \end{pmatrix}
\tag{4}
$$

ρ and θ are iterated using $\Delta\rho$ and $\Delta\theta$, which are solutions of Eq. (4). After three to four steps, the result is satisfies the numerical requirements. We perform this search for all line elements along the sight lines. Two examples of the sight lines for different plasma beta are show in Fig. 5. Note that at the core region, the shape of the flux surface cannot be calculated for the numerical reasons. The geometrical weight matrix L (M×K)) is not very accurate near the magnetic axis.

Since tomographic reconstructions are ill–posed problems, the least square solution of equation (2) is rather unstable; therefore we need some smoothing mechanism or regularization. Phillips-Tikhonov (PT) type regularization[6] is used to solve Eq. (2). In this scheme, minimization of

$$Q = \gamma \sum |CE|^2 + \frac{1}{M} \sum |S - LE|^2. \tag{5}$$

is considered rather than minimizing $\sum |S - LE|^2$ itself. The matrix C acts as Laplacian operator. The first term of the Eq. (5) decreases when the radiation profile is smoothed; parameter γ acts as the control parameter of the profile smoothness.

After the matrix $C^{-1}L$ is SV decomposed as UWV^t,

$$E(\gamma) = \sum_{j=1}^{p} w_j(\gamma) \frac{\boldsymbol{u}_j \cdot S}{\sigma_j} (C^{-1}\boldsymbol{v}_j). \qquad (6)$$

E is now written as a combination of orthogonal patterns $C^{-1}\boldsymbol{v}_j$ (Fig. 6(B)) with weighing factors $w_j(\gamma) = 1/(1 + M\gamma/\sigma_j^2)$. w_j is a decreasing function of j (Fig. 6(A)) and the destabilizing effect due to small–scale structures (higher j components) is suppressed by a proper choice of γ. It is similar to the Fourier–Bessel expansion method [7]. However, the base function for the expansion is determined automatically by the arrangements of the sight lines of the camera system in this method.

We present several results, showing island-like structures, both, from experiments on the TEXTOR tokamak and on the LHD. A dynamic ergodic divertor (DED) has been implemented on TEXTOR tokamak to control the heat fluxes in the edge region. The DED coil system is located on the high-field side of TEXTOR; external perturbation fields with poloidal / toroidal mode numbers m/n = 12/4, 6/2, 3/1 can be applied. When a co-rotating (1kHz) 3/1 perturbation field, which penetrates deeper into the plasma than a 12/4 field, is used, a rotating structure with the same frequency as the applied field is detected by our camera. Four SVD components are shown in Fig.7. The first two Topos (B0, B1) represent the global change of the whole plasma shape. Aside a phase shift, Chronos A2, A3 are synchronous with the external DED coil currents. For Topos B2, B3, we observe that it is a rotating structure. Reconstructed images of TOPOS B2 and B3 are shown in C2, C3. There are m = 2 structures around $\rho \sim 0.4$ in both components; which is consistent with the mode–number analysis using magnetic probe arrays. The radial width of these structure is about 10 ~ 15 % of the minor radius. Precise adjustment of the flux surface is required in this reconstruction. Here, reconstruction of the TOPO B0 is done at first assuming toroidal asymmetry. From the peak position of the reconstructed image, we determine the position of the magnetic axis. Reconstruction of the fluctuating components is done with the improved magnetic surfaces. Beside the m = 2 structures, we can see m = 3 structures (outboard side, bottom). However, ghost images are often observed near the outboard side, this holds even for the test image, when we reconstruct images with an inaccurate current profile. In order to prove the co–existence of the m = 3 modes, further work is needed to evaluate the error in the reconstruction. In LHD, sawtooth-like re-laxation phenomena have been observed near various rational surfaces, e.g., ι = 1/2, 2/3, 1/1 when the pressure gradient exceeds a threshold value. Islands like structures are observed during these relaxation events. In the LHD case, we identify the magnetic axis by the peak of the electron temperature profile as measured by the Thomson scattering. Two examples showing m = 1 and 3 structures are shown in Fig.8. We could successfully invert the image up to m = 3 perturbations. In summary, the data analysis using singular value decomposition has proven to be effective to extract fluctuating components from our video data and to reconstruct the local emission. Thereby we have to know the magnetic field in good approximation in order to be able to do the inversion. If these assumptions are met the reconstructed images do make sense.

5   Ackknowledgement

References

[1] G. Fuchs, Y. Miura, and M. Mori, Plasma Phys. Control. Fusion **36**, 307 (1994).

[2] S. Ohdachi, K. Toi, G. Fuchs, and LHD experimental Group, Proceeding of 14th Stellarator workshop http://www.ipp.mpg.de/eng/for/veranstaltungen/workshops/stellarator_2003/papers/papers_pdf/Ohdachi_076_SWS.pdf (2003).

[3] K. H. Finken, Nucl. Fusion **37**, 583 (1997).

[4] S. Ohdachi *et al.*, Rev. Sci. Instrum **74**, (2003).

[5] C. Nardone, Plasma Phys. Contol. Fusion **34**, (1992).

[6] N. Iwama *et al.*, Appl. Phys. Lett. **54**, 502 (1989).

[7] Y. Nagayama, J. Appl. Phys. **62**, 2702 (1987).

List of Figures

Figure 1: Sketch of the camera system.
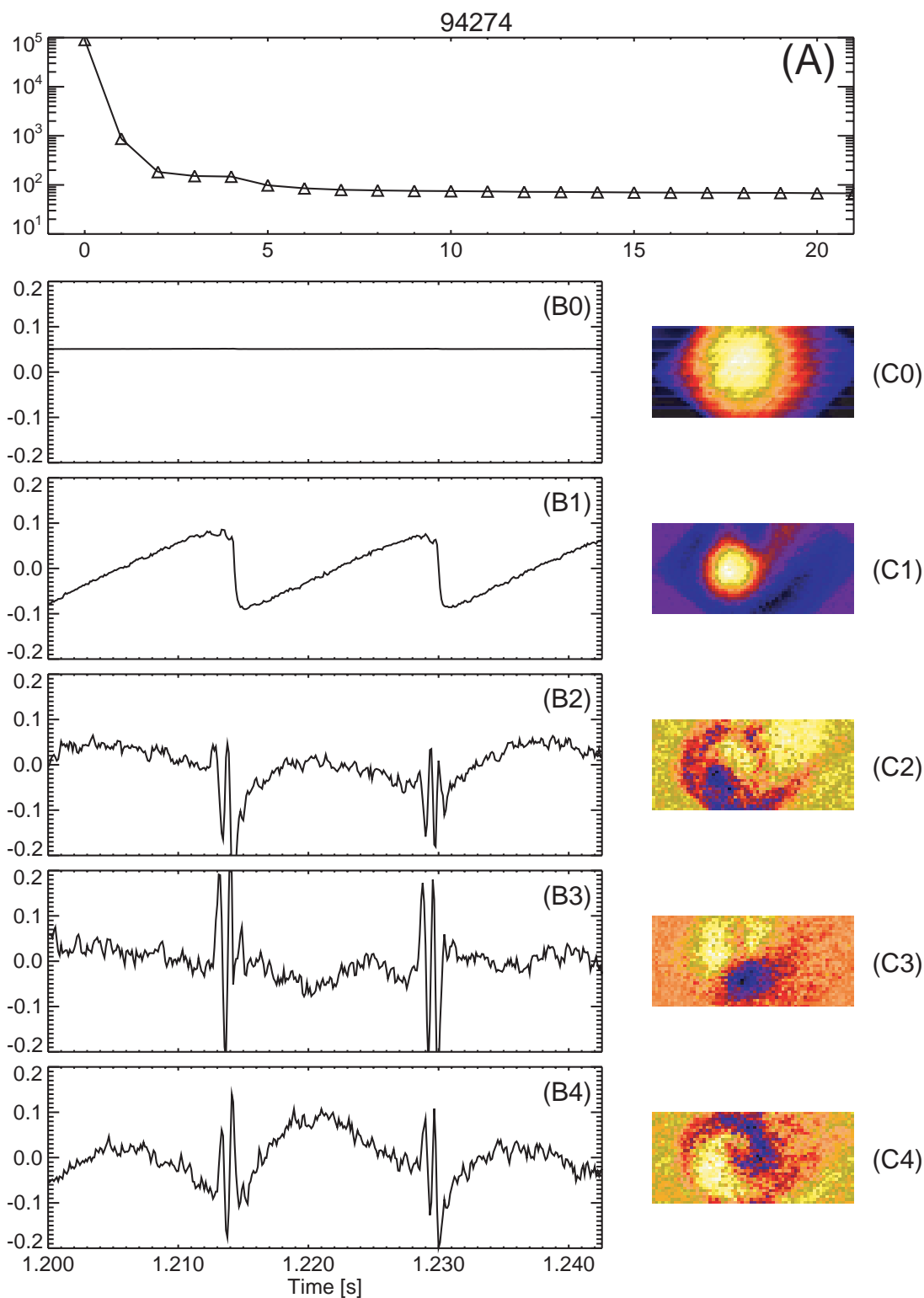
Figure 2: An example of singular value decomposition of the raw video image is shown. In Fig. (A), singular values w_i are shown. In Fig (B0) ~ (B4), time domain components (CHRONOS) are shown. In Fig(C0) ~ (C4), spatial structure (TOPOS) corresponding to (B0) ~ (B4) are shown.
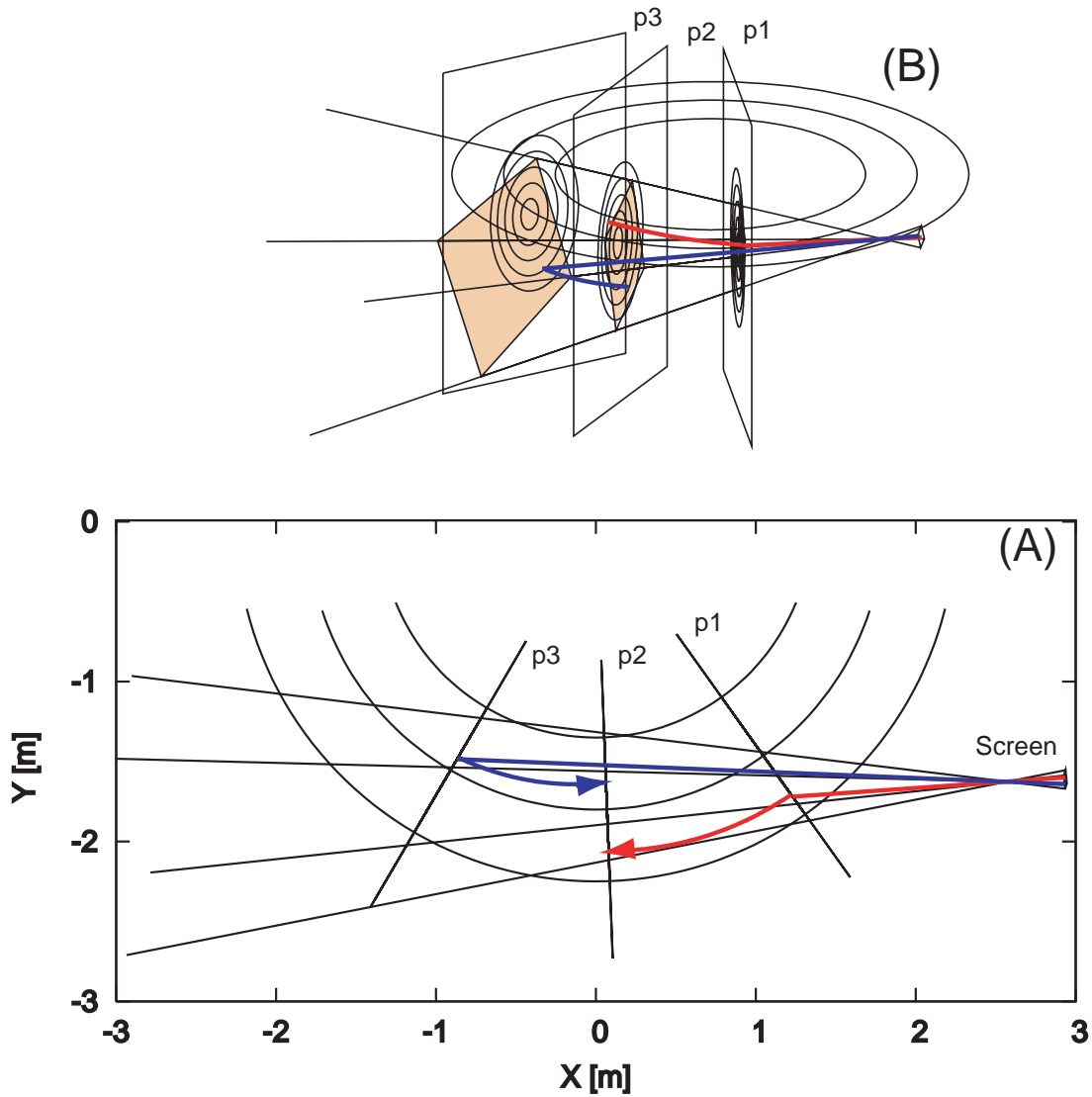
Figure 3: Geometry of the tangentially viewing camera system on TEXTOR. On the equatorial plane (A) and the bird-view diagram (B) are shown. Red and blue lines are drawn to show how the pixels on sight lines at plane P1 or P3 are mapped to the pixels on P2.
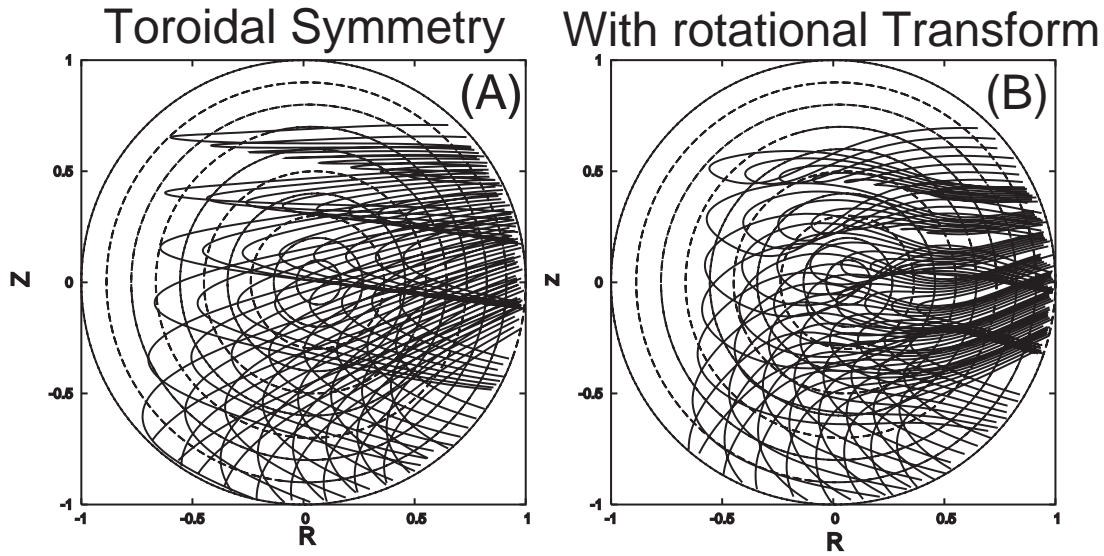
Figure 4: Projection of the sight lines onto a poloidal cross section shown in P2 in Fig. 3.
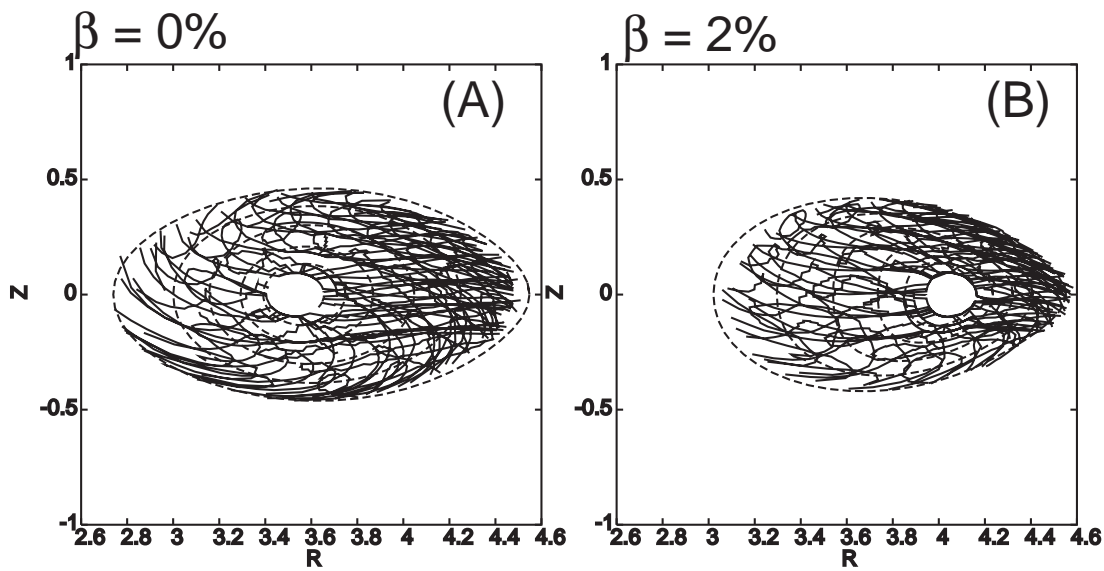
Figure 5: Projection of the sight lines on to a horizontally elongated cross section in LHD. Magnetic axis $R_{ax} = 3.6m$. Averaged beta 0.0% (A) and 2.0% (B) are assumed in the equilibrium calculation, respectively.
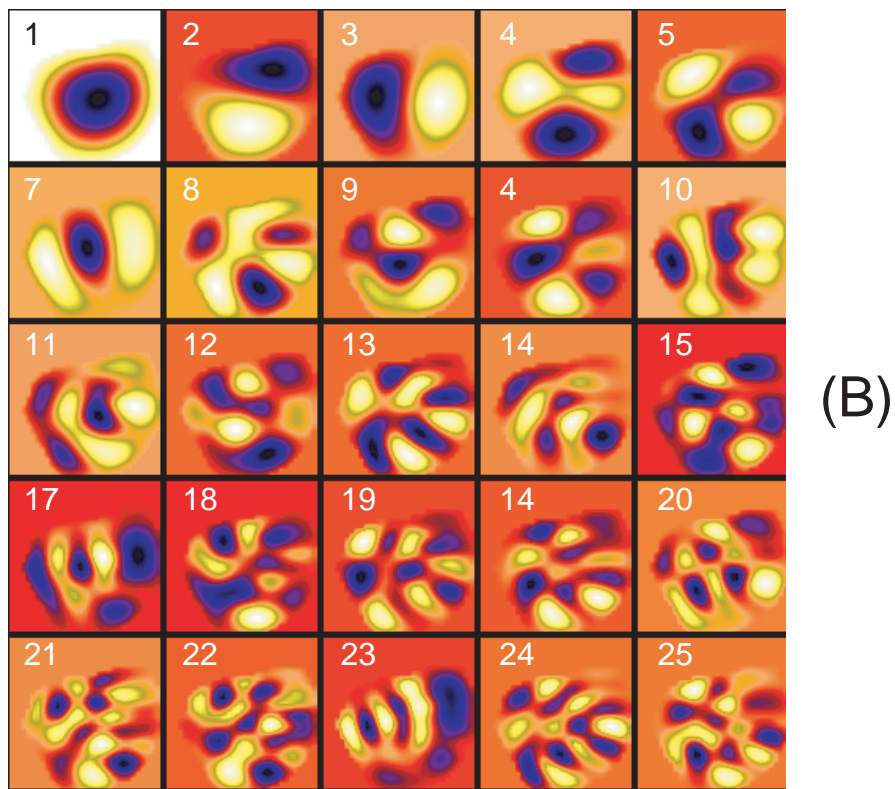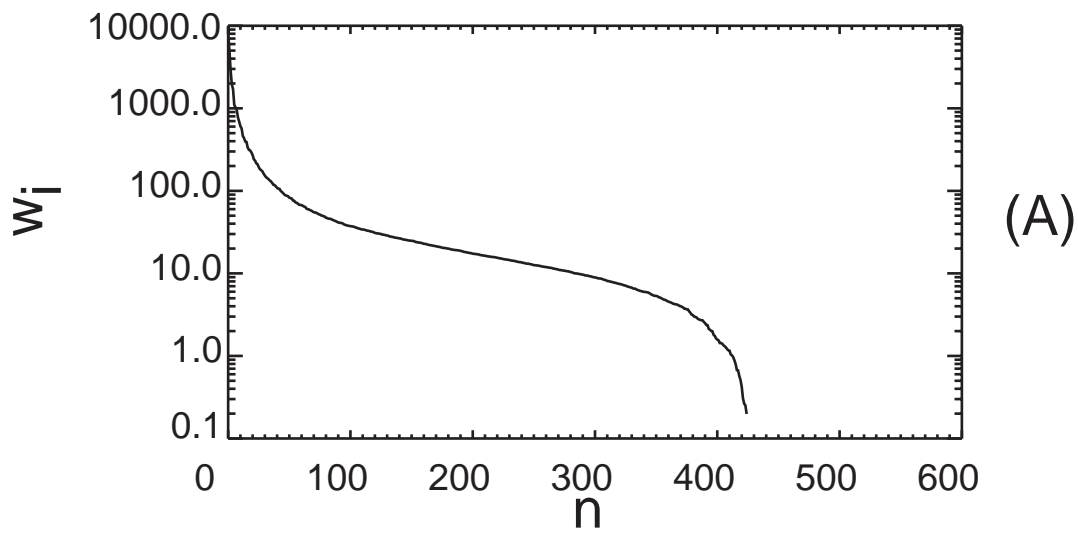
Figure 6: Singular values of the geometrical functions (A) and the first 25 of the eigen functions (B).
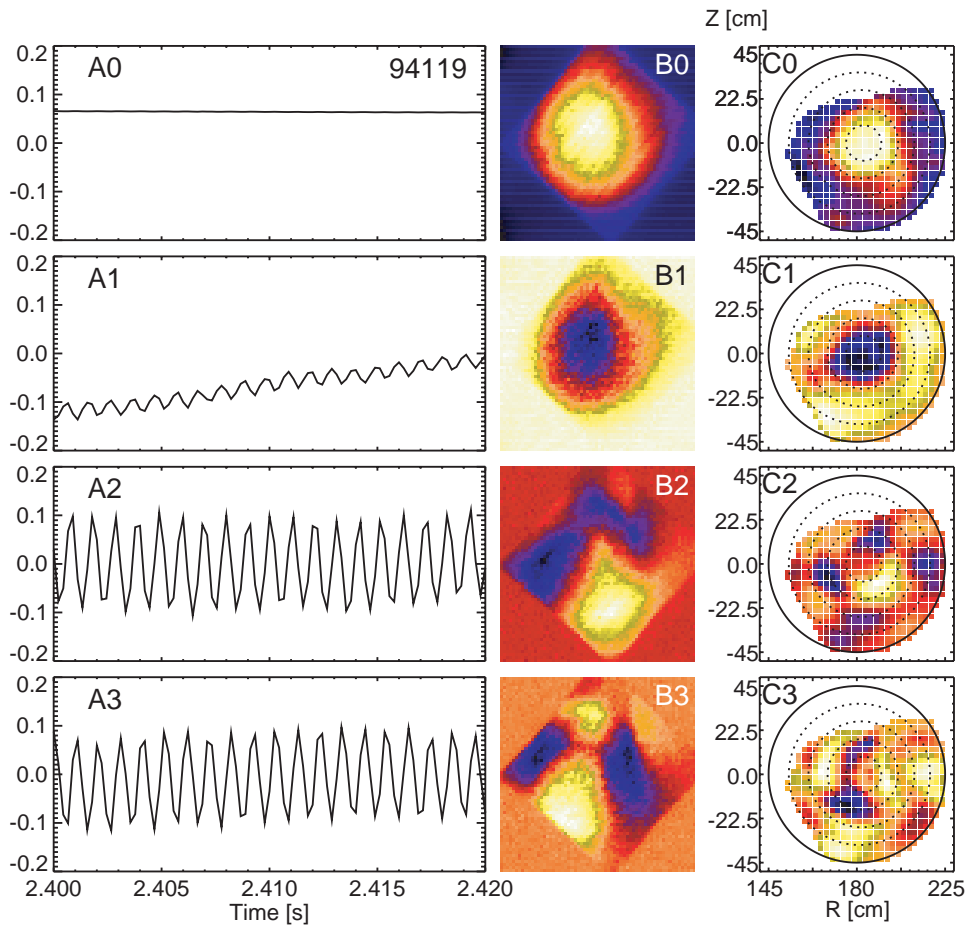
Figure 7: Singular value decomposed CHRONOS (A), TOPOS (B) and the reconstructed image of TOPOS (C) are shown.

(A1)

(B1)

(A2)

(B2)
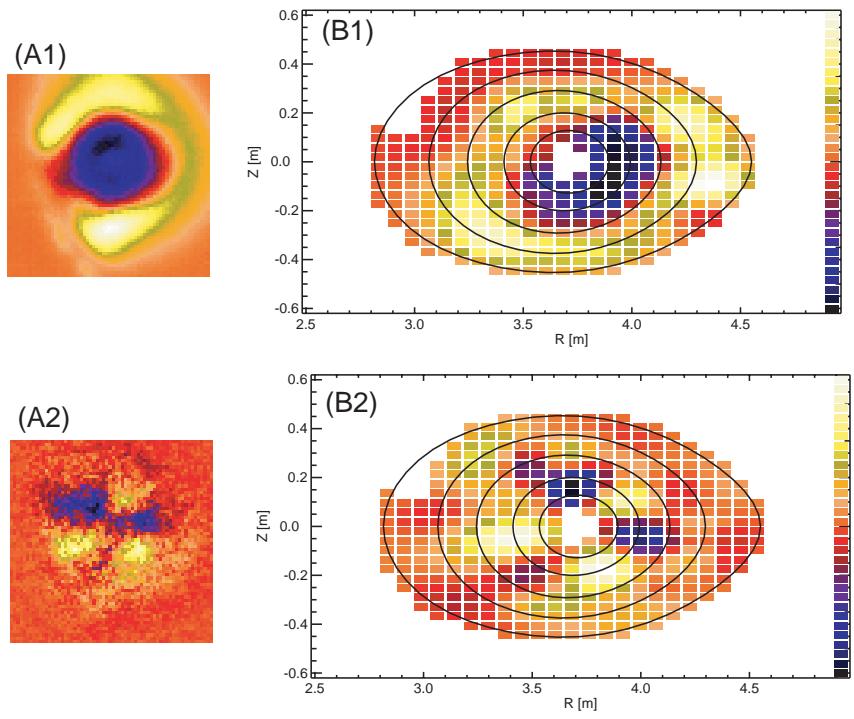
Figure 8: Singular value decomposed TOPOS (A) and the reconstructed images (B) are shown.

Tomographic analysis of central MHD activities and radiation losses on the HL-2A and LHD

Y. Liu[1], B.J.Peterson[2], Dong Yunbo[1],Y. D. Pan[1]

[1]Southwestern Institute of Physics, Chengdu, China

[2]Institute of Advanced Energy, Kyoto University, Japan

ABSTRACT: Results of the two-dimensionally reconstructed distribution of soft X-ray emission in HL-2A and electromagnetic radiation in LHD are presented. Hardware improvements of in-vessel soft X-ray cameras and the development of tomography software have made detailed and visual studies of soft X-ray emission possible in HL-2A. Several algorithms are employed in order to get as much detail as possible in the images while keeping any guiding assumptions to a minimum. Recently we have succeeded in applying a 2D peeling away algorithm for tomographic reconstruction of LHD bolometry data jointly under the China-Japan collaboration. The data analysed so far have been used to study MHD instabilities on HL-2A tokamak and radiation losses on LHD.

1. Introduction

Central MHD activities are routinely observed in tokamaks and can be analysed through soft X-ray tomographic reconstruction techniques. In the measurement of total radiation emission, more details about emissivity profiles will be revealed by a tomographic analysis. A tomographic algorithm taking magnetic flux surfaces into account has been developed to reconstruct an emission image from line-integral measurements. Improvement of the quality of reconstructed images has been obtained using a feedback technique to compensate numerical errors. This tomography technique has been applied in soft x-ray measurements on HL-2A Tokamak and Heliotron J, and used for plasma radiation imaging on the Large Helical Device (LHD)[1] by using AXUVD (bolometer like semi conductive detectors) arrays [2].

In this article we describe the results of plasma emissivity reconstructions obtained from silicon photodiodes arrays on LHD.A modified 2D tomography reconstruction based on pixels is used to analyse radiation patterns on LHD and MHD activities on HL-2A. Section 2 describes the idea of tomographic techniques and a numerical test. Examples of the reconstruction results are shown in Sections 3 and 4. Section 5 contains a discussion.

2. Method used for soft X-ray and bolometric inversion

2.1 Division and expansion on the basis of vacuum flux surfaces

The basic principle of tomography is to reconstruct the emitted radiation from a plasma cross-section along a large number of collimated chord measurements. The reconstruction algorithm employed here is the so-called hybrid methods [3]. We divide the emitting region into annular areas on the basis of real magnetic flux contours. These annular areas can be considered as pixels, as shown in Fig.1. Line integrals $f(p_i, \varphi_i)$ can accurately be represented

by a summation of the contribution, g_k,

from each pixel along the line of sight

$$f(p_i, \varphi_i) = \int_{L_i} g(r, \theta) dL \approx \sum_k a_{ik} \cdot g_{k'}$$

(1)

where p is the distance from the origin to the origin to the tangential point of line of sight to the corresponding surface, the chord angle φ is the polar co-ordinate of the point of tangency. Equation (1) is equivalent to have chosen a series of piecewise linear functions to represent the detected signals. These functions vanish at the plasma boundary, i.e., they satisfy the basic requirement of
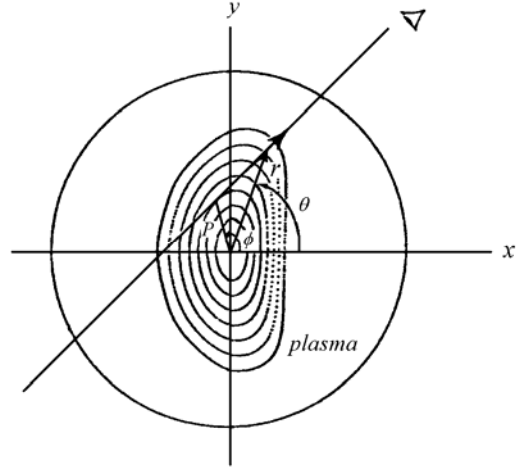
Fig.1. Co-ordinate system for reconstruction of a 2-D image. The emitting region can be divided into annular pixels with real

orthonormality in the same way as Bessel functions. The local emissivity in a pixel, g_k, can be solved by using a 'peeling away' technique given in Ref [4].

To model the variation of emissivity within a pixel in the angular direction, we expand the emissivity on each pixel in Fourier series. Then the local emissivity within a pixel is:

$$g_k = g_{k0} + \sum_m g_{km}^s \sin m\theta + g_{km}^c \cos m\theta \qquad (2)$$

The number of observation directions limits the number of Fourier modes. Higher modes as far as $\sin 2\theta$ mode are ignored if two existing arrays are used.

2.2 Feedback technique

To reduce the error and prevent the error from propagating into the inner pixel, we use a feedback technique to compensate for the error at each pixel. Since the Radon transform for emission (Eq.(1))is linear, if the inversion procedure is represented by the operator $\Re$, such that $g = \Re(f)$, the pseudo signals recalculated from the reconstructed emissivity function g' is given by $f' = \Re^{-1}(g')$, then:

$$g' - g = \Re(f') - \Re(f) = \Re(f' - f) \qquad (3)$$

This leads to a more accurate solution:

$$g = g' - \Re(f' - f) \qquad (4)$$

In other words, the difference between the measured and reconstructed line-integrated signals is fed back as an input data for the inversion process. If the reconstruction itself is stable, the feed back process makes the difference between experimental and reconstructed chord integrated data negligible. Moreover, a regularization of the matrix equation, through

$$\chi^2(\lambda) = \sum_i \frac{(f_i - A \cdot G)^2}{\delta_i^2} + \lambda \left\| \nabla^2 G \right\|_2^2$$

is performed, and the best Lagrangian parameter λ is chosen through the so-called Tikhonov L curve technique.

2.3 Numerical Test

The technique of the reconstruction is examined numerically using a perturbed structure. The source function has a circular hot spot over the flat region in the center [5]. Fig.2 shows the contour plot of the test source function and the hidden-line perspective plot of the reconstructed image for the case of small size hot spot ($r_{spot} \approx 10\%$ of r_s).
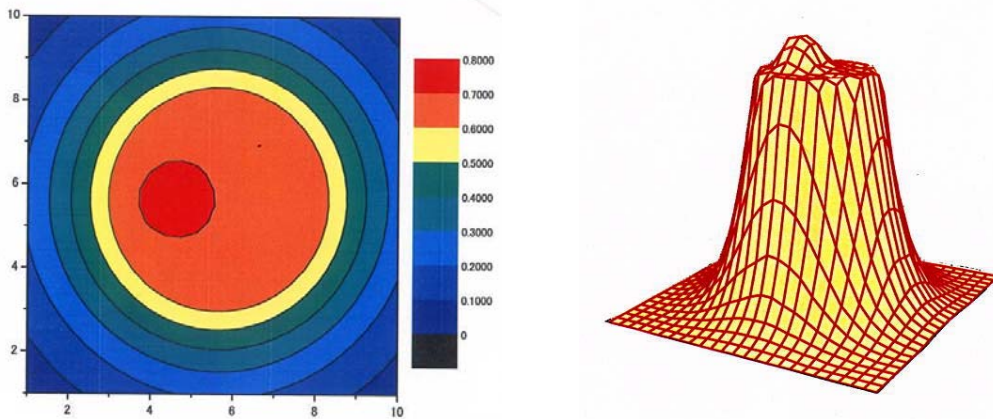
Fig.2. (a) Contour plot of the test source function and (b) surface plot of the reconstructed image.

2. Application of AXUVD measurement on LHD

Two AXUVD arrays (20 channels each) are installed on a semi-tangential cross-section in LHD as seen in figure3. These are used to provide a two-dimensional tomographic image of the plasma radiation at a high time resolution. Part of the emitting volume is only seen from the right side (4-O array). The plasma shape strongly depends on the magnetic axis position, R_{ax}. For smaller R_{ax}, the part not seen from above is bigger, which makes the tomography procedure more difficult. In addition, high spatial resolution requirement near the boundary, strong
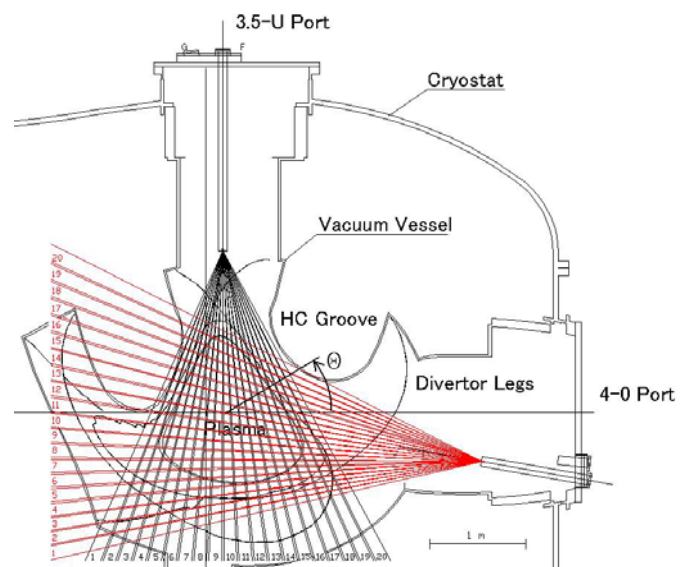
Fig.3. Lines of sight of the bolometric tomography on LHD.

poloidal asymmetries in radiation distribution and the far deviation from circular shape in the edge region create a serious challenge for the inversion technology.

The tomography algorithm described above provides reasonable two-dimensional profiles of plasma emission and a good agreement between experimental and simulated chord integrated emission for different conditions. Small differences between reconstructed and measured chord integrated profiles (4O array) are caused by reconstruction artifacts. Fig.5 shows the emissivity for the same discharge at the moment when the gas puffing is off.
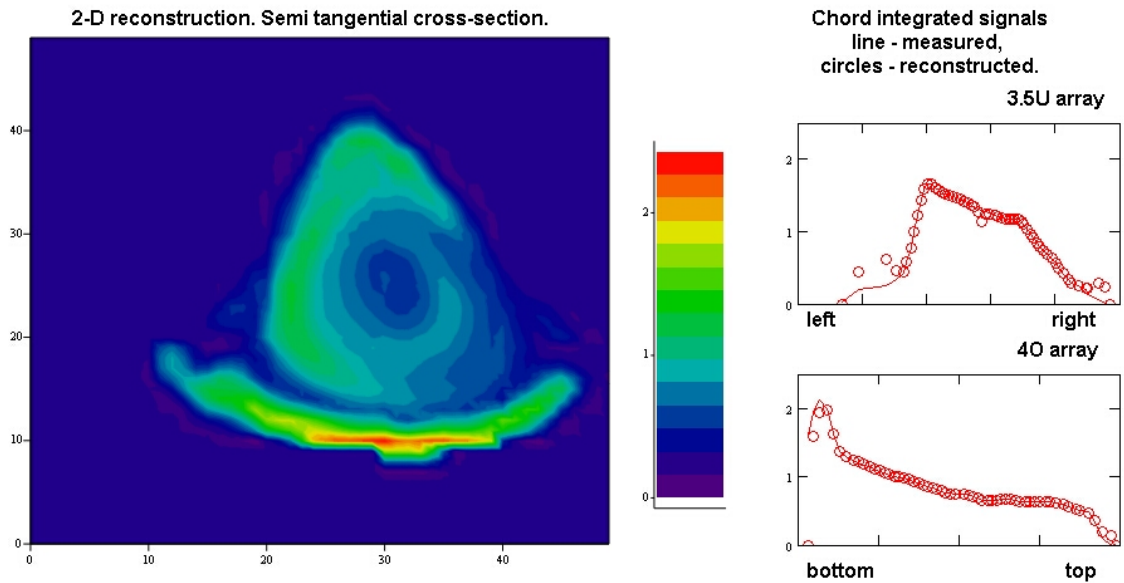
Fig. 4. 2-D bolometric emissivity profile reconstruction in Shot 31721 t=2 s. The bright region at the bottom is due to 3.5L gas puffing .
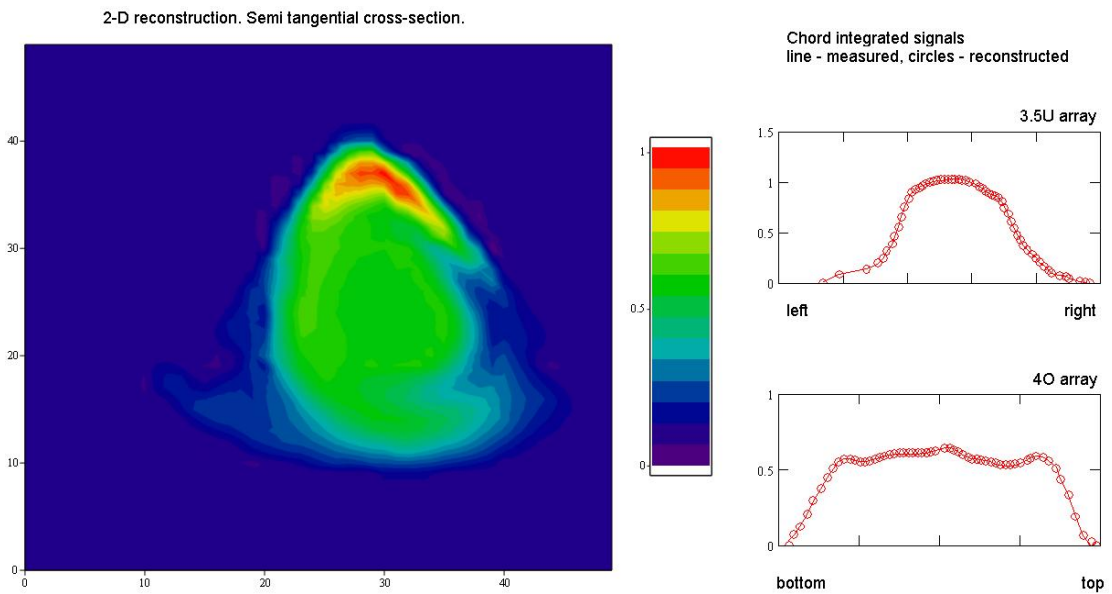
Fig.5 Emissivity for the same discharge at the moment when the gas puffing is off.

4.Application of Soft x-ray measurement on HL-2A

Five soft X-ray cameras are mounted on HL-2A, each viewing the plasma with 20 detectors allowing a spatial resolution of 2cm and a time resolution of $1\ \mu s$. A 25 μm Beryllium foil covers the SX camera. The X-ray imaging arrays on HL-2A are useful for studying several aspects of plasma behavior. For example, the high frequency response of the system provides an excellent means for examining fast magnetohydrodynamic (MHD) instabilities in the plasma, such as sawtooth oscillation and snake oscillation as well as fishbone oscillation. These instabilities are clearly manifested through changes in the soft X-ray signals because of their perturbations on the electron temperature, density, and impurity profiles. A further use of the soft X-ray imaging system is the tomographic reconstruction of the plasma soft X-ray emissivity from poloidal sets of X-ray brightness profiles.

Just before the crash the well-known m=1 precursor is present. The m=1 precursor is mainly present at the central channels. The data of Fig.7 a are plotted three-dimensionally in Fig.7b. The onset and the growth of the m=1 mode can be seen clearly.
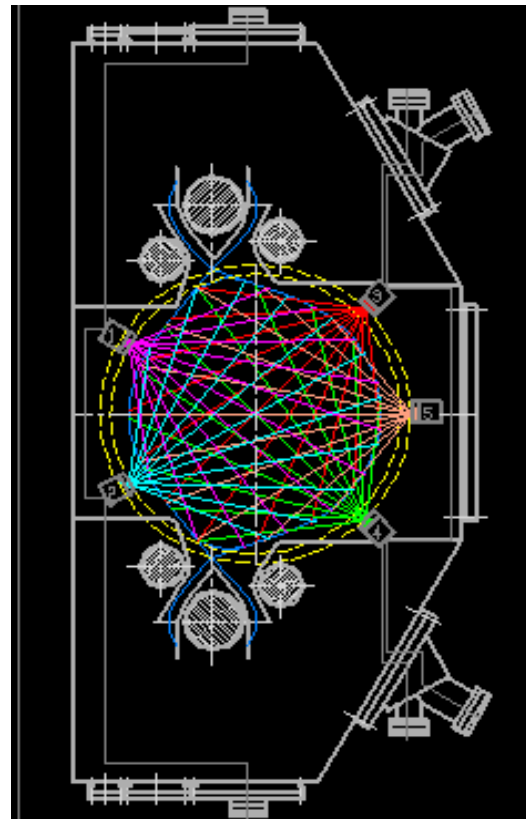
Fig.6. Arrangement of soft X-ray detector arrays on the HL-2A tokamak.
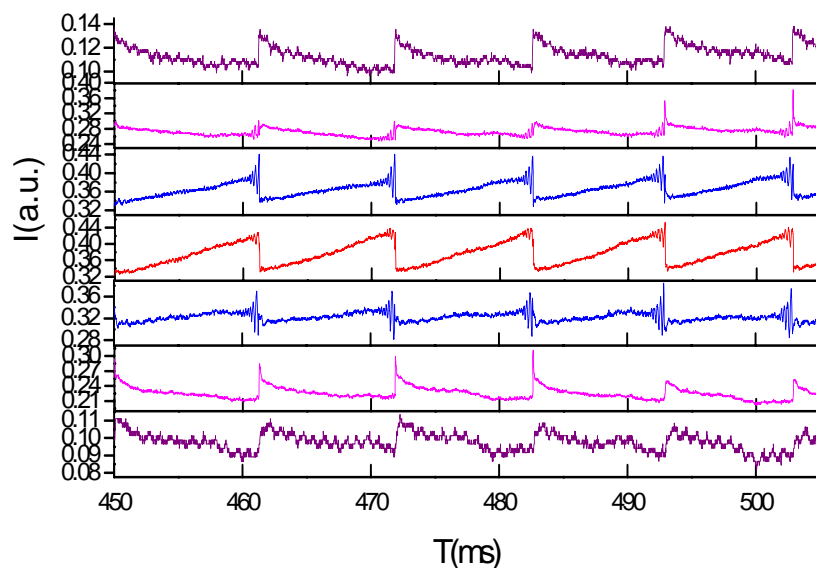
Fig7a.Large sawtooth activities are observed in an ohmic discharge.
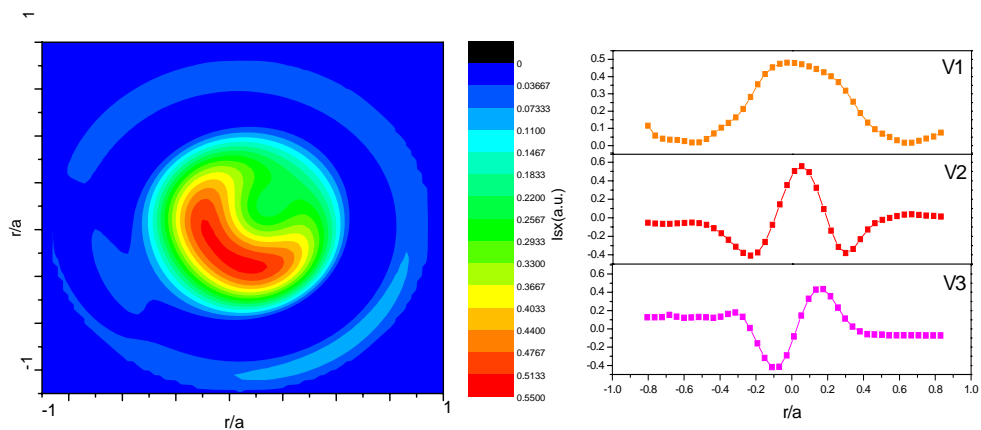
Fig7b.Enhanced tomographic reconstructions of the m=1 mode. On the right is the SVD spatial components, the V3 is the m=1 component.

5. Discussion

The main advantage of the method employed is that the boundary condition is naturally met by solving the equation in the outermost pixel. Taking the complicated real plasma shape into account makes the algorithm start from a grid that is closer to the true plasma radiation contours. It is suitable to be applied in measurements of soft x ray and total radiation on the LHD and Heliotron J with widely arbitrary cross sections. Furthermore, we have modified this tomographic algorithm with a feedback procedure. As a result, the 2-D technique is powerful enough to provide reasonable images in most of the cases. However, since the number of detector arrays is limited, only a finite number of Fourier components can be used in the expansion. In some cases (strong asymmetry or contours of constant radiation emissivity deviate far from magnetic flux surfaces) the reconstruction is not so reasonable, i.e. the difference between experimental and reconstructed chord integrated data drastically diverges in the central part of the image.

6.Conclusion

The numerical test and the results of the 2-D tomography technique applied to the experimental data show that the algorithm is powerful enough to reconstruct complicated asymmetric emissivity distribution.

References

[1] A.Komori et al., Plasma Phys. Control Fusion 42 (2000) 1165.
[2] A.Yu.Kostrioukov et al., Submitted to Rev. Sci. Instrum., 2002.
[3] P.Smeulders, Nucl.Fusion 26, 267 (1986).
[4] R.S.Granetz, P.Smeulders, Nucl.Fusion28, 457 (1988)
[5] Y.Nagayama et al., Rev.Sci.Instrum.65, 3415 (1994)

Study of Particle Behavior for Steady State Operation in JT-60U

H. Kubo and the JT-60 team
Japan Atomic Energy Research Institute, Naka-shi, Ibaraki-ken, 311-0193, Japan
e-mail: kubo@naka.jaeri.go.jp

Abstract
　　　　This paper summarizes recent studies on particle balance in long pulse discharges, long-term erosion/deposition and hydrogen retention for carbon divertor tiles, and particle behavior in SOL and divertor plasmas related to the foregoing two topics in JT-60U. Global saturation of the particle inventory appeared in a latter phase of an ELMy H-mode plasma after several long pulse discharges. As for carbon divertor tiles, erosion was dominant in the outer divertor, and deposition was dominant in the inner divertor. Hydrogen isotope concentration (H+D)/C in the deposition layer was estimated to be ~0.032. The SOL plasma flow towards the inner divertor was observed at the low-field-side midplane, and influence of the E_r x B drift flow from the outer divertor to the inner divertor via the private region on the divertor particle flux was evaluated to be large in the attached divertor plasmas. The preferential deposition in the inner divertor can be a consequence of these flows. For direct observation of hydrogen molecule behavior in the divertor plasmas, hydrogen molecular line emission was measured and the fall in the emission intensity with distance from the divertor plates was reproduced by calculation with a neutral transport code and a collisional radiative model code.

keywords: *tokamak, divertor, SOL, carbon, hydrogen*
PACS: 52.55.Fa

1. Introduction

　　　　In tokamak fusion research, particle control is an essential issue to realize steady state operation [1]. In short discharges, the first wall absorbs hydrogen particles and it works as a pump (wall pumping). The wall pumping is effective to control the plasma density. However, in future tokamak devices, particle inventory in the first wall increases in a long discharge. Then, it is expected that the particle inventory can be saturated and the wall pumping cannot be effective. In addition, in a long operation period, the first wall, especially the divertor tiles under a high heat load, is eroded by plasma-wall interaction, and impurities produced by the erosion of the wall materials are transported and deposited in the vacuum vessel. The erosion can determine the lifetime of the first wall, and the deposition with tritium (co-deposition) can give rise to operational and safety concerns for tritium inventory. In ITER, carbon material is considered to be used for the high-heat-load divertor tiles, because of its high thermal shock resistance and tolerance to off-normal events (ELMs and disruptions) without melting. However, the carbon material has a high erosion rate due to chemical sputtering and a high hydrogen retention rate. Therefore, study of particle behavior in long pulse discharges with carbon divertor plates is significant to establish the steady state operation.

　　　　In this paper, recent studies of particle behavior for steady state operation in JT-60U are presented.   A long pulse operation up to 65 s with NBI (neutral beam injection) of ~12 MW for 30 s has become available [2]. Particle balance has been studied in long-pulse ELMy H-mode discharges with the time scale of particle inventory saturation (Section 2). Studies of plasma material interaction for long-term operation have progressed under joint research between Japanese universities and Japan Atomic Energy Research Institute [3-5]. Long-term erosion/deposition and hydrogen retention for the carbon divertor tiles have been investigated (Section 3). Related to the topics in Sections 3 and 4, particle behavior in the scrape-off-layer (SOL) and divertor plasmas has been investigated in detail with Mach probes and spectrometers. Studies on SOL plasma flow and particle fluxes towards the divertor for understanding the long-term carbon transport and studies on hydrogen molecule behavior in

the divertor for understanding the hydrogen recycling are described in Section 4.

2. Particle balance in long-pulse ELMy H-mode discharges

Particle balance has been investigated by repeating long-pulse ELMy H-mode discharges similar to the discharge shown in Fig. 1 [6]. The baking temperature of the vacuum vessel was ~423K. The NB heating duration was ~30 s, the electron density was kept at 66% of the Greenwald density limit by a feedback control using gas puffing. In the first several discharges, an almost constant gas puff rate was needed to keep the constant electron density. In these discharges, the number of the injected particles was larger than the number of the particles exhausted by the active divertor pumping, whose pumping speed was 21 m^3/s) and the particles accumulated in the vacuum vessel. However, in the succeeding discharges, the gas puff rate gradually decreased in a latter phase of the ELMy H-mode [7]. Figure 1 shows waveforms of such a discharge. The gas puff rate gradually decreased after 19 s (~10 s after the beginning of the ELMy H-mode). Until 19 s, the number of particles in the first wall increased and the wall pumping worked. However, after 19 s, the number of particles in the first wall did not increase and it indicated global saturation of the particle inventory. The result shows that co-deposition was not significant for the wall pumping. The increase rate in the particle inventory before 19 s was about 2.8 x 10^{21} s^{-1}. The carbon deposition rate was evaluated to be 9 x 10^{20} s^{-1} as described in Section 3, and the retention rate by the co-deposition was estimated to be 3.6 x 10^{20} s^{-1} even if D/C was assumed to be ~0.4, which is the maximum saturation value. Since the co-deposition rate is much lower than the increase rate of the particle inventory, it is reasonable that the co-deposition was not significant for the wall pumping. At 28 s, an X-point MARFE appeared and the particle inventory began to decrease. Most of the particle inventory was recovered by the end of the discharge, and such particle behavior was similar in the following discharges. It suggests that the inventory during the ELMy H-mode phase could be attributed to dynamic retention. It is considered that the saturation level of the particle inventory increases under a high particle flux.

For estimation of the local saturation time of the particle inventory, the local particle flux to the first wall was calculated using a Monte Carlo neutral transport code (DEGAS2) [8]. The results suggested that the particle inventory in the divertor plates could reach the saturation level in a second while saturation of the whole area of the main-chamber wall needed several tens of seconds. Therefore, it was estimated that several long pulse discharges were needed for the saturation of the whole area of the main-chamber wall. This estimation agrees with the experimental results, if it is assumed that the static retention of all the area was saturated by repeating several long pulse discharges but the dynamic retention of the divertor area worked in the early phase of the ELMy H-mode.
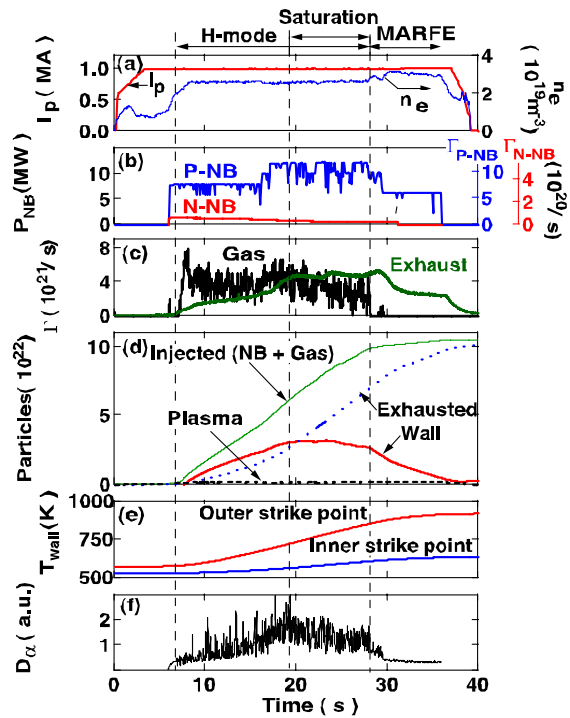
Fig. 1. Waveforms of a long-pulse ELMy H-mode discharge with global saturation of particle inventory. (a) Plasma current and line-averaged electron density, (b) injection power and particle fuel rates of positive-ion and negative-ion based neutral beams, (c) gas puff rate and exhaust rate by the active divertor pumping, (d) numbers of injected particles, exhausted particles, plasma particles and particles retained in the first wall, (e) temperatures of the divertor plates near the inner and outer strike points measured with thermocouples mounted ~5 mm below the surface, (f) intensity of D$_\alpha$ emission from the divertor plasma.

As shown in Fig. 1 (e), the temperature of the divertor plates increased during the NB heating. The temperature was not recovered between the discharges, and the base temperature increased gradually shot by shot. Since the temperature affects the particle retention, effect of the change in the wall temperature should be analyzed as a future study.

3. Carbon erosion/deposition and hydrogen retention of the divertor tiles

The net erosion depth and deposition thickness of the divertor tiles have been measured with a dial gauge [9]. Poloidal distribution of the deposition layer thickness and the erosion depth of the carbon divertor tiles is shown in Fig. 2. The divertor tiles were used in the 1997-1998 and 1999-2002 experimental campaigns, in which ~14000 discharges were performed and the total NB injection time was ~3.0 x 10^4 s. In these experimental campaigns, the baking temperature of the vacuum vessel was usually ~573K. Erosion was dominant for the outer divertor tiles, and deposition was dominant for the inner divertor tiles. The distribution of the erosion depth and that of the deposition layer thickness agreed with the strike point positions. The maximum erosion depth was ~80 μm, and the maximum deposition layer thickness was ~200 μm. Considering the total NB injection time, the erosion and deposition rates were estimated to be ~3 nm/s and ~7 nm/s, respectively. The bulk density of the deposition layer was about half of the original CFC [10]. As a result, increment of carbon was 0.36 kg for the inner divertor tiles, -0.09 kg for the inner dome wing, 0.18 kg for the outer dome wing, and -0.25 kg for the outer divertor tiles. The weight of the dust in the divertor region was 0.007 kg, and deposition in the remote area was very small [4]. Increment of carbon in the divertor region as a whole was 0.21 kg. The total carbon deposition rate in the divertor region was estimated to be 9 x 10^{20} C/s for the NB injection time, and it is similar to that in JET. However, the amount of the deposition in the remote area and the dust was much smaller than that in JET. One of the reasons of the in/out asymmetry is that the temperature in the outer divertor plasma was usually higher than that in the inner divertor. As the sputtering yield increases with the incident particle energy, the temperatures affect the equilibrium between net erosion and net deposition. However, carbon transport is needed to explain the observed long-term erosion and deposition. Some of the carbon deposition in the divertor is considered to be originated from the erosion of the main-chamber wall with preferential deposition in the inner divertor. The preferential deposition in the inner divertor may be a consequence of the SOL flow or drift flow from the outer divertor to the inner divertor via the private region. Study of the SOL plasma flow and the drift flow in the private region is described in Section 4.

The total amount and the depth profiles of hydrogen isotopes (H and D) in the deposition layers and bulk of the carbon tiles were measured by thermal desorption spectroscopy (TDS), secondary ion mass spectroscopy, and nuclear reaction analysis [11-13]. Figure 3 shows results by TDS for the carbon tiles used in the 1997-1998 experimental campaign, where ~3600 deuterium discharges were performed and ~700 hydrogen discharges were performed after the deuterium discharges before air ventilation. The amount of H and D was large for the inner divertor, where deposition was dominant. The H+D amount for the outer divertor, where the erosion was dominant, was small and similar to the amount for the inner divertor tile whose deposition layer
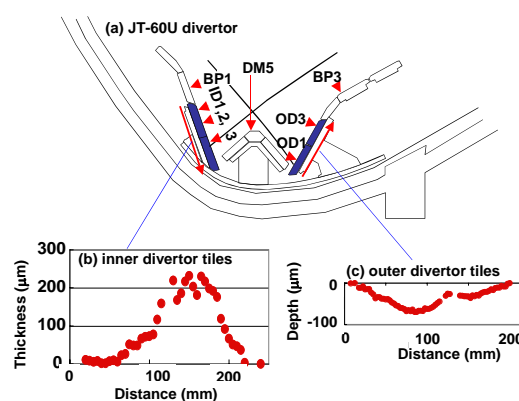
Fig. 2. (a) Poloidal cross section of the JT-60U divertor, and distribution of the deposition layer thickness and the erosion depth of the (b) inner and (c) outer divertor tiles. The divertor tiles were used in 1997-2002. In (a), the sampling positions for thermal desorption spectroscopy shown in Fig. 3 are also indicated.

was removed. In the hydrogen discharges following the deuterium discharges, deuterium retained near the surface was replaced by hydrogen [12,13]. The amount of H and D retained in the inner divertor tiles covered with the deposition layers increased with the thickness of the deposition layers. Hydrogen isotope concentration (H+D)/C in the deposition layers were estimated to be ~0.032. It was much lower than that in other tokamaks. The low hydrogen isotope concentration can be ascribed to temperature rise of the deposition layer due to the heat load during the discharges. Investigation of the deposition layer has shown that the thermal conductivity of the deposition layer was two orders of magnitude lower than that of the CFC [10]. The low thermal

Fig. 3. Amount of H_2, HD, D_2, CH_4-groupe and C_2-group desorbed gas from the carbon tiles used in 1997-1998 measured by TDS. The sampling positions are shown in Fig. 2 (a). The removed shows the ID1 after removal of the deposition layer. The dimensions of the samples are 8 x 8 x 0.5 mm^3.

conductivity can increase the temperature of the deposition layer to reduce the hydrogen isotope retention further. Keeping a high temperature of the deposition layer can be a key to control the tritium retention in fusion reactors with carbon plasma-facing materials [14].

4. Particle behavior in SOL and divertor plasmas
4.1 SOL plasma flow and particle fluxes towards divertor

The SOL plasma flow and particle fluxes towards the divertor are expected to affect impurity transport in the SOL and divertor plasmas. In JT-60U, the SOL flow and particle fluxes has been investigated with reciprocating Mach probes at the midplane on the low field side (LFS), just below the X-point on the LFS, and above the baffle on the high field side (HFS) as shown in Fig. 4 (a) [15].

Figure 4 (b) shows the Mach number profiles measured in an L-mode discharge with the ion ∇B drift towards the divertor (plasma current (I_p): 1.6 MA, toroidal magnetic field (B_t): 3.3 T, NB injection power (P_{NBI}): 4.3 MW, line averaged electron density (n_e): 1.5 x 19^{19} m^{-3}). The SOL flow away from the outer divertor was observed at the midplane on the LFS, and the SOL flow towards the outer divertor was observed near the X-point on the LFS. It suggests that stagnation of the SOL flow occurred between the LFS midplane and X-point. The preferential deposition in the inner divertor described in Section 3 is considered to be attributed to carbon production at the main-chamber wall and the SOL flow towards the inner divertor around the main plasma. The E_r x B drift in the private flux region can be

Fig. 4. (a) Locations of reciprocating Mach probes and (b) Mach number profiles measured in an L-mode plasma with the ion ∇B drift towards the divertor. The profiles near the X-point in the LFS and in the HFS are mapped to the LFS midplane. In (a), the directions of the SOL flow are also shown.

considered as another mechanism for the preferential deposition in the inner divertor. From measurement near the X-point on the LFS, the E_r x B drift in the private flux region has been evaluated. The evaluation showed that the drift flow contributed to particle flux enhancement in the inner divertor and particle flux red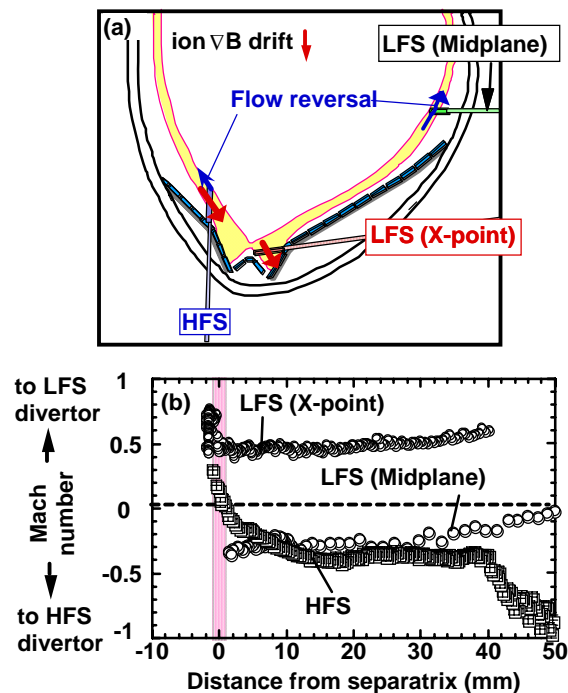uction in the outer divertor. The drift flow from the outer divertor to the inner divertor in the private region might provide a path for carbon impurity to reach the inner divertor. The SOL flow pattern was strongly dependent on the sign of the magnetic field. It suggests that drifts play an important role. The measured flow pattern was reproduced qualitatively using a two-dimensional fluid code (UEDGE) with the plasma drifts included, although the measured flow velocity was higher than the calculated one. Improvement of simulation including the drift effects is required for the quantitative understanding.

4.2 Hydrogen molecule behavior in divertor

Most of the hydrogen particles arriving at the first wall are eventually desorbed in the form of hydrogen molecule. Therefore, direct observation of hydrogen molecules in divertor plasmas is important to understand hydrogen recycling. In the JT-60U divertor, hydrogen molecular line emission has recently been observed and hydrogen molecule behavior has been investigated [16].

Figure 5 (a) shows the intensity of a H_2 Fulcher line as a function of the distance from the outer divertor plates in L-mode hydrogen plasmas. In the attached divertor plasma, the decay length of the line intensity was roughly 1 cm. The line intensity has been calculated using a three-dimensional neutral transport code (DEGAS2) and a collisional radiative model code. The calculated intensity is compared with the measured one in Fig. 5 (a). The fall in the intensity of the H_2 Fulcher line with distance from the divertor plates was reproduced by the calculation. The calculated hydrogen molecule density is shown in Fig. 5 (b). The hydrogen molecules are locally distributed near the strike point. The absolute value of the calculated intensity is smaller by a factor of 2-4 than that of the measured intensity. For further accurate simulation of hydrogen molecule behavior, reliable molecular data are required. In detached divertor plasma with a MARFE, the decay length of the molecular line intensity was ~4 cm, suggesting that hydrogen molecules in the detached divertor plasma penetrated deeper compared with the attached divertor plasma. Molecular assisted recombination was estimated to be as important as H^+-e recombination in the detached divertor plasma.
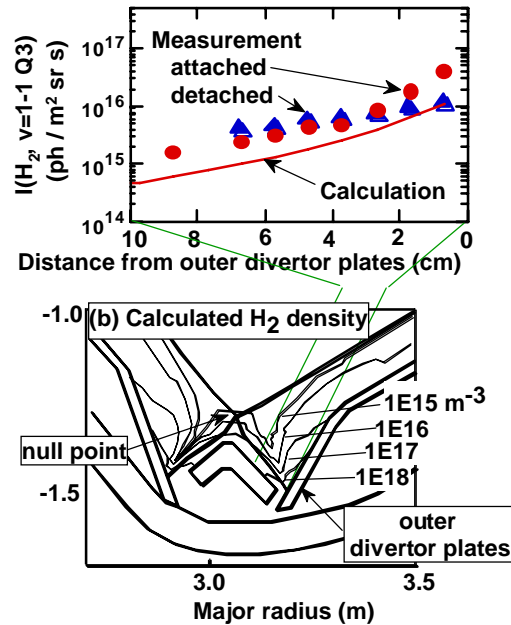
Fig. 5. Measured (circles: attached divertor plasma, triangles: detached divertor plasma) and calculated (continuous curve: attached divertor plasma) intensities of the H_2 Fulcher v=1-1 Q3 line as a function of the distance from the outer divertor plates. (b) Calculated hydrogen molecule density in the attached divertor plasma. The data were obtained in L-mode plasmas (I_p: 1.5 MA, B_t: 3.5 T, P_{NBI}: 4 MW). In the attached divertor plasma, the electron temperature and density near the outer strike point were 20 eV and 0.7×10^{19} m^{-3}, respectively. In the detached divertor plasma, the electron temperature and density near the outer divertor plates were 0.4 eV and 1×10^{20} m^{-3}, respectively. The viewing area is also shown in (b).

5. Summary

In JT-60U, particle behavior was studied for steady state operation. Global saturation of the particle inventory appeared in a latter phase of an ELMy H-mode plasma after several long pulse discharges. The results suggested that static retention could be saturated by repeating several long-pulse ELMy H-mode discharges and the inventory during the ELMy H-mode phase could be attributed to dynamic retention. Since the wall temperature changed in a discharge and shot by shot, effect of the wall temperature change on the particle retention should be analyzed in future. For carbon divertor tiles, erosion was dominant in the outer divertor, and deposition was dominant in the inner divertor. Some of the carbon deposition in the divertor is considered to be originated from the erosion of the main-chamber wall with preferential deposition in the inner divertor. Hydrogen isotope concentration (H+D)/C in the deposition layer was estimated to be ~0.032. The low hydrogen isotope concentration can be ascribed to temperature rise of the deposition layer due to the heat load during the discharges. Keeping a high temperature of the deposition layer can be a key to control the tritium retention in fusion reactors with carbon plasma-facing materials. The SOL plasma flow towards the inner divertor was observed at the low-field-side midplane, and influence of the E_r x B drift flow from the outer divertor to the inner divertor via the private region on the divertor particle flux was evaluated to be large in attached divertor plasmas. The preferential deposition in the inner divertor can be a consequence of these flows. The measured SOL flow pattern was reproduced qualitatively using a two-dimensional fluid code with the plasma drifts included, although the measured flow velocity was higher than the calculated one. Improvement of simulation including the drift effects is required for the quantitative understanding. For direct observation of hydrogen molecule behavior in the divertor plasmas, hydrogen molecular line emission was measured. The decay lengths of the molecular line intensity in the attached and detached divertor plasmas were ~2 cm and ~4 cm, respectively, suggesting that hydrogen molecules in the detached divertor plasma penetrated deeper compared with the attached divertor plasma. In the attached divertor plasma, the fall in intensity of the H_2 line with distance from the divertor plates was reproduced by the calculation. For further accurate simulation of hydrogen molecule behavior, reliable molecular data are required.

Acknowledgement

References
1 Federici G, et al. Nucl. Fusion, 2001, 41: 1967.
2 Ide S and the JT-60 Team submitted to Nucl. Fusion
3 Miya N, Tanabe T, Nishikawa M, et al. J. Nucl. Mater., 2004, 329~333: 74.
4 Masaki K, Sugiyama K, Hayashi T, et al. J, Nucl. Mater., 2005, 337~339: 553
5 Tanabe T, Masaki K, Gotoh Y, et al. in Proc. 20th IAEA Fusion Energy Conference (Vilamoura, 2004) IAEA Vienna, EX/P5-32
6 Nakano T, Asakura N, Takenaga H, et al. submitted to Nucl. Fusion
7 Takenaga H, Asakura N, Higashijima S, et al. J. Nucl. Mater., 2005, 337~339: 802
8 Takenaga H, Nakano T, Asakura N, et al. submitted to Nucl. Fusion
9 Gotoh Y, Yagyu J, Masaki K, et al. J. Nucl. Mater., 2003, 313~316: 370
10 Ishimoto Y, Gotoh Y, Arai T, et al. submitted to J. Nucl. Mater.
11 Hirohata Y, Oya Y, Yoshida H, et al. J. Nucl. Mater., 2004, 329~333: 785
12 Oya Y, Hirohata Y, Shibahara T, et al. to be published in Fusion Eng. Design
13 Hayashi T, Ochiai K, Masaki K, et al. to be published in Nucl. Instrum. Mater.
14 Tanabe T. submitted to Fusion Eng. Des.
15 Asakura N, Takenaga H, Sakurai S, et al. Nucl. Fusion, 2004, 44: 503
16 Kubo H, Takenaga H, Sawada K, et al. J. Nucl. Mater., 2005, 337~339: 161

Divertor Experiments with SMBI and Strong Gas Puffing on HL-2A

X.R. Duan, X.T. Ding, Q.W. Yang, L.W. Yan, L.H. Yao, W.Y. Hong, W.M. Xuan, D.Q. Liu, L.Y. Chen, X.M. Song, J.H. Zhang, Z. Cao, Z.Y. Cui, W. Li, Yi Liu, Y.D. Pan , L. Pan, Y. J. Zeng, Y. Zhou, W.C. Mao, Yong Liu and HL-2A team

Southwestern Institute of Physics, P.O.Box 432, Chengdu 610041, China

Email: duanxr@swip.ac.cn

Abstract

In the HL-2A's 2004 experiment campaign pulsed supersonic molecular beam injection (SMBI) and strong hydrogen gas puffing under the divertor configuration were used for gas fueling. The experimental results show that the SMBI of hydrogen can reduce the heat flux to the divertor target plate. The electron temperature measured by the Langmuir probe array decreases during the injection of the molecular beam, whereas the electron density increases significantly. It indicates that the plasma pressure along the magnetic line tends to be constant at a new equilibrium level. Under our experimental conditions the plasma emission at the tokamak edge increases during the injection of the hydrogen, but in the divertor region it behaves inversely, the Hα and CIII intensities tend to decrease during the SMBI pulse as the electron temperature measured at the target plates does. This shows that the plasma emission in the divertor under our discharge conditions is more sensitive to the electron temperature than to the electron density.

In the divertor plasmas with strong hydrogen gas puffing a high plasma density up to $4.4 \times 10^{19} \mathrm{m}^{-3}$ was achieved. Besides we observed a phenomenon similar to the partially detached divertor regime, which is being studied in the open divertor tokamaks like DIII-D to reduce the peak heat flux on the target plates near the separatrix. After a strong gas puffing the electron temperature measured on the outer divertor target plate near the separatrix decreases till below 5 eV or even lower, but that of the farther outer divertor target plate does not change obviously; the CIII and Hα emission at the plasma edge decreases as expected, but the Hα emission near the X-point increases. This result reveals some interesting characteristics, which need to be studied by modeling and further experiments.

I Introduction

In magnetically confined fusion plasma the plasma-wall interaction has a deleterious effect on plasma performance. Hence, much effort has been devoted to improving wall conditions and modifying the magnetic topology to reduce the influence of the wall. As early as 1951, divertor was proposed by Spitzer to isolate the bulk plasma from the vessel wall[1]. This concept has been realized successfully in ASDEX, where the H-mode (high confinement mode) [2] during high-power neutral beam injection was achieved, and led to a new generation of diverted tokamak experiments. During recent years the success of diverted tokamaks, such as JET,

JT-60U, ASDEX Upgrade, and DIII-D, has been remarkable.

HL-2A is a divertor tokamak reconstructed at the SWIP in Chengdu based on the original ASDEX main components (vacuum vessel and magnet coils) [3,4] and the HL-2A project is an important part of China's fusion research program. In the last two years' campaign of the HL-2A experiment, divertor plasma was achieved. During the 2004 experiments, the supersonic molecular beam injection(SMBI) and strong hydrogen gas puffing were used for gas fuelling, and some unique phenomena were observed. These results will be discussed in the following sections. This paper is organized as follows. The experimental aspects of the HL-2A tokamak are described in Section II. Section III gives some key experimental results of the divertor plasmas with molecular beam injection and strong gas puffing, and related discussions are also given in this section. At the end there is a short summary.

II Experimental Procedures

II.1 HL-2A tokamak

The HL-2A tokamak is characterized by a large closed divertor chamber (see Fig.1), and can be operated in double null, upper single null and lower single null configurations with the same main plasma condition. The vacuum vessel, 16 toroidal field coils, poloidal field coil systems and supporting structure of the former ASDEX are adapted for HL-2A[4]. The other sub-systems of HL-2A, including the pumping system, cooling system, power supply system, diagnostics system, etc. have been or are being constructed.

The main pumping system of HL-2A is composed of eight turbo molecular pumps (3500l/s each) and two sets of cryopumps with two pre-stage pumps. The divertor pumping system is composed of 18 titanium getter pumps installed in the divertor chambers. The vacuum vessel can be baked up to 130^oC-150^oC for degassing and a glow discharge device is installed in the vessel for cleaning the inner surface of the vessel. Eight DC pulse power supply units have been constructed for the coil system of the toroidal field (TF), the Ohmic heating (OH), the vertical field(VF), the radial field(RF), the multipole field(MP), the multipole compensation field(MPC), and so on.

The divertor of the HL-2A tokamak consists of three multi-pole coils MP1, MP2, MP3 and two neutralized targets, each MP2 coil has eight turns and each MP1/MP3 coil four turns respectively. These coils are used to form the divertor configurations with different methods of power supply. According to the results of the equilibrium analysis by the SWEQU code[5], which is the equilibrium analysis code by solving the Grad-Shavranov equation, the ratio of IMP2/Ip is the most crucial for the divertor operation. According to the simulation results by scanning this ratio from 7% to 10% using the SWEQU code, it has been found that the optimum value of IMP2/Ip is ~8%. The details of the HL-2A tokamak can be found in reference 4.

II.2 Diagnostics

A cross section of a diverted HL-2A plasma including the flux surface contour is shown in Fig.1. Some diagnostics are also shown in the figure. To investigate the

plasma features in the divertor, five kinds of diagnostics have been mounted in the lower divertor. The microwave interferometer, target plate Langmuir probe arrays and visible spectrometer are used to measure the profiles of the electron density, electron temperature, and Ha emission, respectively. Four target plate Langmuir probe arrays are fixed on the four target plates, respectively. Each array consists of seven probes with three tips, and the vertical distance between two probes is 1.0 cm. The neutral gas pressure is given by fast ionization-gauge at the divertor chamber. In particular, we use the signals detected by 18 pick-up coils located around the plasma column and Current filament (CF) code, a plasma boundary identification code, to construct the plasma LCFS(Last Closed Flux surface). Besides, about 30 diagnostics have been installed in the main chamber of the device, which include the HCN interferometer, ECE, Thomson scattering, CX neutral particle analyzer, bolometer array(16 channels), VUV spectroscopy, reciprocating probes, and the visible spectrometers at the mid-plane of the device. In the divertor experiments on HL-2A, several methods are used to identify the formation of the divertor configuration. A CCD camera is the most direct tool, which can take the images of the cross-section of the plasma discharges.

III   Results and Discussions

In the 2004 experiment campaign of the HL-2A tokamak, the SN divertor configuration was in operation. The plasma parameters achieved were: $Ip = 320$ kA, $ne = 4.4 \times 10^{19} m^{-3}$, $Bt = 2.2$ T, and plasma duration $T = 1580$ ms.

III.1 Divertor plasma with SMBI

To achieve a high plasma density and better plasma confinement, high pressure (0.3-0.4Mpa) SMBI was adapted for gas fuelling[6]. Fig.2 shows a typical picture of the plasma discharge during a SMBI pulse. The discharge conditions were as follows: the plasma current $Ip = 180$ kA, line averaged electron density $ne = 2 \times 10^{19} m^{-3}$, and toroidal magnetic field $Bt = 2.1$T. Ten SMB pulses were injected into the vacuum chamber via a Laval type nozzle located at the mid-plane of the tokamak's low field side. Each pulse length was 10 ms, and the time interval between two pulses was 20 ms. The first pulse was injected at $t = 200$ ms.

Two bright legs were observed in the lower divertor throats (see Fig.2), which indicated that the plasma had gone into the lower divertor along the magnetic lines. On the left side of the picture there is a bent bright belt, it is due to the SMB injection. Fig.3 provides the experimental results. Ten peaks can be seen clearly from the Ha emission from the plasma edge. This is due to the density increase and temperature decrease at the edge of the plasma during the SMB injection, but the CIII and bremsstrahlung emission decreases obviously after SMB injection because of the decrease in the relative carbon concentration and divertor configuration. After the first pulse the intensity of Ha emission at the mid-plane was lower than its value before the SMB pulse. It was the result of the divertor configuration. During the pulsed SMB injection, the divertor plasma showed some unique results: the electron temperature near the strike point decreased obviously during the SMBI pulses, it indicated a

cooling effect of the SMBI under the divertor configuration, i.e. it could reduce the heat load of the divertor target plate; whereas the electron density measured at the same location increased significantly during the pulse. This contrary tendency of the ne and Te variation indicated that the plasma pressure along the magnetic line tended to be constant at a new equilibrium level, the visible emission including Ha and CIII also changed with the pulse, and during the pulse it reached a minimum. This indicated the variation of visible emission in the divertor was determined mainly by the electron temperature under our discharge conditions. During the SMBI the particle confinement time was increased by a factor of 2.

III.2 Divertor plasma with strong hydrogen gas puffing

Conventional gas puffing was also used for gas fuelling in our experiments. In the 2004 experiment campaign of the HL-2A, gas pulses with different duration and pressure were applied to increase the plasma density, and a high plasma density up to $4.4 \times 10^{19} m^{-3}$ was achieved. In our experiments, an interesting phenomenon was observed during the divertor operation. According to the measurement of the CCD camera, which was arranged tangentially to the tokamak torus, two bright legs of the divertor were observed at the beginning of the divertor regime, and the electron temperature measured at different location on the target plates varied in the same manner, and well above 10 eV, i.e., it worked at the attachment regime. After about 50 ms, only the light belt near the outer divertor throat appeared. The plasma density and current remained unchanged, as shown in Fig. 4. Farther out from the separatrix strike point on the outer target plate (see Fig.5), the electron temperature changed slightly with the discharge time and the electron density changed almost inversely (see Fig. 4(e)), hence the plasma pressure almost kept constant at the location. The Ha and CIII emission from the bulk plasma and bremsstrahlung emission did not vary obviously in the main plasma, but the electron temperature near the separatrix strike point decreased with the time till below 5 eV, at the same time, and the Ha emission measured near the X-point increased. This indicates that the radiation in the vicinity of the X-point is enhanced. From Fig 4 (i) and (j) we can see that the Ha emission and CIII in the divertor decrease as the Te does at z=-82cm. This phenomenon is similar to the partially detached divertor regime observed in the open divertor tokamak such as DIII-D[7-9]

In our experiment, only the Ha and CIII in the vicinity of the separatrix strike point was measured; hence the Ha emission had a similar temporal evolution as the Te near the separatrix strike point. According to the results observed, near the inner divertor throat, there was no obvious emission, but the Ha emission in the vicinity of the separatrix was enhanced, i.e., the majority of the radiation was along the outer divertor leg, and the temperature near the outer strike point (OSP) was significantly decreased, the heat flux reduction was largest near the OSP. Furthermore, the electron pressure near the OSP decreased significantly but only modest changes were observed farther out in the scrape-off layer, i.e., these divertor plasmas were detached near the separatrix, but remained attached farther out in the SOL. Most of the characteristics observed in the discharge were in accordance with those observed on DIII-D during

the PDD operation. According to the report on DIII-D[9], the PDD regime is characterized by reduced target plate heat flux and ion current near the strike point, enhanced upstream impurity radiation, and low plasma temperature in much of the divertor. In addition, the inner leg could be completely detached and cooled up to the X-point to the temperatures below which neither carbon nor deuterium radiate substantially (Te<~1eV). but in our case, the plasma density and temperature were relatively low, although the Ha emission near the separatrix increased, no obvious CIII increase was observed.

As mentioned above, the HL-2A is characterized by a large closed divertor chamber, there is some difference from the point view of the divertor structure, e.g. the open divertor tokamak has a large private flux region. According to Stangeby[10], the neutrals play a very important role in triggering detachment, especially the neutrals from the private flux region, which enter the outer leg SOL by migrating across the separatrix. Hence on HL-2A no significant radiation enhancement was observed.

Here we have only presented some preliminary results concerning the phenomena similar to the PDD , it will be investigated experimentally in more detail by improving some diagnostics near the x-point and in the divertor.

IV   Summary

The divertor experiments with SMBI and strong hydrogen gas puffing have been conducted. The results show that SMBI as a gas fueling technique can improve the particle confinement, and it influences ne and Te in the divertor, and especially can reduce the heat load of the divertor target plate.

In the divertor plasmas with strong hydrogen gas puffing a high plasma density up to $4.4 \times 10^{19} m^{-3}$ has been achieved. Besides, we have observed a phenomenon similar to the partially detached divertor regime, which is being studied in the open divertor tokamaks like DIII-D to reduce the peak heat flux on the target plates near the separatrix. After a strong gas puffing the electron temperature measured on the outer divertor target plate near the separatrix decreases till below 5 eV or even lower, but that of the farther outer divertor target plate does not change obviously; the CIII and Hα emission at the plasma edge decreases as expected, but the Hα emission near the X-point increases. This result has some interesting characteristics, which need to be further studied by modeling and experiments.

References

1   C S Pitcher and P C Stangeby, PPCF 39(1997)779-930
2   The ASDEX Team 1989 Nucl. Fusion 29 1959.
3   J.C. Yan, et al. "Status and Plan of the HL-2A Project", Proceedings of the 19th IEEE/NPSS Symposium on Fusion Engineering, Atlantic City, USA, Jan. 2002.
4   Y.Liu, X.T.Ding, et al. Recent Advances in the HL-2A Tokamak Experiments, 20th IAEA Fusion Energy Conference, Vilamoura, Portugal, 1-6 November 2004.)
5   Li F Z, Xu W B and Shi B R 1989 chin. J. Plasma Phys. 9   12)
6   Lianghua Yao, et al. Nucl. Fusion 38(4) 1998   631

7   Petrie T W et al. 1992 J.Nucl. Mater. 196-198, 848

8   FENSTERMACHER M E et al. Proc. Of 12th Conf. Plasma Surface Interactions, St. Raphael, France 1996.

9   W P West et al. PPCF 39(1997) A295-310.

10 Stangeby P C, 1993   Nucl. Fusion 33 (1695)
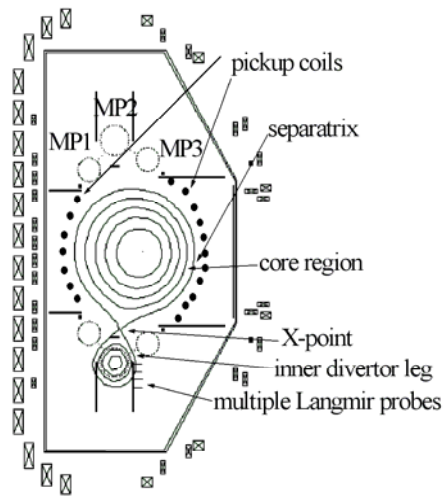
Fig. 1 A cross section of the HL-2A vacuum vessel with separatrix contour plot of a typical lower single-null divertor plasma configuration is shown along with some important diagnostics. The inner and outer divertor leg locations are also shown in the figure.
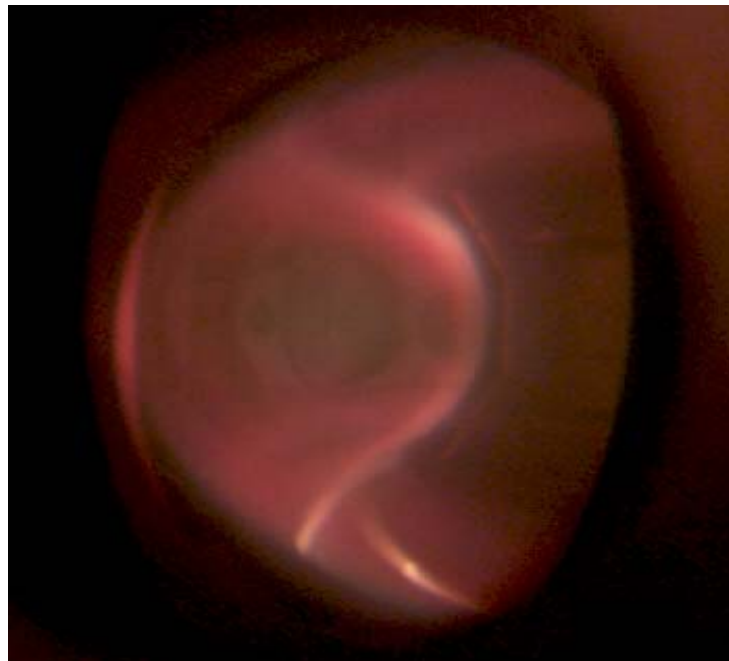
Fig.2 Divertor discharge snapshot during the SMBI. The left belt is due to the SMBI pulse into the plasma, the bottom light belts are the plasma emission in the vicinity of the inner and outer divertors.
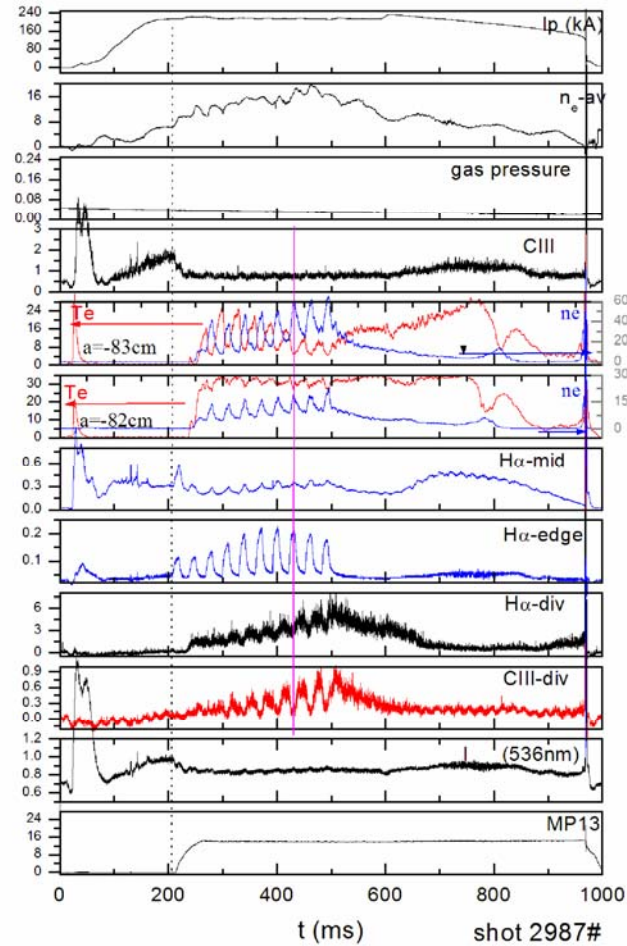
Fig. 3 Time evolution of a typical SN discharge with pulsed-SMBI beginning at 200 ms. The traces shown are, (a) the plasma current (Ip), (b) electron density(ne), (c) gas pressure, (d) CIII emission in the main plasma, (e) electron density and temperature near the separatrix at z=-83 cm, (f) electron Te and ne at z=-83 cm, (g) Ha emission integrated over the mid-plane line, and (h) Ha emission at the plasma edge.
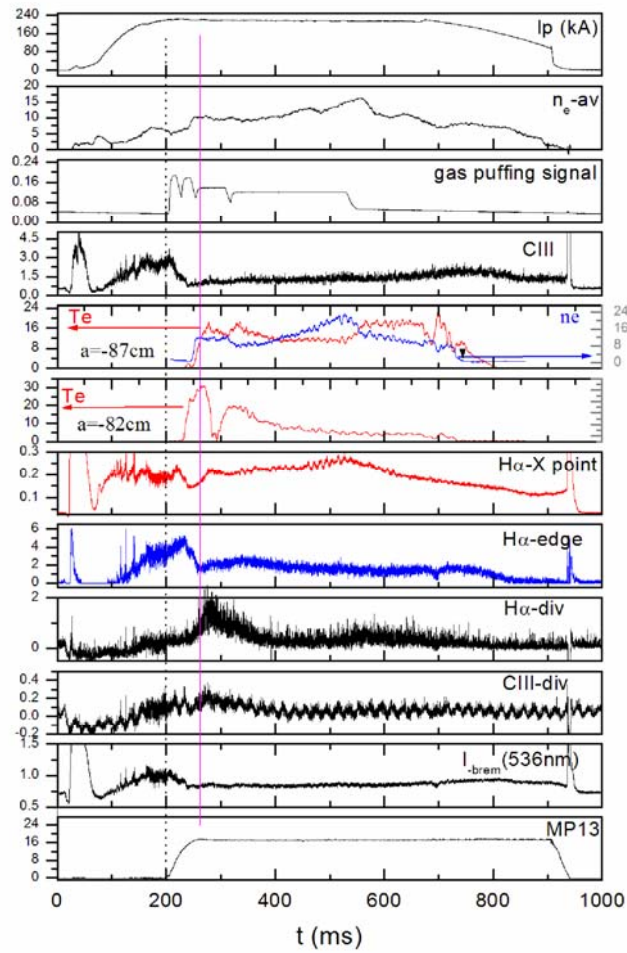
Fig. 4 The traces shown are, (a) the plasma current (Ip), (b) electron density(ne), (c) gas pressure, (d) CIII emission in the main plasma, (e) electron density and temperature near the separatrix at z=-83 cm, (f) electron Te and ne at z=-83 cm, (g) Ha emission integrated over the mid-plan line, and (h) Ha emission at the plasma edge.(i)
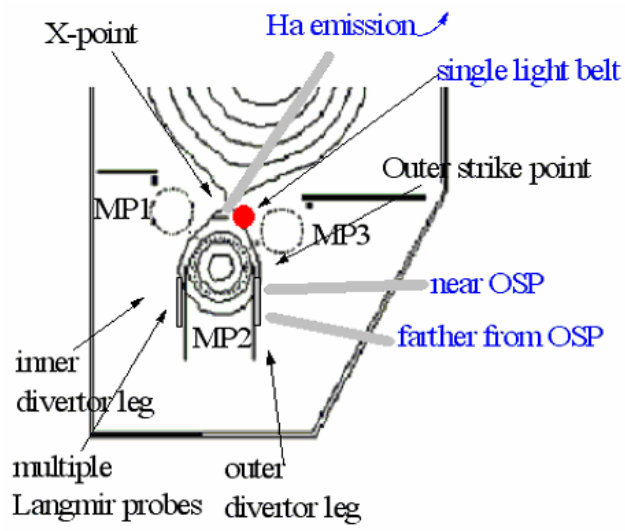
Fig. 5   Schematic diagram of the lower divertor chamber

Review of Divertor Study in LHD

T. Morisaki[1], S. Masuzaki[1], A. Komori[1], N. Ohyabu[1], M. Kobayashi[1], J. Miyazawa[1], M. Shoji[1], X. Gao[2], K. Ida[1], K. Ikeda[1], O. Kaneko[1], K. Kawahata[1], S. Kubo[1], S. Morita[1], K. Nagaoka[1], H. Nakanishi[1], K. Narihara[1], Y. Oka[1], M. Osakabe[1], B. J. Peterson[1], S. Sakakibara[1], R. Sakamoto[1], T. Shimozuma[1], Y. Takeiri[1], K. Tanaka[1], K. Toi, K. Tsumori[1], K. Y. Watababe[1], T. Watari, H. Yamada[1], I. Yamada[1], L. Yan[3], Q. Yang[3], Y. Yang[2], Y. Yoshimura[1], M. Yoshinuma[1], O. Motojima[1] and LHD Experimental Group[1]

[1]National Institute for Fusion Science, Toki, Gifu 509-5292, Japan
[2]Institute of Plasma Physics, China Academy of Sciences, Hefei, China
[3]Southwestern Institute of Physics, Chengdu, China

Abstract   In the Large Helical Device (LHD), two different divertor configurations, i.e. helical divertor (HD) and local island divertor (LID), are utilized to control the edge plasma. The HD with two X-points is an intrinsic divertor for heliotron devices, accompanied with a relatively thick ergodic layer outside the confinement region. Edge and divertor plasma behavior from low density to high density regimes is presented, referring to the divertor detachment. The effect of the ergodic layer on edge transport is also discussed.   On the other hand, the LID is an advanced divertor concept which realizes a high pumping efficiency by the combination of the externally induced magnetic island and the closed pumping system. Experimental results to confirm the fundamental divertor performance of the LID are presented.

Keywords: LHD, divertor, ergodic layer, magnetic island, edge plasma

PACS: 52.55Hc

1. Introduction

In the Large Helical Device (LHD) project, one of the major research goals is to achieve the high performance helical plasma through the edge plasma control [1].   The divertor is expected to play a key role in controlling heat and particle fluxes diffusing out from the confinement region.

Two different divertor configurations, i.e. helical divertor (HD) and local island divertor (LID), are employed in LHD, as shown in Fig. 1 [2].   Since LHD is a heliotron type device, HD which is similar to the tokamak double null divertor is inherently equipped, accompanied with a relatively thick ergodic layer. Although carbon tiles have been installed at the striking points along the torus since the early stage of the LHD program, a pumping system with baffles has not been installed yet.   The construction of the closed full helical divertor is planed in the late stage of the LHD program. Instead of waiting for the closed full helical divertor, as an alternative concept, LID has been employed for the last two experimental campaigns [3,4,5]. The LID is a closed divertor that uses an externally induced static magnetic island with $m/n = 1/1$, where m and n are poloidal and toroidal mode numbers, respectively. The technical ease of hydrogen pumping is the advantage of the LID over the closed full helical divertor because the hydrogen recycling is toroidally and poloidally localized.   Although LID has completely different magnetic configuration and hardware from HD, it can provide important information based on common divertor physics, e.g. the high temperature divertor operation [2].

In this paper, recent progress of edge physics and divertor studies is reviewed.   Before describing the

(a)

(b)
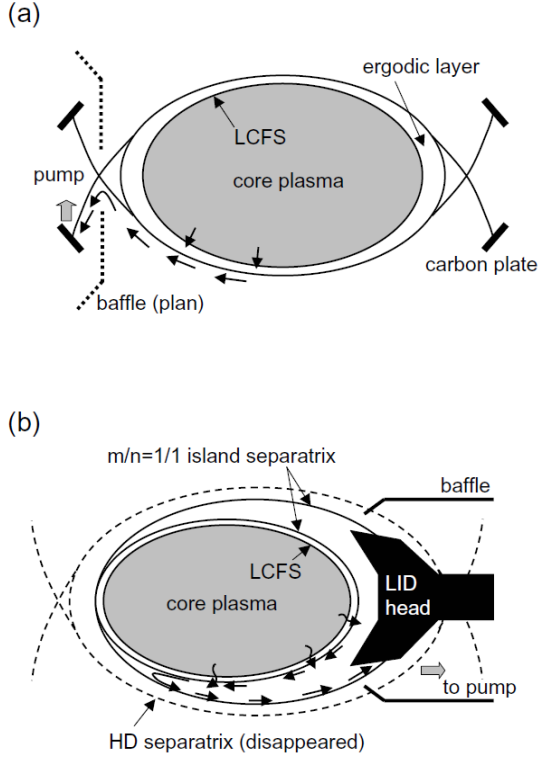
Fig. 1.   Schematic of (a) helical divertor (HD) and (b) local island divertor (LID).

divertor topics, characteristics of the ergodic layer are shown in section 2.   Experimental results of HD and LID are described in sections 3 and 4, respectively, and a summary is given in section 5.

2.   Edge ergodic region

In the heliotron configuration, there exists a relatively thick ergodic layer surrounding the
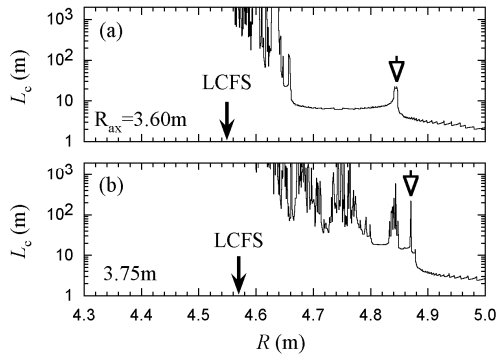
Fig. 2.   Connection length L_c profiles at the outboard side of the torus on the midplane for (a) inward (R_{ax}=3.60m) and (b) outward (3.75m) shifted configurations.

confinement region [6,7].   Especially in the HD configuration, this layer plays an important role in heat and particle transport.   Figure 2 shows the connection length L_c profiles at the outboard side of the torus on the midplane for (a) inward (magnetic axis position R_{ax}=3.60m) and (b) outward (3.75m) shifted configurations in vacuum.   Closed arrow indicates the position where the last closed flux surface (LCFS) exists, and the X-point is presented with open arrow.   In Fig. 2, the region where L_c is fluctuating is corresponding to the ergodic layer.   It can be seen that the layer becomes thick by shifting the magnetic axis outward.

In the radiation profile, P_{rad}, we can see the most featured role of the ergodic layer, as shown in Fig. 3 [8].   In this figure, the region where the normalized minor radius ρ >1 represents the ergodic region.   It is clearly seen that the peak position of P_{rad} is in the ergodic layer (ρ >1) at R_{ax}=3.75m with a thick ergodic layer, while the P_{rad} peak is just inside LCFS at R_{ax}=3.60m with a thin ergodic layer.   The fraction of P_{rad} in the ergodic layer is about 40% with the thick ergodic layer and about 15% with the thin layer.   It is thought that the difference of P_{rad} is caused by the different volume of the radiative mantle, i.e. ergodic layer.   The larger volume of the ergodic layer can radiate larger power.

Another important role of the ergodic layer is an effect on edge transport.   Ergodization of the magnetic field effectively enhances radial transport of energy and particles.   The relationship between edge ergodicity and energy transport was quantitatively investigated [7].   In order to estimate the ergodicity of the edge magnetic field, the
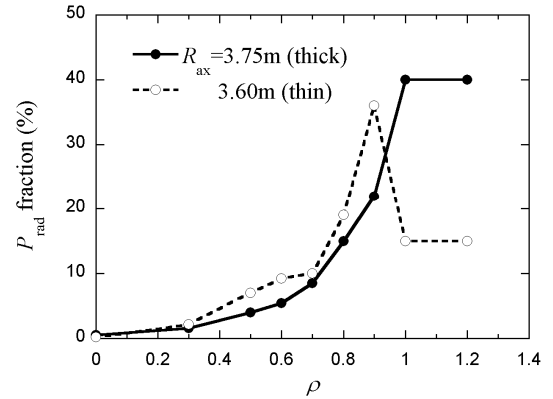
Fig. 3.   Radiation profiles measured with bolometer array.   The ergodic layer exists ρ >1.
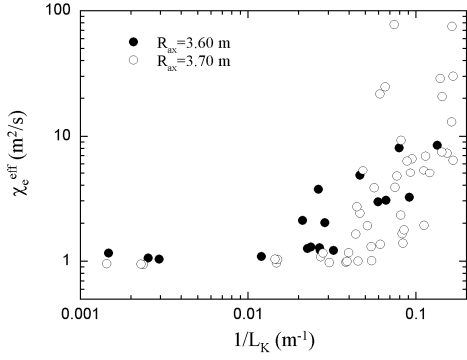
Fig. 4. Radial electron heat conductivity, χ_e^{eff}, as a function of the inverse Kolmogorov length L_K^{-1}.

Kolmogorov length, L_K, was employed. Effective radial electron heat conductivity, χ_e^{eff}, was derived with a simple energy balance equation. Figure 4 shows χ_e^{eff} as a function of the inverse Kolmogorov length L_K^{-1} in different magnetic configurations. In this picture, large L_K^{-1} means large ergodicity. It can be seen that χ_e^{eff} does not change so much when L_K^{-1} is small, however it increases abruptly in the region where L_K^{-1} is more than around 0.2, independent of the magnetic configuration, i.e. thickness of the ergodic layer. This result suggests that the energy transport is affected by the edge ergodicity, instead of its thickness.

3. Helical divertor (HD)

Edge plasma behaviour in the HD configuration was investigated with various magnetic configurations and electron densities [8].

Figure 5 shows (a) electron density, n_e, and (b) temperature, T_e, at edge ($\rho = 0.94$) and divertor plates as a function of line averaged density $\bar{n}_e$ at $R_{ax} = 3.75$m with thick ergodic layer. It is shown that n_e at edge and divertor plates increases monotonically and T_e decreases gradually with an increase of $\bar{n}_e$ up to $\sim 5.6 \times 10^{19}$ m^{-3}. In this density range, the ratio of T_e at edge to divertor plates is almost constant, i.e. the T_e scale length does not change, independently of $\bar{n}_e$. Subsequently obvious changes can be seen in n_e and T_e at divertor plates, i.e. n_e begins to decrease and T_e suddenly decreases faster, independently of T_e at the edge. Accordingly the power flux to the
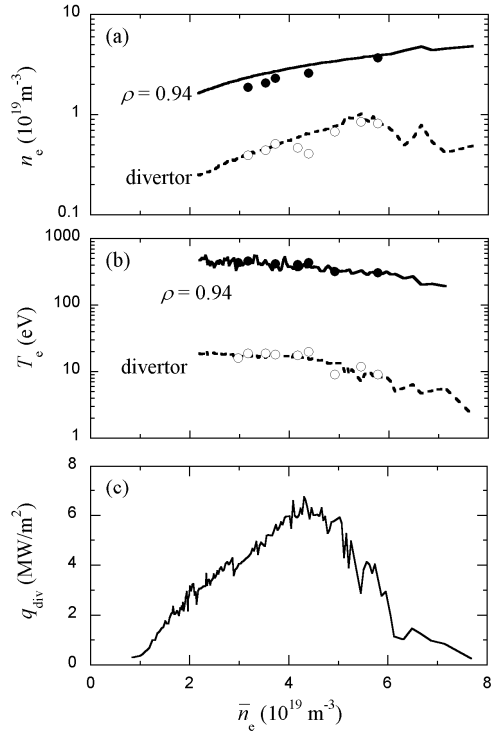
Fig. 5. (a) Electron density, n_e, (b) temperature, T_e, at edge ($\rho = 0.94$) and divertor plates as a function of line averaged density $\bar{n}_e$ at $R_{ax} = 3.75$m with thick ergodic layer. (c) Power flux, q_{div}, to divertor plates is also derived from n_e and T_e.

divertor plates decreases drastically in the density range $\bar{n}_e > 5.6 \times 10^{19}$ m^{-3}, as shown in Fig. 5 (c). These phenomena are similar to the divertor detachment often observed in tokamaks, although it is very unstable in LHD. On the other hand, there is no indication of the divertor detachment in the inward shifted configuration at $R_{ax} = 3.60$m with the thin ergodic layer. At $R_{ax} = 3.75$m with the thick ergodic layer, because of the efficient screening effect on neutrals, n_e in the layer is considered to be higher than that in the thin ergodic layer. The particle flux to the divertor is thus amplified. Furthermore the radiation loss is enhanced at $R_{ax} = 3.75$m with the thick ergodic layer, as mentioned in section 2, then T_e in the ergodic layer consequently decreases. It is considered that these conditions are favourable for the achievement of the divertor detachment.
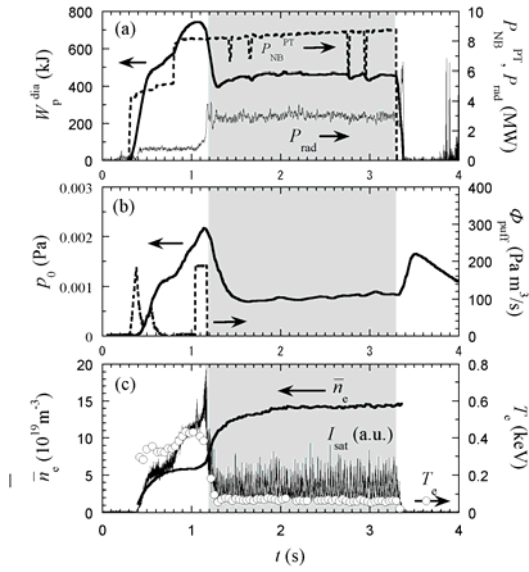
Fig. 6. Typical wave forms with the detachment.

Fig. 7. Radial profiles of (a) T_e and (b) I_{TS} which is a measure of n_e measured with the Thomson scattering. Positions of island separatrix are indicated by solid lines with the schematic of LID.

Recently a new operational regime to achieve the stable divertor detachment has been observed [9]. Figure 6 shows typical time traces of (a) stored energy, W_p^{dia}, neutral beam power (port through), P_{NB}^{PT}, radiation power, P_{rad}, (b) neutral pressure, p_0, gas puff rate, Φ, (c) line averaged density, $\bar{n}_e$, ion flux to the divertor plates, I_{sat} and edge temperature at $\rho = 0.9$, T_e. During the high density regime with careful density control, a strong gas puff of 240 Pa m^3/s is applied for 0.1-0.2s to shrink the plasma column. Then the detachment is achieved with the reduction of p_0 and I_{sat}. Unlike the detachment previously mentioned, this new detachment is sustained for more than 2s without gas puffing. Furthermore it is observed in the inward shifted configuration at $R_{ax} = 3.65$m with a relatively thin ergodic layer. A point in common and/or a point of difference, between two detachments, are now being investigated.

4. Local island divertor (LID)

In the LID configuration, the confinement region is surrounded by the $m/n = 1/1$ island (see Fig. 1 (b)), so that the outward heat and particle fluxes cross the island separatrix, and flow along the periphery of the island to the backside of the LID head. The particles neutralized there are pumped out by a strong pumping system with a baffle which realizes a closed divertor configuration with overall pumping efficiency of larger than 30%. Unlike the conventional pump limiters, blades of the divertor head are located inside the island, thereby being protected from the high heat flow along the island separatrix. Thus there is no leading-edge problem (see Fig. 1 (b)).

Highly efficient pumping is the key in realizing the high temperature divertor operation, where the divertor plasma with temperature of a few keV is
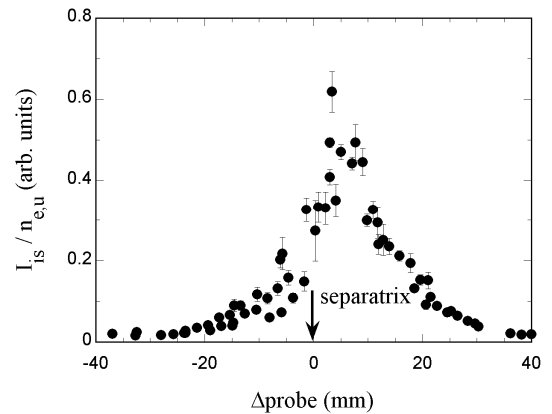
Fig. 8. The ion saturation current profile on the LID head.
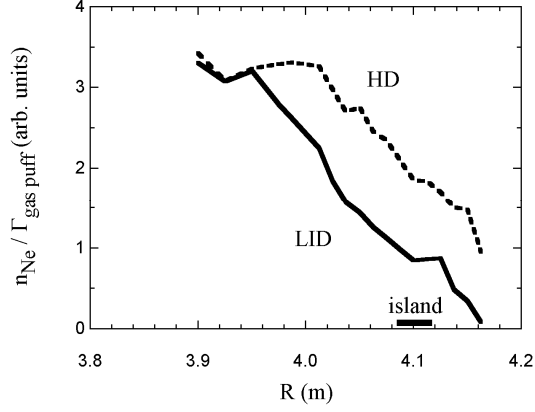
Fig. 9 Radial profiles of Ne density for HD (dashed line) and LID (solid line) configurations, normalized by Ne gas puffing rate.

produced, resulting in a significant improvement of energy confinement [2].   On the other hand, a closed divertor also provides the high plasma plugging efficiency required for the high recycling operation, where a low temperature and high density divertor plasma is produced for radiative cooling.   These two operational modes can be realized in LID [10].   On the above physical concept, the LID experiments have been performed on LHD since 2002.   In the initial experiments, some basic LID functions were confirmed [3,4].

Figure 7 shows the radial profiles of (a) electron temperature, T_e, and (b) I_{TS} which is a measure of electron density, n_e, by the Thomson scattering system.   The magnetic axis position, R_{ax}, was at 3.6 m.   A comparison between two discharges, HD and LID, was performed under the condition with almost the same $\bar{n}_e$ of ~1.9 × 10^{19} m^{-3}.   It was clearly demonstrated that, in the LID configuration, the T_e rose from the inner separatrix of the island, while the low-T_e plasma flowed along the outer separatrix of the island.   In the LID configuration, a clear peak in the n_e profile was seen at the outer separatrix of the island, which indicated the existence of the particle flow along the island separatrix.   Another diagnostic result also convinced us that particles flowed along the (outer) separatrix of the island to the LID head. Figure 8 shows the ion flux profile on the LID head measured with a Langmuir probe array embedded in the carbon tiles on the LID head.   It can be seen that

the peak of the ion flux exists around the outer island separatrix.

The impurity control is also an important function of a divertor.   In the neon (Ne) gas injection experiment to the hydrogen plasma, it was found that the Ne density in LID was lower than that of HD [4], as shown in Fig. 9.   Accordingly LID was demonstrated to be very effective for impurity screening.   Another piece of supporting evidence of impurity screening was tolerance to the radiation collapse with the LID.   Figure 10 shows the time evolution of the LID (solid line) and limiter (dashed line) discharges with the Ne gas injection. Although the heating power (port through) was set to be the same for the two discharges, the absorbed power was different in the two discharges, because of the difference in the target plasma density.   The amount of the injected Ne gas was also the same for the two discharges.   For the limiter configuration, the perturbation coils for generating the $m/n=1/1$ island were switched off, but the LID head was inserted as a limiter.   It was found that the total radiation power was kept low in the LID configuration during the discharge, while it increased
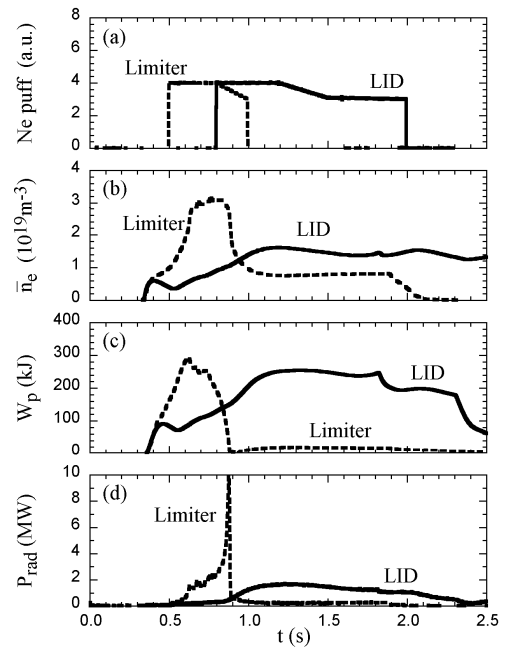
Fig. 10.   Time behaviour of (a) Ne puff rate, (b) line averaged density, $\bar{n}_e$, (c) stored energy, W_p , and (d) radiation power, P_{rad}, from the plasma during Ne injection in the LID (solid line) and limiter (dashed line) configurations.

abruptly with a sudden drop in the stored energy W_{p}, leading to the radiation collapse, in the limiter configuration.

5. Summary

Recent progress of the divertor study in LHD has been reviewed, together with the characteristics of the edge plasma behaviour in the ergodic region.

In the HD configuration, the ergodic layer plays an important role in, e.g., power radiation, heat and particle transport. Furthermore there is a possibility that the ergodic layer has a key part in achieving the divertor detachment. In other words, it may be possible to control the detachment by changing the edge ergodicity.

For LID, basic functions as a divertor have been experimentally confirmed on LHD. Especially in the impurity control, a favourable screening effect or tolerance to the impurities is confirmed to be sufficient. Although the formation of the steep T_{e} gradient is identified, indications of the drastic (transition like) improvement of plasma properties have not been observed yet.

References

1   Motojima O, et al. Phys. Plasma, 1999, 6: 7843
2   Ohyabu N, et al. J. Nucl. Mater., 1999, 266-269: 302
3   Komori A, et al. Fusion Sci. Technol., 2004, 46: 167
4   Morisaki T, et al. J. Nucl. Mater., 2005, 337-339: 154
5   Komori A, et al. Nucl. Fusion, 2005, to be published
6   Ohyabu N, et al. Nucl. Fusion, 1994, 34: 387
7   Morisaki T, et al. J. Nucl. Mater., 2003, 313-316: 548
8   Masuzaki S, et al. N. Nucl. Mater., 2003, 313-316: 852
9   Miyazawa J, et al. J. Plasma Fusion Res., 2005, 81: 331
10   Komori A, et al. Proc. 15th IAEA, 1995, 2: 773.

Predictions for EAST Divertor Performance

S. Zhu [1,*], R. Hiwatari [2], A. Hatayama [3], Y. Tomita [4],

[1] Institute of Plasma Physics, Chinese Academy of Sciences, Hefei, P.R.China
[2] Central Research Institute of Electric Power Industry, Tokyo, Japan
[3] Faculty of Science and Technology, Keio University, Yokohama, Japan
[4] National Institute for Fusion Science, Toki, Japan

Abstract

A detailed study of the divertor performance in EAST has been performed for both its double null (DN) and single null (SN) configurations. The results of application of the SOLPS (B2-Eirene) code package to the analysis of the EAST divertor are summarized. In this work, we concentrate on the effects of increased geometrical closure and of magnetic topology variation on the scrape-off layer (SOL) and divertor plasma behavior. The results of numerical predictions for the EAST divertor operational window are also described in this paper. A simple Core-SOL-Divertor (C-S-D) model was applied to investigate the possibility of extending the plasma operational space of the low hybrid current drive (LHCD) experiments for EAST.

1. Introduction

The scientific mission of EAST is to explore the reactor relevant regimes with long pulse lengths and high plasma core confinement, and to develop and verify solutions for power exhaust and particle control in steady state. To accomplish this aim, both its toroidal and poloidal coils are superconducting magnets and the plasma current (1 MA) will be sustained over long periods of time $\tau_{pulse} = 60 - 1000s$ by LHCD. EAST is designed to have shaped plasma cross-sections and can operate in DN and SN divertor configurations. The EAST divertor should be designed to accommodate the heat load due to the combined heating power of 7.5MW in long duration discharges.

During the last decade, some expected benefits of a closed divertor have been confirmed by the experiments conducted on most existing divertor tokamaks (Alcator C-mod, ASDEX-U, DIII-D, JET and JT-60U, etc) [1]. These experimental devices have modified their divertors to increase the "closure", i.e. to decrease the fraction of recycled neutrals escaping from the divertor region. The experimentally proved effects of the divertor geometry have been considered in the design process of the EAST divertor. In order to increase the degree of closure, the divertor structure has to be designed to minimize its conductance for neutral leakage from the divertor region into the main chamber. So the divertor structure in EAST is deep and consists of inner

and outer vertical target plates, tightly fitting side baffles and a dome baffle in the private flux region, which is close to the divertor concept developed by the ITER JCT [2]

The purpose of this work is to predict the details of the SOL and divertor plasma in the different divertor topologies and to assess the effects of the divertor geometry considered. An assessment of the divertor operational windows in EAST is also described. Two-dimensional numerical calculations with the SOLPS code package [3-5] have been performed. The results of numerical predictions for the divertor are to be described in this paper. A simple Core-SOL-Divertor (C-S-D) model has been applied to investigate the possibility of extending the plasma operational space of the LHCD experiments for EAST.

2. Simulation Model

Tokamak plasma performance generally improves with increased shaping of the plasma cross section. The poloidal field coil system of EAST has the capability to accommodate SN and DN configurations. The major parameters of these configurations are listed in Table 1 and Table 2 separately. Here for the DN configuration, the magnetic connection length is about 31 m, and the divertor depth, i.e. the distance between the X-point and the outer target along the separatrix is about 0.30 m.

The SOLPS code package has been used in the simulations. It couples a multi-fluid plasma code B2 with a Monte-Carlo neutral code Eirene and is capable of taking into account realistic EAST divertor and SOL geometry.

The schematic EAST SN and Connected Double Null (CDN) divertor geometries and the computational meshes used in the present study are shown in Fig. 1. The targets and baffles fit the magnetic geometry tightly to minimize the neutral back flow into the main chamber. The shape of the outer side baffle follows the magnetic flux surface which is at a distance of about 3.5 cm away from the separatrix, measured at the outer midplane. The magnetic equilibriums are generated using EFIT code and are the basis of the numerical grid generation for the SOLPS. The computational domain for the divertor predictive studies covers the whole SOL and divertors. A small region of the plasma core periphery and the private flux region are also included. The whole computational domain is resolved into 120 poloidal divisions and 24 radial divisions.

Only hydrogen is used as plasma species in the present work and C is generated self-consistently by sputtering. For the standard operating scenarios (without impurity injection), we assume that 80% of the total power flows into the entire SOL. The anomalous perpendicular transport model used in the present study is constant in space, with the thermal diffusivities $x_{i\perp} = x_{e\perp}$. Ultra-long discharges will be achieved on the superconducting tokamak EAST, so the wall pumping effect is ignored and the recycling coefficient R is set to 1.0 for the divertor plasma facing components and the vacuum vessel wall.

3. Results of the SOLPS prediction

3.1 Effect of the vertical targets

Vertical targets are adopted in the EAST divertor. The neutrals produced at the target plates are preferentially reflected towards the separatrix and hence ionization is enhanced near the vicinity of the separatrix. Figure 2 shows the 2-D distribution of (a) the neutral density and (b) the ionization source (H^+ ions $m^{-3}s^{-1}$). Since the power is mainly conducted through the region close to the separatrix, this vertical geometry effect is beneficial to improving the power exhaust. As a result, the peak heat flux is reduced and the profile is broader, in comparison with our previous modelling with divertor target plates normal to flux surfaces [6]. The broader heat flux, the more peaked electron density and "inverted" temperature profiles across the lower outboard divertor target are shown in Fig. 3.

3.2 Effect of divertor topology

The poloidal field coil system of EAST allows it to run in SN or DN magnetic configurations for more flexibility in experiments. A single null divertor is a configuration with only one active X-point and the outer separatrix far away or even outside the vacuum vessel. If both X-points are active, i.e. both separatrices coincide, a connected double null (CDN) configuration is created.

The heat flux sharing by the divertors will be strongly affected by the variation in the magnetic topology of the divertor. To assess this effect, we have performed calculations for several operating points. At each point, the density at the core-edge interface (CEI) and the power flux carried by electrons and ions across CEI are specified. A comparison of the electron temperature and peak heat flux between SN and CDN is shown in Table 3. For all cases, the peak heat loads in SN are much higher than that in CDN at about the same operating points.

As the configuration transitions from SN to CDN divertor, there exists a configuration of disconnected double null (DDN). In DDN, if the distance Δ_{sep} between both separatrices at the outer midplane is comparable to the SOL width of the parallel heat flux, then a significant part of the heat flux can still flow along the outer separatrix to the second divertor. Figure 4 shows the contours of the electron temperature and the total heat flux for a DDN.

Sharp change in divertor load due to variation in the magnetic topology of the divertor has been observed in DIII-D and also in our modeling of EAST. Therefore, a sophisticated control over the separatrix distance Δ_{sep} at the outer midplane is essential.

3.3 Divertor operational regimes

To reduce the power load and erosion of the divertor target plates is the main issue in the design of the EAST divertor. Operating in the high recycling or detachment regime can effectively decrease the heat flux flowing to the target and

make the electron temperature low at the target plate. Divertor regimes are very sensitive to the midplane separatrix electron density. For higher densities, the divertor has easier access to the high recycling or detachment regime. According to the Greenwald limit, EAST will be able to run safely with the line average densities $\bar{n}_e$ up to 1.0×10^{20} m^{-3} in Ohmic discharges. But the efficiency of LHCD requires operation at a much lower density. To explore the possibility of achieving various operational regimes and to study the divertor behavior in these scenarios, a density scan has been carried out for CDN.

At a quite low density of about $n_{e,\ sep} = 0.7 \times 10^{19}$ m^{-3}, only the low recycling regime can be attained. In this regime, due to the high parallel heat conduction, the electron temperature shows little drop along the field lines and hence is high at the target. With low densities, recycling losses can be ignored, so the peak heat flux at the target is higher than 5 MW/m^2, which exceeds the engineering constraint.

As the midplane separatrix density is increased, significant gradients of plasma profiles along the field-line can be observed, indicating the accession to the high recycling regime. To reduce the peak heat flux to lower than 3.5 MW/m^2, the midplane density $n_{e,\ sep}$ should be increased further to about 1.4×10^{19} m^{-3}. In this regime, due to the strong ionization sources from recycling neutrals, a plasma with high density and therefore low temperature is formed close to the plate, which reduces target sputtering and makes the Z_{eff} an ideal value of 1.4.

Our modelling indicates that, for EAST, the transition to power detachment occurs at the line average densities $\bar{n}_e \sim 7.8 \times 10^{19}$ m^{-3}, that is about 80% of the Greenwald limit and is much higher than the density limit posed by the LHCD efficiency. Consequently, additional approach such as gas puffing or impurity seeding should be adopted to attempt detachment. But the modelling results at this high density reveal the effect of the divertor geometry on detachment behavior. In this case, the electron temperature is low enough (< 4 eV) throughout most of the inner target and even lower than 2 eV at the separatrix. Although the separatrix temperatures at the outer target become very small below 2 eV, the outer SOL remains at high temperature > 10 eV and thus keeps attached. This may suggest that detachment in EAST starts from the separatrix due to the effect of the vertical divertor geometry (Fig. 5). The result also indicates that complete power detachment is attained for the inner divertor, whereas partial detachment is attained for the outer divertor.

3.4 Extension of the operational space

Consistency between the edge plasma and the core plasma operation is an important issue for the design of fusion devices. A simple Core-SOL-Divertor (C-S-D) model was developed to investigate qualitatively the overall features of the operational space for the integrated core and edge plasma [7]. This model was applied to assess the possibility of extending the plasma operational space of the LHCD experiments for EAST [8]. By using the C-S-D model, it is revealed that gas puffing

is an effective method to extend the operational space toward both lower Φ_p and higher Q_{in} region, where Φ_p is the total particle flux and Q_{in} the total heat flux across the separatrix. On the other hand, the upper boundary of Q_{in} can be extended by the impurity seeding in the SOL-divertor region.

4. Summary and Conclusions

In order to increase the degree of closure, the EAST divertor is designed to be deep and well baffled. Its vertical target plates preferentially reflect neutrals towards the separatrix and hence are beneficial to improving the power exhaust. The vertical divertor geometry also has effects on the detachment behavior.

The heat flux sharing by the divertors will be strongly affected by the variation in the magnetic topology of the divertor. In DDN, if the distance Δ_{sep} between both separatrices at the outer midplane is comparable to the SOL width of the parallel heat flux, a significant part of the heat flux can still flow along the outer separatrix to the second divertor.

Performing in the high recycling or detached divertor operating regimes is of particular importance for heat and particle control in steady state. The operating window, however, is limited due to the density requirement for non-inductive current drive efficiency. To extend the plasma operational space of EAST with LHCD or to attempt to produce detachment for the divertor plasma, additional approach such as gas puffing or impurity seeding should be adopted.

Acknowledgements

References

[1] A. Loarte, Plasma Phys. Control. Fusion **43** (2001) R183-R224

[2] G. Janeschits et al, J. Nucl. Mater. **220-222** (1995) 7

[3] B.J. Braams, A Multi-Fluid Code for Simulation of the Edge Plasma in Tokamaks, NET Report Nr. 68, 1987

[4] D.J. Reiter, J. Nucl. Mater. **196-198** (1992) 80

[5] R. Schneider et al., J. Nucl. Mater. **196-198** (1992) 810

[6] S. Zhu, Contrib. Plasma Phys. **40** (2000) 322

[7] R. Hiwatari et al., Contrib. Plasma Phys. **44** (2004) 76

[8] R. Hiwatari et al., J. Nucl. Mater. **337-339** (2005) 386

*Corresponding author. Tel.: +86-551 5593280; fax: +86-551 5591310
  E-mail address: szhu@mail.ipp.ac.cn (Sizheng Zhu)

Table 1

Major parameters of the EAST CDN configuration

Major radius, R (m)	1.94
Minor radius, a (m)	0.47
Elongation at separatrix, κ_x	1.76
Upper triangularity at separatrix, δ_{ux}	0.56
Lower triangularity at separatrix, δ_{lx}	0.56
Plasma volume, V_P (m^3)	~12.5
Connection length, $L_{/\!/}$ (m)	~ 31

Table 2

Major parameters of the EAST SN configuration

Major radius, R (m)	1.94
Minor radius, a (m)	0.46
Elongation at separatrix, κ_x	1.69
Upper triangularity at separatrix, δ_{ux}	0.32
Lower triangularity at separatrix, δ_{lx}	0.54
Plasma volume, V_P (m^3)	~ 11.9
Connection length, $L_{/\!/}$ (m)	~

Table 3

A comparison of electron temperature and peak heat flux

at the lower outboard divertor target between SN and CDN

Divertor	P_{in} (MW)	$n_{e, sep}$ (10^{19}/m^3)	$T_{e,div}$ (eV)	q_{div} (MW/m^2)
CDN (92948)	1.5	0.31	85	1.0
	2.5	0.55	40	1.1
	5.0	0.98	22	2.0
	10.0	1.65	20	3.6
SN (92102)	1.5	0.37	100	2.0
	2.5	0.67	40	1.8
	5.0	1.16	26	3.0
	10.0	1.88	27	7.0

The list of captions

Figure 1. The schematic EAST divertor geometry and the computational mesh.
(a) SN configuration (b) CDN configuration
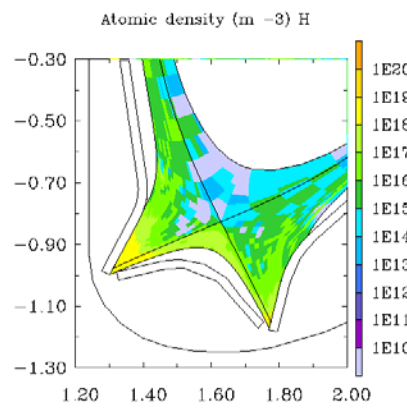
Figure 2. The 2-D distribution of neutral density, showing the preferential reflection of neutrals towards the separatrix by vertical targets.
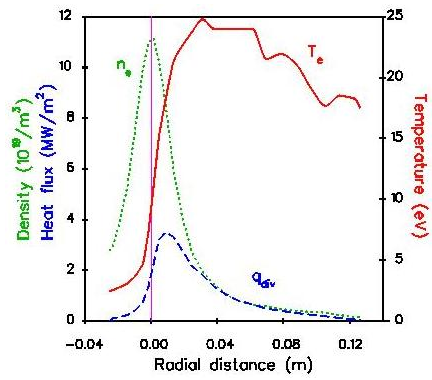
Figure 3. Radial profiles across the SOL at the divertor target for the vertical target. The broadened heat flux, the more peaked electron density and "inverted" temperature profiles are the feature of the vertical target geometry.

electron temperature (eV)   Total parallel energy flux (W) (ABS)
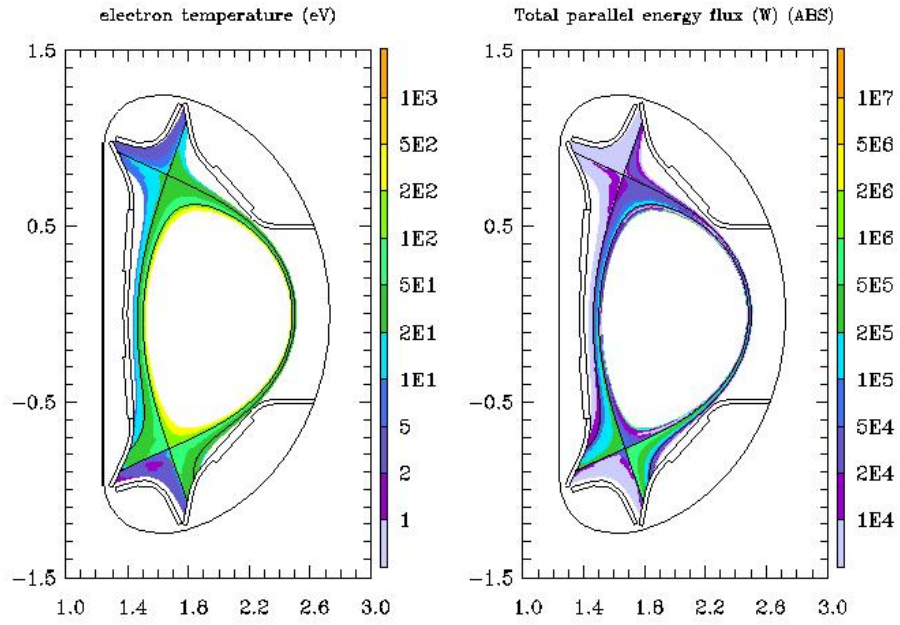
(a)   (b)

Figure 4. (a) Electron temperature (eV) and (b) total parallel energy flux (W) contour in DDN configuration.
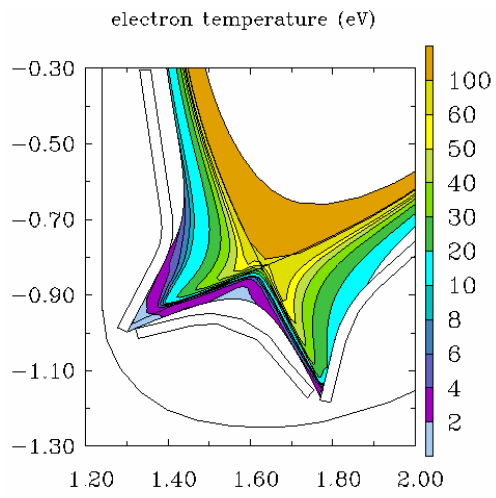
Figure 5. Electron temperature contour in CDN configurations. Complete power detachment is attained at the inner target in CDN.

Zonal Flows and Geodesic Acoustic Mode Oscillations in Tokamaks and Helical Systems

T.Watari, Y.Hamada, A. Nishizawa, T.Notake, and N.Takeuchi[1)]

National Institute Fusion Science,

322-6, Oroshi-cho, Toki-city, Gifu, Japan

[1)] Ariake national college of technology

150 Higashihagio-Machi, Omuta Fukuoka, Japan

Abstract

This paper reviews the theoretical foundations of zonal flow putting emphasis to the linear response function of plasma to the external flow drive. An extension of the theory is made in order to apply it to helical systems and to study the properties of the zonal flow in the low frequency range. Further refinement of the theory is made incorporating the orbital effects of particles more precisely and the role of neoclassical polarization current is identified.

I. Introduction

The zonal flow is interpreted as plasma flow with zero- or low- toroidal and poloidal mode numbers with large radial mode number. Since plasma rotation is related to the radial electric field by $\vec{V} = \vec{E} \times \vec{B} / B^2$, the zonal flow is also viewed as radial electric field with large radial mode number. It is known that there are two branches of zonal flow: the zero-frequency zonal flow and the oscillating geodesic acoustic mode.

Rotation of the plasma creates radial current with the presence of the geodesic curvature of the magnetic lines of force. The $\vec{j} \times \vec{B}$ force due to this current gives the plasma rotation restoring force and therefore the plasma rotation becomes oscillatory [1]. This mode is referred to as geodesic acoustic mode (GAM).

The mechanism of plasma rotation and radial electric field is itself a very interesting research subject and has been investigated by many researchers as a part of neoclassical theory [2]. Particularly, in tokamaks with toroidal symmetry only poloidal viscosity appears. This rather static plasma rotation is referred to zero-frequency zonal flow and is believed in general to have very low damping rate [3-4].

Recent investigations gave experimental evidences of existing zonal flow and GAM oscillations [5-8]. These two modes are energized in torus plasmas with certain mechanisms of excitation. In recent investigations plasma turbulence caused by the micro-instabilities are called for as the mechanisms of excitation. The zonal flow is in turn supposed to regulate the turbulence and, therefore, it is gathering more and more attentions [9].

Figure 1 illustrates the mechanism of the GAM oscillation: Under the presence of the radial electric field $\vec{E}_r$, there exists plasma rotation $(\upsilon_\theta = \vec{E}_r \times \vec{B} / B^2)$. With the existence of the toroidal effect, there occurs the divergence of the flow inside the flux surface causing the up-down asymmetry:

$$\tilde{n}_i = n_{i,0} \int dt \, \frac{2}{R_0} \sin\theta \, \frac{\tilde{E}_r}{B_0} \quad (1)$$

If the plasma motion is adiabatic, this density perturbation causes the uptown asymmetry of the ion

pressure

$$\tilde{p} = \gamma(\tilde{n}_i T_{i,0} + \tilde{n}_e T_{e,0}) \propto \sin\theta . (2)$$

Here, electron pressure is added assuming that electrons moves predominantly inside the flux surface to cancel out the θ dependence of the charge caused by ions. The poloidal pressure gradient causes $\vec{\nabla}p \times \vec{B}$ current across the flux surface,

$$\tilde{j}_r = \frac{1}{B}\frac{1}{r}\frac{\partial\tilde{p}}{\partial\theta} \sim \gamma(\tilde{n}_e T_{e,0} + \tilde{n}_i T_{i,0})n_{i,0}\frac{2}{BB_0 Rr}\cos\theta\int dt\tilde{E}_r , (3)$$

which is integrated to give

$$\int j_r dS = \gamma(\tilde{n}_e T_{e,0} + \tilde{n}_i T_{i,0})n_{i,0}(2\pi)^2\frac{2r}{B^2{}_0 R_0}\int dtE_r . (4)$$

On the other hand, the time varying electric field is accompanied by so-called polarization current:

$$\tilde{j}_\perp \sim \frac{\omega_{p,i}^2}{\omega_{c,i}^2}\frac{1}{4\pi}\frac{dE_r}{dt} \quad (5)$$

which is integrated over the flux surface to give

$$\int j_r dS \sim \frac{\omega_{p,i}^2}{\omega_{c,i}^2}\frac{1}{4\pi}(2\pi)^2 R_0 r\frac{dE_r}{dt} . (6)$$

By equating the two currents Eq.(4) and Eq.(6), we obtain an equation of motion including oscillatory motion:

$$\frac{d^2 E_r}{dt^2} + \omega^2{}_{G,A}E_r = 0 \quad (7)$$

with

$$\omega_{G,A}^2 = \frac{2\gamma}{R^2}\frac{T_{e,0} + T_{i,0}}{m_i} . (8)$$

Thus the GAM oscillation is characterized by $\omega \sim \alpha C_s / R$, with α being a constant of order unity. For more detail readers are requested to confer with references [10-11].

II. Extension to the helical systems and the response function in the low frequency range

So far is the interpretation of the mechanism of GAM oscillation obtained by Winsor et al. [1]. However, since MHD equation is used in this model we need to examine the relevance of the approximation used. Since the formula is derived for tokamaks, the theory has to be extended to helical devices in practical applications. Watari et al [12] attempted new formulation of the GAM

oscillation based on the assumption that the current across the flux surface has to be balanced.

The polarization current j_{pol} and the current due to the geodesic curvature $j_{geo}(\psi)$ are expressed in the following forms using the conductivities σ_{pol} and σ_{geo}.

$$j_{geo}(\psi) = -\sigma_{geo}(\psi)\frac{d\phi}{d\psi} \quad (9)$$

$$j_{pol}(\psi) = -\sigma_{pol}(\psi)\frac{d\phi}{d\psi} \quad (10)$$

Here, $j_{pol} \propto \sigma_{pol}$ is the classical polarization current, which is known to be proportional to ω.

Using the generalized expressions (9) and (10), we obtain the expression of the dispersion relation of GAM oscillations valid to tokamaks and helical systems [12],

$$j_{total} = \tilde{\sigma}_{pol}(\frac{\omega}{i} - \tilde{\tilde{\omega}}_G^2 \sum_{m,n}\eta_{m,n}^2 F_{m,n})\frac{\partial\phi}{\partial\psi} = 0 \quad . (11)$$

In obtaining Eq.(11), the magnetic field is Fourier decomposed in order to facilitate the calculation of geodesic curvature.

$$B^2 = B_0^2(1 + \sum_{m,n}\delta_{m,n}(\psi)\cos(m\theta - n\zeta)) \quad (12)$$

Here, $\eta_{m,n}^2$ and l_ψ^2 are the quantities characterizing the confining magnetic field defined below:

$$\eta^2{}_{m,n} \equiv \frac{(mB_\zeta + nB_\theta)^2\delta^2{}_{m,n}(\psi)}{4B_t^2 l_\psi^2} \quad (13) \quad \text{and} \quad l_\psi^2 \equiv q^2\int\frac{1}{B^2}|\nabla\psi|^2\,d\theta d\zeta \quad (14)$$

Equation (13) contains $\delta_{m,n}$, which represents the geodesic curvature of (m-,n-) ripple component.

It is easy to show that Eq.(11) reduces to tokamak formula putting n=0; $\delta_{m=1,n=0}$ is $1/R_0$ as it appears in Eq.(1) and represents the geodesic curvature of a tokamak of circular cross section. Since the direction of the ion current depends on the sign and the amplitude of the geodesic curvature, it is predicted that the density perturbation in a helical system takes the maximum and minimum values along the lines of $(m\theta - n\zeta) = \pm\pi/2$, respectively. The magnetic lines force short circuit these incremental and decremental regions and, therefore, GAM oscillation is expected to occur under limited conditions in helical devices.

The $F_{m,n}$ in Eq.(11) is expressed as follows:

3

$$F_{m,n} = F_i(\zeta_{m,n}) + F_e(\zeta_{m,n}) = -2\frac{1}{ik_{\|,m,n}\upsilon_T}(Z_{geo,1}(\zeta_{m,n}) + \frac{T_e}{T_i}Z_{geo,2}(\zeta_{m,n})) \qquad (15)$$

where the argument $\zeta_{m,n} = \omega / k_{\|,m,n}\upsilon_T$ is calculated by using the wave number

$k_{\|,m,n} = (mB^\theta - nB^\zeta)/B$. The involved two dispersion functions $Z_{geo,1}(\zeta)$ and $Z_{geo,2}(\zeta)$

are defined as follows [13]:

$$Z_{geo,1} = \frac{1}{\sqrt{\pi}}\int \frac{1}{x-\zeta}((x)^4 + (x)^2 + \frac{1}{2})\exp(-x^2)dx \qquad (16)$$

$$Z_{geo,2} = \frac{1}{\sqrt{\pi}}\int \frac{1}{x-\zeta}(x^2 + \frac{1}{2})\exp(-x^2)dx \qquad , \qquad (17)$$

which differ from the well known plasma dispersion function

$$Z_p = \frac{1}{\sqrt{\pi}}\int \frac{1}{x-\zeta}\exp(-x^2)dx \qquad (18)$$

by the weights in the integrand, $((x)^4 + (x)^2 + \frac{1}{2})$ and $(x^2 + \frac{1}{2})$. Figures 2(a)-(c) show the

calculations of the three dispersion functions (16-18), in which we find unique structures around

$\zeta = 0$ for $Z_{geo,1}(\zeta)$ and for $Z_{geo,2}(\zeta)$. These dispersion functions are series expanded around

$\zeta = 0$ as follows:

$$Z_{geo,1} \approx \frac{1}{2}\zeta - \frac{1}{3}\zeta^3 + i\sqrt{\pi}\left(\frac{1}{2} + \zeta^2 + \zeta^4\right)\exp(-\zeta^2)$$

$$Z_{geo,2} \approx -\frac{4}{3}\zeta^3 + i\sqrt{\pi}(\frac{1}{2} + \zeta^2)\exp(-\zeta^2) \qquad (19)$$

$$Z_p \approx -(2\zeta - \frac{4}{3}\zeta^3) + i\sqrt{\pi}\exp(-x^2)$$

It is noted that the first order terms of $Z_{geo,1}(\zeta)$ and $Z_p(\zeta)$ in $\zeta = \omega / k_\|\upsilon_T$ have

proportionality constants of $1/2$ and -2, respectively. The former has a positive sign and,

therefore, $Z_{geo,1}(\zeta)$ behaves like classical polarization current. This unique feature in the low

frequency range is due to the presence of the factor $((x)^4 + (x)^2 + 1/2)$ in Eq. (16), which is

attributed to the geodesic curvature and the associated particle motion. In later section we will

associate this current with so-called neo-classical polarization current.

III. A few applications to specific problems:

A. Low Frequency GAM

Shown in Fig.3 is the calculation of the dispersion relation using the full kinetic dispersion function instead of series expansion. In the figure, the polarization current j_{pol} and the geodesic current $j_{geo}(\psi)$ is plotted versus $\zeta = \omega / k_{\parallel} \upsilon_T$. The cross point of these two curves gives solutions i.e., the frequencies of the GAM oscillations are determined. It is noted that $j_{geo}(\psi)$ is very much different from that obtained from MHD equations due to the appearance of the neo-classical polarization current. This modification in the low frequency range makes another solution to appear in the lower frequency range than the well-known GAM frequency, which we referred to as low frequency GAM [13].

B. Tokamak GAM and Helical GAM.

Practical toroidal stellarators have both tokamak type field ripple and helical type field ripple and equation (11) allows inclusion of such multi-helicity. Fig.4 (a) and (b) show the solution of Eq. (11) for two different values of $\eta (= \eta_{M,N} / \eta_{m=1,n=0})$: $\eta = 2$ and $\eta = 3$. The other parameters are same (N=8,M=2, $T_e / T_i = 10$). Two peaks are found both in Fig.5(a) and (b), the ones at lower frequency are attributed to the tokamak type geodesic curvatures and the ones at higher frequency are attributed to helical type geodesic curvature. Since η represents the intensity of the helical ripple with respect to the tokamak ripple. Fig.5 (a) and (b) read that the solution to Eq.(11) show a jump on slight variation of η. In toroidal stellarators, the helical ripples increase with minor radius and, therefore, this jump may occur with the variation of the radial position [13].

IV. Refinement of the theory including Orbital Effects

The discussion above is mostly based on references [12-13], where we have made use of the drift kinetic equation. However, for approximation, the velocity change of the particles along the magnetic lines of force has been ignored. Therefore, orbital effects of particles, particularly those of trapped ions, have not been properly included.

While GAM oscillation has been studied by using the MHD equation, the zero frequency branch has been studied in neoclassical physics using drift kinetic equation; Recent work by Sugama et al., gives extension to helical systems using the gyro-kinetic equation [14].

Rosenbluth and Hinton [3-4], gave the potential ϕ_0 excited in response to the external charge $q_{turbulence}$ in the following form:

$$\phi_0 = -q_{turbulence} / (\chi^0_{classical}(1 + 1.6q^2 / \sqrt{\varepsilon})) \quad (20)$$

The second term in the denominator $1.6q^2 / \sqrt{\varepsilon}$ is interpreted as due to the neoclassical polarization current. Recently, an improvement has been made to our previous works; variation of the parallel velocity is included in solving the drift kinetic equation and the following form of the response function has been obtained [15]:

$$\phi_0 = \frac{-q_{turbulence}}{\chi^0_{classical} + (\chi_2^{m=0} + \chi_2^{m \neq 0}) + \chi_e} \quad (21)$$

with

$$\chi_2^{m=0} = +(ie^2\omega)(ik_\psi)^2 \frac{1}{2} \int \sqrt{g} d\theta d\zeta \sum_\sigma \frac{2\pi}{m_i^2} \frac{Bdwd\mu}{|\upsilon_\parallel|} \frac{\partial f}{\partial w} G_0(\theta, w, \mu) \frac{1}{-i\omega} \quad (22)$$

$$\chi_2^{m \neq 0} = (+ie^2\omega)(ik_\psi)^2 \frac{1}{2} \int \sqrt{g} d\theta d\zeta \sum_\sigma \frac{2\pi}{m_i^2} \frac{Bdwd\mu}{|\upsilon_\parallel|} \frac{\partial f}{\partial w} \sum_{m \neq 0} G_m(\theta, w, \mu) \frac{1}{-i(\omega + m\Omega)} \quad (23)$$

Here, $\Omega = \Omega(w, \mu)$ is the frequency of circulation for passing particles and the frequency of banana motion for trapped particles. In the low frequency range, an approximation $\omega / m\Omega \ll 1$ is valid so that $\chi_2^{m=0} \gg \chi_2^{m \neq 0}$. Therefore, Eq.(21) is reduced to a simpler form:

$$\phi_0 = \frac{-q_{turbulence}}{\chi^0_{classical} + \chi_2^{m=0}} \quad . \quad (24)$$

We can show that Eq.(22) is transformed to

$$\chi_2^{m=0} = (+ie^2\omega)(ik_\psi)^2 \frac{1}{-i\omega} \int \sum_\sigma \frac{2\pi}{m^2} dwd\mu \frac{\partial f}{\partial w} \oint \frac{dl_p}{B_p} [\overline{\left(\frac{I\upsilon_\parallel}{\omega_c}\right)^2} - \overline{\left(\frac{I\upsilon_\parallel}{\omega_c}\right)}^2] \quad (25)$$

which agrees with Eq.[14] in ref [3] and, therefore, reproduces Eq.(20).

Through these considerations, Eq. (21) is regarded as the unified expression of the response functions covering the zero- frequency zonal flow through GAM oscillations. The denominator of the Eq.(21) is transformed to the following form by utilizing the nature of the particle orbit:

$$D = e^2(ik_\psi)^2 \int \sqrt{g} d\theta d\zeta \sum_\sigma \frac{2\pi}{m_i^2} \frac{Bdwd\mu}{|\upsilon_\parallel|} \frac{\partial f}{\partial w} [-(|\nabla \psi|)^2 \frac{1}{2} \frac{\upsilon_\perp^2}{\omega^2_{c,i}} - \frac{1}{2} \sum_{m \neq 0} G_{m,\sigma}(\theta, w, \mu) \frac{(m\Omega)^2}{(\omega^2 - m^2\Omega^2)}] + \chi_e$$

(26)

This formula has similar structures as the dispersions obtained in ref [12-13], i.e., Eq.(11) in the present paper, and an elaborations of the theory has been made by including the particle orbit effects more precisely.

[1]   N.Winsor, J.L.Johnson, and J.M.Dawson, Phys. Fluids **11**, 2448 (1968)

[2]   S.V.Novakovskii, C.S.Liu, R.Z.Sagdeef, and Rosenbluth, Phys. Plasmas, **4**, 4272 (1997)

[3]   M.N.Rosenbluth and F.L.Hinton, Phys.Rev.Lett. **80**, 724 (1998)

[4]   F.L.Hinton and M.N.Rosenbluth, Plasma Phys. Control Fusion, **41**, A653 (1999)

[5]   Y.Hamada, A.Nishizawa, T.Ido, et al., Nuclear Fusion, 45, 81 (2005)

[6]   T.Ido, Y.Miura, K.Hoshino, Y.Hamada, Y.Nagashima, H.Ogawa, K.Shinohara, K.Kamiya
         A.Nishizawa, Y.Kawasumi, Y.Kusama, and JFT-2M group,
         "Electrostatic Fluctuation and Fluctuation-induced Particle Flux during Formation of the
         Edge Transport Barrier in the JFT-2M Tokamak",
         (in CD proceedings of 20th IAEA Conf. on Fusion Energy, 2004, Portugal, IAEA)
         EX/4-6Rb

[7]   A.Fujisawa, K.Itoh, H.Iguchi, et al., Phys. Rev. Letters, 93, 165002-1 (2004)

[8]   G. S. Xu, B. N. Wan, M. Song, and J. Li, Phys. Rev. Lett. 91, 125001 (2003)

[9]   K.Itoh and S-I.Itoh., Plasma Phys. Controlled Fusion 38,1 (1996)
         Plasmas 6, 922 (1999)

[10]   P.H. Diamond, S.-I. Itoh, K. Itoh, and T.S. Hahm, to be published
         in Plasma Phys. Controlled. Fusion

[11]   T.S.Hahm, Plasma Phys. Controlled. Fusion 44, A87 (2002)

[12]   T.Watari, Y.Hamada, A. Fujisawa, K.Toi, and K.Itoh, Phys. Plasmas **12**, 062304 (2005)

[13]   T.Watari, Y.Hamada, T.Notake, N.Takeuchi, K.Itoh, "Geodesic Acoustic Mode Oscillation
         in the Low Frequency Range", submitted to Phys. Plasmas.

[14]   H.Sugama, and T.H.Watanabe, Phys.Rev.Lett. **94**, 115001 (2005)

[15]   T.Watari, Y.Hamada, A.Nishizawa, J.Todoroki, "Unified Linear Response Function for the
         Stationary Zonal Flow and the Geodesic Acoustic Mode", (NIFS -815, internal report in
         NIFS).
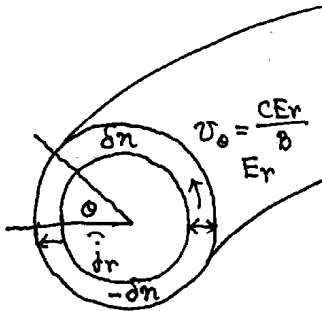
Fig.1 Illustration of the mechanism of GAM oscillation for tokamaks
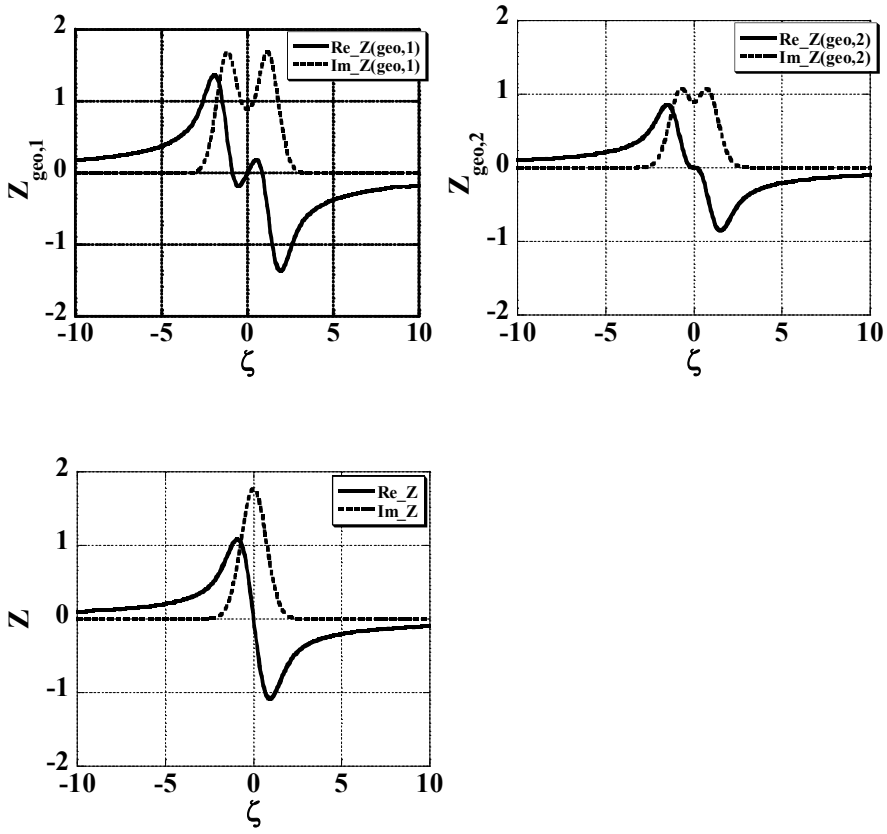
Fig.2. The comparison of the three Z-functions, $Z_{geo,1}$, $Z_{geo,2}$, and Z_p, defined by Eq.(14) Eq.(15)

and Eq.(16) respectively. $Z_{geo,1}$ is an increasing function of ζ in the vicinity of $\zeta = 0$ revealing the

unique response of ions due to the kinetic weighs in their drift motion.
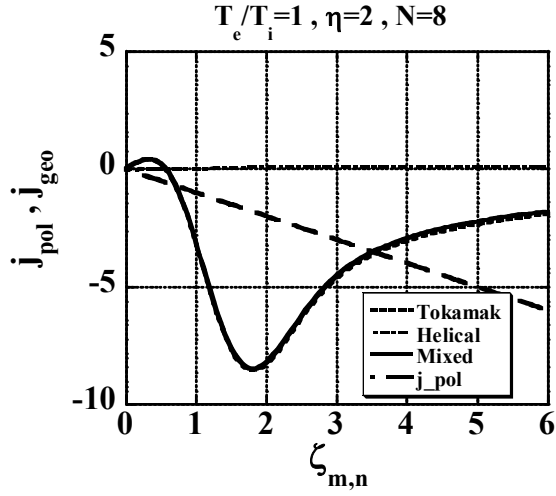
Fig.3   The polarization current and the geodesic current versus $\zeta_{m,n}$. The oscillation frequencies

of GAM are given from the ζ values where they cross. In this Figure, two such frequencies are

found: one at $\zeta_{m,n} = 0.7$ and the other at $\zeta_{m,n} = 3.5$. The larger solution is that we found in the

previous paper and the smaller solution is new. The new solution appears due to the reversed
geodesic current in the low frequency range.
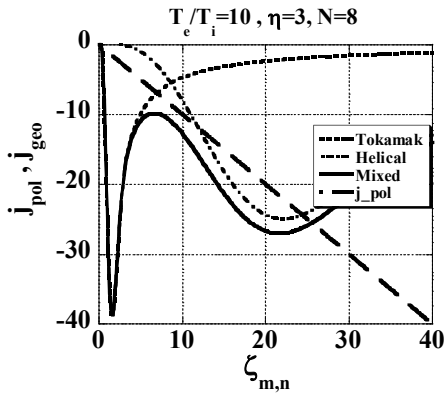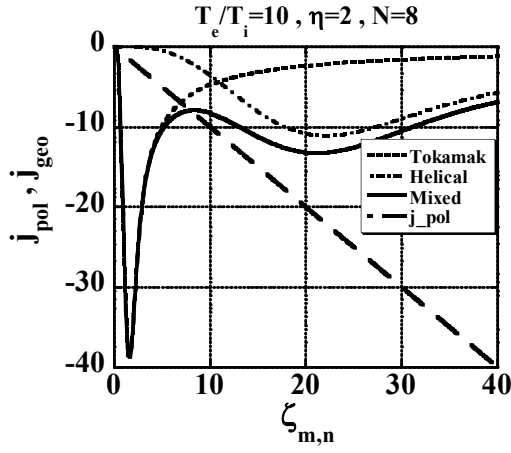
Figure.4.   The GAM frequency of the toroidal helicity systems.

Toroidal helical systems in practice have both toroidal and helical ripples. Used parameters are $\eta^2 = 2$ and $\eta^2 = 3$ in Fig3.(a) and Fig3.(b), respectively. Other parameters are same: $T_e / T_i = 10$ and $N = 8$. For the geometric factor, $\eta^2 > 3$, the GAM jumps to helical type GAM.

Measurement of Zonal Flows in a Tokamak

Using Langmuir Probe Array

G.S.Xu, B.N.Wan

Institute of Plasma Physics, Chinese Academy of Sciences, Hefei, China, gsxu@ipp.ac.cn

Abstract

Zonal flows have been measured with several novel Langmuir probe arrays on the HT-7 tokamak since the year 2002. Based on the original idea of the Reynolds stress triple-tip array, we designed the forked probe and its improved generation, the farmer fork probe. And in order to measure the radial shearing rate of zonal flows, we designed the pyramid probe. This paper addresses the technical aspects regarding this new application. Since the zonal flow dynamics is now widely believed crucial to plasma confinement physics, this has opened up an important application possibility for the Langmuir probe.

Langmuir probes are still one of the most popularly applied diagnostics in tokamak plasma edge. This has resulted from the relative simplicity of the method and the spatially localized nature of the measurements. Since the turbulence and anomalous transport are still recognized as one of the most undemonstrated fields in plasma physics, the application of probes to fluctuation measurements often remains to be preferred diagnostics in the plasma edge, although the non-perturbing spectroscopic methods have already become rather powerful. Using an electrical probe to detect fluctuations does not involve the problems in Langmuir probe theory, primarily lying in the interpretation of the electron-side probe voltage-current characteristics in strong magnetic fields. Applying an electrical probe to fluctuation measurements has already become an independent application field for Langmuir probe diagnostics.

The zonal flows have recently been recognized by theorists as a potential regulating factor, possessing possible importance on plasma turbulence and relevant transport. The theoretical effort has been followed by extensive simulation demonstrations. And the predictions from theories and simulations are supported by several recent experiments. (See review paper [1] and references therein) The distinctive features of zonal flows, by which we mean azimuthally symmetric band-like shear flows, are that they can be spontaneously generated by turbulence vie the action of the Reynolds stress and in return suppress turbulence through the E×B decorrelation mechanism. These features give rise to a feed back loop between zonal flows and turbulence, making the plasma turbulence exist in a self-regulated state mediated by zonal flows. So it is expected that the zonal flows/turbulence dynamics control the fluctuation level and, as a result, the turbulent transport. It is well known that zonal flows are a ubiquitous phenomenon in nature, such as the Jupiter belts and zones, and the terrestrial atmospheric jet stream; these are familiar to nearly everyone. The ubiquity of zonal flows in nature makes most plasma physicists believe in the existence of zonal flows in laboratory fusion plasma with enough reasons and confidence. As a result zonal flows physics have recently become the subject of intense interest and investigation in the magnetic confinement plasma field.

(See P.H.Diamond's overview in IAEA2004 [2])

In the context of the tokamak configuration, zonal flows are toroidally and poloidally symmetric, and radially localized potential perturbations. That means only in the radial direction do they have finite wavelength. Therefore, essentially the wave field of zonal flows is just potential fluctuations between nested magnetic flux surfaces. In the strong toroidal magnetic field B_ϕ of the tokamak, the E×B flows will be driven by the time-varying Er and flow mostly in a poloidal direction. That is why we call them zonal flows. The suppressing ability of higher frequency zonal flows is weaker than the low frequency components [3], so the latter are more interesting to us. The generation process of such flows is the radial turbulent transport of poloidal momentum, i.e. the Reynolds stress. This process is the same as the radial turbulent bipolar transport. In this process time-varying radial currents Jr are produced and repeatedly charge the magnetic flux tube, subsequently time-varying Er are built up between nested magnetic flux surfaces and consequently the E×B flows. This generation process is the key of zonal flow physics, and so an experiment to demonstrate the existence of zonal flows must present information on this generation process, in other words, measure the turbulence Reynolds stress. It is well known that the direct measurement of the Reynolds stress in fusion plasmas is not easy. Fortunately, Langmuir probe arrays provide a simple approach. Up to now, besides the Langmuir probe, heavy ion beam probes and several spectroscopic diagnostics have been used for measurements of zonal flows, but only the Langmuir probe can provide direct information on the Reynolds stress. This primarily benefits from the spatially localized nature of the measurement. Although at present the experimental demonstrations of zonal flows are still not sufficient, it has already been widely recognized and accepted that zonal flows are really playing a role in nearly all cases and regimes of laboratory fusion plasma, indeed, so much so that this classic problem has now become a hot topic in the plasma physics research.[1]

To present the direct measurement of the Reynolds stress and zonal flows, we designed a novel probe array, namely, the forked probe array in the year of 2002 (see figure 1). The specially designed probe array has two probe heads poloidally separated by 31.4 mm, which is much longer than the poloidal correlation length $L_{c\theta}$ of turbulence at the plasma edge, which is usually around 1 cm. On each of the two heads a triple tip array is used to provide local measurement of the radial electric field E_r and electrostatic Reynolds stress $\left\langle \tilde{V}_r \tilde{V}_\theta \right\rangle$,

where $\left\langle \cdots \right\rangle$ denotes an ensemble average. All tips are used to measure the floating potential (ϕ_{f1}, ϕ_{f2}, …, ϕ_{f6}). Then the radial and poloidal E_r fluctuations can be calculated as $\tilde{E}_{r1} = \left(\tilde{\phi}_{f1} - \tilde{\phi}_{23} \right) \big/ \delta_r$ and $\tilde{E}_{\theta1} = \left(\tilde{\phi}_{f2} - \tilde{\phi}_{f3} \right) \big/ \delta_\theta$, ignoring the contribution from electron temperature [4], where $\tilde{\phi}_{23} = \left(\tilde{\phi}_{f2} + \tilde{\phi}_{f3} \right) \big/ 2$. Thus, the poloidal and radial E×B flows are calculated as $\tilde{V}_{\theta1} = \tilde{E}_{r1} \big/ B_\phi$ and $\tilde{V}_{r1} = \tilde{E}_{\theta1} \big/ B_\phi$. Similarly, the triple tips on the right probe head give $\tilde{V}_{\theta2} = \tilde{E}_{r2} \big/ B_\phi$. This probe array structure has the merit that the middle point between tip2

and tip3 is at the same poloidal location as tip1 so that the simply calculated potential $\tilde{\phi}_{23} = \left(\tilde{\phi}_{f2} + \tilde{\phi}_{f3}\right)\!/2$ is very close to the floating potential at the middle point between tip2 and tip3, thus this structure will not introduce phase shift within Er measurement. Because calculating the Reynolds stress needs an ensemble average from a large quantity of data, a little phase shift will accumulate a material error and make the measured Reynolds stress meaningless. The probe is mounted on the top of the tokamak along the central line and operated with shot-to-shot scanning. Feedback control of the plasma position ensures that the two heads are located on the same magnetic flux surface. Both the probe tips and the shield tubes are made of graphite to allow the reliable measurement inside the last closed flux surface (LCFS). The data are usually sampled at 1 or 2MHz with 12-bit resolution using a multi-channel digitizer. The boundary profiles of plasma parameters are measured with a fast reciprocating Langmuir probe using a standard triple tip array. All measurements are made in the laboratory setting.

The experiments are carried out on the HT-7 tokamak, which is a superconducting tokamak with two circular poloidal limiters toroidally separated by $180°$ and a high-field-side belt limiter. In SOL the flows suffer from the obstruction of limiters, so they can only be found in the confinement region. In order to enable the probe to make reliable measurements deeply inside the LCFS, we usually conduct this experiment in low plasma current I_p ohmic heated discharges. The typical parameters are $R_0 = 122$ cm, a = 27 cm, $B_\phi \cong 1.8\sim2.0$ T, $I_p \cong 80$ kA, $\overline{n}_e \cong 1.5\times10^{19}$ m^{-3}, $T_{e0} \cong 0.4$ keV, $n_{\text{e-edge}} \cong 1.5\sim4\times10^{18}$ m^{-3}, $T_{\text{e-edge}} < 50$ eV and discharge duration $\cong$ 1s. Empirically, such low plasma current can ensure reliable measurement 4 cm inside LCFS. When the probe is inserted 4.5 cm inside LCFS, the secondary electron emission rapidly bursts out after about 100 ms discharge. In such low parameters discharges, the edge safety factor q_a>7 and there is no sawtooth and very little MHD activity. It should be mentioned here that the probe array configuration has a merit in that it can avoid the interference signal from MHD perturbations. Because low mode (m = 2 or 3) MHD perturbations occur in the plasma core and rapidly propagate outwards. The radial distance between tip1 and tip2/tip3 is no more than 5 mm. When MHD perturbations pass through such a short interval, the phase difference and magnitude decay will be very small. The difference between two radial spaced floating potential $\tilde{E}_{r1} = \left(\tilde{\phi}_{f1} - \tilde{\phi}_{23}\right)\!/\delta_r$ will offset the MHD perturbations. However, this function does not act on zonal flows, because zonal flows have shear in the radial direction, their small radial scale can be comparable with the radial distance.

High-resolution of poloidal wave number ($-1< k_\theta <1$ rad/cm) can be achieved using this forked probe, so that small k_θ components of poloidal E×B flows can be distinguished from the ambient turbulence. Application of this method to discerning the large-scale flows requires that the lifetime of turbulence eddies is shorter than the transit time of turbulence eddies across the long distance. This condition is satisfied for the specially designed probe. The decorrelation time of floating potential fluctuations at the plasma edge is about $\tau_c \cong 8$ μs. The equilibrium flow velocity is about 2 km/s, resulting in a 16 μs transit time τ_d across the 31.4

mm spatial separation, so that $\tau_c < \tau_d$. The zonal flows are expected to correlate between two points with long poloidal space, while the correlation in ambient turbulence will decay with the increase of distance. Therefore, using the two-point correlation method between the two probe heads, the coherent low frequency flows can be extracted from the background fluctuations.

To measure the radial wave number k_r of this low-frequency mode, one probe head is made 1 cm longer than the other one, so the two probe heads are not only poloidally separated by 31.4 mm but also radially separated by 10 mm (see figure 2). Through the long distance correlation between $\tilde{V}_{\theta 1}$ and $\tilde{V}_{\theta 2}$, the wave number $\vec{k} = \vec{k}_\theta + \vec{k}_r$ with two components is obtained. Since the k_θ of low-frequency zonal flows is about zero, its k_r can be approximately estimated as $k_r \cong k$. The k_r can be used to calculate a turbulence-shearing rate $\omega_s = d\tilde{V}_\theta / dr = 2\tilde{V}_\theta^{pp} / \lambda_r$, where λ_r is the radial wavelength and $\tilde{V}_\theta^{pp}$ is the peak-to-peak value of zonal flows fluctuations.

The zonal flows' generation mechanism has been considered as a three-wave coupling process in which smaller-scale turbulences transfer their energy nonlinearly to larger-scale zonal flows through the Reynolds stress [5], the energy is transferred via the inverse cascading of fluctuation spectra. So the process of zonal flows generation can be investigated using the cross-bicoherence analysis $b^2(f) = \sum_{f=f_1+f_2} \left\langle \tilde{V}_r(f_1)\tilde{V}_\theta(f_2)\tilde{V}_\theta^*(f) \right\rangle$ [6], namely, that of the radial and poloidal E×B velocities of the turbulence with the zonal flows, where the $\tilde{V}_r$ and $\tilde{V}_\theta$ are directly measured with the forked probe. [7]

The experiment in 2002 only demonstrated the existence of zonal flows at the plasma edge, since theory not only predicted the zonal flows' generation but also predicted that zonal flows could suppress turbulence through the shear decorrelation mechanism, and as a result important to transport, the next step would be researching this shear process. So we improved the forked probe, increased a probe head, as shown in figure 3. The modified probe array was named the farmer fork probe. It has three probe heads, and the middle one toroidally shifts a little to avoid sheltering the poloidal flows. On the top of the middle head a traditional triple tip array was used to measure the radial particle flux $\Gamma_e(t) = \left\langle \tilde{V}_r \tilde{n}_e \right\rangle = \dfrac{\left\langle \tilde{E}_\theta \tilde{n}_e \right\rangle}{B_\phi} \propto \left\langle \tilde{E}_\theta \tilde{I}_s \right\rangle$, where

E_θ fluctuations were calculated as $\tilde{E}_\theta = \left(\tilde{\phi}_{f8} - \tilde{\phi}_{f9}\right)/\delta_\theta$, $\tilde{I}_s$ was the ion saturation current fluctuation measured by the center tip7. By researching the correlation between the turbulence-driven particle fluxes and the zonal flows measured by another two probe heads, we could extract the information on the interaction between turbulence transport and zonal flows. The theory predicted that zonal flows could modulate the turbulence flux by the so-called random shear process. The farmer fork probe presented the unique diagnostic function in this process.

The farmer fork probe has been applied to HT-7 for three years, 2003, 2004 and 2005. The

radial shearing rate of zonal flows is very interesting to theorists. However, the direct measurement of shearing rate need at least three points in the radial direction, the farmer fork probe can not do this. So we designed a new probe array in the year 2003, we named it the pyramid probe, as shown in figure 4. This probe array has three layers, with a bilateral symmetry. Using this probe the radial-three-points-floating-potentials measurement can be achieved. The time-dependent radial shearing rate of zonal flows can be simply calculated as

$$\frac{\partial \tilde{E}_r}{\partial r}(t) = \frac{\tilde{\phi}_1 + \tilde{\phi}_{45} - 2\tilde{\phi}_{23}}{\delta_r^2}, \quad \text{where} \quad \tilde{\phi}_{45} = \left(\tilde{\phi}_{f4} + \tilde{\phi}_{f5}\right)/2 \text{ and } \tilde{\phi}_{23} = \left(\tilde{\phi}_{f2} + \tilde{\phi}_{f3}\right)/2. \text{ Simultaneously}$$

tip6 measures the ion saturation current Is, so on the middle layer the triple tip array can measure the fluctuations driven radial particle flux, and similar to the forked probe the Reynolds stress is measured by tip1, tip2 and tip3.

In conclusion, this paper addresses a recently arisen application of the Langmuir probe on fusion plasma diagnostics: direct measurement of zonal flows. Although the Langmuir probe is one of the oldest diagnostics, their theories and experimental techniques are still in progress. Using electrical probes to detect fluctuations does not involve the problems in the Langmuir probe theory, primarily lying in the interpretation of the electron-side probe voltage-current characteristics in strong magnetic fields, therefore with an elaborately designed probe array configuration, the Langmuir probe can present the unique diagnostic function in a series of dynamic processes related to zonal flows. Since the zonal flow dynamics is now widely believed crucial to plasma confinement physics, this new application of the Langmuir probe has already contributed and will continue contributing to this important field.

References

[1] P. H. Diamond, S.-I. Itoh, K. Itoh, T. S. Hahm, "Zonal flows in plasma – a review" Plasma Phys. Control. Fusion **47**, R35-R161(2005). P.H. Diamond, S.-I. Itoh, K. Itoh and T. S. Hahm, "Review of Zonal Flows", Oct. 2004, NIFS-805 research report, Toki Japan.
[2] P. H. Diamond, 20th IAEA Fusion Energy Conference, 1-6 November 2004, overview talk.
[3] T. S. Hahm, *et al.*, Phys. Plasmas **6**, 922 (1999).
[4] R. A. Moyer *et al.*, Phys. Plasmas **2**, 2397 (1995).
[5] P. H. Diamond *et al.*, *Proceedings of the 17th IAEA Fusion Energy Conference, Yokohama, 1998* (IAEA, Vienna, 2001).
[6] P. H. Diamond and M. N. Rosenbluth *et al.*, Phys. Rev. Lett. **84**, 4842 (2000).
[7] G. S. Xu, et al., Phys. Rev. Lett. **91**, 125001 (2003).

Figure 1 the configuration of forked probe array.
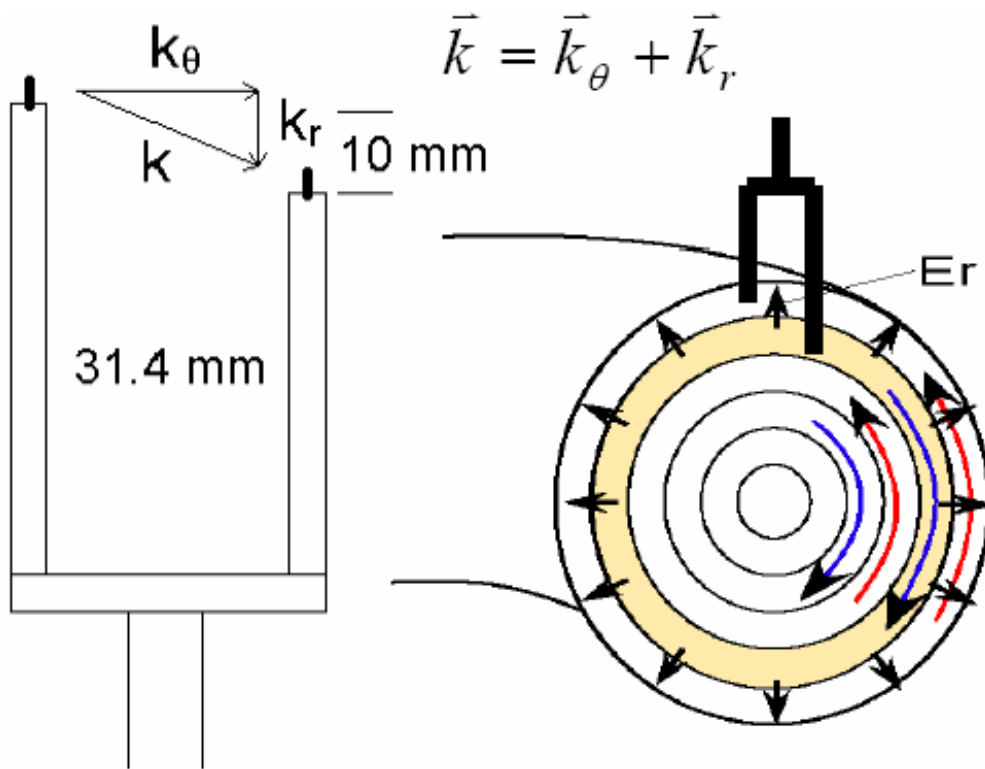
Figure 2 the scheme of k_r measuring principle using the forked probe array.
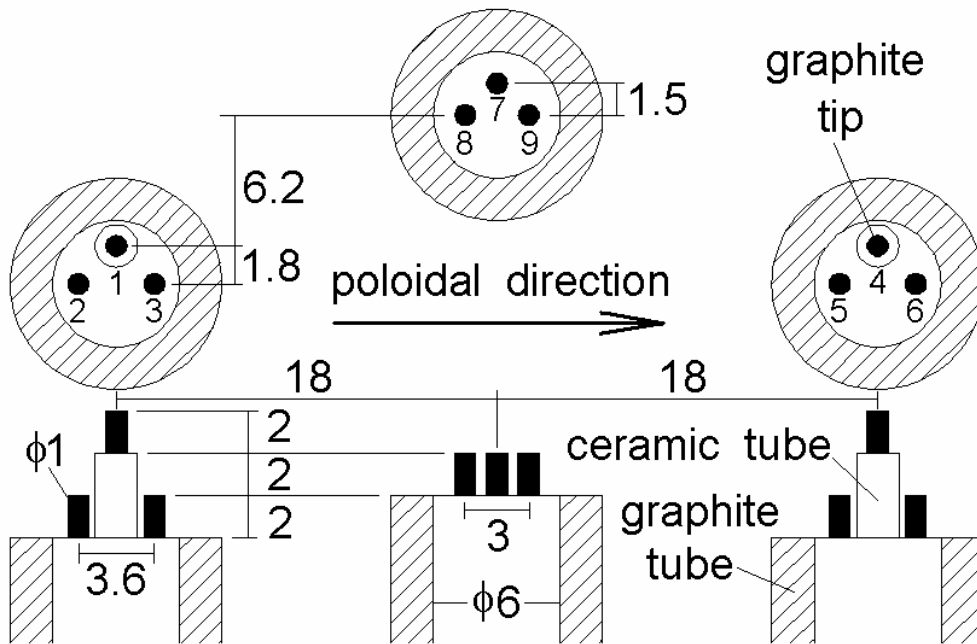
Figure 3 the configuration of farmer fork probe array.
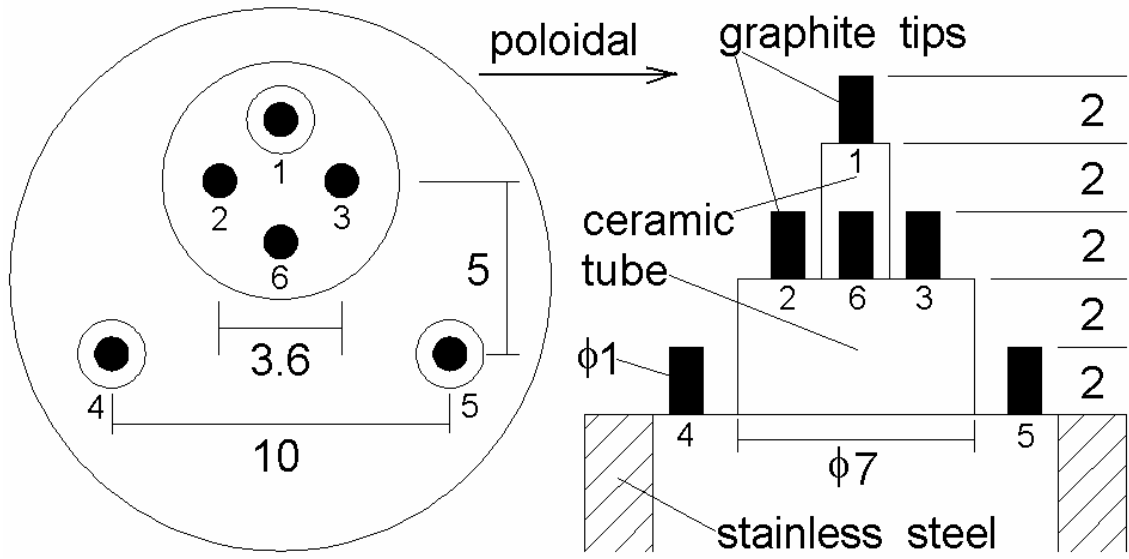
Figure 4 the configuration of pyramid probe array.

Suppression of neoclassical tearing modes towards stationary high-beta plasmas in JT-60U

A. Isayama and the JT-60 team

Naka Fusion Research Establishment, Japan Atomic Energy

Research Institute,

Naka, Ibaraki 311-0193, Japan

Abstract. Results from stabilization of neoclassical tearing modes (NTMs) in JT-60U are described. NTM stabilization and confinement improvement have been demonstrated by employing a real-time NTM stabilization system, where the identification of the location of an NTM and the optimization of the injection angle of electron cyclotron wave are performed in real time. Also, a high-beta plasma with the normalized beta of 3 has been sustained by suppressing NTM by applying electron cyclotron current drive (ECCD) before the onset ('preemptive ECCD'). In addition, a simulation code for analysis of NTM evolution has been developed by combining the modified Rutherford equation with the transport code TOPICS. It is found that the simulation well reproduces NTM behavior in JT-60U. The simulation also shows that ECCD width is also important for NTM stabilization, and that EC wave power for complete stabilization can be reduced by narrowing the ECCD profile.

1. Introduction

In a fusion reactor such as ITER, stationary sustainment of a high-beta and high-confinement plasma is essential. In JT-60U, a high-β_p mode plasma and a reversed shear plasma have been developed as candidates for the Advanced Tokamaks [1]. The high-β_p mode plasma is characterized by a weak positive shear with the central safety factor above unity, and stationary sustainment of a high-β_p H-mode plasma with high integrated performance has been demonstrated in JT-60U [2–6]. In optimizing the discharge scenario of the high-β_p mode plasma, suppression of neoclassical tearing modes (NTMs) is the most critical issue. The NTM is attributed to bootstrap current and appears at a beta value below the ideal limit in positive shear plasmas [7]. Thus, development of a discharge scenario for NTM suppression is an urgent and essential issue. In JT-60U, two scenarios have been developed the NTM suppression: NTM *avoidance* through the optimization of pressure and current profiles, and NTM *stabilization* with electron cyclotron current drive (ECCD) at the mode rational surface. The latter has been performed since the installation of the 110 GHz electron cyclotron (EC) wave injection system in JT-60U. Progress has been also made in simulation of NTM evolution: the transport code TOPICS has been extended by combining with the modified Rutherford equation (MRE) which describes the NTM [8, 9]. The TOPICS simulation enables detailed analysis on magnetic island evolution and NTM stabilization.

This paper describes results from NTM stabilization with ECCD in JT-60U. In Sec. 2, results from simulation of NTM evolution are shown and compared with experimental results. Section 3 describes real-time NTM stabilization experiments. In Sec. 4, results from 'preemptive' ECCD applied to a high-beta plasma are described. Section 5 shows the effect of ECCD profile on stabilization investigated by TOPICS

simulation. And summary of this paper is described in Sec. 6

2. Simulation of NTM stabilization with TOPICS

Evolution of magnetic island associated with an NTM is described by the modified Rutherford equation [7, 10]:

$$\mathrm{d}W/\mathrm{d}t = \Gamma_{\Delta'} + \Gamma_{\mathrm{BS}} + \Gamma_{\mathrm{GGJ}} + \Gamma_{\mathrm{pol}} + \Gamma_{\mathrm{EC}} \tag{1}$$

Here, W is the full width of the magnetic island normalized by the volume-averaged minor radius ρ. $\Gamma_{\Delta'}$, Γ_{BS}, Γ_{GGJ}, Γ_{pol} and Γ_{EC} stand for effects of the equilibrium current profile, the bootstrap current, the toroidal geometry (Glasser-Greene-Johnson effect [11]), the ion polarization current, and the EC-driven current, respectively. Each term contains coefficient which cannot be determined by theory alone. In JT-60U, the coefficients have been determined based on NTM experiments [9].

Temporal evolution of magnetic island width of an $m/n = 3/2$ NTM evaluated with the TOPICS code is shown in Fig. 1(a). Here, m and n are poloidal and toroidal mode numbers, respectively. In this simulation, equilibrium and pressure profile in an NTM experiment are used, and EC wave power P_{EC} of 2.6 MW, which corresponds to 4-unit injection in JT-60U, is injected from $t = 7.6$ s. Other typical parameters are as follows: plasma current $I_{\mathrm{p}} = 1.5$ MA, toroidal field B_{t}=3.6 T, safety factor at 95% flux surface $q_{95} = 3.9$, island width before EC wave injection $W(7.5\text{ s}) = 0.125$, full-width at half-maximum (FWHM) of ECCD profile $W_{\mathrm{EC}} = 0.12$, mode rational surface $\rho_{\mathrm{s}} = 0.4$ in the volume-averaged normalized minor radius ρ. If EC wave is deposited at the island center, the 3/2 NTM is completely stabilized in 1.3 s at $t = 8.8$ s (case A in Fig. 1(a)). Note that the island width quickly decreases when it reaches about 0.04. This spontaneous decay is attributed to the polarization current effect, and it is also
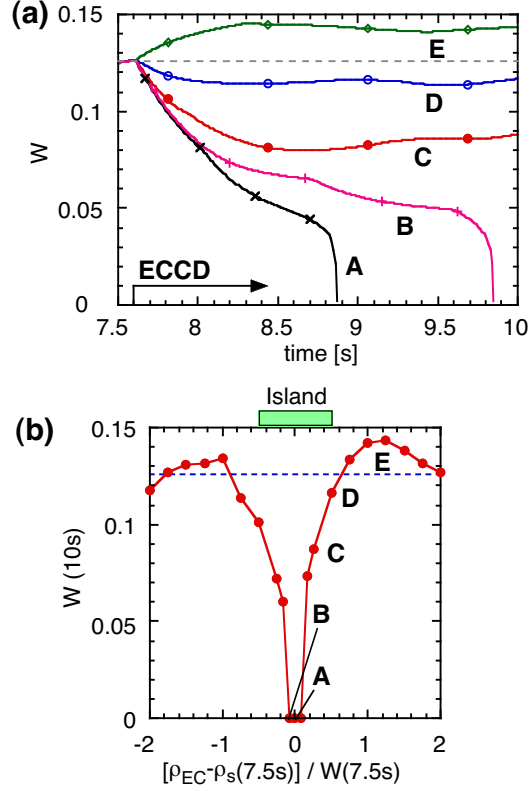
Figure 1. (a) Temporal evolution of magnetic island width for different ECCD locations, and (b) island width at $t = 10$ s. In this simulation, ECCD location is fixed at $\rho = 0.40$ (A), 0.39 (B), 0.43 (C), 0.46 (D), 0.55 (E).

observed in JT-60U experiments.

If the deposition location is misaligned by 0.01 in $\rho = 0.1$, time for stabilization is prolonged (case B in Fig. 1(a)). Figure 1(b) shows the island width at $t = 10$ s, $W(10$ s$)$, for different deposition locations. As shown in this figure, stabilization effect by ECCD is significantly decreased with increasing the distance between ρ_s and ECCD location ρ_{EC}. Complete stabilization can be achieved within the misalignment of $(\rho_{EC} - \rho_s)/W(7.5$ s$) \sim 0.5$, that is, half of the island width. This suggests that precise adjustment of ECCD location is essential, as recognized in experiment. It is notable that island width *increases* when the deposition location is misaligned by about W.

Simulation shows that it is attributed to destabilization effect of the ECCD term due to the misaligned injection.

The above characteristics have been observed in JT-60U experiments [12]. Figure 2 shows a discharge where ECCD location is scanned in a discharge by changing the steering mirror angle. This scan corresponds to the change in the ECCD location from 0.68 to 0.46 in ρ, by which ECCD location crosses the mode rational surface ($\rho \sim 0.5$). Also, an $m/n = 3/2$ mode persists throughout the discharge. Figure 2(b) shows temporal evolution of magnetic perturbations with $n = 2$. The amplitude of the magnetic perturbations first increases ($t =$8.4–9.4 s), suggesting the destabilization effect. The amplitude starts to decrease at $t =$9.4–10.2 s, showing the appearance of the stabilization effect. As the injection angle further increases, the amplitude begins to increase. The scan shows that the optimum injection angle is 43° and actually the NTM is located at $\rho \sim 0.5$.

3. Real-time NTM stabilization

Experiments and simulations show that deposition location of EC wave has to be determined with high accuracy. In addition, mode location can change during a discharge due to current evolution. TOPICS code simulation shows that ECCD can also alter the local current density near the deposition location and thus cause a shift of the mode rational surface, which will result in misalignment of the ECCD location [9]. From this viewpoint, development of real-time NTM stabilization is highly desirable.

In JT-60U, a real-time NTM stabilization system has been developed [5] to track the mode location and optimize the ECCD location during a discharge. In this system, mode location is identified in real time from electron temperature perturbation profile, and EC wave injection angle is adjusted so that EC wave is deposited at the island
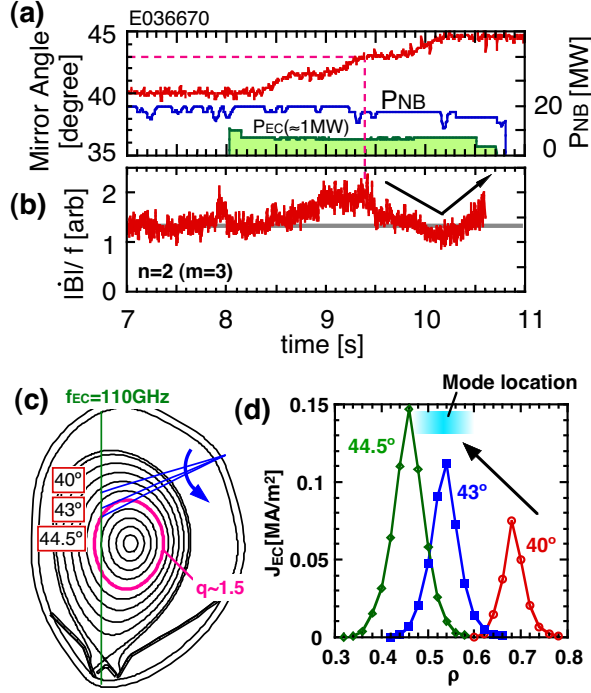
Figure 2. Typical discharge where the injection angle of EC wave is scanned during a discharge. (a) Steering mirror angle and injection power of NB and EC wave, (b) amplitude of magnetic perturbations with $n = 2$, (c) plasma cross section and ray trajectory of EC wave, and (d) EC-driven current density profile.

center. Typical discharge of real-time NTM stabilization is shown in Fig. 3, where a 3/2 NTM is stabilized at $t = 8.8$ s after the EC wave injection at $t = 7.6$ s. As shown in this figure, during the stabilization, angle of the steering mirror is changed according to the result from electron cyclotron emission (ECE) measurement. Values of the normalized beta β_N increases as the NTM is stabilized, and it reaches 1.67 at $t = 10.6$ s. The normalized beta continues to increase even after the turn-off of EC wave, showing that confinement is also improved. Actually confinement enhancement factor against the ITER L-mode scaling H_{89PL} [13] increases from 1.8 to 1.9.

Profile of increment of electron temperature after the EC wave injection is shown in Fig. 3(f), where the peak position of the increment profile corresponds to the deposition
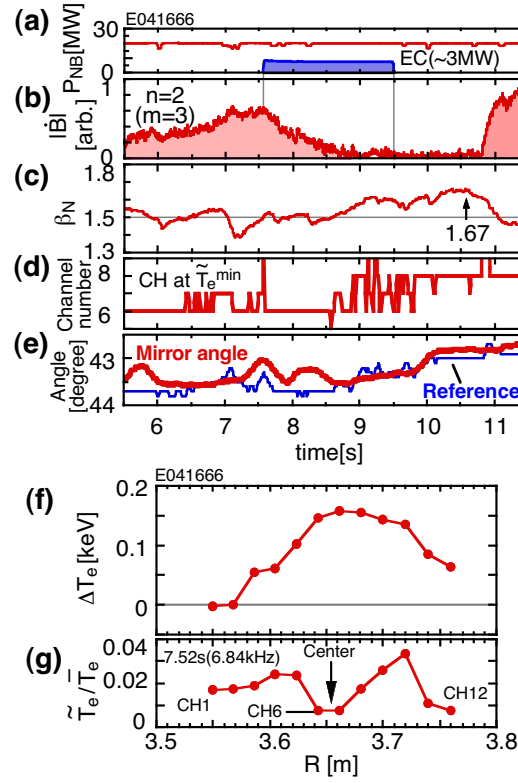
Figure 3. Typical discharge of real-time NTM stabilization. (a) injection power of NB and EC wave, (b) amplitude of magnetic perturbations with $n = 2$, (c) the normalized beta, (d) channel number of ECE diagnostic at minimum amplitude, (e) steering mirror angle, (f) increment profile of electron temperature, and (g) profile of electron temperature perturbation at mode frequency.

location of the EC wave. Amplitude of electron temperature perturbation at the mode frequency (6.8 kHz) is shown in Fig. 3(g). The center of the M-shaped profile corresponds to the island center. The fact that the peak position of the increment profile nearly coincides with the local minimum of the perturbation profile shows that EC wave is actually deposited at the island center.

4. Stabilization with preemptive ECCD

Reduction of EC wave power for NTM stabilization is an important issue because it leads to a more economical reactor. In JT-60U, as a new stabilization scenario, 'preemptive' ECCD has been developed, where EC wave is injected before the onset of an NTM. It was shown that the preemptive ECCD suppresses NTM onset, and that EC wave power required for complete stabilization is smaller by about 20% than the ECCD after the saturation of NTM growth [14].

This scenario has been also applied to high-beta discharges. Figure 4 shows temporal evolution of the normalized beta, auxiliary injection power, and frequency spectrum of magnetic perturbations. In these discharges, the beta value is controlled at $\beta_N = 3$ by feedback on NB power. While a 3/2 NTM is suppressed in shot E44098, it appears in shot E44101 where ECCD location is different by 0.06 in ρ. Improvement in confinement due to the NTM stabilization can be seen in NB power: $\beta_N = 3$ is sustained by smaller amount of NB power in shot E44098. Actually, H_{89PL} in shot E44098 is 2.1 while it is 1.9 in shot E44101.

Details of the mechanism for the efficient stabilization effect of the preemptive ECCD have not been fully understood. In JT-60U, it was shown that the M-shaped amplitude like Fig. 3(f) is not observed for preemptive ECCD [6]. This may suggest that preemptive ECCD can affect the seed island formation and cause different evolution.

As for real-time NTM stabilization, different scheme has to be developed for identification of the mode location because perturbation profile cannot be obtained before the NTM onset. In JT-60U, a system for real-time current profile control has been developed, where safety factor profile is evaluated in real time with motional Stark effect diagnostic [15]. It is expected that the system can be applied for real-time preemptive
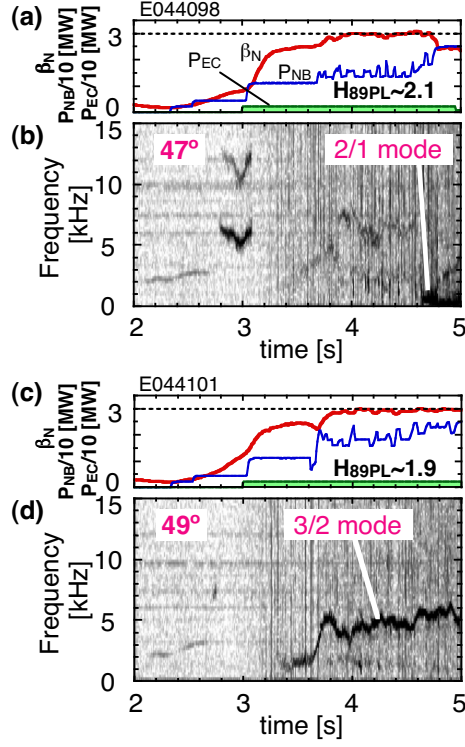
Figure 4. Typical discharges of preemptive ECCD. (a) and (c): the normalized beta and injection power of NB and EC wave; (b) and (d): frequency spectrum of magnetic perturbations.

ECCD.

5. Effect of ECCD profile on stabilization

In NTM stabilization, ECCD profile is important as well as injection power [16]. The effect has been numerically evaluated by TOPICS simulation. Temporal evolution of magnetic island width obtained by the TOPICS simulation is shown in Fig. 5(a), where the FWHM of ECCD profile W_{EC} is changed from 0.09 to 0.24 at fixed EC wave power of 2.6 MW, EC-driven current of 52 kA. Here, $W(7.5 \text{ s})$ is magnetic island width at $t = 7.5$ s (before ECCD) evaluated with ECE diagnostic. It can be seen that the stabilization effect strongly depends on the width of ECCD profile, and that complete
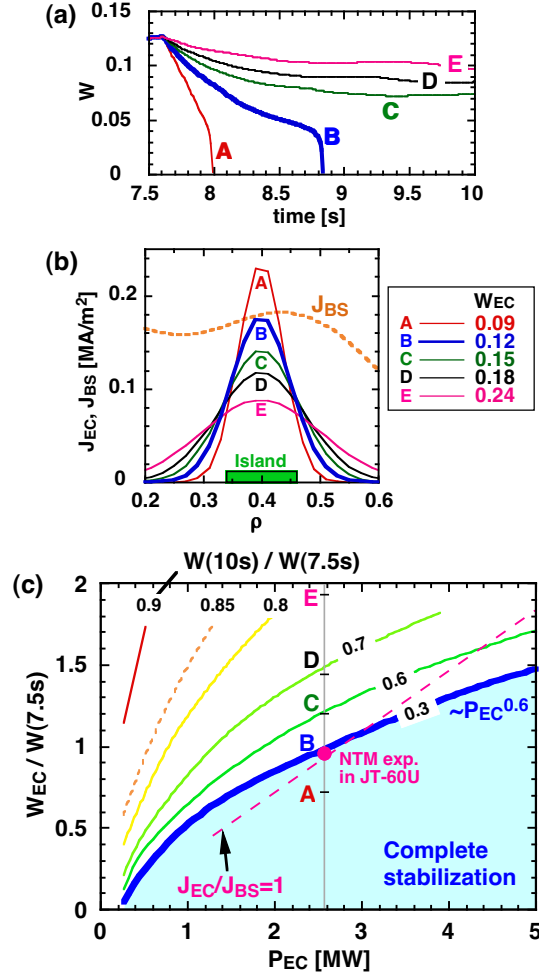
Figure 5. (a) Temporal evolution of magnetic island width, (b) ECCD profile with different values of FWHM, and (c) island width during ECCD as a function of ECCD width and EC wave power.

stabilization can be achieved for cases A and B, that is, $W(7.5 \text{ s})/W_{\text{EC}} \lesssim 1$ at this EC wave power.

The maximum value of the ECCD profile decreases with increasing W_{EC} since injected power is fixed, as shown in Fig. 5(b). Thus, both W_{EC} and P_{EC} must be considered in evaluating the stabilization effect. In Fig. 5(c), island width at $t = 10$ s (during ECCD), $W(10 \text{ s})$, normalized by $W(7.5 \text{ s})$ is plotted as a function of $W_{\text{EC}}/W(7.5 \text{ s})$ and P_{EC}. Magnetic island associated with an NTM is spontaneously

decays due to the polarization current effect when its width is decreased to a certain value. In JT-60U, complete stabilization can be achieved for $W(10 \text{ s})/W(7.5 \text{ s}) \sim 0.3$. The TOPICS code simulation shows that the threshold for complete stabilization increases with $P_{\text{EC}}^{0.6}$.

In the NTM experiment in JT-60U, EC-driven current density J_{EC} is comparable to the bootstrap current density J_{BS} at the mode rational surface (B in Fig. 5(b)). Since the ECCD profile is close to the Gaussian distribution function, the maximum current density linearly increases with decreasing the FWHM under a fixed injection power. This suggests that complete stabilization can be achieved even with $J_{\text{EC}}/J_{\text{BS}} < 1$ if narrow ECCD profile is obtained. ECCD profile is also affected by plasma configuration due to finite Doppler shift: narrower ECCD profile can be obtained when EC wave is injected tangentially with respect to the mode rational surface (see 43° injection in Fig. 2(c)). Thus, optimization of plasma configuration including ECCD profile is essential to achieve effective NTM stabilization.

6. Summary

In JT-60U, experiments and simulations of NTM stabilization using ECCD have been extensively performed with a view to obtaining a stationary high-beta plasma. Complete stabilization and increase in β_{N} and $H_{89\text{PL}}$ have been achieved with a real-time NTM stabilization system. Preemptive ECCD has proven effective also in high-beta regime, and $\beta_{\text{N}} = 3$, $H_{89\text{PL}} = 2.1$ have been sustained without NTM onset. It is shown that TOPICS code simulation well reproduces experimental observations such as narrow range of stabilization effect and destabilization for misaligned ECCD. The simulation also shows that the width of ECCD profile strongly affects the stabilization effect, and narrow ECCD profile is effective in stabilizing the NTMs.

Acknowledgements

[1] Y. Kamada *et al.*, Fusion Sci. Tech. **42**, 185 (2002).

[2] Y. Kamada *et al.*, *Fusion Energy 1996* (Proc. 16th IAEA Fusion Energy Conf., Montreal, 1996), vol. 1, p. 247 .

[3] Y. Kamada *et al.*, Nucl. Fusion **39**, 1845 (1999).

[4] A. Isayama *et al.*, Nucl. Fusion **41**, 761 (2001).

[5] A. Isayama *et al.*, Nucl. Fusion **43**, 1272 (2003).

[6] A. Isayama and the JT-60 Team, Phys. Plasmas **12**, 056117 (2005).

[7] O. Sauter *et al.*, Phys. Plasmas **4**, 1654 (1997).

[8] N. Hayashi, T. Ozeki, K. Hamamatsu, and T. Takizuka, Nucl. Fusion **44**, 477 (2004).

[9] N. Hayashi, A. Isayama, K. Nagasaki, and T. Ozeki, J. Plasma Fusion Res. **80**, 605 (2004).

[10] C. C. Hegna and J. D. Callen, Phys. Plasmas **4**, 2940 (1997).

[11] A. H. Glasser, J. M. Greene, and J. L. Johnson, Phys. Fluids **19**, 567 (1976).

[12] A. Isayama *et al.*, Plasma Phys. Control. Fusion **42**, L37 (2000).

[13] P. N. Yushmanov *et al.*, Nucl. Fusion **30**, 1999 (1990).

[14] K. Nagasaki, A. Isayama, S. Ide, and JT-60 Team, Nucl. Fusion **43**, L7 (2003).

[15] T. Suzuki *et al.*, *Fusion Energy 2004* (Proc. 20th IAEA Fusion Energy Conf., Vilamoura (IAEA, Vienna)), IAEA-CN-116/EX/1-3 (2004).

[16] T. Ozeki, K. Hamamatsu, A. Isayama, and G. Kurita, Fusion Eng. Design **53**, 65 (2001).

Overall feature of EAST operation space by using simple Core-SOL-Divertor model

R. Hiwatari, A. Hatayama[1], S.Zhu[2], T.Takizuka[3] and Y. Tomita[4]
Central Research Institute of Electric Power Industry, Tokyo, JAPAN
[1]*Faculty of Science and Technology, Keio University, Yokohama, JAPAN*
[2]*Institute of Plasma Physics, Chinese Academy of Sciences, Hefei, P.R.China*
[3]*Naka Fusion Energy Establishment, Japan Atomic Energy Research Institute, Ibaraki, Japan*
[4]*National Institute for Fusion Science, Toki, JAPAN*
E-mail: hiwatari@criepi.denken.or.jp

Abstract

We have developed a simple Core-SOL-Divertor (C-S-D) model to investigate qualitatively the overall features of the operational space for the integrated core and edge plasma. To construct the simple C-S-D model, a simple core plasma model of ITER physics guidelines and a two-point SOL-divertor model are used. The simple C-S-D model is applied to the study of the EAST operational space with lower hybrid current drive experiments under various kinds of trade-off for the basic plasma parameters. Effective methods for extending the operation space are also presented. As shown by this study for the EAST operation space, it is evident that the C-S-D model is a useful tool to understand qualitatively the overall features of the plasma operation space.

Keywords: Core transport, SOL-Divertor transport, operation space, EAST

1. Introduction

Consistency between the edge plasma operation and the core plasma operation is an important issue for the design of ITER and the future fusion power plant. In case of the ITER divertor predictive modeling, the fitting scaling laws for divertor plasma property are built with a two dimensional (2D) divertor transport code, and these are used as boundary conditions for the core plasma analysis[1]. Prior to such detailed and massive calculations by multi-dimensional transport codes, it is useful to understand qualitatively the overall features of the plasma operational space including the requirements for the SOL and divertor plasma. For this purpose, we are developing a simple Core-SOL-Divertor (C-S-D) model. The basic concept of the C-S-D model is presented in ref. [2]. In the present paper, we improve the neutral transport model by using the experimental database, and apply this C-S-D model to investigating the steady state plasma operational space of low hybrid current drive (LHCD) experiments for EAST[3].

2. Simple Core-SOL-Divertor Model
2.1. Core plasma and SOL-divertor plasma model

We apply the 0D plasma model based on ITER physics guidelines to the core plasma transport[4]. The usual definitions for the global particle and power balance are applied in the present paper[2], and the particle and energy confinement times are required to solve 0D plasma transport model. The scaling law of the L-mode energy confinement time τ_E^{ITER89L} [4] is applied to the energy confinement time $\tau_E = f_H \tau_E^{\text{ITER89L}}$, where $f_H(=2.0)$ is the confinement improvement factor for H-mode. The particle confinement time τ_p is defined by $\tau_p = C_p \tau_E$, where C_p is the correction factor for each species. In the present paper, $C_p = 1.0$ is assumed. The L-H transition condition is also installed in the same fashion as in ref. [5], where the experimental scaling law[6] is applied to the threshold power.

The two-point model[7] under steady state conditions can be applied with a time dependent core transport model, because the time scale of core plasma transport is much longer than that of SOL-divertor plasma. Basic equations of the usual two-point model are as follows:

$$\left(1 - f_{\text{mom}}^{div}\right) n_s T_s = \left(1 + M_d^2\right) n_d T_d, \tag{1}$$

$$\frac{7}{2}\left(1 - f_{\text{imp}}\right) L_s q_\perp = n_d M_d C_s(T_d) \Delta \left[\varepsilon + \left(\gamma + M_d^2\right) T_d\right], \tag{2}$$

$$\Delta = \frac{5}{2} \chi_\perp \frac{n_s T_s}{q_\perp}, \tag{3}$$

$$L_d^2 q_\perp = \frac{4\kappa_0 \Delta}{49} T_s^{7/2} \left[1 - \left(\frac{T_d}{T_s}\right)^{7/2}\right], \tag{4}$$

where n and T are density and temperature. The subscript "s" and "d" express the upstream SOL and divertor region, respectively. The heat flux from the core plasma, temperature decay length, and Mach number at the divertor plate are defined by $q_\perp$, Δ, and M_d, respectively. The coefficients f_{mom}^{div} and f_{imp} are the fraction of momentum loss and impurity radiation loss. The coefficient $\gamma (\approx 7.0)$ is the sheath energy transmission coefficient, and the heat load $\varepsilon (\approx 21.8 \text{eV})$ on the plate comes from the recombination and radiation process[8].

2.2. Particle balance to determine the upstream SOL density

In order to integrate the core and edge plasma model, the upstream SOL density n_s should be given in a self-consistent manner both for the core plasma and for the edge plasma. For this purpose, the particle balance equation in the SOL and divertor regions is used. We assume that all neutral particles originate at the divertor plate at the rate proportional to the total particle flux to the divertor plate. Consequently, the total neutral source rate at the edge region N_n including gas puff term N_{puff} is as follows:

$$N_n = C_n \frac{1}{2}\left(1 - \frac{1}{e^2}\right) n_d M_d C_s 2\pi R \Delta_n \sin(\psi) + N_{\text{puff}}, \tag{5}$$

where Δ_n is the density decay length. We assume that $\Delta_n = 2\Delta$. ψ is the angle of the magnetic field to the divertor plate. The term $\left(1/2\right)\left(1 - 1/e^2\right)$ comes from the integration of the radial direction (from the separatrix to the density decay length Δ_n) on the divertor plate. The coefficient C_n is a calibration factor and $C_n = 0.5$ is assumed (This value is derived from the following comparison with the experimental database). By using the simple neutral model and the particle flux across the separatrix, Γ_{core}, from the 0-D core plasma calculation, the particle balance equation for the SOL-divertor region becomes

$$\Gamma_{\text{core}} S_{\text{core}} + N_n^{\text{sol}} + N_n^{\text{div}} = \frac{1}{2}\left(1 - \frac{1}{e^2}\right) n_d M_d C_s 2\pi R \Delta_n \sin(\psi) \tag{6}$$

where $N_n^{\text{div}} = f_{\text{ion}}^{\text{div}} N_n$ and $N_n^{\text{sol}} = f_{\text{ion}}^{\text{sol}}\left(1 - f_{\text{ion}}^{\text{div}}\right) N_n$. $f_{\text{ion}}^{\text{div}}$ and $f_{\text{ion}}^{\text{sol}}$ are the ionization fraction in the divertor and the SOL region, respectively. S_{core} is the core plasma surface normal to the particle flux. The ionization fraction in the divertor region is modeled by[9]

$$f_{\text{ion}}^{\text{div}} = 1 - \exp\left(-\frac{L_d \sin(\psi)}{\lambda_{\text{ion}}^{\text{div}}}\right) \tag{7}$$

where $\lambda_{\text{ion}}^{\text{div}} = v_n / \left(n_d < \sigma v >_{\text{ion}}\right)$ is defined by the ionization cross section $< \sigma v >_{\text{ion}}$, which is the strong function of T_d, and the neutral velocity $v_n = \sqrt{T_n / m}$. In the present paper, the neutral temperature of $T_n = T_d$ is assumed. The ionization fraction in the SOL region is defined by

$$f_{\text{ion}}^{\text{sol}} = \frac{A_{\text{sol}}}{A_{\text{core}} + A_{\text{sol}} + A_{\text{pump}}} \tag{8}$$

where A_{core}, A_{sol} and A_{pump} are the effective areas for the core region, the SOL region, and the pumping effect from the divertor region, respectively. In this paper, the effective areas of A_{core} and A_{sol} are assumed by each cross section area on the plasma midplane, i.e., $A_{core} = 2\pi R \cdot a$ and $A_{sol} = 2\pi R \cdot \Delta_n$. The effective area of A_{pump} is defined by $A_{pump} = C_{pump}/(v_n/4)$, where C_{pump} is the speed of the pumping system[10], but the pumping effect is not considered in the present paper($C_{pump} = 0.0$).

To check the validity of this C-S-D model, comparison with the edge transport code (B2-EIRENE) is carried out. We have focused on the JT-60U L-mode discharge in the high recycling state (Table 1)[11]. The density and the temperature for divertor-SOL region against the total particle flux across the separatrix Φ_p are shown in Figure 1, where the superscripts of "CSD" and "B2" correspond to the C-S-D model and B2-EIRENE code, respectively. Qualitatively, the result of the C-S-D model is similar to that of B2-EIRENE. Quantitatively, the difference in temperature becomes large over $\Phi_p = 1.5 \times 10^{22}$ (s^{-1}), mainly because B2-EIRENE result corresponds to the detached plasma state, which is not considered in the present C-S-D model. From this comparison, it is noted that the results by the C-S-D model are reasonable in a qualitative sense. Around $\Phi_p = 1.0 \times 10^{22}$ (s^{-1}) density of the C-S-D model suddenly increases and temperature decreases sharply in Figures 1, which is considered to be the transition from a low to a high recycling state[12].

Comparison with the JT-60U divertor recycling database[13] is also carried out. In this simple neutral model, the total ion flux on the plate is the key parameter, and Figure 2 shows its comparison between the C-S-D model (P$_{NBI}$=0.5~4.0MW, Bt=4T) and the database (P$_{NBI}$=1~12MW, Bt=2~4T). The result from C-S-D model is quantitatively consistent with the database, and it also reproduces the nonlinearity of the total ion flux against the plasma density. The comparison of the total neutral flux from the divertor region is shown in Figure 3. In the case of the calibration factor $C_n = 0.5$ in eq.(5), the result from the CSD model is roughly agreeable with the database and this calibration factor is applied in the present paper.

3. EAST fully non-inductive operation space by low hybrid current drive
3.1. Main trade-offs for the operation space

In the initial phase of the EAST plan, current drive experiments are planned to be carried out by LHCD[3]. Low density operation is preferable for good current drive efficiency. On the other hand, such operation is disadvantageous to the divertor performance, because it generally results in a high heat load on the divertor plates. As for the steady state experiment with high performance plasma such as H-mode, reduction of the heat load onto the divertor plate is a critical issue. Considering discussions above, we take into account the following trade-offs, or constraints, i.e., 1) available LHCD power, 2) allowable heat load to the divertor plates, 3) available heating power for sustaining the steady state power balance in the core and also 4) threshold power for L-H transition.

Based on the particle and power balance of the core plasma[2,4], the total particle flux Φ_p and the total heat flux Q_{in} across the separatrix are $\Phi_p = (n_{20}V_p)/(C_p\tau_E)$ and $Q_{in} = (0.048n_{20}TV_p)/\tau_E$, respectively ($V_p$ is the plasma volume). From these quantities and the definition of the energy confinement time, the temperature and the density of the core plasma are written as $T = C_T Q_{in}/\Phi_p$ and $n_{20} = C_d \Phi_p^{10/9}/Q_{in}^{5/9}$, respectively (where C_T and C_d are functions of the core plasma parameters). With these equations, we express the following trade-offs, or constraints as functions of (Q_{in}, Φ_p), and discuss the plasma operation space on (Q_{in}, Φ_p).

The power required for LHCD is estimated by the following model[14];

$$P_{\text{LHCD}} = \frac{R\ln\Lambda I_{\text{p}}}{0.122\left(j^*/p^*\right)}\frac{n_{20}}{T} \tag{9}$$

The available LHCD power and plasma current I_{p} in Eq.(9) are set to be 3.5 MW and 1.0 MA for the EAST[3]. Then, Eq. (9) is written as

$$\frac{R\ln\Lambda}{0.122\left(j^*/p^*\right)}C_{\text{n}}\Phi_{\text{n}}^{19/9}C_{\text{T}}^{-1}Q_{\text{in}}^{-14/9} \le 3.5. \tag{10}$$

where $\left(j^*/p^*\right) = 10$ is assumed in the present paper. In addition, the total heating power for the EAST is set to be 7.5 MW[3], then the following relationship has to be considered,

$$P_{\text{LHCD}} \le Q_{\text{in}} \le 7.5. \tag{11}$$

The left inequality in Eq.(11) is rewritten as

$$Q_{\text{in}}^{23/19} \le \frac{R\ln\Lambda I_{\text{p}}}{0.122\left(j^*/p^*\right)}\frac{C_{\text{n}}}{C_{\text{T}}}\Phi_{\text{p}}^{19/9} \tag{12}$$

The scaling law of the threshold power for the LH transition can also be written as the function of Φ_{p} and Q_{in},

$$Q_{\text{in}} \ge P_{\text{thr}} = 2.75B_{\text{t}}^{0.96}R^{1.23}a^{0.76}M_{\text{i}}^{-1}C_{\text{n}}^{0.77}\left(\frac{\Phi_{\text{p}}^{7.7}}{Q_{\text{in}}^{3.85}}\right)^{1/9} \tag{13}$$

where M_{i} is the average ion mass (amu). The heat flux q_{div} to the divertor plates is limited to the maximum allowable heat flux q_{max} from the engineering viewpoint. This condition is expressed as

$$q_{\text{div}} = \left[\varepsilon + \left(\gamma + M_{\text{d}}^2\right)T_{\text{d}}\right]n_{\text{d}}M_{\text{d}}C_{\text{s}}\sin(\psi)\sin(\theta) \le q_{\text{max}} \tag{14}$$

where θ denotes the inclination angle of the divertor plate to the magnetic lines force in the poloidal plane. Eq.(14) can also be expressed by Φ_{p} and Q_{in} defined above. The q_{max} is taken to be 3.5MW/m², which corresponds to the averaged value estimated in ref.[3]. Finally, we obtain the four inequalities, i.e., Eqs.(10), (12), (13) and (14), for the trade-off relationships of LHCD experiments.

3.2. Basic and qualitative features for EAST operational space

The main parameters of EAST are summarized in Table 1[3]. With these parameters, we explore the possible operation space in the $\left(Q_{\text{in}},\Phi_{\text{p}}\right)$ space as shown in Figure 4. The operational space is painted, and each boundary is the operation condition as mentioned in the previous subsection. Figure 4 indicates that the allowable heat flux to the divertor plate is a key parameter to extend the possible operation space. The upper boundary of Q_{in} is limited to $3.0-3.5(\text{MW})$ by $q_{\text{div}} \le 3.5(\text{MW/m}^2)$. The boundary of $q_{\text{div}} \le 3.5(\text{MW/m}^2)$ for $Q_{\text{in}} \le 3.0(\text{MW})$ region implies a decrease of q_{div} by the transition from the low to the high recycling state. The upper boundary of the particle flux Φ_{p} is dominated by the power balance requirement for the low Q_{in} region, while it is limited by the available LHCD power for higher Q_{in}. In other words, the available power for the LHCD tends to be a key parameter to extend the operation density of the core plasma in this high Q_{in} regime. In this exploration, no gas puffing in the divertor region is assumed. The sudden changes in the curve for the required LHCD power and the power balance around $\left(Q_{\text{in}},\Phi_{\text{p}}\right) \approx \left(1.5\,\text{MW}, 1.5\times10^{21}\,\text{s}^{-1}\right)$ are caused by the LH transition.

To extend the operational space, the following methods have been investigated in a qualitative sense. In this series of investigations, the remaining parameters except the key parameter in the following methods are kept at the same values as those in Figure 4. To extend the operational space, the divertor temperature has to be reduced. Gas puffing in the edge region is one of the candidates for the decrease of

the divertor temperature. When $N_{\text{puff}} = 1.0 \times 10^{21}\,\text{s}^{-1}$ (which corresponds to about 5% of the total neutral source rate N_{n}) is fuelled in the divertor region, the operational space is extended toward both the lower particle flux range of $\Phi_{\text{p}} \approx 1.0 \times 10^{21}\,\text{s}^{-1}$ and the higher heat flux range of $Q_{\text{in}} = 3.3 - 4.0$ MW(Figure 5(a)). The impurity seeding in the SOL-divertor region is also one of the candidates to extend the operation boundary. When it is possible to increase up to $f_{\text{imp}} = 0.6$ of the impurity radiation loss fraction similar to the ITER divertor design, then the upper boundary of Q_{in} is extended up to $Q_{\text{in}} \approx 5.0$MW (Figure 5(b)). Of course, the impact of the impurity seeding on the core plasma performance should be carefully checked by more detailed numerical simulations, because f_{imp} is given as the input parameter in the C-S-D model. In addition, the effect of impurity seeding on the efficiency of LHCD is not calculated, either. By using the C-S-D model, it is revealed that gas puffing is an effective method to extend the operational space toward both the lower Φ_{p} and higher Q_{in} region. On the other hand, achievement of $f_{\text{imp}} = 0.6$ has the possibility to extend up to $Q_{\text{in}} \approx 5.0$ MW region.

4. Summary

The C-S-D model has been developed to investigate the overall and integrated features of the core and edge plasma in tokamaks, and applied to the analysis of the EAST operational space. The basic features of possible operational space have been studied for the LHCD steady-state operation. Various kinds of trade-off have been taken into account in the analysis. Furthermore, we have confirmed that gas puffing and impurity seeding in the edge region have the potential to extend the operational space. From these applications to the study of the EAST operation space, the C-S-D model is shown to be a useful tool to understand qualitatively the overall features of the operational space for future reactors under various kinds of trade-off.

Acknowledgement

References

[1] A. S. Kukushkin,*et al*, IAEA-CN77/CT/P-07, *Proc. 19th IAEA Fusion Energy Conf. (Lyon, France, 2002),* G. W. Pacher, *et al.*, Nucl. Fusion **43** (2003) 188.
[2] R. Hiwatari, *et al*, Contrib. Plasma Phys 44(2004)76.
[3] S.Zhu, Contrib. Plasma Phys. **40**(2000)322.
[4] N. Uckan and ITER Physics Group 1990 ITER Physics Design Guidelines:1989 *ITER Documentation Series No.10*
[5] T. Yamamoto, *et al.*, Fusion Eng. Des. **39-40**(1998)143.
[6] ITER Physics Expert Groups on Confinement and Transport and Confinement Modeling and Database, ITER Physics Basis Editors, Nucl. Fusion **39**(1999)2175.
[7] K.Borrass, Nucl. Fusion **31**(1991)1035.
[8] S.Takamura, J. Plasma Fusion Res. **72**(1996)866 (in Japanese).
[9] N.Hayashi, et al., J. Phys. Soc. Japan **66**(1997)3815.
[10] M. Sugihara, et al., J. Nucl. Mater. **241-243**(1997)299-304.
[11] A. Hatayama, *et al.*, Nucl. Fusion **40**(2000)2009, J. Nucl. Mater. **290–293**(2001)407.
[12] M. Sugihara, *et al.*, J. Nucl. Mater. **128–129**(1984)114.
[13].T.Takizuka, *et al.*, "Development of Database for the Divertor Recycling in JT-60U and Its Analysis" JAERI-Research 2003-010 (2003) (in Japanese)

[14] S.Takamura, Purazuma Kanetsu Kisoron, Nagoya Daigaku Shuppankai (1986) (in Japanese).

Table 1. Main plasma parameters of
JT-60U[11] and EAST[3].

	JT-60U	EAST
R/a (m)	3.4/0.8	1.97/0.5
κ_{95}/δ_{95} (−)	1.5/0.5	1.6/0.8
B_t (T)	3.5	3.5
I_p (MA)	1.8	1
P_{LHCD}/P_{aux} (MW)	-/-	3.5/7.5
Q_{in} (MW)	2.5	-
L_s/L_d (m)	50/3.0	31/4.3
f_{imp} (−)	0.3	0.3

Figure 3.Total neutral flux from the divertor region. The shaded region (the dot) corresponds to C-S-D model (JT-60U recycling database[13]). The calibration factor $C_n = 0.5$ for the neutral transport model is applied.

Figure 1. The SOL-divertor parameters vs. the total particle flux Φ_p: (a) density, (b) temperature by the C-S-D model and the B2-EIRENE.
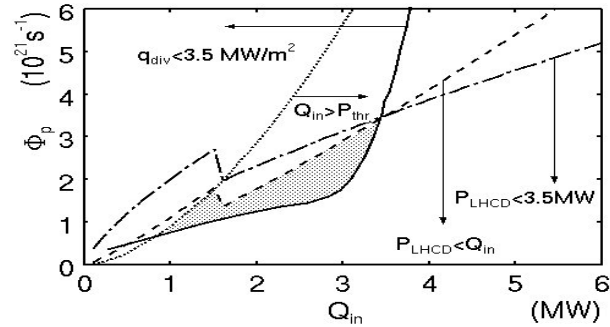
Figure 4. Qualitative features of EAST operational space.

Figure 2. Total ion flux to the divertor plates. The shaded region (the dots) corresponds to C-S-D model (JT-60U recycling database). The ion flux to the plates has a nonlinearity(~n_e for low density region, ~$n_e^{1.5}$ for high density region)[13].

Figure 5. The effect on gas puffing (a) and the impurity seeding (b) on the EAST operational space.

6

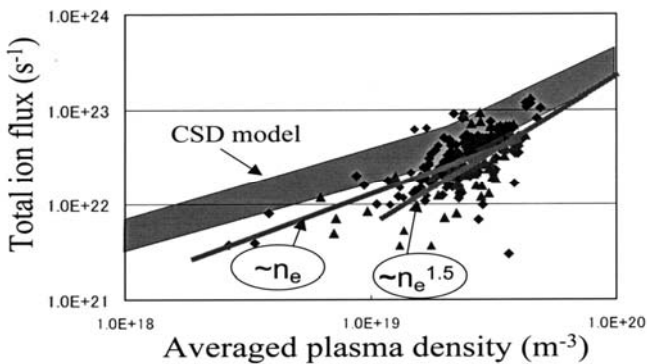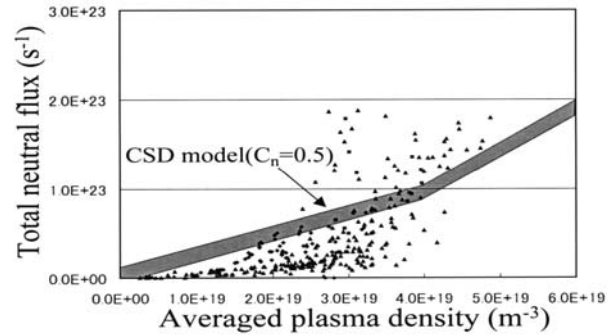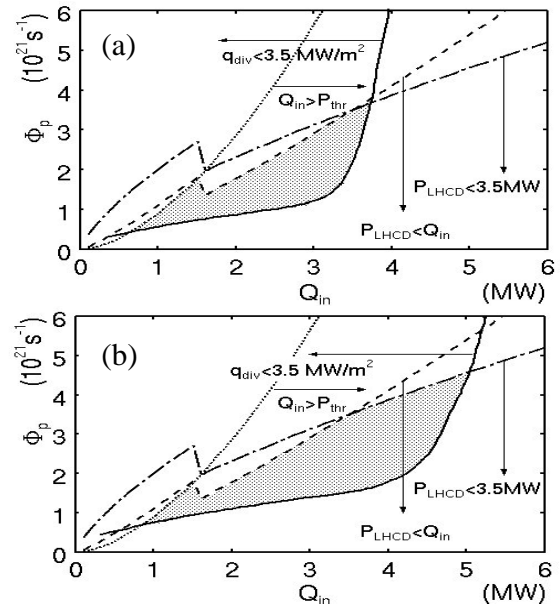# Assessments of flow drive by use of Ion Bernstein Wave on Heliotron-J and EAST devices

Yuki Torii, Hiroyuki Okada, Tetsuo Watari[1], Hiroki Kitagawa[2], Yasuhiro Suzuki[1], Masayuki Yokoyama[1], Yanping Zhao[3], Kazunobu Nagasaki

Institute of Advanced Energy, Kyoto University, Uji, Japan
[1]National Institute for Fusion Science, Toki, Japan
[2]Graduate school of Energy Science, Kyoto University, Kyoto, Japan
[3]Institute of Plasma Physics, Hefei, China

e-mail : torii@center.iae.kyoto-u.ac.jp

Abstract

The assessments of poloidal flows driven by ion Bernstein waves in Heliotron J and EAST plasma are carried out by use of a ray tracing method. Sheared poloidal flow is expected to suppress plasma turbulences. In Heliotron J and EAST plasma, the rays travel into the central region with oscillations along the magnetic lines of force and the power are absorbed by ions at the cyclotron resonance layers. Momentum inputs are estimated by a simple method and the poloidal flows are estimated with the neoclassical viscosities. In both devices, the momentum inputs with variation of their sign with the minor radii are obtained and sheared poloidal flows are driven.

Introduction

Turbulence suppression of magnetic confined plasma is one of key roles for nuclear fusion research. A sheared poloidal flow driven by ion Bernstein waves (IBWs) is expected to the turbulence suppression[1]. In some tokamaks, it is reported that confinement improvement was observed during IBW heating[2].

In this research, we estimated wave trajectories, power absorption, and momentum inputs of IBW on Heliotron J and EAST (HT-7U) device. The driven poloidal flows are also estimated by use of the neoclassical viscosity.

Heliotron J device and EAST device

Heliotron J is an l=1/ m=1 helical axis heliotron device and is composed of straight sections and corner sections. In the corner sections, the magnetic configuration is

similar to that in tokamaks. In this research, the ray of IBWs is started at this section.

EAST device is tokamak device with super conducting coils and is being constructed at Institute of Plasma Physics, Chinese Academy of Science. In this research, for simplicity, it is assumed that the magnetic field configuration is that of an axisymmetric tokamak with a circular poloidal cross-section, of which the magnetic field is defined in Ref. [3]. The major and minor radii are assumed to be 1.7m and 0.4m, respectively, which are the same of those of the EAST.

Wave trajectory and power deposition

In the ray tracing calculation, since only IBWs propagate in plasma, the dispersion relation of electrostatic waves is used.

A ray trajectory in Heliotron J plasma is shown in Fig. 1. In this calculation, the ray of IBW with 16.8MHz of the frequency and 3.0m^{-1} of the wave number parallel to the magnetic field starts at the point of $\rho=0.89$ on the equatorial plane in the corner section, where ρ is the normalized minor radius. The working gas is deuterium, the magnetic field strength on the axis is chosen to be 1.3T, and the second harmonic deuterium ion cyclotron resonance layer is located at $\rho=0.65$. The density and temperature profiles are assumed as $n_e=n_{e0}(1-\rho^8)$ and $T_e=T_i=T_{e0}(1-\rho^2)$ and the central values of the electron density n_{e0} and temperature T_{e0} are $1.0\text{X}10^{19}\text{m}^{-3}$ and 200eV, respectively. The ray travels into the central region with an oscillation along the magnetic line of force. In the vicinity of the second harmonic ion cyclotron resonance layer, almost all wave power is absorbed through the ion cyclotron damping.

A wave trajectory in EAST is plotted in Fig. 2. In this calculation, the working gas and the magnetic field strength on the axis are deuterium and 3.5T, respectively. The central electron density and temperature are $5.0\text{X}10^{19}\text{m}^{-3}$ and 800eV, respectively. The profiles are the same as those in Heliotron J. A ray with 48MHz of the frequency and 5.0m^{-1} of the parallel wave number is started at $\rho=0.875$ on the equatorial plane. The second harmonic ion cyclotron resonance layer is located at $\rho=0.5$. Similar to that in Heliotron J, the ray travels into the central region with an oscillation along the magnetic line of force. Almost all wave power is absorbed by ions through ion cyclotron damping in the vicinity of the ion cyclotron resonance layer.

Momentum input

By use of the ray tracing calculation, momentum input is estimated. In this research, the momentum input is calculated by taking analogy with quantum mechanics, where momentum of a photon is $\hbar\vec{k}$ with $\hbar$, the Planck constant. Momentum input may be written as

$$\Delta\vec{p} = -\Delta(I\vec{k}) \qquad (1)$$

where I is the ratio of the wave power to the initial wave power.

Figure 3 shows the radial profile of the momentum input in Heliotron J. The broken and solid lines show momentum input parallel to the magnetic field, $\Delta p_{//}$,

and that parallel to $\vec{B}\times\nabla\Psi$, $\Delta p_{\perp}$, where $\vec{B}$ and Ψ are the magnetic field and the

toroidal magnetic flux, respectively. The $\vec{B}\times\nabla\Psi$ direction is almost the poloidal direction. Hereafter, $\Delta p_{//}$ and $\Delta p_{\perp}$ are referred to as the parallel and perpendicular momentum input. Until the cyclotron damping occurs, the parallel momentum input occurs and varies its sign with the minor radius since the ray trajectory has the oscillation. In a similar way, the perpendicular momentum inputs varies its sign, but the amplitude of the variation is small. The momentum input in the radial direction, which is not shown in the figure, is locally strong at the cyclotron resonance layer. This is due to the local cyclotron damping of the power of the IBW with the large perpendicular refractive index. However, this component does not drive the poloidal flow.

The momentum input in EAST is shown in Fig. 4. As in the case of the results of Heliotron J, both the parallel and perpendicular momentum inputs vary their sign before the cyclotron damping, except that the amplitudes of the variation of the parallel and perpendicular inputs are about the same. The strong momentum input in the radial direction occurs.

Driven poloidal flow

For estimation of flow velocity, viscosity needs to be considered. The parallel and toroidal viscosities are [4]

$$\begin{cases} \left\langle \vec{B}\cdot\nabla\cdot\vec{\ddot{\pi}} \right\rangle = 3\left(\mu^{P}\vec{V}\cdot\nabla\theta + \mu^{t}\vec{V}\cdot\nabla\zeta\right) \\ \left\langle \vec{B}_{t}\cdot\nabla\cdot\vec{\ddot{\pi}} \right\rangle = 3\left(\mu_{t}^{P}\vec{V}\cdot\nabla\theta + \mu_{t}^{t}\vec{V}\cdot\nabla\zeta\right) \end{cases} \qquad (2)$$

where, $\vec{B}_{t}$, $\vec{\ddot{\pi}}$, and $\vec{V}$ are the toroidal magnetic field, the viscosity tensor, and the

flow velocity, respectively, and μ^P, μ^t, μ_t^P, and μ_t^t are coefficients related to viscosity. Here, the Hamada coordinates (V, θ, ζ) are used, where V, θ, and ζ are the volume enclosed by the toroidal flux, the poloidal and toroidal angles, respectively. The angle bracket denotes the averaging along the flux surface. The employed conditions both of Heliotron J and of EAST are in the plateau regime. The four coefficients in this regime are written in Ref. [4]. By coupling with Eq. (2) and the MHD equation in steady state, poloidal flow velocity in non-axisymmetric configuration is obtained as

$$V^\theta = \frac{\mu_t^t \left\langle \vec{B} \cdot \vec{F}_{\text{ext}} \right\rangle - \mu^t \left\langle \vec{B}_t \cdot \vec{F}_{\text{ext}} \right\rangle}{3\left(\mu^P \mu_t^t - \mu_t^P \mu^t\right)} \qquad (3)$$

where $V^\theta = V \cdot \nabla \theta$ and $\vec{F}_{ext}$ are the poloidal contravariant components of the flow velocity and the external force, respectively. In the case of axisymmetric configuration, where μ^t, μ_t^P, and μ_t^t become zero, the poloidal flow velocity is obtained as

$$V^\theta = \frac{\left\langle \vec{B} \cdot \vec{F}_{\text{ext}} \right\rangle}{3\mu^P} \qquad (4)$$

Regarding the external force as the momentum input per unit volume and time, the flow velocity is estimated. The flow velocity profiles in Heliotron J and EAST plasma are shown in Fig. 5 and 6, respectively. In both cases, the injected power is 200kW. It is noted that, in EAST configuration, angles θ and ζ in Hamada coordinates are approximated by the orthogonal poloidal and toroidal angles, respectively. In the case of Heliotron J, poloidal flow is driven before the cyclotron damping occurs and varies its sign with the minor radius. In the same way of the momentum input, the variation of the poloidal flow is due to the oscillatory motion of the ray. As in the case of Heliotron J, the driven poloidal flow in EAST varies its sign with the minor radius.

The poloidal flow shears in the case of Heliotron J and EAST are in the order of 10^7/sec, which exceeds those observed in practical experiments in tokamaks such as PBX-M[5]. The results imply that heating by traveling ion Bernstein waves with narrow $k_{//}$ spectrums drives strong sheared poloidal flow.

Summary

   In order to assess the poloidal flow driven by IBWs in Heliotron J and EAST plasma, the ray trajectories and the power absorption are estimated. In the both case of Heliotron J and EAST, the rays travel into the central regions with oscillations along the magnetic lines of force and almost all wave power are absorbed by ions in the vicinity of the second harmonic ion cyclotron resonance layers. Momentum inputs are calculated by taking an analogy with quantum mechanics. In plasma both of Helitron J and of EAST, the perpendicular and parallel momentum inputs with variations of their sign with the minor radii are obtained before the cyclotron damping occurs. By taking the viscosity in the plateau regime, the poloidal flow velocity driven through the momentum input is estimated. The poloidal flows are driven before the cyclotron damping occurs and varies its sign with the minor radii in both configurations and the obtained poloidal flow shears are larger than those observed in IBW heating experiments in tokamaks. Obtained result may imply that strong sheared flow is driven by traveling waves of ion Bernstein waves with narrow spectrum of the parallel wave number.

References
[1] E. F. Jaeger, L. A. Berry, D. Batchelor, Phys. Plasmas, 7 (2000) 641
[2] M. Ono, Phys. Fluids B, 5 (1993) 241
[3] K. L. Wong, M. Ono, Nucl. Fusion, 23 (1983) 805
[4] K. C. Shaing, S. P. Hirshman, J. D. Callen, Phys. Fluids, 29 (1986) 521
[5] B. LeBlanc, S. Batha, R. Bell, et al., Phys. Plasmas, 2 (1995) 741

Figure caption

Fig. 1

Top view of a ray trajectory in Heliotron J plasma. The ray starts at (x, y, z)=(1.49m, 0.0m, 0.0m) and the power is absorbed near the 2nd ion cyclotron resonance layer.

Fig. 2

Top view of a ray trajectory in EAST plasma. The ray starts at (x, y, z)=(2.05m, 0.0m, 0.0m) and the power is absorbed near the 2nd ion cyclotron resonance layer.

Fig. 3

Radial profile of momentum input in Heliotron J plasma. Solid and broke lines show the profiles of $\Delta p_{\perp}$ and $\Delta p_{//}$, respectively.

Fig. 4

Radial profile of momentum input in EAST plasma. Solid and broke lines show the profiles of $\Delta p_{\perp}$ and $\Delta p_{//}$, respectively.

Fig. 5

Radial profile of the poloidal flow velocity in Heliotron J plasma.

Fig. 6

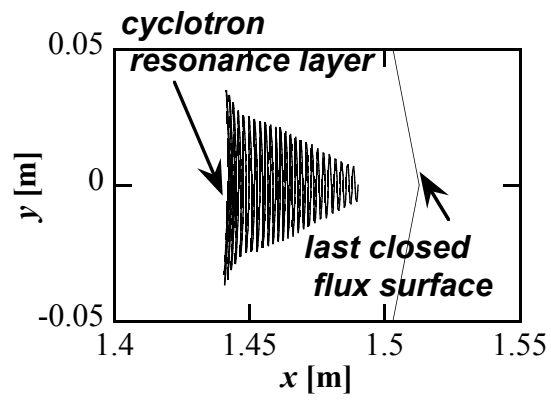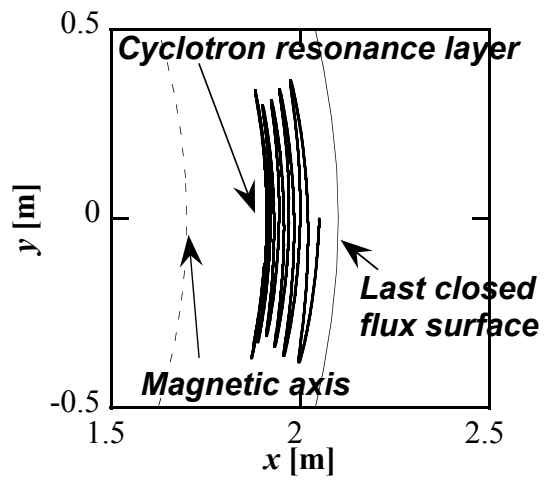Radial profile of the poloidal flow velocity in EAST plasma.

Figure 1:

Figure 2:

1

Figure 3:

Figure 4:

2

Figure 5:

Figure 6:

3
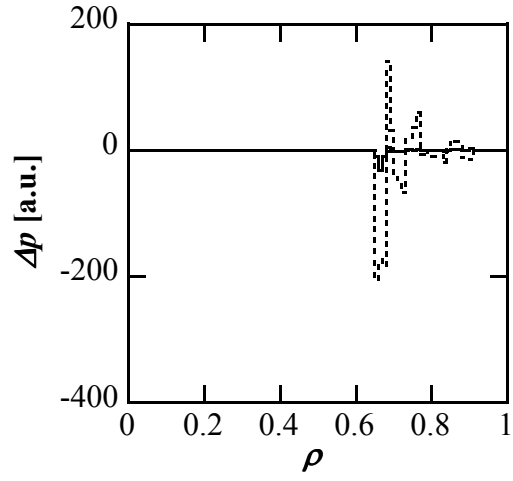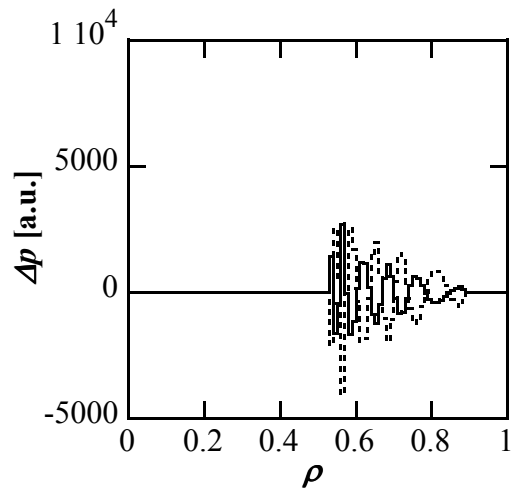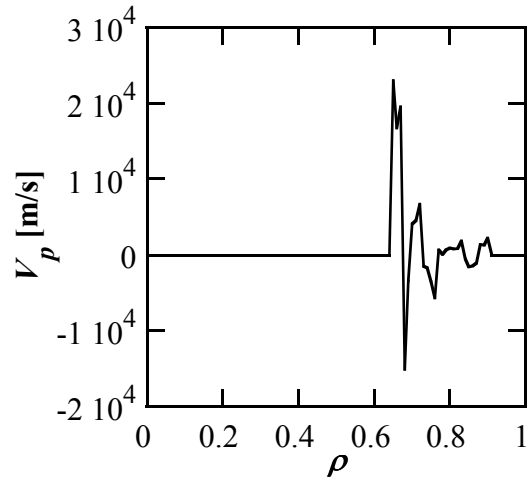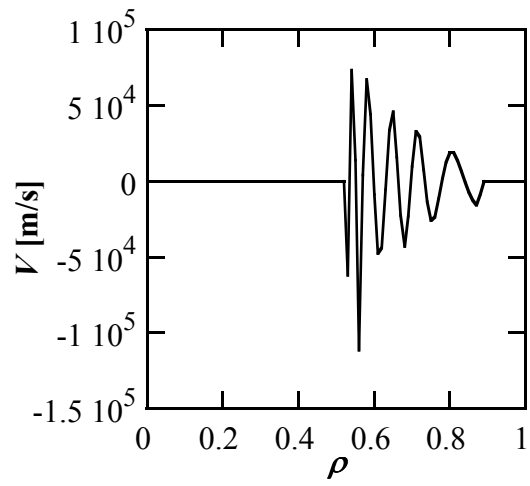
Advanced Tokamak Equilibrium Theory

Shaojie Wang and Jun Yu

Institute of Plasma Physics, Chinese Academy of Science

ABSTRACT

A theoretical model is proposed to study the advanced tokamak equilibrium configuration with plasma current density reversal. With the proposed Grad-Shafranov-Helmholtz equation, an approximate analytical solution is found in the toroidal coordinate system for a circular cross-section tokamak, and an exact analytical solution is found in the cylindrical coordinate system for a rectangular cross-section tokamak.

The analytical solution shows that current density reversal equilibrium configurations exist with continuous current density and finite plasma pressure, and that the central current density reversal is accompanied by axisymmetric magnetic islands and pressure gradient reversal.

In applying the theory to model the recent alternating current operation [Huang, et al., Nucl. Fusion 2000], it is found that the theoretical results agree well with the experimental measurements in the loop voltage, the current density, the beta value, and the flux surface.

Magnetic Sensorless Control of Plasma Position

and Shape in a Tokamak

K. Nakamura, J. R. Luo[1], H. Z. Wang[1], Z. S. Ji[1], H. Wang[1], F. Wang[2], N. Qi[1],

K. N. Sato, K. Hanada, M. Sakamoto, H. Idei, M. Hasegawa,

S. Kawasaki, H. Nakashima, A. Higashijima

Research Institute for Applied Mechanics, Kyushu University,

Kasuga City, Fukuoka, 816-8580 Japan

[1] *Institute of Plasma Physics, Chinese Academy of Sciences,*

P. O. Box 1126, Hefei, 230031, P. R. China

[2] *Interdisciplinary Graduate School of Engineering Sciences, Kyushu University,*

Kasuga City, Fukuoka, 816-8580 Japan

e-mail: nakamura@triam.kyushu-u.ac.jp

Abstract

Magnetic sensorless sensing and control experiments of the plasma horizontal position have been carried out in the superconducting tokamak HT-7. The sensing is made focusing on the ripple frequency component of the power supply with thyristor and directly from them without time integration. There is no drift problem of integrator of magnetic sensors. Two kinds of control experiments were carried out, to keep the position constant and swing the position in a triangular waveform. And magnetic sensorless sensing of plasma shape is discussed.

keywords: *sensorless control, drift problem, HT-7, shape control, EAST*

1. Introduction

In a nuclear fusion reactor, some kinds of diagnostic systems should be used for reactor protection and plasma control. Since the sensors are used under severe irradiation circumstances, the number of diagnostic sensors placed near by a plasma is desired to be small or zero and must not have a drift problem. Therefore it is important to develop a sensorless sensing or control system in which there are no sensors of the controlled object and need not time integration.

The sensorless control has been developed in two ways. For example, in a device with active magnetic bearings as actuators, the rotor displacement velocity was calculated from the voltage and current in the coil, and the displacement was obtained by integration [1]. On the other hand in an active levitation control, the electromagnet is driven by a pulse width modulated (PWM) signal. The PWM carrier frequency component of the magnetic coil current is a function of the coil inductance. The gap between the electromagnet and the levitated object was calculated directly from the inductance without integration [2].

In this paper, we focus on the application to a plasma horizontal position control system, where the position is controlled by a vertical field coil. The voltage of the power supply for the vertical field coil is controlled by phase shift of the thyristor, and has ripples, whose frequency is higher than that of position controlling current. The ratio of the ripple frequency components of the coil voltage and current is a function of the coil inductance. Since the inductance depends on the plasma horizontal position, the position can be calculated directly from the inductance without integration.

This sensing method has been applied to the superconducting tokamak HT-7. The ratio of the ripple frequency (300 Hz) components of the vertical field coil voltage and current is calculated by Fourier expansion of the wave forms sampled every 0.1 ms for 3.3 ms before and after the time. We calibrated the equivalent circuit parameters in the relation between the ratio and the plasma horizontal position by a least square method. The calculated sinusoidal waveform of the position coincides with the one obtained from flux loop signal. The error is less than 2 % of the plasma minor radius [3].

Using the equivalent circuit parameters calibrated above, feedback control of horizontal position was tested on HT-7 in 2004. Because of real-time control, only past data for each one-ripple period were used to calculate the position based on sensorless sensing. Two kinds of experiments were carried out, to keep the position constant and swing the position in a triangular waveform.

Improvement of the magnetic sensorless control system has been endeavored. And magnetic sensorless sensing of plasma shape is discussed in analogous fashion to the plasma position sensing.

2. Experimental device and magnetic sensorless sensing principle

The superconducting tokamak HT-7 (the toroidal field $B_T = 2.5$ T, the major radius $R = 1.22$ m, the minor radius $a = 0.26\text{-}0.30$ m) of ASIPP [4], has thermal radiation shields between the plasma and the superconducting toroidal field coil, and between the toroidal field coil and the vertical field coil. The shield acts as a stabilizing shell for plasma equilibrium and the position is measured by flux loops taking the shell effect into account. The plasma horizontal position is controlled by the vertical field coil power supply, where phase of the thyristor is controlled at the frequency of 300 Hz.

In a feedback control system of the plasma horizontal position x_P, this is controlled by a vertical magnetic field made by vertical field coil current I_V driven by the applied voltage E_V. When the plasma shifts outward horizontally, a voltage is induced in the vertical field coil. In a voltage controlled power supply, I_V is increased, and in a current controlled power supply, E_V is reduced. Therefore we can obtain some information on x_P from the E_V and I_V, and we can deduce the x_P from them.

First, we consider the electrical equivalent circuit equations of the vertical field coil (V), thermal radiation shield (S) and plasma (P), and reduce I_S and I_P from these equations:

$$\begin{pmatrix} Z_V & Z_{VS} & Z_{VP} \\ Z_{SV} & Z_S & Z_{SP} \\ Z_{PV} & Z_{PS} & Z_P \end{pmatrix} \begin{pmatrix} I_V \\ I_S \\ I_P \end{pmatrix} = \begin{pmatrix} E_V \\ 0 \\ 0 \end{pmatrix}$$

$$\left\{ \left(Z_V - Z_{VS}^2 / Z_S \right) - \frac{\left(Z_{VP} - Z_{VS} Z_{SP} / Z_S \right)^2}{\left(Z_P - Z_{PS}^2 / Z_S \right)} \right\} I_V = E_V$$

If we approximate Z as a series element of a resistance and an inductance, and neglect the resistance of the shield and the plasma compared with that of the coil:

$$\frac{E_V}{I_V} = \left(\left(R_V + sL_V \right) - \frac{\left(sM_{VS} \right)^2}{\left(R_S + sL_S \right)} \right) - \frac{\left(\left(sM_{VP} \right) - \frac{\left(sM_{VS} \right)\left(sM_{SP} \right)}{\left(R_S + sL_S \right)} \right)^2}{\left(\left(R_P + sL_P \right) - \frac{\left(sM_{PS} \right)^2}{\left(R_S + sL_S \right)} \right)},$$

$$\frac{E_V}{R_V I_V} = \left(\left(1 + s\tau_V \right) - \frac{s\tau_V^{VS}\tau_S^{VS}}{\tau_S} \right) - \frac{s\left(\tau_V^{VP} - \frac{\tau_V^{VS}\tau_S^{SP}}{\tau_S} \right)\left(\tau_P^{VP} - \frac{\tau_S^{VS}\tau_P^{SP}}{\tau_S} \right)}{\left(\tau_P - \frac{\tau_P^{PS}\tau_S^{PS}}{\tau_S} \right)},$$

where s is an operator for Laplace transformation, R, L and M are resistance, self and mutual inductance, and τ is time constant defined as ratio L/R or M/R. Since the plasma inductance and the mutual inductances (M) between the plasma and the others depend on x_P linearly in the first-order approximation concerning elongation ratio and inverse aspect ratio,

$$\frac{E_V}{R_V I_V} = 1 + s\,\tau_{VS}^{eff} - s\,\tau_{VP}^{eff}\left(1 + \frac{x_P}{x_0}\right).$$

Consequently, the position (x_P) can be calculated directly from E_V and I_V, and the time integration is not necessary for deriving the position.

The position is expressed as a fractional or a linear function of the ratio (E_V/I_V). But this simple expression results from the above approximate linearization, neglecting the low-frequency components to apply it finally for feedback control of plasma position, since high speed is necessary in detecting the plasma position. On the other hand, since high accuracy is also necessary, we express the position as a first-order lag element of the ratio to raise the degree of precision. The amplitude of the voltage and current ripple is calculated from the fundamental Fourier component of each ripple.

The time resolution of the plasma horizontal position measurement based on magnetic sensorless sensing is limited by the ripple frequency as well as that obtained from the flux loop signal.

3. Experimental results of magnetic sensorless sensing and discussions

In the superconducting tokamak HT-7, the effect of eddy current in the thermal radiation shield must be taken into account. The plasma horizontal position is swept horizontally (the amplitude is smaller than 1 cm) at 7 Hz in the shot number 45160. Since I_S is not measured, we cannot determine the mutual inductances, M_{VS} between the vertical field coil and the shield, and M_{SP} between the shield and the plasma separately. We can determine only the effective mutual impedance (M_{VP}- M_{VS} M_{SP} / L_S) between the plasma and the vertical field coil.

The ratio of the ripple frequency (300 Hz) components of the vertical field coil voltage and current is calculated by Fourier transformation of the waveforms sampled every 0.1 ms. From the equations in the previous section, the ratio is expressed as a fractional function of x_P. But practically a first order transfer function should be sufficient to take into account the resistive effect. The relation between the ratio (impedance) and the plasma horizontal position is calibrated from the waveform of the shot number 45160 from 200 ms to 800 ms, i.e. the gain and time constant of the lag element, and the pedestal are determined.

Using these parameters, we applied this method to evaluate x_P in the shot number 45165, where x_P was swept at the different frequency of 10 Hz. The error of the derived plasma position is lower than 2 % of the plasma minor radius, and only the calculated position in the first cycle just after 200 ms depends on the starting position [3]. Although the error amount of 2 % is sufficient with respect to the required accuracy of the plasma position control, it may be too high with respect to the SOL and with respect to the position of the X-point in a divertor machine. But in the divertor machine, the waveforms of the divertor coil current and voltage would give more information on them, especially on the position of the X-point, and the error amount would decrease.

4. Experimental results of magnetic sensorless control and discussions

In the magnetic sensorless sensing, we have made analysis of the data from HT-7

off-line. In order to apply the magnetic sensorless sensing method to feedback control of plasma position, we must take into account the real time processing, the noise rejection, the accuracy and the calculation time.

Before the calculation of the fundamental Fourier component, necessary is the pre-processing for extracting the ripple component. In the real-time control system, only the past data are available in reducing the low frequency component and the high frequency noise from the raw current signal. The time lag due to the past data should be compensated by adjusting the time constant of the first order lag element. There is a method to utilize the discrete orthogonality of Chebychev polynomial. Since it, however, does not use the data at regular intervals, a simple averaging method is adopted here.

Using the equivalent circuit parameters calibrated above, feedback control of horizontal position was tested on HT-7 in 2004. Because of real-time control, only past data for each one ripple period were used to calculate the position based on sensorless sensing. In the first experiment to keep the position constant, it goes inward linearly in time as shown in Fig. 1. In the second to swing the position in a triangular waveform, it follows outward shift well, but does not inward one as shown in Fig. 2.

The asymmetric behavior suggests an asymmetric cause of sensorless sensing. It may be caused by increase in the ripple frequency as the phase-controlled voltage increases. In this control experiment, however, the calculation of the pre-processing for extracting the ripple component and the fundamental Fourier component were made by fixing the period of the thyristor ripple for simplicity. The easiest way of adjusting the variable period is to input the command signal for constant-voltage control of the power supply for vertical field coil and calculate the period from the time derivative.

The phase of the ripple depends on the firing angle. The amplitude of the current ripple is very small, although that of the voltage ripple is large. The current ripple component depends on the frequency, and the ratio to the main current of low frequency (almost DC) component is about 0.3 %. The small current ripple changes according to the plasma shift via change in the effective mutual inductance. The current ripple changes by 0.2 % per plasma shift of 10 mm. Consequently, the current ripple should be amplified beforehand, so that the plasma displacement dependence on the ripple component could be detected with 12-bit AD converter, or we should adopt with 16-bit AD converter.

The ohmic coil voltage and current are to be measured and analyzed to take the effect into account, although the ripple frequency is 600 Hz, which is two times as high as that of vertical field coil. We should endeavor on making fast the calculation without deteriorating the accuracy. Neural network could shorten the time, although it takes much time for the training.

5. Magnetic sensorless sensing of plasma shape

In order to measure elongation ratio based on magnetic sensorless sensing, we pay attention to quadrupole component of poloidal field coils as in Fig. 3(a). Taking into account the ripple frequency of 300 Hz, we consider the quadrupole current profile in plasma surface and the magnetic coupling with the quadrupole coil component (Fig. 3(b)). As in magnetic sensorless sensing of plasma position, the current ripple component decreases with ripple frequency for fixed elongation ratio of 2 (Fig. 4(a)). For fixed ripple frequency of 300 Hz, the current ripple component changes as a function of the elongation ratio (Fig. 4(b)).

Therefore, magnetic sensorless sensing of elongation ratio is possible in principle. In Fig. 3, the major and minor radii of the quadrupole coil positions are about the same

as in HT-7 for comparison with the position sensing. In case of EAST [5], poloidal coils are also superconducting, and the time constant is long. Although the current ripple may be too small, it decays hardly at all in time.

6. Summary

Sensorless sensing experiments were carried out in the superconducting tokamak HT-7. The plasma horizontal position was estimated from the vertical field coil current and voltage. The plasma horizontal position was directly calculated from the ratio of the fundamental Fourier components of the voltage and the current without time integration. Therefore this technique is very advantageous for the application to long pulse tokamak discharges without suffering from the drift problem in time integration of magnetic signals.

In the magnetic sensorless control experiment on HT-7, the plasma position could be controlled stably based on magnetic sensorless sensing method under disturbances from other poloidal coils and thermal radiation shield, if the asymmetric cause of sensorless sensing were eliminated.

Magnetic sensorless sensing of elongation ratio was studied. This sensorless control concept may be extended to the one of triangularity, and resistive wall mode.

References

[1] D. Vischer, H. Bleuler, A New Approach to Sensorless and Voltage Controlled AMBs Based on Network Theory Concepts, Proc. 2nd Int. Symp. on Magnetic Bearing, Tokyo (1990) 301-306.

[2] K. Matsuda, Y. Okada, Self-Sensing Magnetic Levitation Control by Using the PWM Driving Method, J. Japan Soc. Appl. Electromagnetics and Mechanics, Vol. 3, No. 1 (1995) 23-29.

[3] K. Nakamura, Z. Ji, B. Shen, P. J. Qin, et al., Plasma Science & Technology, Vol. 6, No. 5 (2004) 2459-2462.

[4] Y. Wan, HT-7 Team, HT-7U Team, Overview of Steady State Operation of HT-7 and Present Status of the HT-7U Project, Nucl. Fusion, Vol. 40, No. 6 (2000) 1057-1068.

[5] S. T. Wu, W. Y. Wu, Y. N. Pan, et al., Progress of the Engineering Design for the HT-7U Steady-State Superconducting Tokamak, Fusion Science and Technology, Vol. 42, No. 1 (2002) 146-154.
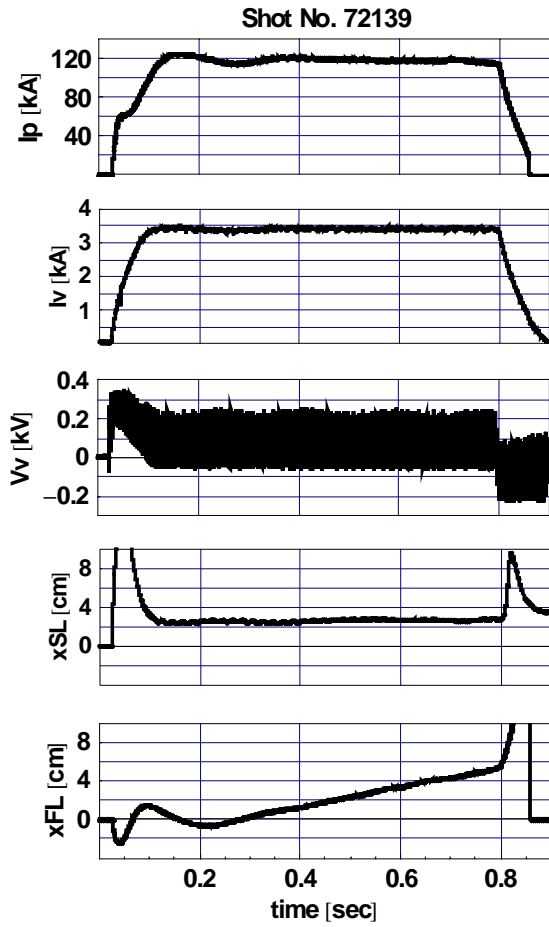
Fig. 1. The first experiment to keep the position constant based on sensorless control. Ip: plasma current, Iv: vertical field coil current, Vv: vertical field voltage, xSL: plasma position based on sensorless sensing, xFL: plasma position deduced from flux loop signal. Although xSL is almost constant by feedback control, xFL goes inward linearly.

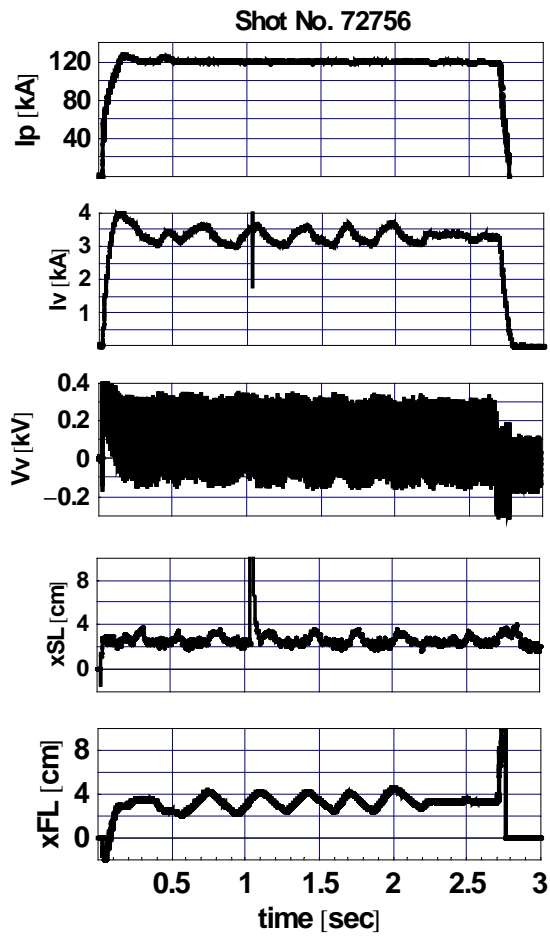Fig. 2. The second experiment to swing the position in a triangular waveform according to flux loop signal. The notations are the same as in Fig. 2. Although xSL follows outward shift well, it does not inward one.
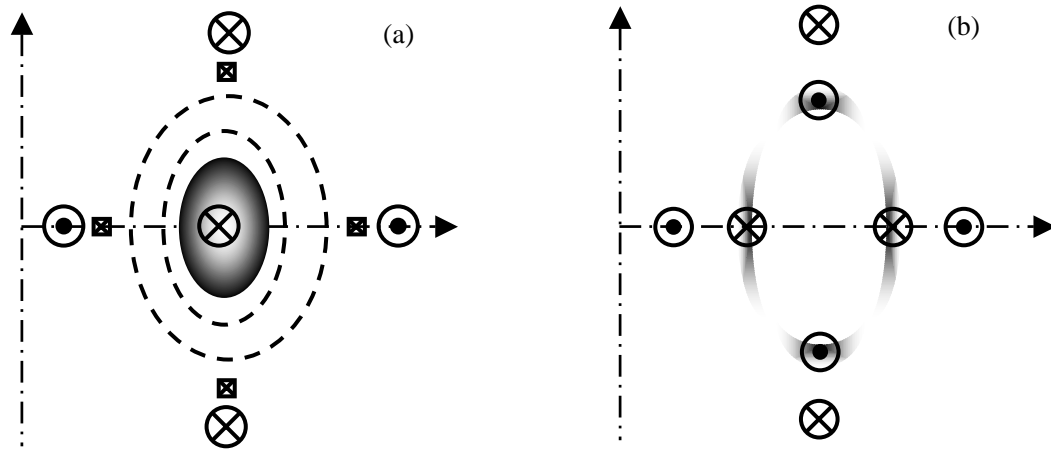
Fig. 3. Poloidal magnetic field is decomposed into dipole and quadrupole (a) field components. Plasma surface current profile is also decomposed into dipole and quadrupole (b) current profile components.
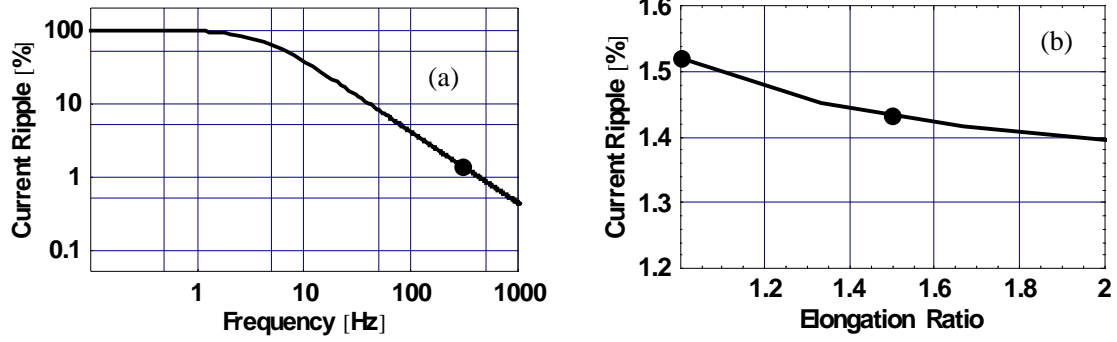
Fig. 4. (a) Current ripple component for fixed $\kappa = 2$ is anticipated to be about 1.4 % of DC current for f = 300 Hz. (b) Current ripple component for fixed f = 300 Hz is anticipated to decrease by 0.1 % for increase of 0.5 in κ.

Observation of Low Frequency Instability in a Magnetized Plasma Column

JinLin Xie, Yu Zhi, Changxuan Yu, Wandong Liu

CAS Key Laboratory of Basic Plasma Physics
University of Science and Technology of China, Hefei, Anhui, 230026

Abstract:

Detailed analysis of the low frequency instability is performed in a linear magnetized steady state plasma device. Identification and modification of the instability are achieved.

■Introduction:

During the early years in plasma physics, many studies were devoted to plasma instabilities in laboratory plasmas, especially in linear magnetized plasma devices. Many of them were related to anomalous transport in magnetically confined fusion plasmas. In order to control were turbulent state and the related transport, it is very important to achieve a better understanding of the mechanisms of instability of the system.

In linear magnetized plasma devices, low frequency fluctuations are easily observed.[1,2] There are many factors causing these fluctuations, such as resistive drift wave, K-H instability and Rayleigh-Taylor instability. In order to identify the instability, careful analyses should be conducted to make a detailed study of the radial profile of the plasma parameter.

■Experimental setup:

The experiments are performed in the Linear Magnetized Plasma Device (LMP) at USTC. A detailed scheme is displayed in Fig. 1. The device consists of two large stainless steel chambers (60cm in diameter and 50cm in length) separated by an insulated column (25cm in diameter and 200cm in length) immersed in a solenoid. The magnetic field inside the column is generated by ten equally spaced water-cooled coils. The

maximum field strength is 1000 Gauss with a current of 170A in the solenoid. One of the large chambers is used as a hot-filament DC discharge multipolar source, with argon as the working gas. Plasma parameters are determined with the Langmuir probes, emissive probes and quad-probes. The typical parameters are Density: $10^9 cm^{-3}$, Te: 1~3eV.

■Preliminary result in LMP

1. Observation of low frequency instability

Until the field strength reaches a threshold, no significant fluctuations are observed. Fig. 2 shows the revolution of the spectrum of the ion saturation current at a certain radial position.

2. Identification of the low frequency instability

Fig.3 shows the typical radial profiles of the ion saturation current and its spectrum. The radial location of the maximum fluctuation corresponds to the position of the maximum current gradient. The propagation velocity of the fluctuation is calculated based on the probe tip distance and the cross relation function between the two floating voltages. Due to the existence of the radial electrical field, the induced Doppler shift (ExB drift) should be subtracted. The phase velocity measured at r=-1.7cm is approximately 172m/sec and the wave propagates in the direction of the electron diamagnetic drift. These results are summarized in Fig.4. Also, it is found that the density fluctuation leads the potential's. All the observed characteristics are consistent with the model of the drift wave.

Drift wave is a low frequency wave driven by a pressure gradient. According to a simple model, the phase velocity of the drift wave driven by density gradient is given by $V_D = \frac{KT_e}{neB^2} \nabla n \times B$, where K is the Boltzmann constant, n is the plasma density, and B is the magnetic field strength. A more accurate model should take into account the parallel propagation of the adiabatic electrons.[3] The calculated phase velocity is approximately

200m/sec, which agrees with the measured value very well.

3. Modification of the low frequency instability

Usually, the insulated stainless steel column is grounded, the same with the large chambers. When the column is biased with a positive voltage, the profile of the low frequency instability is greatly modified (see Fig.5). It has proved to be a very useful way to change the plasma from a quiet state to weak turbulence, then to full developed turbulence. However, further studies are still ongoing to investigate the mechanism.

■Conclusion and summary

Detailed analysis of the low frequency instability in LMP is given. The observed fluctuation is identified as the drift wave. With the positive biased column, the modification of the low frequency is achieved.

■Acknowledgements

References

1. E. Gravier, etc. Phys. Plasmas **11**, 529 (2004)

2. H. W. Hendel, T. K. Chu, and P. A. Politzer, Phys. Fluids **11**, 2426 (1968)

3. A. Hasegawa, C. G. Maclennan, and Y. Kodama, Phys. Fluids **22**, 2122 (1979)
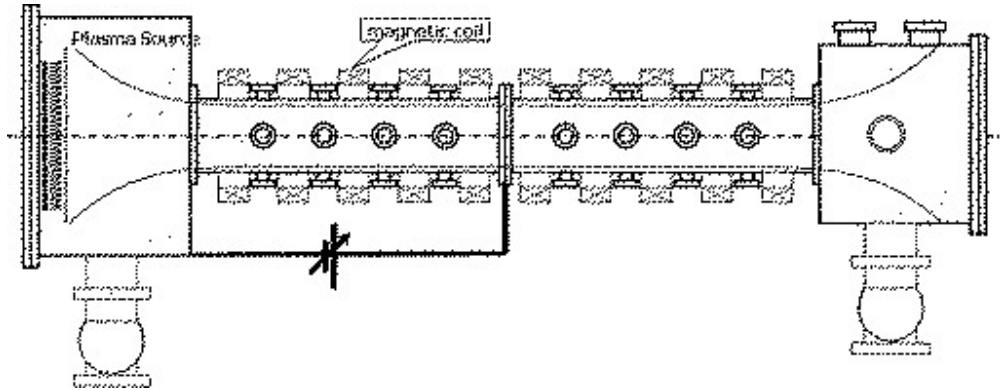
Fig1: The scheme of the linear magnetized steady state plasma device
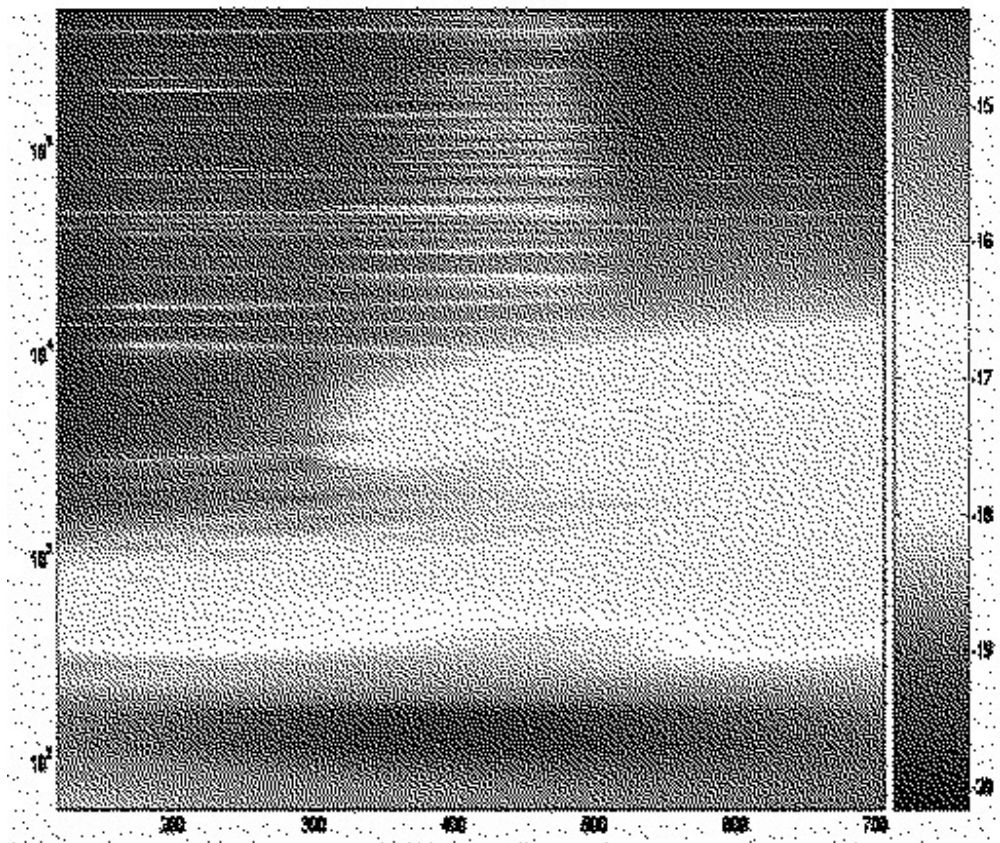
Fig2: The revolution of the power spectral density (PSD) of the ion saturation current at certain radial position r=-1.7cm (r=0cm at the center of the column). The horizontal axis is the B field (Gauss), the vertical axis is the PSD.
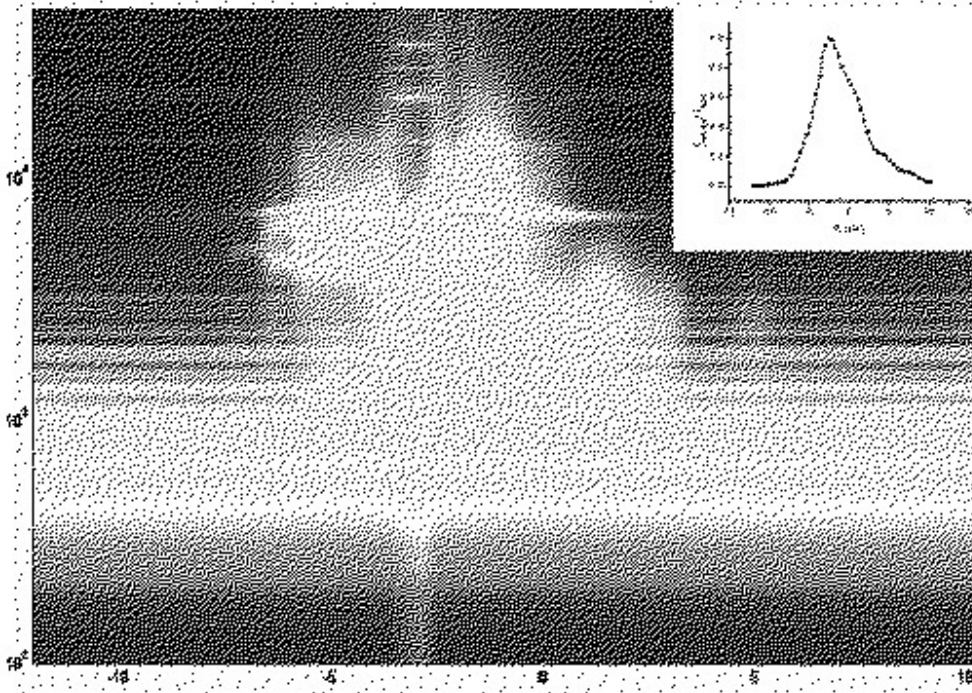
Fig3: The radial profile of the low frequency instability (B at 700Gauss). Right top is the radial profile of the normalized ion saturation current.

peak freq: 7KHz

Fig4: Top is the coherence of the two floating voltages, middle is their cross spectral density, and bottom is the phase angle between them.

Fig5: The radial profile of the low frequency instability (the column is biased +4 volt), the horizontal axis is the radial position (cm)

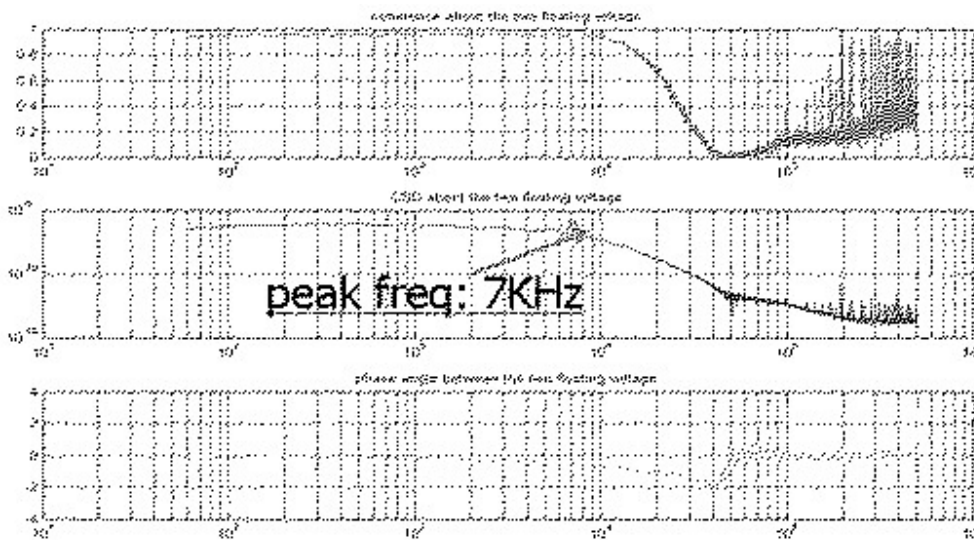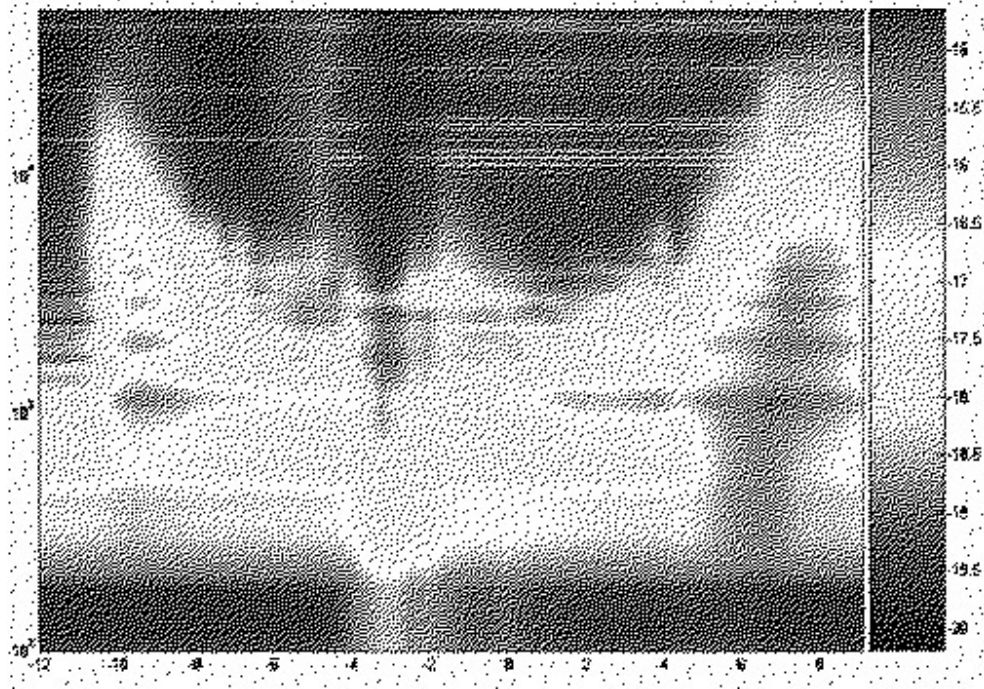# Spectroscopic studies on impurity transport of core and edge plasmas in LHD

Shigeru MORITA*, Motoshi GOTO and Sadatsugu MUTO

National Institute for Fusion Science, Toki 509-5292, Japan

Ryuji KATAI and Hisamichi YAMAZAKI

Department of Fusion Science, Graduate University for Advanced Studies, Toki 509-5292, Japan

Hideaki NOZATO

National Institute of Advanced Industrial Science and Technology, Tsukuba 305-8563, Japan

Atsushi IWAMAE, Makoto ATAKE, Takashi FUJIMOTO, Atsushi SAKAUE

Department of Engineering Physics, Kyoto University, Kyoto 606-8502, Japan

Hiroaki NISHIMURA

Institute of Laser Engineering, Osaka University, Osaka 565-0871, Japan

Ikuya SAKURAI, Chiho MATSUMOTO, Akihiro FURUZAWA, Yuzuru TAWARA

EcoTopia Science Institute, Nagoya University, Nagoya 464-8603, Japan

Mitsutoshi ARAMAKI, Yuji OKUMURA, Koichi SASAKI

Department of Electrical Engineering and Computer Science, Nagoya University, Nagoya 464-8603, Japan

Xianzu GONG, Jiangang LI, Baonian WAN

Institute of Plasma Physics, Chinese Academy of Sciences, Hefei 230031, China

Zhengying CUI

Southwestern Institute of Physics, Chengdu 610041, China

*morita@nifs.ac.jp

Abstract

Spectroscopic diagnostics have been extensively developed for studies of impurity and neutral particle transports at core and edge plasmas in LHD. Diagnostics of core plasmas are similar to the tokamak case, i.e., Z_{eff} from visible bremsstrahlung, K-x-ray measurements from x-ray spectroscopy using Si(Li) detectors and a compact crystal spectrometer, and high-Z impurity diagnostics from VUV spectroscopy using a flat-field EUV spectrometer.   A combination of impurity pellet injection and the visible bremsstrahlung is an active tool for the determination of the diffusion coefficient D and the convective velocity V. Using this tool the spatial structures of D and V are obtained and discussed with the neoclassical effect. On the other hand, the spectroscopic method for edge diagnostics is considerably different from the tokamak case because of the existence of a thick ergodic layer in addition to the x-points necessarily included in the diagnostic chord view. In order to break this negative situation, Zeeman and polarization spectroscopy were adopted to LHD edge plasmas. As a result, 2-dimensional emission contours of HeI and Hα were successfully obtained. Laser absorption spectroscopy was employed in an attempt to measure hydrogen neutrals directly.   Radial profiles of edge impurities were also measured with a mirror-assembled 3m VUV spectrometer. Recent results and the progress on LHD spectroscopy are briefly reviewed.

1. Introduction

Experiments of the Large Helical Device (LHD: R/<a>=3.6m/0.64m, B_t<3T, V_p=30m^3) have been carried out with a complete set of superconducting coils and carbon divertor plates installed on the vacuum chamber (SS316L) at 4 divertor sections. Successful discharges have been obtained without any serious problem on impurity radiation. Helical plasmas, however, have a high degree of freedom for density profile formation in comparison with tokamaks, where the peaked, flat and hollow density profiles usually appears as functions of B_t, T_e, n_e and so on. It becomes very important for LHD to study the relation between the formation of such a variety of density profiles and the core impurity transport. On the other hand, the magnetic field structures in LHD are characterized by the presence of a relatively thick ergodic layer, which is created by intermediately closed magnetic field lines, surrounding the main plasma within ρ=1. It is a common feature in non-axisymmetric devices. Especially in LHD, the averaged thickness of the ergodic layer λ_n (~10cm) is much greater than the neutral penetration length, λ_i (=1-3cm). Therefore, it also becomes important to study the transport of impurities and neutral particles in relation to the chaotic B-field structure in the ergodic layer.

Many kinds of impurity diagnostics have been developed in LHD for the purpose of above-mentioned key issues. In this paper, recent progress on the impurity diagnostics in LHD are briefly interpreted with some experimental results.

2. Core impurity diagnostics

The effective charge Z_{eff} is a typical measure of core impurity concentration[1]. A radial profile measurement of the Z_{eff} with 80 view chords has been developed using visible bremsstrahlung in a range of 5315Å. At present, the Z_{eff} profile has not been sufficiently obtained because of a mixture of visible line emissions mainly from the x-points. Nevertheless, the contribution of line emissions can be reduced by selecting an appropriate magnetic configuration and density range. A typical profile of Z_{eff} is shown in Fig.1. Data are taken at a density of 5×10^{13}cm^{-3}. The Z_{eff} profile seems to be flat, indicating a small increase in the plasma center. The density profile is also flat, but the error bars of $n_e(r)$ are considerably large. Therefore, the error bars of $Z_{eff}(r)$ become large inevitably. Recently, a fairly good density profile has been measured in LHD by a Thomson scattering and CO_2 laser interferometer. The detailed study of the Z_{eff} profile will progress further in the near future in addition to the technical improvement of the Z_{eff} measurement.

The impurity transport has been studied in a combination of the visible bremsstrahlung measurement and an impurity pellet injection[2]. The cylindrical pellets of C, Al and Ti were adopted in this study with a velocity range of 150 to 300m/s and a size range of 0.5-0.9mm. Typical waveforms of the visible bremsstrahlung after C pellet injection are traced in Fig.2(a) as a parameter of the electron density. The decay time of the signals depends strongly on the density level. The impurity pellets were injected in a variety of NBI (≤10MW) discharges. In order to analyze the impurity transport using the diffusion coefficient D and the convective

velocity V, the following model is assumed with radial structures;

$$\Gamma_q = -D_q(r)\frac{\partial n_q}{\partial r} + V_q(r)n_q \tag{1}$$

$$V_q(r) = \frac{V(a)}{1-\rho*} \times \left(\frac{r}{a} - \rho*\right) \qquad (r > \rho*), \tag{2}$$

and $\qquad V_q(r) = 0 \qquad\qquad (r < \rho*). \tag{3}$

Here, Γ_q, n_q, D_q and V_q are the particle flux and the ion density of qth charge state, the diffusion coefficient and the convective velocity, respectively. The value of $\rho*$ means the inflection point of the assumed radial profile of V, as shown in Fig.2(b). The present model is consistent with the normally used conventional model, when $\rho*$ is 0. The time behavior of the impurity density profile is thus calculated by the following equation with the ionization balance of impurity ions;

$$\frac{\partial n_q}{\partial t} = -\frac{1}{r}\frac{\partial}{\partial r}(r\Gamma_q) + \alpha_{q-1}n_{q-1}n_e + \beta_{q+1}n_{q+1}n_e - (\alpha_q + \beta_q)n_q n_e + S_q. \tag{4}$$

In the equation α, β and S_q represent the ionization and recombination rate coefficients and an initial particle source given by the impurity pellet, respectively.

Since the collision frequency of impurities is high at standard plasma parameters, the impurity ions generally stay in a collisional regime. The particle flux Γ and the diffusion coefficient D in the collisional region are described by the neoclassical theory;

$$\Gamma_q = -D_{imp}\frac{\partial n_q}{\partial r} + D_{imp}q\left(\frac{1}{n_p}\frac{\partial n_p}{\partial r} - \frac{1}{2}\left(1-\frac{1}{q}\right)\frac{1}{T_{imp}}\frac{\partial T_{imp}}{\partial r}\right)n_q, \tag{5}$$

$$D_{imp} = 2.24\times10^{-23}(2q_s^2 + 1)\ln\Lambda\frac{n_p}{\sqrt{T_e}B^2}, \tag{6}$$

and $\qquad V_q = D_{imp}q\left(\frac{1}{n_p}\frac{\partial n_p}{\partial r} - \frac{1}{2}\left(1-\frac{1}{q}\right)\frac{1}{T_{imp}}\frac{\partial T_{imp}}{\partial r}\right), \tag{7}$

where n_p is the proton density, q_s the safety factor and $\ln\Lambda$ the Coulomb logarithm. These equations indicate that the D is independent of the impurity charge state q, but V_q is proportional to q in addition to the proton density gradient. Then, Eq.(2) is replaced by the following equation to include such q dependence on V;

$$V_q(r) = \frac{V(a)}{1-\rho*} \times \left(\frac{r}{a} - \rho*\right)\left(\frac{q}{Z}\right) \qquad (r > \rho*). \tag{8}$$

The time trace of the measured bremsstrahlung shows a fairly good agreement with the spatially constant D and the V modeled by Eqs. (3) and (8). The value of $\rho*=0.6$ is thus obtained as a result of the best data fitting.

The density dependence of D and V at $\rho=0.8$ is shown in Fig.3 (a) and (b), respectively

as one of the typical results of the impurity transport study. The diffusion coefficients are nearly constant for the three elements of C, Al and Ti and also for the density. Values predicted by the neoclassical theory are also plotted in the figure. It is clear that the experimentally obtained coefficients are much higher than the predictions. The inward velocities, on the other hand, have a considerably strong dependence on the density and the charge state. This result seems to be consistent with the prediction from the neoclassical theory (see Eq.(7)). However, no temperature gradient dependence on the V is observed. Replacing the density of the figure into the collisionality ν_{imp}, which ranges in the Pfirsch-Schlüter regime, we obtain a clearer result that the D is also constant for a variety of ν_{imp} and the V becomes more negative when ν_{imp} increases, e.g., V(0.8)=0 for $\nu_{imp}/\nu_{PS}=1$ and V(0.8)=-3m/s for $\nu_{imp}/\nu_{PS}=10^3$. In LHD a helical ripple becomes dominant at $\rho \geq 0.5$. The present result on the D may suggest that the impurity transport is not affected by the existence of such a helical ripple.

X-ray emissions from core metallic impurities have been routinely monitored using the Si(Li) and Ge detectors. Radial profiles are also measured by scanning the line-of-sight of 4 Si(Li) detectors in a steady phase of LHD discharges[3] (see Fig.4). From this measurement the density of iron is determined to be in the order of 10^{-4} to the electron density. The radial extent of the Kα lines is mainly determined by the central electron temperature having a weak dependence on the impurity transport coefficient. In order to observe core impurity transport coefficients using passive spectroscopy, a compact crystal spectrometer is being constructed. Figure 5 (a) shows a schematic view of the Johann-type spectrometer (LiF(220): 2d=2.848Å, 2R=43cm, 15x15mm^2). The spectrometer covers an energy range of 6.4-7.0keV in which Fe Kα lines emitted from their all charge states can be observed, when a CCD detector with a total size of 26mm (1024ch) is used. One of calculated results on the Fe ions radial profile (D=0.2m^2/s, T_e(0)=2keV) is traced in Fig.5(b). The charge state distribution of Fe at the plasma center becomes a considerably strong function of D in LHD, because T_e(0) typically ranges in 2-3keV and partially ionized ions like Fe^{+20}-Fe^{+24} still remain in the plasma center. The Fe Kα lines obtained from LHD are also expected for comparison with those from astrophysical plasmas observed by the ASTRO-E2 x-ray satellite[4], in which some of Kα x-rays are emitted by a different excitation mechanism.

A flat-field EUV spectrometer with an incident angle of 87.0° has been constructed for a quantitative analysis of core impurities. The image of spectral lines can be focused linearly by the use of a varied-line-spaced grating. This focusing mechanism yields a relatively high spectral resolution over a wide wavelength range of 100-400Å in combination with a back-illuminated CCD (26.6x6.6mm^2, 1024ch) as an EUV detector. The spectral resolution of 0.4Å is designed at λ=200Å. A mechanically ruled grating is used at present. In the near future a laminar-type holographic grating will be used in place of this one in order to reduce the reflectivity of higher order light. The spectrometer is also aimed for understanding the atomic structures of Sn and Xe ions injected into LHD, as one of several joint projects related to an

EUV light source development $(130\text{-}140\text{Å})$[5] for next-generation lithography based on laser-illuminated plasmas.

2. Edge impurity diagnostics

Figure 7 shows (a) $H\beta$, (b) HeI and (c) CII chord-integrated radial profiles observed vertically at a horizontally elongated plasma position[6]. No sufficient explanation can be derived from the data for the behavior of the edge particle because those profiles are too strange. In LHD there exists a thick ergodic layer and two x-points outside the main plasma. The line-of-sight from the diagnostic ports always includes such edge structures. In order to break this deadlock the Zeeman spectroscopy has been adopted for better understanding.

Figure 8(a) shows a chord-integrated HeI spectrum, which is recorded with a chord denoted with (a) in Fig.8(e) passing through an inner and an outer part of the edge plasmas. The Zeeman-split spectrum can be then explained by a combination of two magnetic field strengths of 1.99T (inboard edge) and 1.51T (outboard edge)[7]. The positions of σ and π components are indicated with solid (1.99T) and dashed (1.51T) lines in Fig.8(a). Using this technique a 2-dimensional emission contour was successfully obtained analyzing basically the radial profiles data of Fig.7(b). The result is plotted in Fig.8(e). The intensities of the HeI emissions expressed by the size of closed squares are dominant in the inboard side of the edge plasma. According to a theoretical prediction the particles coming out of the main plasma reach the inboard-side divertor in this configuration. The enhanced HeI emissions at the inboard side are believed to be a result of enhanced interaction between the particles and the carbon divertor plates.

On the other hand, the technique became a failure when it was applied to $H\alpha$. The $H\alpha$ spectrum could not be resolved into each σ and π component since those were widely broadened and mixed with each other (see Fig.8(b)). We therefore further attempted with polarization spectroscopy in addition to Zeeman spectroscopy to resolve this problem[8]. The experimental results are shown in Fig.8(c) and (d). In LHD the rotational transform is large at the plasma edge $(\iota/2\pi\sim1.5)$, and then the polarization becomes different between the inboard and outboard sides due to different directions of the magnetic field lines. The e-ray shown in Fig.8(c) indicates approximately a combination of π component at the inboard side and σ component at the outboard side, and the o-ray in Fig.8(d) indicates a σ component at the inboard side and π component at the outboard side. Here, the e-ray and o-ray, which were separated by a polarization separation prism, mean different polarization angles crossed at right angles. Both spectra are analyzed using two different temperatures of cold and hot components. We thus obtain an absolute position of $H\alpha$ emissions shown by open circles in Fig.8(e). In the figure only the result from a single chord is plotted, but the 2-dimensional $H\alpha$ contour has been analyzed as well as the HeI case.

A direct measurement of hydrogen neutrals was attempted using laser absorption

spectroscopy[9]. A diode laser fixed to Hα wavelength of 6562.8Å, which is tunable in a wavelength range of 1Å with a line width of 4MHz, was transferred by an optical fiber to an LHD diagnostics port and the laser power passing through the plasma was monitored with a PMT thorough an Hα interference filter and a visible spectrometer at the opposite diagnostics port. When the laser power is absorbed by the hydrogen neutrals in an excited level of 2s state, the detected power is reduced. A typical result on the laser absorption spectroscopy is shown in Fig.9. Data of some interest is obtained at the end of discharges during t=1.25-1.35s (see Fig.9(c)). The signal from a lock-in-amplifier, which is used to eliminate the background Hα light from the plasma, traced in Fig.9(d) clearly indicates a reduction of the injected laser power meaning the absorption by the neutrals. At present no quantitative analysis is made. However, the present result demonstrates a possibility on the direct measurement of edge neutrals in fusion devices.

A 3m normal incident VUV spectrometer has been developed to measure radial profiles of edge impurities with the use of view-angle adjustable mirrors set in front of an entrance slit and the back-illuminated CCD detector[10]. Full vertical profiles of CIV (1550Å) are recorded from high-density and low B_t discharges (see Fig.10(a)). In these discharges the outer boundary of plasmas shrink inside LCFS due to a large edge energy loss. The ergodic layer and x-points disappear. As a result, the profiles become symmetric. In LHD a direction of grad-B drift of particles is not as simple as the tokamak in which the up and down asymmetry is observed. This result suggests that the effects of the grad-B drift and helically trapped particles are small at least in such a collisional regime. The profile at t=1.8s indicates the plasma decay phase after NBI pulse is switched off. The edge radial profiles of the carbon ions in each charge state are also measured. A preliminary result is shown in Fig.10(b). The data are taken from limiter plasmas, and then the value of z=0 means the position of the limiter head. The radial positions of carbon ions are a function of the (inward) convective velocity in addition to the edge T_e profile. These data are expected to be useful for understanding the formation mechanism of the inward velocity and the impurity transport at plasma edge.

3. Concluding remarks

A variety of spectroscopic instruments have been developed for impurity and neutral particle diagnostics in LHD during the past ten years and new ideas have been also attempted. Some of them have produced successful results. Besides the above-mentioned diagnostics, the ion temperature measurement by a high-resolution crystal spectrometer[11] and the monitoring of impurity by several VUV spectrometers have been routinely done in every discharges. Diagnostics using visible forbidden lines has been newly started. Joint efforts are being continuously made for future development of the impurity transport study in LHD in collaboration with many universities and institutes.

Acknowledgements

This work is partly supported by JSPS-CAS Core University Program in the field of Plasma and Nuclear Fusion. The authors are also thankful to all members of the LHD group and all Chinese visitors for their useful discussions and technical assistant.

References

1 Morita S, Goto M, et al. Physica Scripta 2001, T91: 48

2 Nozato H, Morita S, Goto M, et al. Phys. Plasmas, 2004, 11: 1920

3 Muto S, Morita S. Rev. Sci. Instrum., 2001, 72: 1206

4 Mitsuda K, Kunieda H, Inoue H, Kelley R. Proc.SPIE, 2004, 5488: 177

5 Nishimura H, Shigemori K, Nakai M, et al. J. Plasma Fusion Res., 2004, 80: 325

6 Wan B N, Goto M, Morita S. NIFS-Tech-7, 1999

7 Goto M, Morita S. Phys. Rev. E, 2002, 65: 026401

8 Iwamae A, Hayakawa M, Atake M, Fujimoto T, Goto M, Morita S. Phys Plasmas, 2005, 12: 042501

9 Aramaki M, Okumura Y, Goto M, Muto S, Morita S, Sasaki K. to be published in Jpn. J. Appl. Phys., 2005, 44:

10 Morita S, Goto M. Rev. Sci. Instrum., 2003, 74: 2036

11 Morita S, Goto M, Takeiri Y, Miyazawa J, et al. Nucl.Fusion 2003, 43: 899
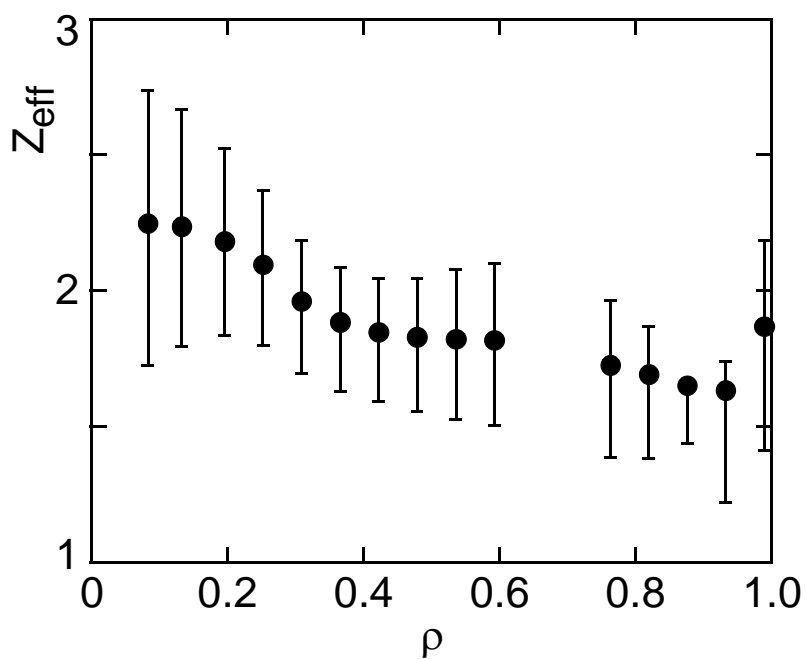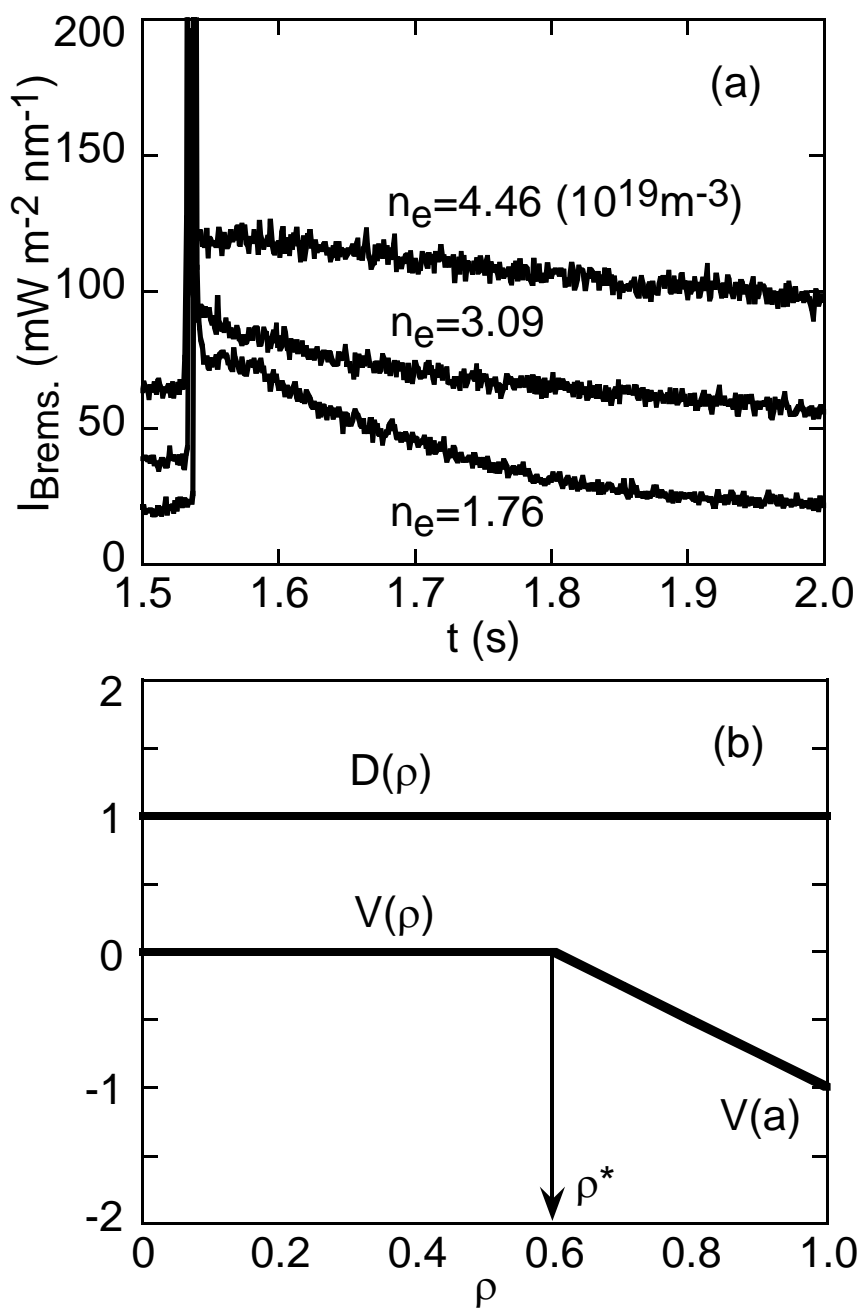
Fig.1 Typical Z_{eff} profile in LHD.

Fig.2 (a) Time traces of visible bremsstrahlung after carbon pellet injection and
(b) models of diffusion coefficient and inward velocity profiles.
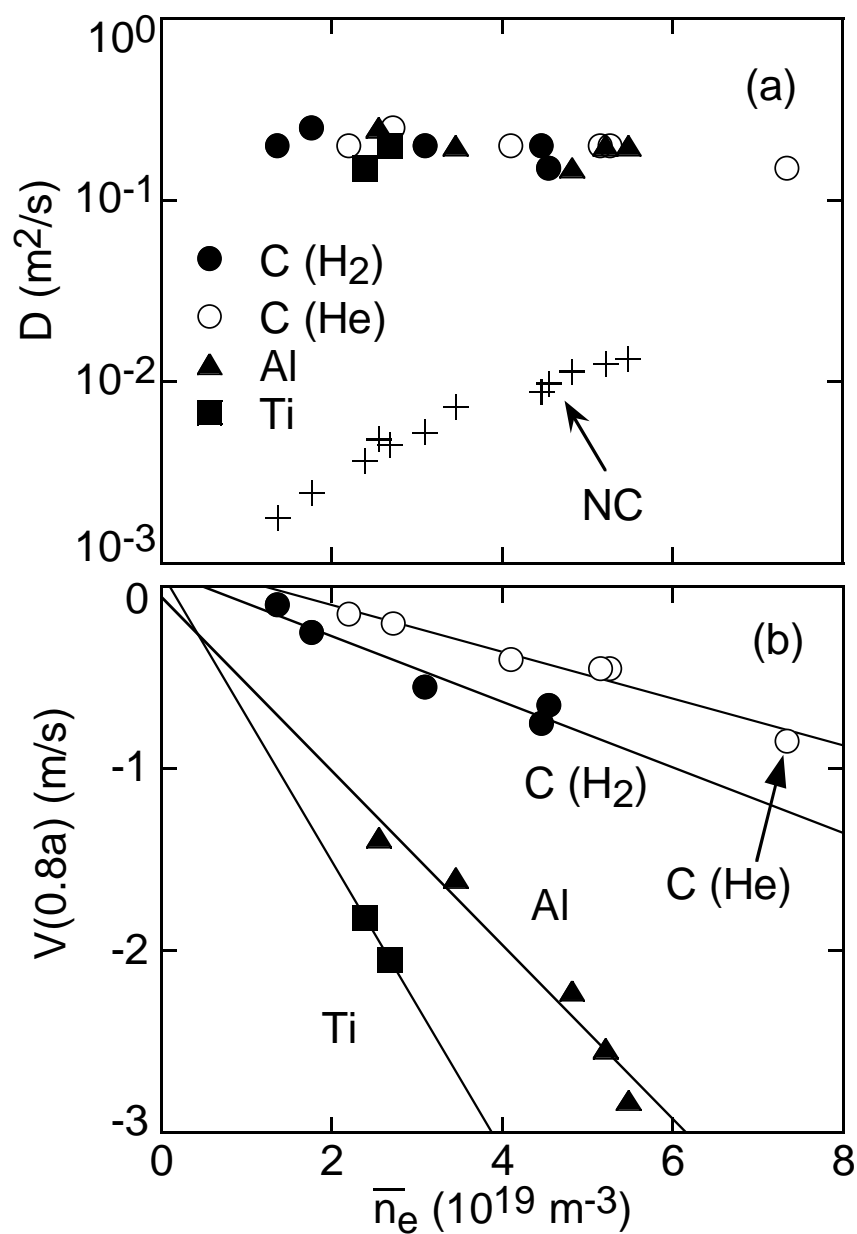
Fig.3 (a) Diffusion coefficients and (b) inward velocities as a function of line-averaged electron density. Points denoted with crosses mean neoclassical values.
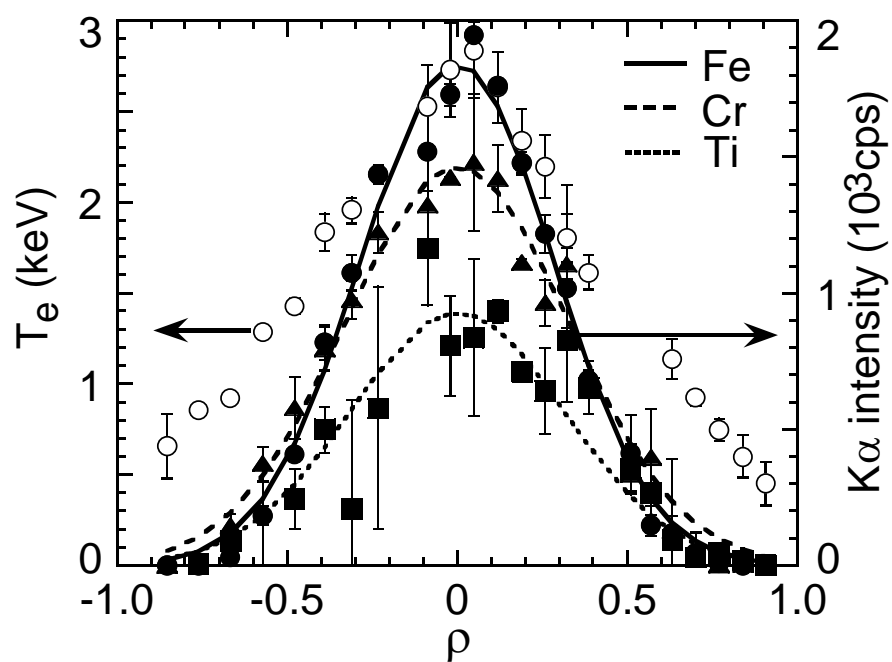
Fig.4 Radial profiles of (a) T_e (open circles) and
(b) Kα x-ray intensities from Ti, Cr and Fe impurities.
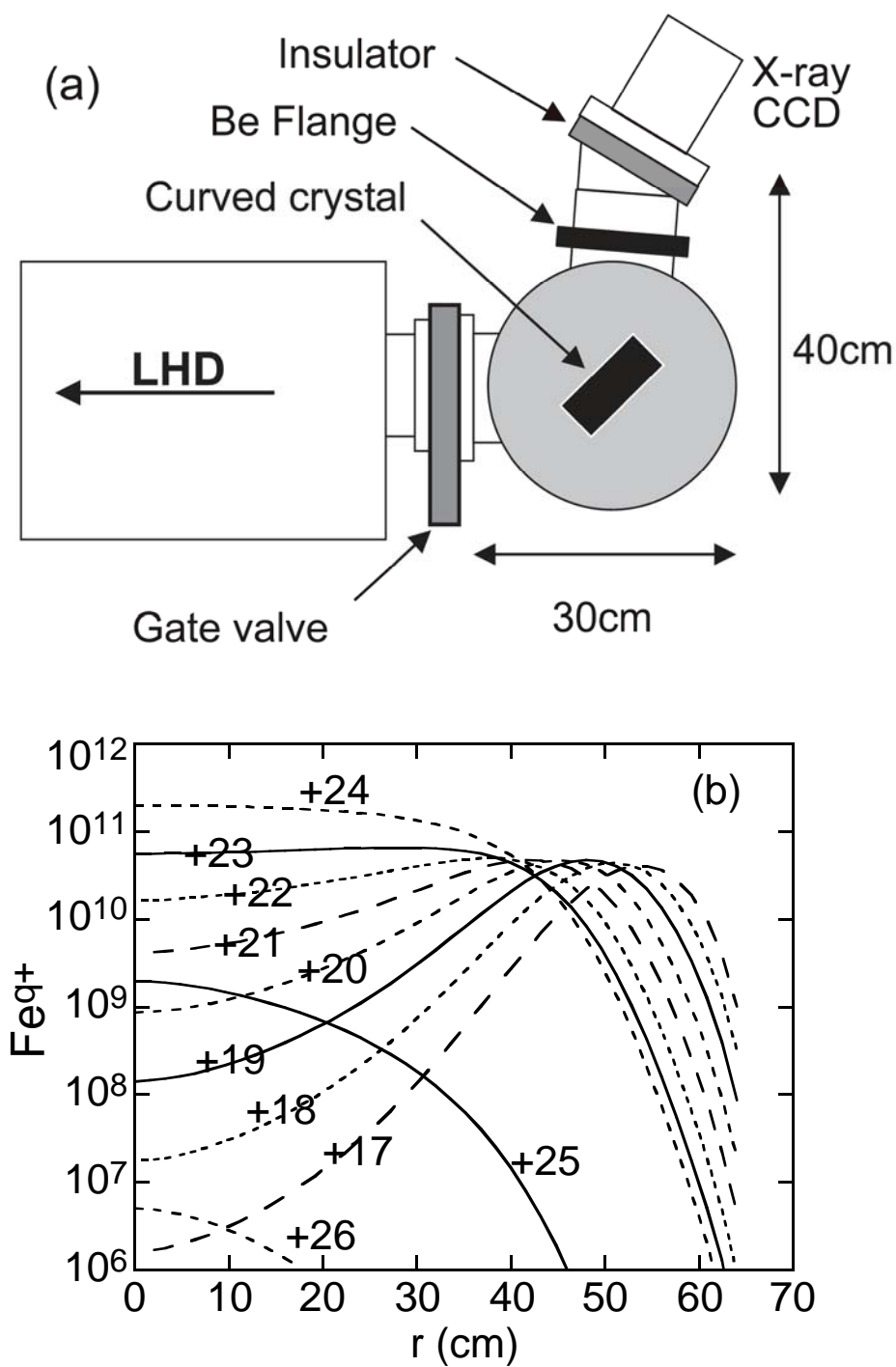
Fig.5 (a) Schematic view of compact crystal spectrometer and
(b) calculated radial profiles of Fe impurity ions in LHD (D=0.2m^2/s, T$_e$=2keV).
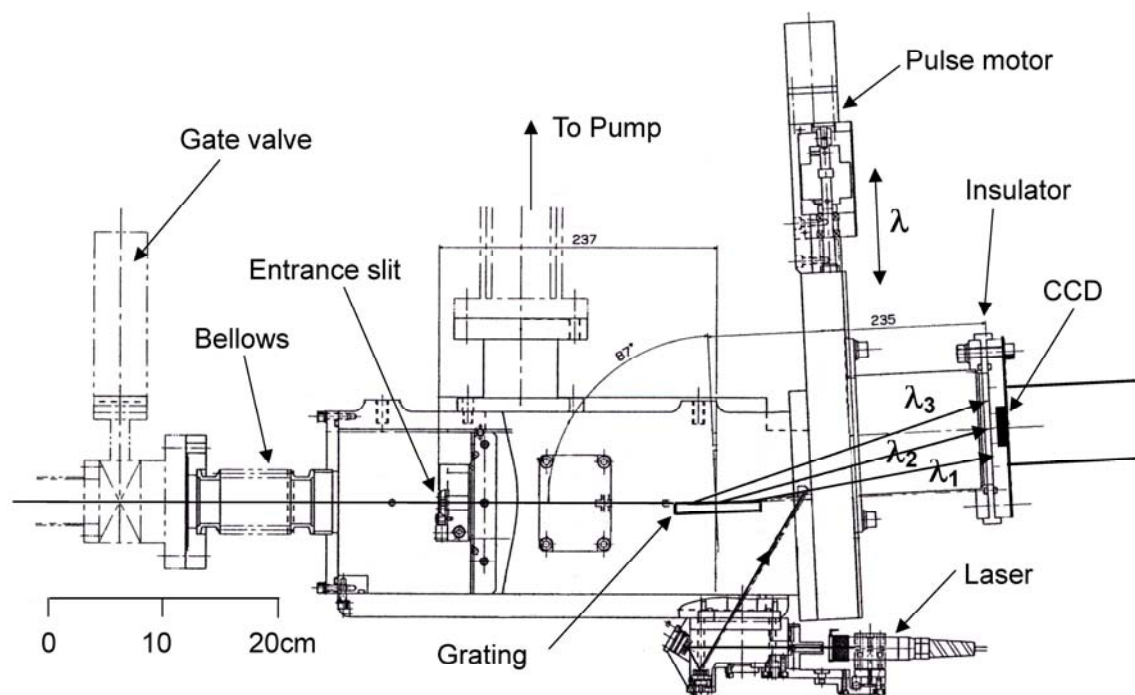
Fig.6 Flat-field EUV spectrometer.
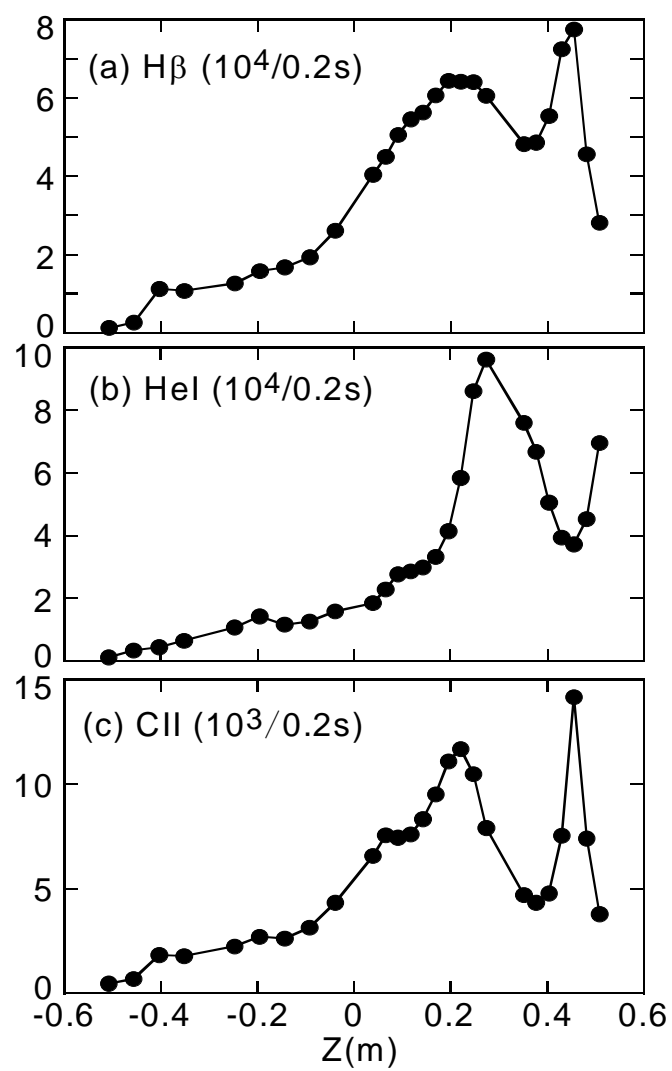
Fig.7 Vertical profiles of visible lines from (a) Hβ, (b) HeI and (c) CII.
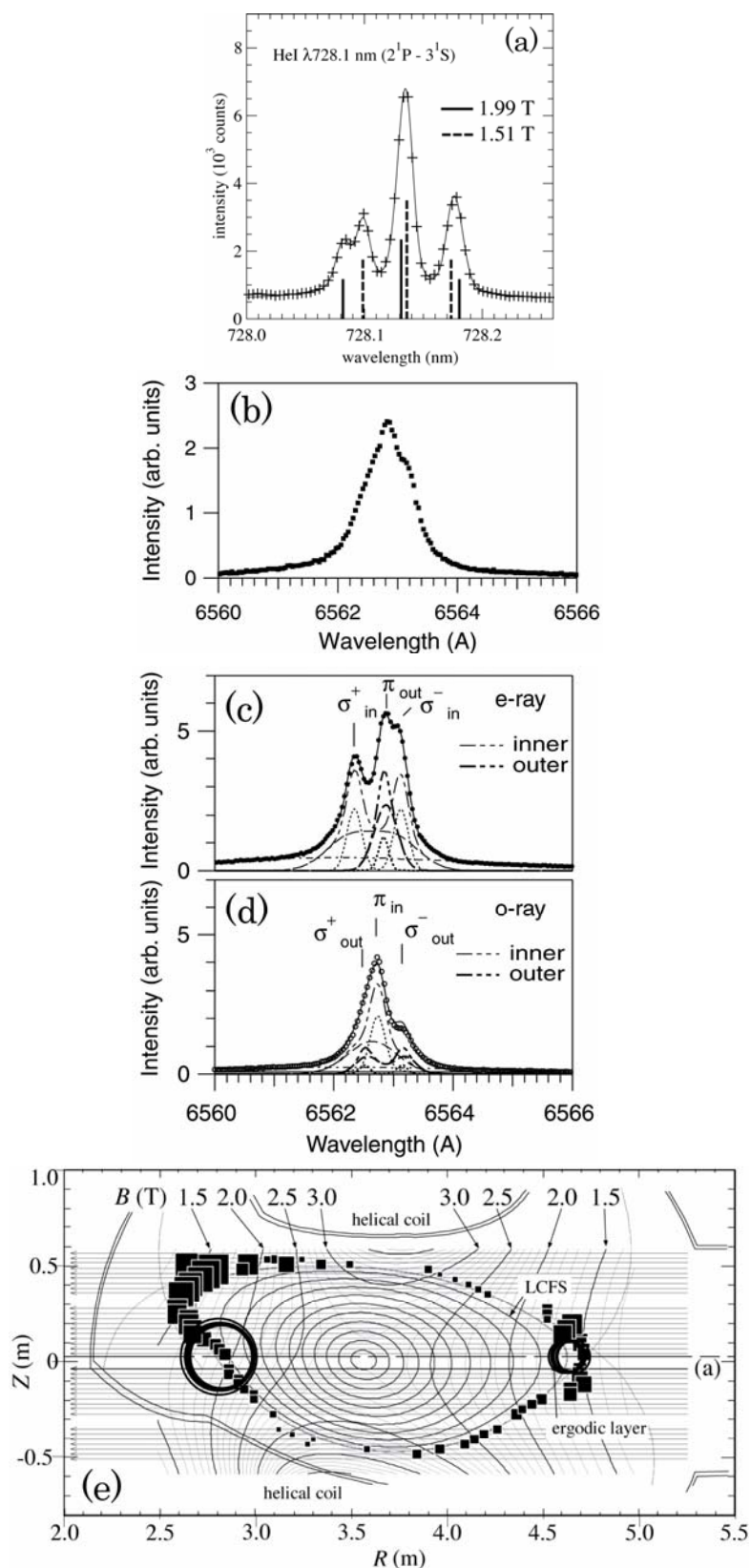
Fig.8 (a) HeI line profile split by Zeeman effect and (b) Doppler-broadened Hα line profile,
(c) e-ray and (d) o-ray of Hα components separated by polarization separator, (e)
2-dimensional distributions of HeI (closed squares) and Hα (open circles).
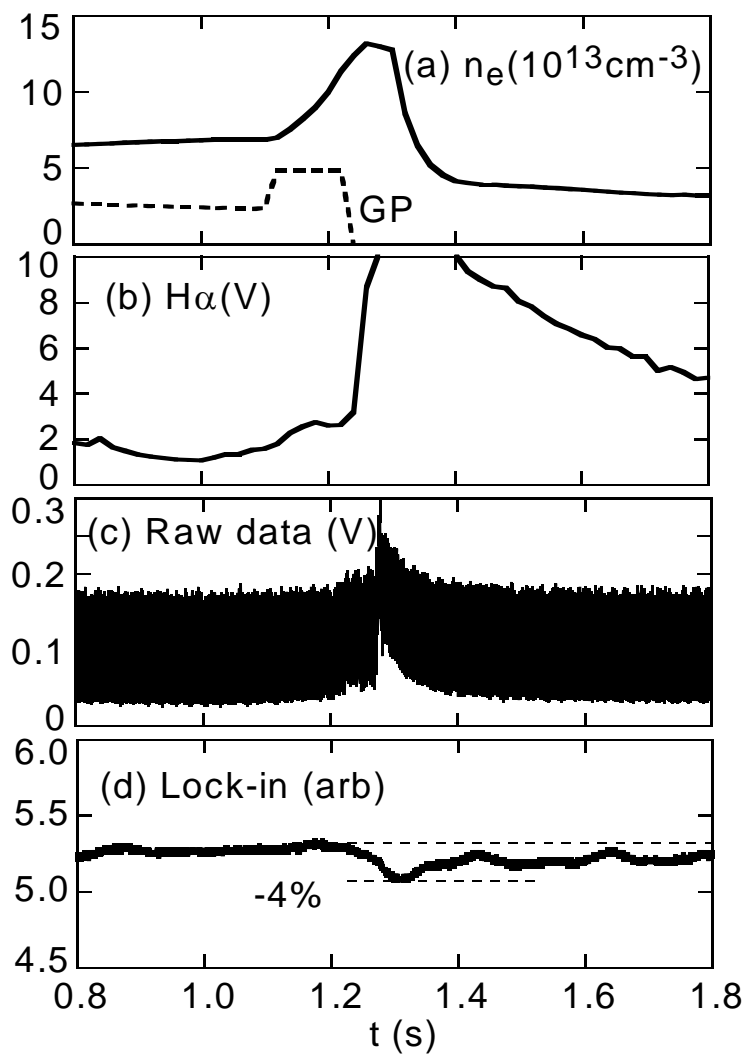
Fig.9 Time traces of (a) electron density, (b) Hα, (c) raw signal from LHD plasma detected through chopper before lock-in-amplifier and (d) signal after lock-in-amplifier.
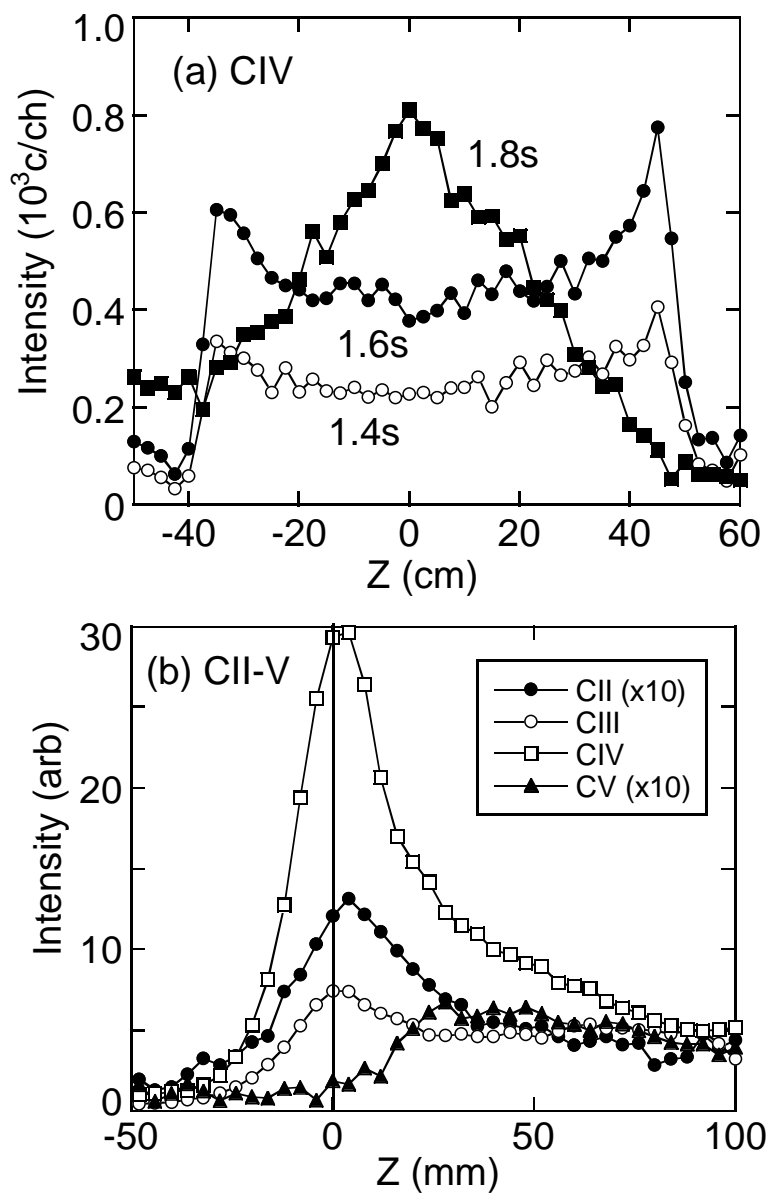
Fig.10 (a) Full vertical profiles of CIV and (b) edge vertical profiles of CII-CV.

Impurity Measurement and Study on HL-2A Divertor Tokamak [*]

Zhengying CUI, Ping SUN, Yudong PAN, Wei LI, Quanming WANG, Xueu DUAN

Southwestern Institute of Physics, P. O. Box. 432, Chengdu, Sichuan 610041, China

Abstract: The HL-2A tokamak with two close divertors has been in full operation since 2003. In the 2004 experimental campaign the divertor configuration was successfully formed and the siliconization as a wall conditioning was performed on this device for the first time. The diagnostics for impurity measurement are described in this paper. The divertor configuration can be reconstructed by the CFc code. Impurity behaviors were investigated during the experiments with the divertor configuration and wall conditioning. The reduction of impurity was clearly evident under both conditions of the divertor configuration and siliconization.

Key words: plasma, wall conditioning, impurity

PACS: 52.55.F, 52.25. Vy

1, Introduction

Over the past decades impurity behavior has been seen as one of the principal factors governing the achievement of fusion reactor plasma conditions. Fuel dilution of the central plasma is often unacceptably high and impurity radiation near the edge is the likely limiting factor on achievable plasma density. The principal task of tokamak impurity studies is to explain impurity levels in the main plasma and to indicate means of control. In order to avoid destroying the vessel wall and poisoning the plasma, yet at the same time, to efficiently extract the waste product of the fusion process from the system, divertors have been proposed right from the beginning to handle such problems in many machines[1].

The HL-2A with two close divertors was successfully constructed in 2002[2]. It is the first divertor tokamak in China. The parameters are as follows: the major radius R=1.64m, the minor radius a=0.4m, the toroidal magnetic field Bt=2.8T, and the toroidal plasma current Ip=480kA. Impurity study and control as one of the critical

issues will generally be undertaken during the initial operation period since the content of impurity may be high and will strongly affect the discharge operation and plasma quality.

Different kinds of impurity diagnostics have been developed on the HL-2A device including measurement of impurity radiation, line emission, Zeff, etc. This issue is discussed in Section 2 of this paper. The experimental results regarding the impurity on the divertor configuration as well as the experimental results of siliconization are described in Section 3. The last section presents a summary.

2, Impurity diagnostics

A monochromator in the VUV spectral range has been installed on HL-2A to examine the impurity behaviors in the main plasma region[3]. It is a Seya-Namioka vacuum monochromator with a wavelength range of 20nm-200nm and a sensitive material coating on the surface of the detector. The line of sight goes through the plasma center mainly for the investigation of impurities of helium, boron, carbon, oxygen, iron, cupper, silicon, etc.

The visible spectroscopy in the main plasma chamber is comprised of bremsstrahlung measurement with 6-channels for plasma effective charge, Zeff, and of Hα measurement with two arrays. Each array includes 23 channels. There are four other channels for independent Hα measurement which are located along the toroidal direction of which the line of sight of one channel goes through the plasma edge and the others go through the plasma core. In the divertor chamber some visible fibers with the filter are also installed for Hα, CIII and OII measurement. Detail information is presented in reference[4]. In the 2005 experimental campaign a new Ha array with 92 channels has been installed for a horizontal view of the main plasma chamber.

In the early operation stage of HL-2A there are only one array of bolometer with 16 channels. The detector is Absolute Extreme Ultra Violet silicon photodiodes, AXUV, which is characterized by a fast response, high sensitivity and wider bandwidth. Nevertheless, it is not sensitive to the particle loss. The energy range of the detector is from 10keV to 1eV. The array is mounted on the horizontal port of the device with a fan-shaped line of sight[5]. For the 2005 campaign two new bolometer

arrays with 16 channels for each array and the same detector with the old bolometer are installed in the main plasma chamber.

The plasma discharge with a single divertor (down) was successfully formed in the 2004 campaign[6]. The reduction of impurity was obvious when the divertor configuration was formed. The siliconization as a wall conditioning had been done for the first time on HL-2A since the start of the device's operation. By using siliconization a decrease in impurity was achieved. The characteristics of the siliconization and the effect of the wall conditioning on the plasma as well as on wall recycling were investigated.

3, Experimental Results

3.1, Effect of Divertor on Impurity

The plasma discharge can typically extend to more than 1s on HL-2A. The longest discharge achieved in 2004 campaign was 1.58s. A typical discharge with the divertor configuration has distinct regimes: the limiter phase in the early stage of a discharge without X-point, and the divertor phase with X-point, shown in Fig.1.
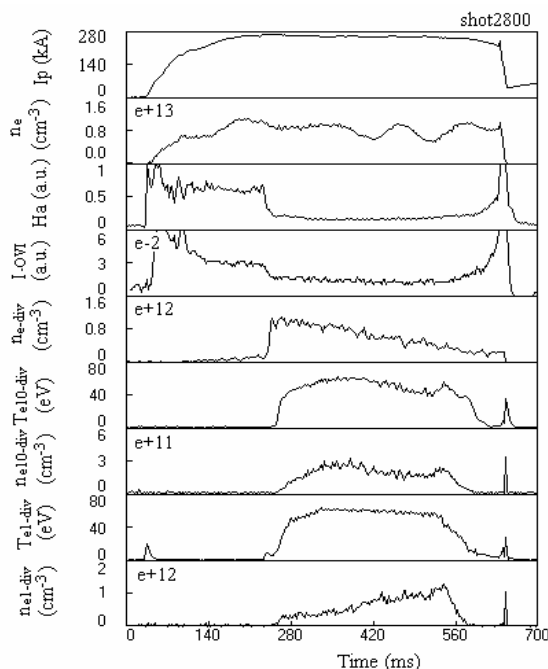

Fig.1, Typical waveforms of shot 2800

From top to bottom the parameters are plasma current I_p, line averaged electron density n_e, H_α intensity, intensity of OVI emission (103.2nm) I_{OVI} measured by VUV

monochromator, electron density in the divertor n_{e-div} measured by microwave interferometer, electron temperature $T_{e10-div}$ and density $n_{e10-div}$ in the high field side divertor chamber measured by probes located at the neutralized target plate, electron temperature T_{e1-div} and density n_{e1-div} in the low field side divertor chamber also measured by probes. The divertor configuration has been formed from 270ms to 600ms. When the divertor is fully formed the temperatures at the target plate both in the inner divertor and in the outer divertor increase to about 50eV. The electron density in the inner divertor chamber is higher than that in the outer divertor chamber which are $9.5\times10^{11}cm^{-3}$ and $2.7\times10^{11}cm^{-3}$, respectively. H_{α} intensity in the main plasma region decreases dramatically from 600a.u. to 160a.u. The decreasing rate is about 73%. During the whole discharge there is only the background gas puff. Therefore, the changes in the H_{α} intensity and the density in the divertor chamber are absolutely caused by the particle pumping capability of the divertor. In the main plasma region the emission from light Z impurity such as oxygen shown in item 4 obviously decreases from 28a.u. to 13a.u. with a total decreasing rate of 53%. The effect of the divertor on impurity and recycling of the wall can always be observed as soon as the divertor is fully formed.

By using a plasma transport code, B2, which is transferred from Germany and is only available in the scrape-off layer (SOL) and the divertor region [7], the distribution of the electron density and temperature in the plasma edge and the divertor region are calculated. The power, which goes through the separatrix from the plasma confinement region into the SOL region, is one of the important input parameters in the code. It is assumed to be 500kW under the condition of ohmic heating. The results are shown in fig.2. The distribution of the electron density is on the left and that of the temperature is on the right. Different colors are related to different values of density and temperature. The density is about $3-6\times10^{12}cm^{-3}$ and temperature is about 30-50eV near the last closed magnetic field surface. The calculated values of both density and temperature are very similar with the experimental values. It means that during the first operation stage of the divertor in the ohmic heating case on HL-2A the typical value of the plasma density is lower. Therefore, the typical temperature at the divertor

target plate is slightly higher than that of the other device with additional heating power. The experimental result is confirmed by the results of B2 code.
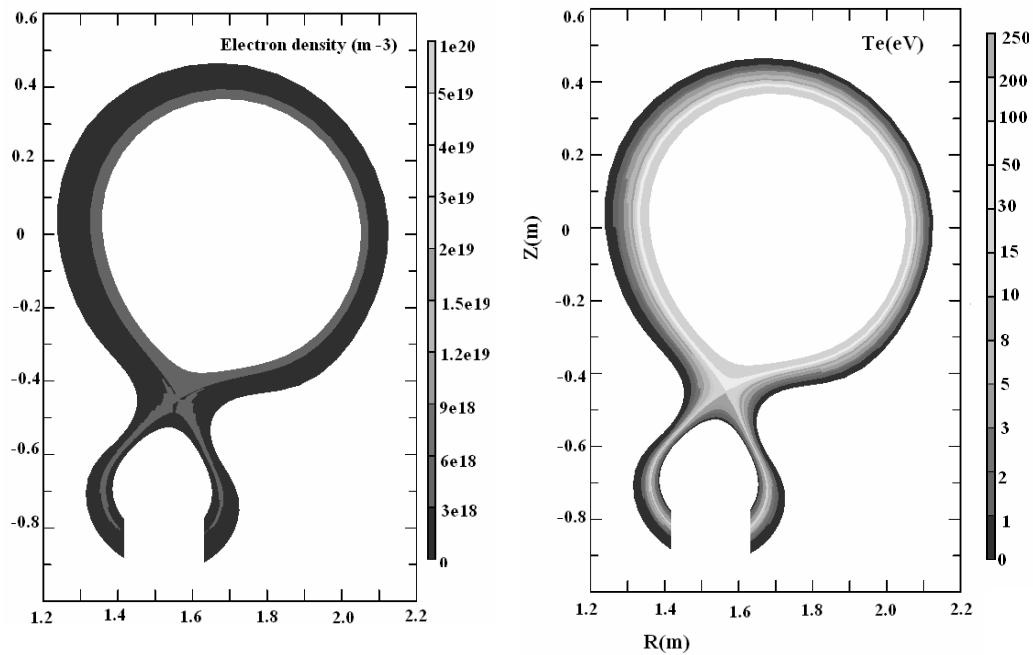
Fig.2   The results calculated by B2 code on the SOL and divertor

3.2, Effect of Siliconization on Impurity

Inside the vacuum vessel of HL-2A there are four pairs of fixed limiters and a segment of the moveable limiter. All of the fixed and moveable limiters are closed to the joint sections of the vacuum vessel and covered by the graphite tiles. The two domes of the divertors are also covered by the graphite tiles. The ratio of the area covered by graphite to the total inner surface of the vessel is about 0.1%. The vacuum volume and inner surface of HL-2A are $26m^3$ and $76m^2$, respectively. The main pump systems of HL-2A are comprised of six molecular pumps: 6×3500 (ls^{-1}) and two cryogenic pumps: 2×12000 (ls^{-1}), and pre-pump systems with two Roots pumps: 2×600 (ls^{-1}) and mechanical pumps: 2×70 (ls^{-1}), respectively. The volume of the two divertors is about $2\times7.2m^3$. The total leakage rate is 9×10^{-5} ($Pam3s^{-1}$) [8]. The obtained highest vacuum is 4.6×10^{-6} Pa up to now. At the beginning of an experimental campaign the vacuum chamber of the device is normally baked up to the temperature of120^0C. When the temperature of the wall is back to the room temperature the glow discharge cleaning with helium gas is taken, and then the plasma discharge is followed. Since the two big divertor chambers with the ratio of the divertor volume to the whole

vacuum volume being about 55% are as a huge reservoir of gas, they strongly affect the electron density of the plasma. Related research has been published as in reference [9]. The experimental results of the siliconization are presented below.

By using the glow discharge cleaning (GDC) with the mixture gas of SiH_4+He the containing film of silicon is coated on the internal surface of the vacuum vessel. The evaporation is continued for about 40 minutes each time. Before and after siliconization there is GDC with helium, and on each day 30-minute helium GDC is routinely taken just before the plasma discharge. Compared to boronization, siliconization can strongly absorb oxygen. Therefore, the intensity of oxygen is remarkably decreased after siliconization. Presented in figure 3 is the time evolution of the oxygen intensity comparing the discharges before and after siliconization.
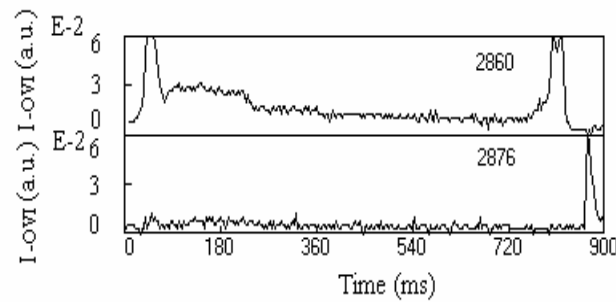
Fig.3, Comparison of oxygen before and after siliconization

Shot 2876 is the discharge after siliconization and shot 2860 is the one before siliconization. The plasma current of both shots are similar as I_p=213kA for shot 2860, I_p=228kA for shot 2876, respectively. The toroidal magnetic field and electron density of both shots are the same as 2.1T and $0.9\times10^{13}cm^{-3}$, respectively. The intensity of oxygen of the fifth ionization stage after siliconization is about ten times lower than that before the wall conditioning. Its intensity of the radiation drops from 70a.u. to 8a.u. at the peak and from 12a.u. to 5a.u. at the plateau of the discharge. The intensity on the radiation at the peak drops nearly 14 times after the wall conditioning. It means the reduction of impurity by siliconization is clear. The emission of carbon before and after siliconization has also been compared. The change in the intensity of carbon is similar with oxygen decreasing about ten times on its radiation peak and about one time on its plateau after siliconization.

The effect of siliconization on the whole plasma radiation measured by the bolometer array is also notable which is shown in figure 4. Shot 2870 and shot 2860 are the discharges after siliconization and before siliconization, respectively. The radiation profiles are directly gotten from the integral signal along the line of sight of the detector. The plasma parameters are similar for both shots. The total radiation level of plasma is very high and goes up to 40kW/m^{-2} before siliconization. After siliconization the total radiation drops down to 5 kW/m^{-2}. The ratio of the radiation before wall coating to that after coating is about 8 times. The capability of controlling impurity radiation loss of siliconization is very effective.
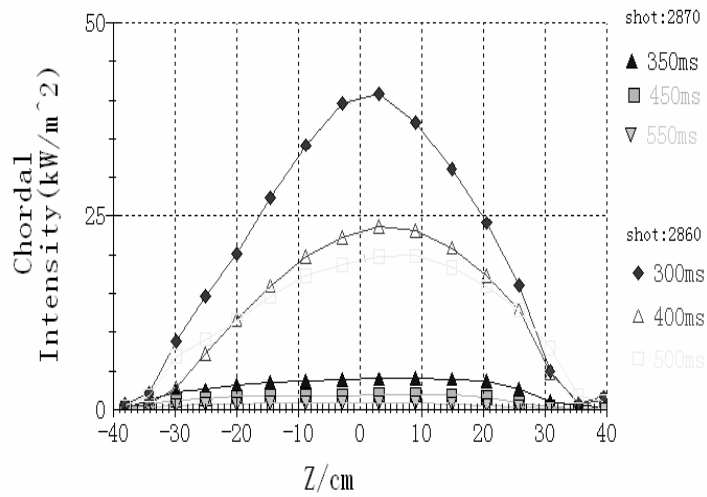
Fig.4, Plasma bolometer profile of line integration

3.3, Lifetime of Siliconization

It is hard to exactly define the lifetime of a coating. In general, the lifetime of the silicon coating is characterized by the shot numbers in which the coating has an obvious influence on the plasma performance. In the normal case, after siliconization impurity radiation decreases obviously, the quality of the discharge is improved, and the effective performance with good repetition is obtainable. The emission directly from the ionization stage of silicon has been investigated after siliconization. It is shown in fig. 5 with the emissions of SiIV（139.4nm） measured by VUV monochromator. The intensity of silicon rapidly decreases shot by shot just after siliconization. Shots 2874, 2875 and 3011 are the discharge of the first, the second

and the 34th plasma discharge after siliconization, respectively. The plasma currents for these shots are similar as 212kA, 219kA and 207kA, respectively. The toroidal magnetic field and line averaged electron density of the three shots are the same being 2.1T and $1 \times 10^{13} cm^{-3}$, respectively. For the first shot, 2874, the intensity of silicon is stronger at the value of about 20a.u. The intensity of silicon on the second shot, 2875, decreases to a half of the value of the first shot. And after 34 discharges the silicon intensity nearly disappears.
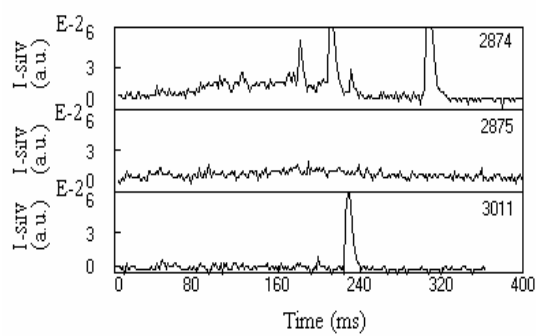
Fig. 5, Time evolution of silicon intensity of three shots just taken after siliconization
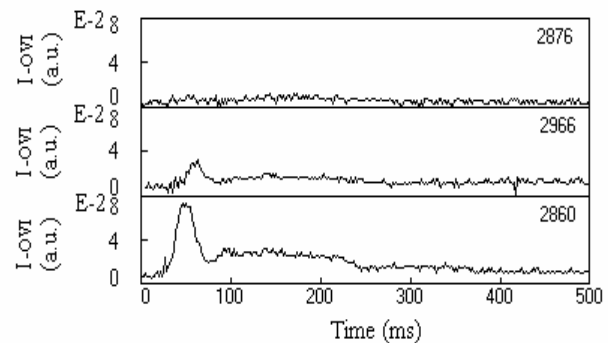
Fig.6, The intensity of oxygen vs. discharge number.

The intensity of silicon decreases shot by shot very quickly. It means that the slack layer of the atomic silicon on the coating surface loses quickly. The hard layer of the compound of silicon is present and it has a strong influence on impurity. Although the line emissions of silicon decreases rapidly as a function of the discharge number, even almost disappears, the effect of siliconization on the plasma properties is present all along and decreases gradually for a large number of discharges. Here let us focus on the effect of siliconization on impurity, which is shown in figure 6, with the intensity of oxygen (OIV 103.2nm). Shot 2876 and shot 2966 are the third and 92nd discharge after siliconization, and shot 2860 is the discharge before siliconization. The plasma parameters of the three shots are also similar. It is shown in figure 8 that the intensity of oxygen increases to a half of the value of shot 2876. The effect of the siliconization can be maintained to 160 or 180 discharges with the similar discharge parameters. In the normal case there may have 30 shots on one day. Therefore, the

effect of siliconization can extend to five or six days. This suggests that the lifetime of siliconization coating is not short and is comparable with the result of 140 shots on HL-1M. We should mention that HL-2A is a new device while HL-1M is a device being operated for seven years. Consequently, it may be due to the divertor configuration that keeps the wall away from the bombardment of the particle from plasma. That is just the function of the divertor on a tokamak. Impurity is obviously controlled by the divertor configuration and wall conditioning on HL-2A.

4, Summary

HL-2A is China's first divertor tokamak with two X-points. It was successfully operated under the condition of full divertor configuration formed in the 2004 experimental campaign. The reduction of impurity was clearly observed when the divertor configuration was formed. The siliconization as a wall conditioning was done for the first time on HL-2A in the 2004 campaign. The radiation of impurity was reduced by a large margin after the wall of the device was coated by silicon. The recycling of the wall was also affected by the wall conditioning. It is obvious that impurity is controlled by the divertor configuration and wall conditioning on HL-2A.

Acknowledgments

References

1　Pitcher C S, Stangeby P C, Plasma Phys. Control. Fusion, 1997, 39: 779

2　Liu Y, Ding X T, Yang Q W, et al, 20th IAEA Fusion Energy Conference, 2004, Vilamoura, Portugal, Nov.1-6 OV/5-1Ra

3　Cui Z Y, Wang Q M, Dong J F, et al, Plasma Science & Technology, 2004, 6: 2359

4　Li W, Cui Z Y, et al, 31ST EPS Conference on Plasma Physics, London, UK, 2004

5　Pan Y D, Hong W Y, Yi P, Internal report, 2004, CNIC／A－2004110, GF－A0081431 SWIP／A－2003050 (in Chinese)

6　Yang Q W, et al, Chinese Physics Letter, 2004, 21: 2475

7   Y.D Pan, 2003 Proc. of the 30th EPS Conference on Controlled Fusion and Plasma Physics, St. Petersburg **27A** P-1.148

8   Cao Z, et al, Nuclear Fusion and Plasma Physics, 2005, 25: 59 (in Chinese)

9   Wang M X, et al, Nuclear Fusion and Plasma Physics, 2004, 24: 265 (in Chinese)

Vertical One-dimensional Electron Cyclotron Emission Imaging Diagnostic for HT-7 Tokamak[*]

Jun WANG[1] , Xiaoyuan XU [1], Yizhi WEN [1], Changxuan YU[1], Baonian WAN [2]
N.C.Luhmann[3], Jian Wang[3], and Z.G. Xia[3]

[1]*Department of Modern Physics, University of Science and Technology of China, Hefei 230027, China*

[2]*Institute of Plasma Physics, the Chinese Academy of Sciences, Hefei 230031, China*

[3]*Department of Applied Science, University of California, Davis, California 95616*

Abstract A vertical resolved 16-channel electron cyclotron emission imaging (ECEI) diagnostic has been developed and installed on the HT7 Tokamak for measuring plasma electron cyclotron emission with a temporal resolution of 0.5 us. The system is working on a fixed frequency 97.5GHz in the first stage. The sample volumes of the system are aligned vertically with a vertical channel spacing of 11 mm, and can be shifted across the plasma cross-section by varying the toroidal magnetic field. The high spatial resolution of the system is achieved by utilizing a low cost linear mixer/receiver array and an optical imaging system. The focus location may be shifted horizontally via translation of one of the optical imaging elements. The detail of the system design and laboratory testing of the ECE Imaging optics are presented, together with HT7 plasma data.

Keywords: Electron cyclotron emission imaging, optical and electronic setting, electron temperature and its fluctuations

PACS: 52.70.Gw, 52.35.Hr, 52.25.Xz

1. Introduction

In magnetized toroidal plasmas such as those in tokamaks, the electron cyclotron emission (ECE) arises from the gyro motion of electrons. In optical thick plasma, the intensity of the ECE radiation is proportional to the local T_e. As the ECE frequency depends on the magnetic field, which is a monotonically decreasing function of the major radius, local T_e can be obtained by frequency resolved ECE measurements [1].

Conventional ECE radiometry uses a single antenna/receiver aligned along a horizontal chord in the direction of the major radius to measure electron temperature. It has been standard diagnostics for measuring plasma electron temperature profiles in magnetized toroidal plasmas since 1974 [2]. Its spatial resolution in the transverse direction of the sight line is limited by the

divergence of the beam pattern of the antenna, typically about 2-3 cm. And it is generally limited to 1D horizontal measurement along the major radius. The poloidal spatial resolution of such a system is very poor.

Recently, a novel plasma diagnostic, electron cyclotron emission imaging (ECEI)[3], has been developed and operated on the Texas Experimental Tokamak Upgrade (TEXT-U)[4, 5], the Rijnhuizen Tokamak Project (RTP)[6], the Torus Experiment for Technology Oriented Research (TEXTOR)[7, 8] tokamaks and the Large Helical Device (LHD) [9]. The principle of the diagnostic is illustrated in Fig.1. Instead of using a receiving horn antenna, it utilizes a vertically aligned schottky barrier diode mixer/receiver array [10] and special imaging optics so that it can achieve a high spatial resolution about 1cm. These diagnostic systems have demonstrated excellent poloidal spatial resolution and two dimensional measurement capabilities, and have proved to be an extremely useful tool for the study of fine scale structures of T_e profiles and small amplitude plasma fluctuations [4, 6, 11].

In continuation of this diagnostic development research, a two dimensional ECEI system will be installed on the HT-7 Tokamak. As the first stage of this project, a one-dimensional vertical 16 channel ECEI system working at a fixed 97.5GHz has been installed on the HT-7 Tokamak. In Sec.2, the ECEI optical design and its performance are discussed in detail. The details of the electronic system are presented in Sec.3. Preliminary plasma data are presented in Sec.4.

2. ECEI OPTICAL DESIGN AND PERFORMANCE

The optical layout of the HT-7 ECEI system is illustrated in Fig. 2. The system uses a horizontal diagnostic port window (HDPE, 40 cm high, 8 cm wide). The positions and focusing properties of lenses 1-3 and the substrate lens are designed to image the ECE layer onto the mixer array which resides on the back of the substrate lens. It includes four lenses: one substrate lens, two E plane focusing lens (lens 2 and lens 3), and one H plane focusing lens (lens 1). Both the E plane and H plane focusing lenses are cylindrical lenses so that the E plane and H plane can be focused individually. That makes it easy to adjust the focusing planes. By the translation of Lens 2, the E focusing plane can be easily shifted horizontally. And it also makes the lens easy to fabricate.

The antenna array is borrowed from Prof. Luhmann's group of U.C. Davis. It is the backup antenna array for ECEI system installed on TEXTOR. It is a dual dipole antenna, which offers numerous advantages over the slot bowtie antenna, including superior H-plane antenna patterns and a wider intermediate frequency (IF) bandwidth [7]. Because the array is not designed for using in 97.5GHz, the antenna pattern is not good as shown in Fig.3. This makes the spot size larger than the channel spacing and introduces some cross channel talk in the nearby channels.

Prior to the installation on HT-7, the channel positions and focal plane beam patterns of the ECEI system were characterized in the laboratory. The E Plane (vertical direction) focal plane patterns measured at 97.5GHz with d=640 mm

are shown in Fig.4. It is seen that the interchannel spacing is a uniform 11 mm on all channels, with a 1/e beam spot size that varies from 13 to 17 mm and with relatively low side lobe levels. The H plane (toroidal direction) spot size is approximately 23 mm, with an interchannel (staggered) spacing of 19 mm.

A fixed Gunn oscillator working at 97.5GHz with an output power of 40 mW is utilized as the local oscillator. This Gunn oscillator is made by RPG. The output of the Gunn oscillator is coupled to the mixer array by one spherical lens and one cylindrical lens comprised of HDPE. The two HDPE lenses transform the output from a W-band horn antenna to an elliptical beam, focused at the mixer array.

3. ECEI ELECTRONICS

Shown in Fig. 5 is the block diagram of one of the 16-channel IF detection circuits. Each signal from the array mixer is preamplified (~48 dB) by MiniCircuits's low noise amplifiers. Passed through the bandpass filters, the IF signals are converted into video signals by Metelics Corporation's MSS20000 series zero bias Schottky detector diodes. The diode detectors, video amplifiers, and low pass filters are integrated into compact, low cost IF detectors that are enclosed in shielding boxes approximately 7.5x6.5x4 cm^3 in size. The output voltage of the IF signal power (and thus proportional to T_e), and to match the ADC's dynamic range of -2.5-2.5 V. In order to apply the auto-correlation technique, The 3 dB frequency of the low pass filters is set to 1 MHz. A total of 16 IF detectors are fabricated for the 16 mixer channels. The IF frequency response, sensitivity, and video response of the 16 IF detectors have been tested and the maximum variation between channels is within 20%.

The signals coming out of the video amplifiers are recorded by four simultaneous DAQ cards: ACQ16PCI, which is made by D-TACQ. It could provide a sample rate up to 6 MSPS for 16 channels with 14 Bit resolution and 16 M sample length. The DAQ system uses differential input with a dynamic range of -2.5-2.5V and has a good immunity to the interference.

4. INITIAL EXPERIMENTAL RESULTS

The ECEI system was just installed on HT-7 in May 2005. The operational time has been very limited. It has only been tested in Ohmic discharges. Plotted in Fig. 6 are time histories of four ECEI signals for HT-7 shot 79227, normalized to unity and offset to better compare signals, showing significant sawtoothing activity during Ohmic discharges. The discharge conditions are: B$_0$=1.78T, Ipa=165kA, $\bar{n}_e = 2 \times 10^{13} cm^{-3}$. The corresponding radial location is at R=124cm The experimental data are still under processing. Improvement of the uniformities of the 16 channels are being made.

5. Acknowledgement

References

1. Hutchinson, I.H., *Principles of plasma diagnostics*. 1987, Cambridge [Cambridgeshire]; New York: Cambridge University Press. xv, 364 p.

2. A.E.Costley, R.J.H., J.W.M.Paul, J.Chamberlain, *Electron Cyclotron Emission from a Tokamak Plasma: Experiment and Theory*. Phys. Rev. Lett., 1974. **33**: p. 758.

3. Deng, B.H., et al., *ECE imaging of electron temperature and electron temperature fluctuations (invited)*. Review of Scientific Instruments, 2001. **72**(1): p. 301-306.

4. Deng, B.H., et al., *Mode structure of turbulent electron temperature fluctuations in the Texas Experimental Tokamak Upgrade*. Physics of Plasmas, 1998. **5**(12): p. 4117-4120.

5. Deng, B.H., et al., *ECE imaging of plasma T-e profiles and fluctuations*. Fusion Engineering and Design, 2001. **53**: p. 77-85.

6. Deng, B.H., et al., *Electron cyclotron emission imaging diagnostic system for Rijnhuizen Tokamak Project*. Review of Scientific Instruments, 1999. **70**(1): p. 998-1001.

7. Wang, J., et al., *Two-dimensional electron cyclotron emission imaging diagnostic for TEXTOR*. Review of Scientific Instruments, 2004. **75**(10): p. 3875-3877.

8. Deng, B.H., et al., *Electron cyclotron emission imaging diagnostic on TEXTOR*. Review of Scientific Instruments, 2001. **72**(1): p. 368-370.

9. Mase, A., et al., *Progress in millimeter-wave imaging diagnostics*. Fusion Science and Technology, 2003. **43**(1T): p. 237-242.

10. Hsia, R.P., et al., *Hybrid electron cyclotron emission imaging array system for Texas experimental tokamak upgrade*. Review of Scientific Instruments, 1997. **68**(1): p. 488-491.

11. Cima, G., et al., *Electron heat diffusivity in the sawtoothing tokamak core*. Plasma Physics and Controlled Fusion, 1998. **40**(6): p. 1149-1158.
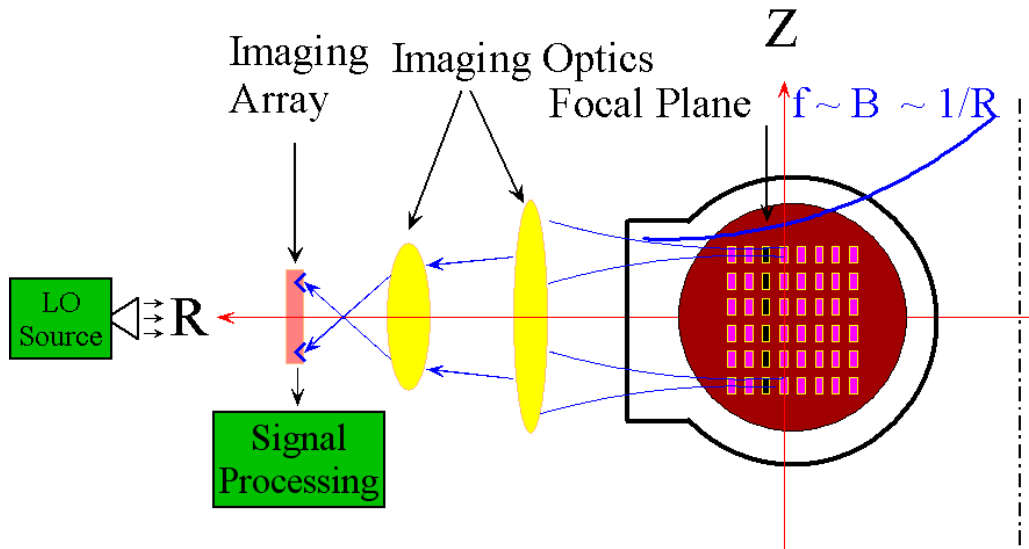
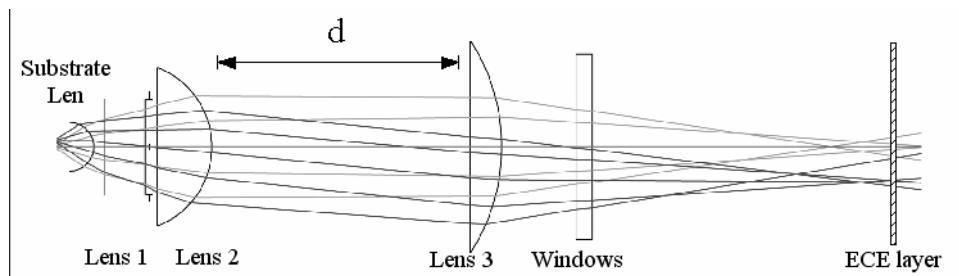FIG.1. Principle of the ECE imaging diagnostic
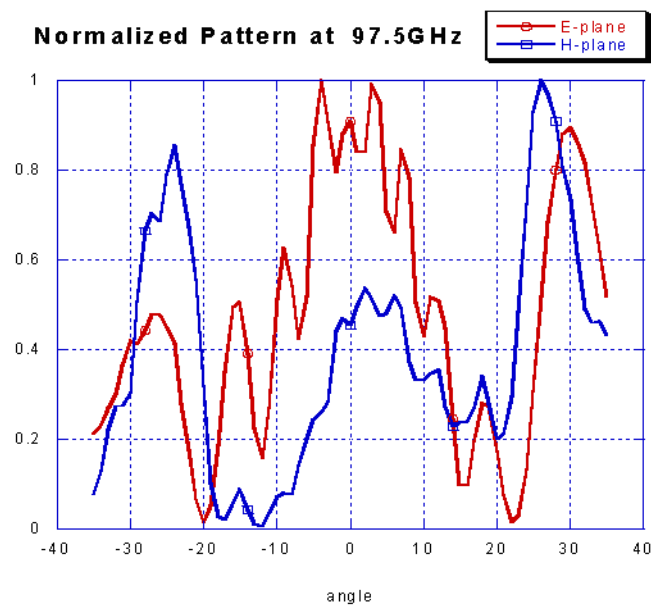

FIG. 2. Optical Layout of the HT-7 ECEI system

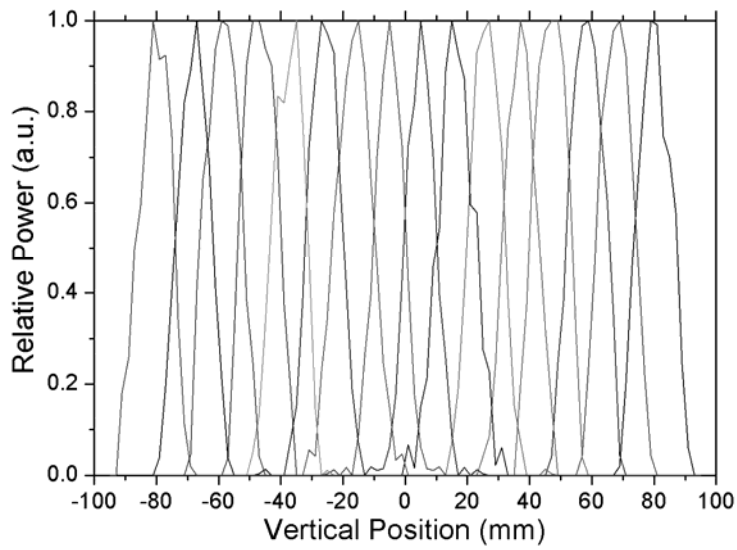FIG.3. The antenna pattern of the antenna array in 97.5GHz.

FIG.4. Focal plane (E) beam patterns, measured at 97.5GHz with d=640 mm.
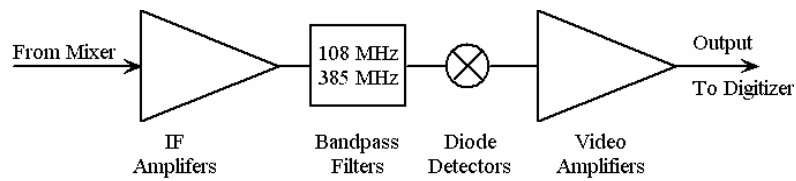

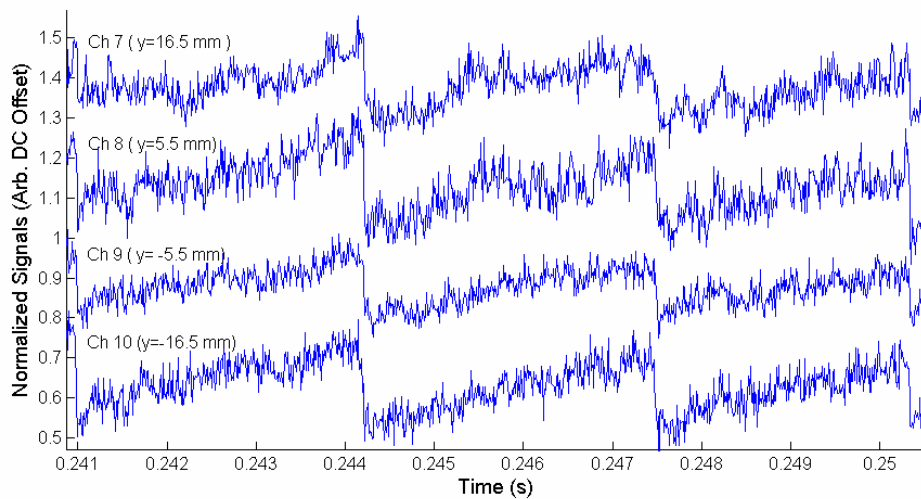FIG. 5 Block diagram of one of the 16-channel IF signal detection circuits.

FIG. 6 Time evolution of four ECEI signals.

Induced Charge of Spherical Dust Particle on Plasma-Facing Wall in Non-uniform Electric Field

Y. Tomita, R. Smirnov [1], S. Zhu [2]

National Institute for Fusion Science, 322-6 Oroshi-cho, Toki 509-5292 Japan
[1] The Graduate University for Advanced Studies, 322-6 Oroshi-cho, Toki 509-5292 Japan
[2] Institute of Plasma Physics, the Chinese Academy of Sciences, Hefei 230031, China

e-mail: tomita@nifs.ac.jp

Abstract

Induced charge of a spherical dust particle on a plasma-facing wall is investigated analytically, where non-uniform electric field is applied externally. The one-dimensional non-uniform electrostatic potential is approximated by the polynomial of the normal coordinate toward the wall. The bipolar coordinate is introduced to solve the Laplace equation of the induced electrostatic potential. The boundary condition at the dust surface determines the unknown coefficients of the general solution of the Laplace equation for the induced potential. From the obtained potential the surface induced charge can be calculated. This result allows estimating the effect of the surrounding plasma, which shields the induced charge.

Keywords: dust particle, induced charge, non-uniform electric field

1. Introduction

As the duration of plasma confinement in fusion devices becomes longer, the dust particles can be important to the behavior as an impurity to the core plasma and potential formation near plasma-facing plates. The absorption of radioactive tritium to the dust causes the safety issue in fusion reactors. In several fusion devices (TEXTOR-94, ASDEX-U, LHD, DIIID, NSTX etc.), the dust particles have been collected and their characteristics analyzed [1, 2], where the radii are wide-ranging between a few nm and a few tens μm. These dusts are composed mainly of metals and hydro-carbons, which are used for most divertors and plasma-facing materials. The understanding of the characteristics of dust particles in plasma, such as charging, absorption current, and acting forces, can be quite important for suppressing and controlling their behavior in plasma. The dust density in fusion devices usually is too low to bring collective effects. The investigation of the behavior of a single dust particle in boundary plasma is important. In this study we theoretically investigate the induced charge of the conducting dust particle with a spherical shape on the

plasma-facing wall in a non-uniform electric field.

2 Electrostatic potential

A spherical conducting dust particle with a radius R_d is attached on an infinitely extended conducting plane wall. The local electrostatic potential is composed of the sum of the external one ϕ_{ex} and the one ϕ_{in} due to induced charges on the conducting dust particle.

$$\phi(r,z) = \phi_{ex}(z) + \phi_{in}(r,z) \tag{1}$$

where (r,z) is the conventional cylindrical coordinate, where the origin is located at the contacting point of the spherical dust to the plane wall (Fig.1).
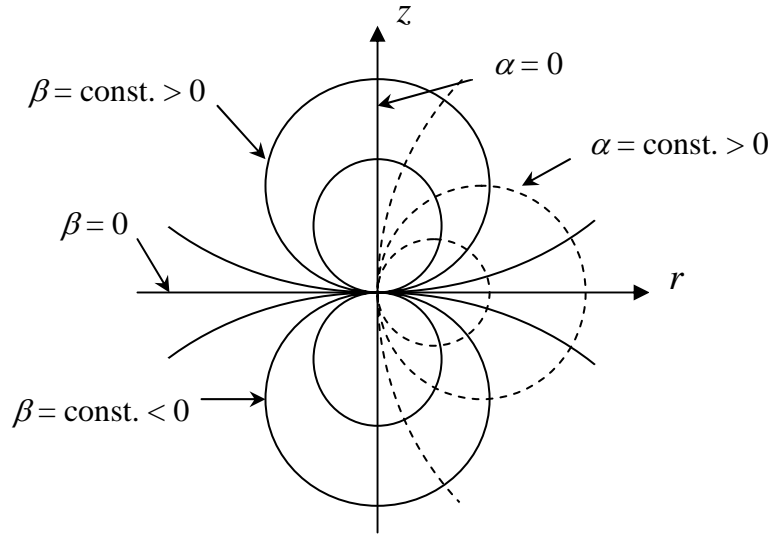
Fig.1　The cylindrical coordinate (r,z) and the bipolar coordinate (α,β). The infinitely extended conducting plane wall and the surface of the spherical dust are indicated by $\beta = 0$ and $1/2$, respectively.

In this study the externally applied potential is approximated to be non-uniform toward the normal direction to the plane wall, i.e. z,

$$\phi_{ex}(z) = \sum_{k=0}^{k_{max}} h_k z^k. \tag{2}$$

At the surface of the plane wall ($z = 0$) the external potential corresponds to the biased wall ϕ_w,

$\phi_{ex}(z=0) = \phi_w$, which is the same as the surface of the conduction dust. The potential ϕ_{in} due to

the induced charge satisfies the Laplace equation:

$$\frac{\partial}{\partial\alpha}\left(\frac{\alpha}{\alpha^2+\beta^2}\frac{\partial\phi_{in}}{\partial\alpha}\right) + \frac{\partial}{\partial\beta}\left(\frac{\alpha}{\alpha^2+\beta^2}\frac{\partial\phi_{in}}{\partial\beta}\right) = 0 \tag{3}$$

in the bipolar coordinate (α, β) [3]. The relation between the cylindrical coordinate (r,z) and the bipolar coordinate (α,β) is

$$z + i\,r = \frac{i\,R_d}{\alpha + i\,\beta},\qquad(4)$$

where i denotes the imaginary unit. Here the ranges of α and β are $0 \le \alpha \le \infty$ and $-\infty \le \beta \le \infty$, respectively (Fig.1). The plane $z = 0$, i.e. $\beta = 0$, corresponds to the wall surface and $\beta = 1/2$ ($\equiv \beta_0$) indicates the surface of the spherical dust particle. The general solution of the Laplace equation (3), which satisfies the condition $\phi_{in} = 0$ at $\beta = 0$, is given by

$$\phi_{i\,n}(\alpha,\beta) = \sqrt{\alpha^2 + \beta^2}\ \sum_{n=1}^{\infty} c_n\, I_{\lambda n}(\alpha,\beta)\ ,\qquad(5)$$

and

$$I_{\lambda n}(\alpha,\beta) \equiv \int_0^{\infty} d\lambda\ \lambda^n e^{-\beta_0 \lambda}\ \frac{\sinh(\beta\lambda)}{\sinh(\beta_0 \lambda)}\ J_0(\lambda\alpha),\qquad(6)$$

where J_0 is the first kind Bessel function of the 0-th order and the coefficients c_n's are determined by the boundary condition at the surface of the spherical dust. The external potential is also expressed in (α,β):

$$\phi_{ex}(\alpha,\beta) = \sum_{k=0}^{k_{\max}} h_k\, z^k = \sum_{k=0}^{k_{\max}} h_k \left(\frac{R_d \beta}{\alpha^2 + \beta^2} \right)^k,\qquad(7)$$

where the coefficient h_0 corresponds to the biased wall potential ϕ_w. With the aid of the relation

$$(-1)^n \frac{d^n}{d\beta^n} \frac{1}{\sqrt{\alpha^2 + \beta^2}} = \int_0^{\infty} d\lambda\,\lambda^n e^{-\beta\lambda}\, J_0(\lambda\alpha) \equiv I_n(\alpha,\beta),\qquad(8)$$

the external potential is expressed by the function $I_n(\alpha,\beta)$. The total electrostatic potential $\phi(\alpha,\beta)$ is obtained as a combination of the externally applied potential ϕ_{ex} and the induced potential ϕ_{in}. In the case of $k_{\max} = 4$,

$$\phi(\alpha,\beta) = \phi_{ex}(\alpha,\beta) + \phi_{in}(\alpha,\beta)$$

$$= \phi_w + \sqrt{\alpha^2 + \beta^2}\ \Big[\big(h_1 R_d + \frac{h_2 R_d^2}{3\beta} + \frac{h_3 R_d^3}{5\beta^2} + \frac{h_4 R_d^4}{7\beta^3} \big)\ I_1(\alpha,\beta)$$

$$+ \big(\frac{h_2 R_d^2}{3} + \frac{h_3 R_d^3}{5\beta} + \frac{h_4 R_d^4}{7\beta^2} \big)\ I_2(\alpha,\beta)$$

$$+ \big(\frac{h_3 R_d^3}{15} + \frac{2\,h_4 R_d^4}{35\beta} \big)\ I_3(\alpha,\beta) + \frac{h_4 R_d^4}{105}\ I_4(\alpha,\beta)\ \Big]$$

$$+ \sqrt{\alpha^2 + \beta^2}\ \sum_{k=1}^{\infty} c_k\, I_{\lambda k}(\alpha,\beta)\ ,\qquad(9)$$

where the first and second terms of the RHS of eq.(9) are the external potential and the last term corresponds to the induced potential. From the boundary condition at the surface of the spherical dust $\beta = \beta_0 = 1/2$:

$$\phi_{ex}(\alpha,\beta_0)+\phi_{in}(\alpha,\beta_0)=\phi_w,\tag{10}$$

the coefficients c_n's are expressed by the known quantities,

$$c_1=-(h_1 R_d+\frac{h_2 R_d^2}{3\beta_0}+\frac{h_3 R_d^3}{5\beta_0^2}+\frac{h_4 R_d^4}{7\beta_0^3}),$$

$$c_2=-(\frac{h_2 R_d^2}{3}+\frac{h_3 R_d^3}{5\beta_0}+\frac{h_4 R_d^4}{7\beta_0^2}),$$

$$c_3=-(\frac{h_3 R_d^3}{15}+\frac{2h_4 R_d^4}{35\beta_0}),$$

$$c_4=-\frac{h_4 R_d^4}{105},\text{ and}$$

$$c_k=0: k>5.\tag{11}$$

Note that the relation $I_n(\alpha,\beta_0)=I_{\lambda n}(\alpha,\beta_0)$ at the dust surface is used to derive the relations (11). Finally we obtain the total local potential consisting of the external and induced ones for the case of $k_{max}=4$:

$$\phi(\alpha,\beta)=\phi_{ex}(\alpha,\beta)+\phi_{in}(\alpha,\beta)$$

$$=\phi_w+\sqrt{\alpha^2+\beta^2}\ \{\ h_1 R\ I_{s1}+\frac{h_2 R^2}{3}\ (\frac{\beta_0-\beta}{\beta_0\beta}\ I_1+\frac{I_{s1}}{\beta_0}+I_{s2})$$

$$+\frac{h_3 R^3}{5}\ (\frac{\beta_0^2-\beta^2}{\beta_0^2\beta^2}\ I_1+\frac{I_{s1}}{\beta_0^2}+\frac{\beta_0-\beta}{\beta_0\beta}I_2+\frac{I_{s2}}{\beta_0}+\frac{I_{s3}}{3})$$

$$+\frac{h_4 R^4}{7}\ [\frac{\beta_0^3-\beta^3}{\beta_0^3\beta^3}\ I_1+\frac{I_{s1}}{\beta_0^3}+\frac{\beta_0^2-\beta^2}{\beta_0^2\beta^2}\ I_2+\frac{I_{s2}}{\beta_0^2}+\frac{2(\beta_0-\beta)}{5\beta_0\beta}\ I_3+\frac{2I_{s3}}{5\beta_0}+\frac{I_{s4}}{15}]\}\tag{12}$$

Here the function I_{sn} is defined as

$$I_{sn}(\alpha,\beta)\equiv\int_0^\infty d\lambda\ \lambda^n\frac{\sinh[(\beta_0-\beta)\lambda]}{\sinh(\beta_0\lambda)}\ J_0(\lambda\alpha).\tag{13}$$

3. Induced charge

The electric field of the normal direction to the spherical dust surface gives the charge density $\sigma_s(\alpha)$ at the spherical dust surface ($\beta=\beta_0=1/2$):

$$\sigma_s(\alpha)=\varepsilon_0 E_n\big|_{\beta=\beta_0=1/2}=\ \varepsilon_0\frac{\alpha^2+\beta_0^2}{R_d}\ \frac{\partial\phi}{\partial\beta}\bigg|_{\beta=\beta_0=1/2}$$

$$=-\varepsilon_0\frac{(\alpha^2+\beta_0^2)^{3/2}}{R_d}\{\ h_1 R_d\ I_{c20}(\alpha)$$

$$+\frac{h_2 R_d^2}{3}\left[\frac{I_{10}(\alpha)}{\beta_0^2}+\frac{I_{c20}(\alpha)}{\beta_0}+I_{c30}(\alpha)\right]$$

$$+\frac{h_3 R_d^3}{5}\left[\frac{2I_{10}(\alpha)}{\beta_0^3}+\frac{I_{c20}(\alpha)}{\beta_0^2}+\frac{I_{20}(\alpha)}{\beta_0^2}+\frac{I_{c30}(\alpha)}{\beta_0}+\frac{I_{c40}(\alpha)}{3}\right]$$

$$+\frac{h_4 R_d^4}{7}\left[\frac{3I_{10}(\alpha)}{\beta_0^4}+\frac{I_{c20}(\alpha)}{\beta_0^3}+\frac{2I_{20}(\alpha)}{\beta_0^3}+\frac{I_{c30}(\alpha)}{\beta_0^2}+\frac{2I_{30}(\alpha)}{5\beta_0^2}\right.$$

$$\left.+\frac{2I_{c40}(\alpha)}{5\beta_0}+\frac{I_{c50}(\alpha)}{15}\right],\tag{14}$$

where $I_{n0}(\alpha)\equiv\int_0^\infty d\lambda\ \lambda^n e^{-\beta_0\lambda}\ J_0(\lambda\alpha)$ and

$$I_{cn0}(\alpha)\equiv\int_0^\infty d\lambda\ \lambda^n\frac{J_0(\lambda\alpha)}{\sinh(\beta_0\lambda)}.\tag{15}$$

The induced charge Q_{din} on the conducting spherical dust is obtained

$$Q_{din}=\int_{S_d}\sigma_s dS=-2\pi\varepsilon_0 R_d^2\int_0^\infty\frac{\alpha}{(\alpha^2+\beta^2)^2}\frac{\partial}{\partial\beta}(\phi_{ex}+\phi_{in})\bigg|_{\beta=\beta_0=1/2}d\alpha$$

$$=-2\pi\varepsilon_0 R_d^2\left(d_1 h_1+d_2 h_2 R_d+d_3 h_3 R_d^2+\cdots\right)\tag{16}$$

where σ_s and S_d are the surface charge density (eq.(14)) and the dust surface area, respectively. In the case of $k_{\max}=4$, the numerical coefficients d_k's are

$$d_1=I_{qc2}$$

$$d_2=\frac{1}{3}\left(\frac{I_{q1}}{\beta_0^2}+\frac{I_{qc2}}{\beta_0}+I_{qc3}\right)$$

$$d_3=\frac{1}{15}\left[\frac{6I_{q1}}{\beta_0^3}+\frac{6(I_{q2}+I_{qc2})}{\beta_0^2}+\frac{3I_{qc3}}{\beta_0}+I_{qc4}\right]$$

$$d_4=\frac{1}{105}\left[\frac{45I_{q1}}{\beta_0^4}+\frac{15(I_{qc2}+2I_{q2})}{\beta_0^3}+\frac{3(5I_{qc3}+2I_{q3})}{\beta_0^2}+\frac{6I_{qc4}}{\beta_0}+I_{qc5}\right],\tag{17}$$

where $I_{qn}\equiv\int_0^\infty d\alpha\frac{\alpha I_{n0}(\alpha)}{\sqrt{\alpha^2+\beta_0^2}}=\int_0^\infty d\alpha\frac{\alpha}{\sqrt{\alpha^2+\beta_0^2}}\int_0^\infty d\lambda\ \lambda^n e^{-\beta_0\lambda}\ J_0(\lambda\alpha)$

$$=\int_0^\infty d\lambda\ \lambda^{n-1}e^{-2\beta_0\lambda}=\Gamma(n)/(2\beta_0)^n\tag{18}$$

and $\quad I_{qcn}\equiv\int_0^\infty d\alpha\frac{\alpha I_{cn0}(\alpha)}{\sqrt{\alpha^2+\beta_0^2}}=\int_0^\infty d\alpha\frac{\alpha}{\sqrt{\alpha^2+\beta_0^2}}\int_0^\infty d\lambda\ \lambda^n\frac{J_0(\lambda\alpha)}{\sinh(\beta_0\lambda)}$

$$= \int_0^\infty d\lambda \frac{\lambda^{n-1} e^{-\beta_0 \lambda}}{\sinh(\beta_0 \lambda)} = 2\, \Gamma(n)\, \varsigma(n) / (2\beta_0)^n \qquad (19)$$

Here $\Gamma(n)$ and $\zeta(n)$ are the Gamma and Rieman's Zeta functions, respectively. The first term of the RHS corresponds to the charge in the uniform electric field.

4. Conclusion

The induced charge of the conducting spherical dust particle on the conducting wall in the non-uniform electric field is calculated theoretically as well as the local electrostatic potential. The non-uniform electrostatic potential is approximated by the polynomial of the normal coordinate toward the wall. These results can be compared to the results from the particle computer simulation [4], where the total charge includes both the effects of the induced charges and plasma shielding. This theoretical analysis is useful to understanding the dust behavior in the boundary plasma [5].

References

[1] J. Winter, Plasma Phys. Control. Fusion, **40** (1998) 1201.

[2] J. Sharpe, et al., J. Nucl. Mater., **313-316** (2003) 455.

[3] N.N. Levedev and I.P. Skai'skaya, Z. Tech. Phys. **32** (1962) 375.

[4] R. Smirnov, Y. Tomita, T. Takizuka, and D. Tskhakaya, to appear in Contr. Plasma Phys.

[5] S. Krasheninnikov, Y. Tomita, R. Smirnov, and R. Janev, Phys. Plasma, **11** (2004) 3141.

Agenda

JSPS-CAS Core University Program Seminar on Production and Steady State Confinement of High Performance Plasmas in Magnetic Confinement Systems
27--29 July, 2005, Hefei, China
(each one with 25 min durations including 5 min. for discussion)

July 27, Wednesday, 2005

No	Start	End	Dura. min.	Title	Chairman	Speaker	Affiliation
	9:00	9:10	10	Opening ceremony	B. N. Wan	Coordinators	Japan China
1	9:10	9:35	25	Long pulse operation of high performance plasmas in JT-60U	B. N. Wan	S. Ide	JAERI
2	9:35	10:00	25	HT-7 long pulse experiments		Junyu Zhao	ASIPP
3	10:00	10:25	25	Long pulse ICRF discharges in LHD		R. Kumazawa	NIFS
4	10:25	10:50	25	IBW and ICRF experiment in HT-7 tokamak		Yanping Zhao	ASIPP
	10:50	11:05	15	Coffee break			
5	11:05	11:30	25	High Power Neutral Beam Injection in LHD	T. Watari	K. Tsumori	NIFS
6	11:30	11:55	25	Experiment observation of the pulse high pressure gas puffing on HL-2A		X. T. Ding	SWIP
7	11:55	12:20	25	Formation of edge transport barrier by LH transition and large reversed plasma current on LHD		K. Toi	NIFS
8	12:20	12:45	25	Dynamics of secondary large-scale structures in ETG turbulence simulation		Jiquan Li	SWIP
	12:45	14:00	75	Lunch break			
9	14:00	14:25	25	Formation of low aspect ratio torus equilibria by ECH	K. Toi	T. Maekawa	Kyoto Univ.
10	14:25	14:50	25	Preliminary experiment of plasma current startup by ECR wave on SUNIST spherical tokamak		Yexi He	Tsinghua Univ.
11	14:50	15:15	25	Density modulation experiments on HT-7 and LHD		K. Tanaka	NIFS
12	15:15	15:40	25	Dual-electrode Biasing Experiment in A Toroidal Plasma		Yi YU	USTC
	15:40	15:55	15	Coffee break			
13	15:55	16:20	25	ICRF Experiments and Potential Formation on the GAMMA 10 Tandem Mirror	Yexi He	M. Ichimura	Tsukuba Univ.
14	16:20	16:45	25	MHD flow layer formation at boundaries of magnetic islands in tokamak plasmas		Jiaqi Dong	SWIP
15	16:45	17:10	25	Magnetic islands observed by a fast-framing tangentially viewing soft X-ray camera on LHD and TEXTOR		S. Ohdachi	NIFS
16	17:10	17:35	25	Tomographic analysis of central MHD activities and radiation losses on the HL-2A and LHD		Yi Liu	SWIP
	19:00	21:00		Reception party			

July 28, Thursday, 2005

No	Start	End	Dura. Min.	Title	Chairman	Speaker	Affiliation
1	9:00	9:25	25	Divertor study in JT-60U	S. Ide	H. Kubo	JAERI
2	9:25	9:50	25	Poloidal divertor experiment in HL-2A		X. R. Duan	SWIP

3	9:50	10:15	25	Review of divertor study on LHD		T. Morisaki	NIFS
4	10:15	10:40	25	Divertor design for EAST		Shizeng Zhu	ASIPP
	10:40	10:55	15	Coffee break			
5	10:55	11:20	25	Theory of zonal flow in tokamak and helical plasmas	Shaojie Wang	T. Watari	NIFS
6	11:20	11:45	25	Measurement of zonal flow in HT-7 tokamak		Guosheng Xu	ASIPP
7	11:45	12:10	25	Suppression of neoclassical tearing modes towards stationary high-beta plasmas in JT-60U		A. Isayama	JAERI
8	12:10	12:35	25	Overall feature of EAST operation space by using simple Core-SOL-Divertor model		Y. Hiwatari	CRIEPI
	12:35	14:00	85	Lunch break			
9	14:00	14:25	25	Assessments of flow drive by use of Ion Bernstein Wave on Heliotron-J and HT-7 devices	Jiaqi Dong	Y. Torii	Kyoto Univ.
10	14:25	14:50	25	Advanced Tokamak Equilirium Theory		Shaojie Wang	ASIPP
11	14:50	15:15	25	Magnetic sensorless control of plasma position and shape in a tokamak		K. Nakamura	Kyushu Univ.
12	15:15	15:40	25	Low Frequency Instability in Magnetized Plasma Column		Jin-lin XIE	USTC
	15:40	15:55	15	Coffee break			
13	15:55	16:20	25	Spectroscopic study on impurity transport of core and edge plasmas in LHD	K. Nakamura	S. Morita	NIFS
14	16:20	16:45	25	Impurity Measurement and Study on HL-2A divertor tokamak		Z. Y. Cui	SWIP
15	16:45	17:10	25	Development of A New ECE Imaging System for Core		Jun WANG	USTC
16	17:10	17:35	25	Dust particle behaviors in boundary plasma of a fusion device		Y. Tomita	NIFS
	17:35	18:00	25	Closing acticity			
	18:10			Bus departure for hotel			
				July 29, Friday, 2005			
				Discussion of CUP working group			

List of Participants

Zhengying CUI
Southwestern Institute of Physics
P.O. Box 432, Chengdu, Sichuan, 610041, P. R.China
Tel: +86+28+82850312   Fax: +86+28+82850300
Email: cuizy@swip.ac.cn

Jiaqi DONG
Southwestern Institute of Physics
P.O. Box 432, Chengdu, Sichuan, 610041, P. R.China
Tel: +86+28+ 82932652   Fax: +86+28+ 82932202
Email: jiaqi@swip.ac.cn

Xuru DUAN
Southwestern Institute of Physics
P.O.Box 432, Chengdu, 610041 Chengdu, P.R.China
Tel: +86-28 82850 311   Fax: +86-28 82850 300
Email: duanxr@swip.ac.cn

Yexi HE
Department of Engineering Physics, Tsinghua University
Beijing 100084, P. R. China
Tel: +86-10-62791874   Fax: +86-10-62782658
Email: yexihe@mail.tsinghua.edu.cn

Ryouji HIWATARI
Nuclear Techonolgy Research Laboratory,
Central Research Institute of Electric Power Industry
2-11-1, Iwado Kita, Komae-shi, Tokyo 201-8511 JAPAN
Tel: +81-3-3480-2111-2567   Fax: +81-3-3480-2493
Email: hiwatari@criepi.denken.or.jp

Makoto ICHIMURA
Plasma Research Center, University of Tsukuba
1-1-1 Tennoudai, Tsukuba, Ibaraki 305-8577, JAPAN
Tel: + 81-29-853-6228   Fax: + 81-29-853-6202
Email: ichimura@prc.tsukuba.ac.jp

Shunsuke IDE
Large Tokamak Experiment and Diagnostics Division
Naka Fusion Research Establishment, JAERI
801-1 Mukouyama, Naka, Ibaraki, 311-0193 JAPAN
Tel: +81-29-270-7594   Fax: +81-29-270-7419
Email: ide@naka.jaeri.go.jp

Satoshi IDOH
Department of Administration
National Institute for Fusion Science
322-6 Oroshi-cho, Toki 509-5292, Japan
Tel: +81-572-58-2022   Fax: +81-572-58-2603
Email: ido.satoshi@nifs.ac.jp

Akihiko ISAYAMA
Naka Fusion Research Establishment
Japan Atomic Energy Research Institute
801-1, Mukoyama, Naka, Ibaraki, 311-0193 Japan
Tel: +81-29-270-7592   Fax: +81-29-270-7449
Email: isayama@naka.jaeri.go.jp

Akiko KATO
National Institute for Fusion Science
322-6 Oroshi-cho, Toki 509-5292 Japan
Tel: +81-572-58-2028   Fax: +81-572-58-2603
Email: kato.akiko@nifs.ac.jp

Hirotaka KUBO
Naka Fusion Research Establishment
Japan Atomic Energy Research Institute
801-01 Mukoyama, Naka-shi, Ibaraki-ken, 311-0193 Japan
Tel: +81- 29-270-7349   Fax: +81-29-270-7419
Email: kubo@naka.jaeri.go.jp

Ryuhei KUMAZAWA
National Institute for Fusion Science
322-6 Oroshi-cho, Toki 509-5292 Japan
Tel: +86-572-58-2194   Fax: +86-572-58-2622
Email: kumazawa@nifs.ac.jp

Jiangang LI
Institute of Plasma Physics, Chinese Academy of Science
P.O. Box 1126, Hefei, Anhui 230031, P.R. China
Tel: + 86-551-5591371   Fax: +86-551-5591310
Email: j_li@ipp.ac.cn

Jiquan LI
Southwestern Institute of Physics
P.O. Box 432, Chengdu, Sichuan, 610041, P. R.China
Tel: +86+28+82932520   Fax: +86+28+82932202
Email: lijq@swip.ac.cn

Yi LIU
Southwestern Institute of Physics
P.O. Box 432, Chengdu, Sichuan, 610041, P. R.China
Tel: +86-28-82850312   Fax: +86-28-82850300
Email: yiliu@swip.ac.cn

Takashi MAEKAWA
Faculty of Energy Science
Kyoto University, Kyoto 606-8501, Japan
Tel: +81-75-753-4730 Fax: +81-75-753-4732
Email: maekawa@energy.kyoto-u.ac.jp

Tomohiro MORISAKI

National Institute for Fusion Science
322-6 Oroshi-cho, Toki 509-5292 Japan
Tel: +86-572-58-2146   Fax: +86-572-58-2618
Email: morisaki@nifs.ac.jp

Shigeru MORITA
National Institute for Fusion Science
322-6, Oroshi-cho,Toki, 509-5292, Japan
Tel: +86-572-58-2226   Fax: +86-572-58-2618
Email: morita@LHD.nifs.ac.jp

Kazuo NAKAMURA
Research Institute for Applied Mechanics, Kyushu
University
6-1 Kasuga-koen, Kasuga City, Fukuoka, 816-8580
Japan
Tel: +81-92-583-7984   Fax: +81-92-573-6899
Email: nakamura@triam.kyushu-u.ac.jp

Chusei NAMBA
National Institute for Fusion Science
322-6, Oroshi-cho,Toki, 509-5292, Japan
Tel: +81-572- 8–2263   Fax: +81-572-58–2628
Email: namba@nifs.ac.jp

Satoshi OHDACHI
National Institute for Fusion Science
322-6, Oroshi-cho,Toki, 509-5292, Japan
Tel: +81-572-58-2230   Fax: +81- 72-58-2624
Email: ohdachi@nifs.ac.jp

Huasheng QIU
Bureau of International Cooperation, Chinese Academy
of Science
52, Sanlihe Road, Beijing, 100864, P. R. China
Tel: +86-10-68597224   Fax: +86-10-68511095
Email: hs-qiu@cashq.ac.cn

Zhongbin SHI
Southwestern Institute of Physics
P.O. Box 432, Chengdu, Sichuan, 610041, P. R.China
Tel: +86+28+82850310   Fax: +86+28+82850300
Email: shizb@swip.ac.cn

Kenji TANAKA
National Institute for Fusion Science
322-6 Oroshi-cho, Toki-shi 509-5292, Japan
Tel: +86-572-58-2231   Fax: +86-572-58-2624
Email: ktanaka@nifs.ac.jp

Kazuo TOI
National Institute for Fusion Science
322-6 Oroshi-cho, Toki-shi 509-5292, Japan
Tel: +81-572-58-2224   Fax: +81-572-58-2624
Email: toi@nifs.ac.jp

Yukihiro TOMITA
Theory and Computer Simulation Center
National Institute for Fusion Science
322-6 Oroshi-cho, Toki 509-5292 Japan
Tel: +81-572-58-2378   Fax: +81-572-58-2626
Email: tomita@nifs.ac.jp

Yuki TORII
Institute of Advanced Energy, Kyoto University
611-0011, Gokasho, Uji, Kyoto, Japan
Tel: +81-774-38-4745   Fax: +81-774-38-3535
Email: torii@center.iae.kyoto-u.ac.jp

Katsuyoshi TSUMORI
Particle Beam Heated Research Div
National Institute for Fusion Science
322-6 Oroshi Toki, Gifu 509-5292, Japan
Tel: +81-572-58-2206   Fax: +81-572-58-2622
Email: tsumori@nifs.ac.jp

Baonian WAN
Institute of Plasma Physics, Chinese Academy of
Science
P.O. Box 1126, Hefei, Anhui 230031, P.R. China
Tel: +86-551-5591352   Fax: +86-551-5591310
Email: bnwan@ipp.ac.cn

Jun WANG
CAS Key Laboratory of Plasma Physics
Department of Modern Physics
University of Science and Technology of China, Hefei
230026, China
Tel: +86-551-3603072   Fax: +86-551-3606149
Email: wangjun1978@ustc.edu

Kongjia WANG
Institute of Plasma Physics, Chinese Academy of
Science
P.O. Box 1126, Hefei, Anhui 230031, P.R. China
Tel: +86-551-5591319   Fax: +86-551-5591310
Email: kjwang@ipp.ac.cn

Shaojie WANG
Institute of Plasma Physics, Chinese Academy of
Science
P.O. Box 1126, Hefei, Anhui 230031, P.R. China
Tel: +86-551-5593268   Fax: +86-551-5591310
Email: sjwang@ipp.ac.cn

Testuo WATARI
National Institute for Fusion Science
322-6 Oroshi-cho, Toki-shi 509-5292, Japan
Tel: +81-572-58-2212   Fax: +81-572-58-2622
Email: watari@nifs.ac.jp

Yizhi WEN
Department of Modern Physics

University of Science and Technology of China,
Hefei 230026, China
Tel: +86-551-3603014   Fax: +86-551-3601164
Email: wenyz@ustc.edu.cn

Jikang XIE
Institute of Plasma Physics, Chinese Academy of Science
P.O. Box 1126, Hefei, Anhui 230031, P.R. China
Tel: +86-551-5591626   Fax: +86-551-5591310
Email: jkxie@ipp.ac.cn

Jinlin XIE
CAS Key Laboratory of Plasma Physics
Department of Modern Physics
University of Science and Technology of China, Hefei 230026, China
Tel: +86-551-3602852   Fax: +86-551-3606149
Email: jlxie@ustc.edu.cn

Guosheng XU
Institute of Plasma Physics, Chinese Academy of Science
P.O. Box 1126, Hefei, Anhui 230031, P.R. China
Tel: +86-551-5593282   Fax: +86-551-5591310
Email: gsxu@ipp.ac.cn

Hideyuki YAMAGUCHI
Beijing Office, Japan Society for the Promotion of Science
616, Library of Chinese Academy of Sciences
33 Beisihuan Xilu, Zhongguancun, Beijing 100080, P. R. China
Tel: +86-10-62538332   Fax: +86-10-62538664
Email: beijing@jsps.org.cn

Yi YU
CAS Key Laboratory of Plasma Physics,
Department of Modern Physics,

University of Science and Technology of China,
Hefei 230026, China
Tel: +86-551-360 3072   Fax: +86-551-3606149
Email: yuyi@mail.ustc.edu.cn

Junyu ZHAO
Institute of Plasma Physics, Chinese Academy of Science
P.O. Box 1126, Hefei, Anhui 230031, P.R. China
Tel: +86-551-5593274   Fax: +86-551-5591310
Email: zhaoj@ipp.ac.cn

Yanping ZHAO
Institute of Plasma Physics, Chinese Academy of Science

P.O. Box 1126, Hefei, Anhui 230031, P.R. China
Tel: +86-551-5593329   Fax: +86-551-5591310
Email: zhao_yp@ipp.ac.cn

Sizheng ZHU
Institute of Plasma Physics, Chinese Academy of Science
P.O. Box 1126, Hefei, Anhui 230031, P.R. China
Tel: +86-551-5593280   Fax: +86-551-5591310
Email: szhu@ipp.ac.cn

Liqun HU
Institute of Plasma Physics, Chinese Academy of Science
P.O. Box 1126, Hefei, Anhui 230031, P.R. China
Tel: + 86-551-5591604   Fax: +86-551-5591310
Email: lqhu@ipp.ac.cn

Shaohua DONG
Institute of Plasma Physics, Chinese Academy of Science
P.O. Box 1126, Hefei, Anhui 230031, P.R. China
Tel: + 86-551-5591601   Fax: +86-551-5591310
Email: shdong@ipp.ac.cn